



# Functional Nanomaterials from the Bottom-up Assembly of Colloidal Nanoparticles

## A Strategy Towards Efficient Thermoelectrics

Maria Ibáñez Sabaté

**ADVERTIMENT.** La consulta d'aquesta tesi queda condicionada a l'acceptació de les següents condicions d'ús: La difusió d'aquesta tesi per mitjà del servei TDX ([www.tdx.cat](http://www.tdx.cat)) ha estat autoritzada pels titulars dels drets de propietat intel·lectual únicament per a usos privats emmarcats en activitats d'investigació i docència. No s'autoritza la seva reproducció amb finalitats de lucre ni la seva difusió i posada a disposició des d'un lloc aliè al servei TDX. No s'autoritza la presentació del seu contingut en una finestra o marc aliè a TDX (framing). Aquesta reserva de drets afecta tant al resum de presentació de la tesi com als seus continguts. En la utilització o cita de parts de la tesi és obligat indicar el nom de la persona autora.

**ADVERTENCIA.** La consulta de esta tesis queda condicionada a la aceptación de las siguientes condiciones de uso: La difusión de esta tesis por medio del servicio TDR ([www.tdx.cat](http://www.tdx.cat)) ha sido autorizada por los titulares de los derechos de propiedad intelectual únicamente para usos privados enmarcados en actividades de investigación y docencia. No se autoriza su reproducción con finalidades de lucro ni su difusión y puesta a disposición desde un sitio ajeno al servicio TDR. No se autoriza la presentación de su contenido en una ventana o marco ajeno a TDR (framing). Esta reserva de derechos afecta tanto al resumen de presentación de la tesis como a sus contenidos. En la utilización o cita de partes de la tesis es obligado indicar el nombre de la persona autora.

**WARNING.** On having consulted this thesis you're accepting the following use conditions: Spreading this thesis by the TDX ([www.tdx.cat](http://www.tdx.cat)) service has been authorized by the titular of the intellectual property rights only for private uses placed in investigation and teaching activities. Reproduction with lucrative aims is not authorized neither its spreading and availability from a site foreign to the TDX service. Introducing its content in a window or frame foreign to the TDX service is not authorized (framing). This rights affect to the presentation summary of the thesis as well as to its contents. In the using or citation of parts of the thesis it's obliged to indicate the name of the author.

Programa de Doctorat en Física

# **Functional Nanomaterials from the Bottom-up Assembly of Colloidal Nanoparticles.**

## **A Strategy Towards Efficient Thermoelectrics**

Tesis que presenta Maria Ibáñez Sabaté  
per optar al títol de Doctor per la Universitat de Barcelona

Directors de la tesis:

**Dr. Andreu Cabot Codina**  
Professor agregat

i

**Prof. Joan Ramon Morante**  
Professor Catedràtic

Departament d'Electrònica  
Grup Materials Electrònics i Energia (M-2E)  
Institut de Recerca en Energia de Catalunya (IREC)



UNIVERSITAT DE BARCELONA





# Content

Acknowledgments .....	7
List of Publications .....	9
Authors' contributions .....	11
Preface .....	15
Summary of Results .....	17
Block 1: Colloidal synthesis .....	17
Block 2: Solution processing approach to produce bulk nanomaterials and their thermoelectric characterization .....	18
Block 3: Solution processing approach to produce highly homogenous bulk nanocomposites and their thermoelectric characterization .....	19
Resum en Català .....	21
Bloc 1: síntesi col·loïdal .....	21
Bloc 2: Producció de nanomaterials en bulk a partir de l'assemblament de nanopartícules processades en solució i la seua caracterització termoelèctrica. ....	22
Bloc 3: Producció de nanocompostos altament homogenis en <i>bulk</i> a partir de l'assemblament de nanopartícules heterogènies processades en solució i la seua caracterització termoelèctrica. ....	23
Chapter 1 .....	27
1.1 Colloidal Nanoparticles .....	27
1.2 Colloidal synthesis of NPs .....	28
1.2.1 Nucleation event.....	29
1.2.2 Growth.....	31
1.2.3. Purification of NP.....	32
1.2.4 Shape control.....	33
1.2.5 Synthesis of colloidal nanoheterostructures .....	35
1.3 Macroscopic arrays of nanoparticles .....	37
1.4 Thermoelectricity .....	39
1.4.1 Thermoelectric devices .....	40
1.4.2 Interdependence of the thermoelectric parameter .....	43
1.4.3 Enhancements by nanostructuring .....	44
1.4.4 Production of bulk nanomaterials .....	45



1.5 References .....	46
Chapter 2 .....	55
2.1 Abstract .....	55
2.2 Introduction .....	56
2.3 Experimental .....	58
2.4 Calculations .....	59
2.5 Results and Discussion.....	62
2.6 Conclusions .....	80
2.7 Referencies .....	80
Chapter 3 .....	84
3.1 Abstract .....	84
3.2 Introduction .....	85
3.3 Experimental .....	86
3.4 Results and Discussion.....	89
3.5 Conclusions .....	98
3.6 References .....	98
Chapter 4 .....	101
4.1 Abstract .....	101
4.2 Introduction .....	102
4.3 Experimental Section .....	104
4.4 Results and Discussion.....	107
4.5 Conclusions .....	121
4.6 References .....	121
Chapter 5 .....	125
5.1 Abstract .....	125
5.2 Introduction .....	126
5.3 Experimental .....	127
5.4 Results and Discussion.....	130
5.5 Conclusions .....	137
5.6 References .....	137
Chapter 6 .....	139
6.1 Abstract .....	139
6.2 Introduction .....	140

6.3 Experimental Section .....	142
6.4 Results and Discussion .....	145
6.5 Conclusions.....	157
6.6 References.....	157
Chapter 7 .....	161
7.1 Abstract.....	161
7.2 Introduction.....	162
7.3 Experimental.....	165
7.4 Results and Discussion .....	168
7.5 Conclusions.....	189
7.6 References.....	189
Conclusions .....	195
Future work .....	197
Curriculum Vitae .....	199
Annex .....	205



# Acknowledgments

I've been thinking for a while how to write this section. Somehow, it is really important to me to express my gratitude to the ones who have really helped me in this amazing journey. Since my first interview with Prof. Morante, I have been learning new things almost every day. During these last 4 years, I have met people who have changed the course of my life. So, this section is made for all of them. People, who have helped me, taught me or just listened to me.

My first block of acknowledgements is designated to Prof. Morante, for the chance he present to me and all his wisdom advises, to my FPU fellowship which financially support my life and visits to foreign laboratories, and to Dr. Cabot for introducing me, from my point of view, to one of the most exciting fields of research.

I would like to remark my gratitude to Dr. Cabot. Professionally, he has influenced me more than I ever could possibly imagine. He has opened my eyes, my mind to a new world and boosted my need to learn more and more every day. He gave me freedom and trusted my instincts. He encouraged and criticized my ideas equally to improve myself. He allow me to travel and visit important research group over the world. I must say, it is impossible to imagine all the experience lived during my PhD without him by my side. He has been the best mentor I could ever ask for. So, thank you so much for accepting me as your first student.

Now I would like to thank the people from the Functional Nanomaterials group, and specially Alexey. I strongly believe that without him most of my work would have taken at least double of time. Our talks about chemistry were always really inspiring and teach full. It's been a real pleasure to work by his side. Also I would like to say thank to Pablo, Fan, Wenhua, Doris, Raquel, Alex, Joost, Zhishan, Silvia, Ariadna and Joana for all the

unforgettable moments in the lab. It has been real pleasure to meet them all and share this journey.

A special mention should be done to Jordi and Reza, the TEM people. They fulfill the gaps on my knowledge about materials characterization and introduce the beauty into my papers with the most wonderful TEM images. Thank you very much for all your nice work.

I would also thank Stéphane who has performed the measurements of the thermal conductivity and heat capacity of all my samples.

I wish to express my acknowledgment to all the professors who have received me in their group: Prof. Reiss, Prof. Talapin, Prof. Snyder and Prof. Robinson. Also I want to thank all the people in their groups who help me to accommodate and showed me everything I needed to have a fruitful visit.

I also want to thank the people from Serveis Científicotècnics and UB with a special mention to Joan Mendoza for his incredible patience. Also, I want to thank all the people from the Advanced Materials Area at IREC. I hope the friendship we start doesn't end when our life path diverges.

And finally, I want to express my gratitude to my loved family and friends. I don't think it would be possible to fulfill my PhD without them.

Em sembla que a la vida camines i camines amb un objectiu i de vegades no t'adones de les coses que pots perdre pel camí. Durant aquest darrers quatre anys he estat absent, dedicant gairebé tota la meua energia a aquest projecte, sense destinar gaire temps a les persones que estimo. A pesar d'això, ells no m'han permès deixar-los enrera. Ells han omplert d'amor i esperança els meus dies més tristos. Sense ells no seria aquí, sense ells no me n'hauria sortit. Per això vull dedicar-los aquest treball. A la Mare, el Pare, en Ramon, en Raül, l'Anna, l'Arnau, la Núria, el Pep, l'Albert, i la Rosa. A la meua gent. Us estimo!

# List of Publications

The 6 publications contained in the list below are the ones to be considered for the evaluation of this PhD Dissertation. A copy of the published manuscripts with the integrated supporting information is presented as chapters 2 to 7 in the thesis. The as published version could be found in the Annex. A complete list of the author's publications, up dated on January 24<sup>th</sup>, is included in the Curriculum Vitae.

1. **M. Ibáñez**, P. Guardia, A. Shavel, D. Cadavid, J. Arbiol, J. R. Morante, and A. Cabot; "Growth Kinetics of Asymmetric Bi<sub>2</sub>S<sub>3</sub> Nanocrystals: Size Distribution Focusing in Nanorods"; *J. Phys. Chem. C*, 2011, 115 (16), 7947–7955
2. **M. Ibáñez**, D. Cadavid, R. Zamani, N. García-Castelló, V. Izquierdo-Roca, W. Li, A. Fairbrother, J. D. Prades, A. Shavel, J. Arbiol, A. Pérez-Rodríguez, J. R. Morante, and A. Cabot; "Composition Control and Thermoelectric Properties of Quaternary Chalcogenide Nanocrystals: The Case of Stannite Cu<sub>2</sub>CdSnSe<sub>4</sub>" *Chem. Mater.*, 2012, 24 (3), 562–570
3. **M. Ibáñez**, R. Zamani, A. LaLonde, D. Cadavid, W. Li, A. Shavel, J. Arbiol, J. R. Morante, S. Gorsse, G. J. Snyder, and A. Cabot; "Cu<sub>2</sub>ZnGeSe<sub>4</sub> Nanocrystals: Synthesis and Thermoelectric Properties" *J. Am. Chem. Soc.*, 2012, 134 (9), 4060–4063
4. **M. Ibáñez**, R. Zamani, W. Li, A. Shavel, J. Arbiol, J. R. Morante, and A. Cabot; "Extending the Nanocrystal Synthesis Control to Quaternary Compositions" *Cryst. Growth Des.*, 2012, 12, 1085-1090
5. **M. Ibáñez**, D. Cadavid, U. Anselmi-Tamburini, R. Zamani, S. Gorsse, W. Li, A. Shavel, A. M. López, J. Arbiol, J. R. Morante, and A. Cabot; Crystallographic Control at the Nanoscale

*to Enhance Functionality: Polytypic Cu<sub>2</sub>GeSe<sub>3</sub> Nanoparticles as Thermoelectric Materials*,  
*Chem. Mater.* 2012, 24 (23), 4615–4622

6. **M. Ibáñez**, S. Gorsse, R. Zamani, J. Fan, S. Ortega, D. Cadavid, J. Arbiol, J. R. Morante, and A. Cabot; *Core-shell nanoparticles as building blocks for the bottom-up production of functional nanocomposites: PbTe-PbS thermoelectric properties*, *ACS Nano* just accepted.

# Authors' contributions

The work presented in this dissertation has been carried out at the Electronics Department of the Physics Faculty at the University of Barcelona. The PhD student, **Maria Ibáñez**, has had primary responsibility for all the experimental work, data analysis, and manuscript writing and design in all the publications presented and the co-authors contributions for each paper are specified below these lines. Additionally the impact factor in 2011 of the corresponding journal is provided for each publication. None of these publications has been previously presented in any other PhD dissertation.

In all the publications J. R. Morante and A. Cabot have secured funding and planned research proposals. A. Cabot coordinated and strongly participated in the designing and writing of all the papers.

**Chapter 2: M. Ibáñez**, P. Guardia, A. Shavel, D. Cadavid, J. Arbiol, J. R. Morante, and A. Cabot; "*Growth Kinetics of Asymmetric Bi<sub>2</sub>S<sub>3</sub> Nanocrystals: Size Distribution Focusing in Nanorods*"; *J. Phys. Chem. C*, 2011, 115 (16), 7947–795

Impact factor 2011: **4.805**

P. Guardia and D. Cadavid participated in the materials synthesis and characterization. A. Shavel participated actively in the results discussion. J. Arbiol performed the HRTEM and atomic models.

**Chapter 3: M. Ibáñez**, R. Zamani, W. Li, A. Shavel, J. Arbiol, J. R. Morante, and A. Cabot; "*Extending the Nanocrystal Synthesis Control to Quaternary Compositions*" *Cryst. Growth Des.*, 2012, 12, 1085-1090

Impact factor 2011: **4.720**



R. Zamani and J. Arbiol performed the HRTEM analysis and atomic models. W. Li and A. Shavel participated in the materials synthesis.

**Chapter 4: M. Ibáñez**, D. Cadavid, R. Zamani, N. García-Castelló, V. Izquierdo-Roca, W. Li, A. Fairbrother, J. D. Prades, A. Shavel, J. Arbiol, A. Pérez-Rodríguez, J. R. Morante, and A. Cabot; “Composition Control and Thermoelectric Properties of Quaternary Chalcogenide Nanocrystals: The Case of Stannite  $Cu_2CdSnSe_4$ ” *Chem. Mater.*, 2012, 24 (3), 562–570

Impact factor 2011: **7.286**

D. Cadavid provided insight during thermoelectric measurements. R. Zamani and J. Arbiol performed the HRTEM analysis and atomic models. N. García-Castelló and J. D. Prades performed the *ab initio* calculations. V. Izquierdo-Roca, A. Fairbrother and A. Pérez-Rodríguez, performed Raman measurements and analysis. W. Li and A. Shavel participated in the materials synthesis.

**Chapter 5: M. Ibáñez**, R. Zamani, A. LaLonde, D. Cadavid, W. Li, A. Shavel, J. Arbiol, J. R. Morante, S. Gorsse, G. J. Snyder, and A. Cabot; “ $Cu_2ZnGeSe_4$  Nanocrystals: Synthesis and Thermoelectric Properties” *J. Am. Chem. Soc.*, 2012, 134 (9), 4060–4063

Impact factor 2011: **9.907**

R. Zamani and J. Arbiol performed the HRTEM analysis and atomic models. A. LaLonde and J. Snyder contributed in the Hot Pressing of the samples and the discussion of the thermoelectric results. D. Cadavid and S. Gorsse provided insight during thermoelectric measurements. W. Li and A. Shavel participated in the materials synthesis.

**Chapter 6: M. Ibáñez**, R. Zamani, W. Li, D. Cadavid, S. Gorsse, N. A. Katcho, A. Shavel, A. M. López, J. R. Morante, J. Arbiol, and A. Cabot; Crystallographic Control at the

*Nanoscale to Enhance Functionality: Polytypic Cu<sub>2</sub>GeSe<sub>3</sub> Nanoparticles as Thermoelectric Materials*, *Chem. Mater.* 2012, 24 (23), 4615–4622

Impact factor 2011: **7.286**

D. Cadavid, S. Gorsse and N. A. Katcho, participated in the thermoelectric analysis. R. Zamani and J. Arbiol performed the HRTEM analysis, atomic models and participated in the crystallographic discussion. W. Li, A. Shavel participated in the materials synthesis. A. M. López revised the manuscript critically.

**Chapter 7: M. Ibáñez**, S. Gorsse, R. Zamani, J. Arbiol, J. R. Morante, and A. Cabot; *Core-shell nanoparticles as building blocks for the bottom-up production of functional nanocomposites: PbTe-PbS thermoelectric properties*, *ACS Nano* Just Accepted

Impact factor 2011: **11.421**

S. Gorsse, S. Ortega and D. Cadavid participated in the thermoelectric analysis. R. Zamani and J. Arbiol performed the HRTEM analysis and atomic models. J. Fan performed the XPS analysis.

Dr. Andreu Cabot

and Prof. Joan Ramon Morante

certify the information provided above is true.

Barcelona, 24<sup>th</sup> of February 2013



# Preface

The work developed during this PhD has embraced several topics that I divide in three blocks. Each block contains two chapters in this dissertation. Additionally, a general introduction of the different topics is provided (Chapter 1). The first block corresponds to the study of colloidal synthetic routes to produce functional nanoparticles (Chapter 2 and 3). In the second block the developed nanoparticles are used to produce bulk nanostructured materials. The functional properties of the nanomaterials are also characterized in this second block. As the paradigmatic application for such bottom-up assembled nanostructured materials I considered thermoelectricity (Chapter 4 and 5). In the last block, I go one step beyond and design and prepare multiphase nanoparticles as building blocks for the bottom up production of nanocomposites with improved thermoelectric performance (Chapter 6 and 7).



# Summary of Results

## **Block 1: Colloidal synthesis**

---

Initially the study of colloidal synthesis for the production of functional nanomaterials has been carefully carried out (Chapter 2 and 3). The objective was to obtain the proper knowledge and skills to prepare colloidal nanoparticles that would allow us to design nanomaterials for fundamental studies and feasible applications. The first system studied was highly asymmetric nanocrystals:  $\text{Bi}_2\text{S}_3$  nanorods (Chapter 2). Nanorods with different aspect ratios were produced by controlling the reaction parameters (temperature and growth time). Furthermore a diffusion-reaction kinetic model to explain the growth kinetic of the ensemble of nanorods was developed. The model took into account the nanocrystal growth in the longitudinal and radial direction separately, and evaluated them as a function of their surface free energy, the monomer concentration and the nanorod dimensions. The results obtained and presented in Chapter 2 were published in *Journal of Physical Chemistry C* in 2011.

The next system studied was copper-based quaternary compounds:  $\text{Cu}_2\text{-II-IV-VI}_4$  (Chapter 3). Quaternary diamond-like chalcogenides nanostructures have generated a great deal of attention due to their multiple applications, such as photovoltaics, non-linear optics, thermoelectrics and topological insulators. The potential of these applications is strongly dependent on the nanoparticles properties: size, shape and composition. Nonetheless, there was a very limited control over such properties on these compounds due to complexity of the thermodynamics and kinetics of nucleation and growth of such complex structures. With the aim to cover such gap, the mechanism to achieve unprecedented size, shape and composition control in  $\text{Cu}_2\text{-II-IV-VI}_4$  nanocrystals were investigated. Additionally, the synthetic process designed was carefully chosen to be cost-effective and scalable to assure its relevance in a

future industrial implementation. The results obtained were published in *Crystal Growth and Design* in 2012.

## **Block 2: Solution processing approach to produce bulk nanomaterials and their thermoelectric characterization**

---

Several theoretical and experimental studies reveal the promising thermoelectric properties of  $\text{Cu}_2\text{XSnY}_4$  ( $\text{X}=\text{Zn}, \text{Cd}$ ;  $\text{Y}=\text{S}, \text{Se}$ ) compounds. Their complex crystallographic structures provide the material with an intrinsic low thermal conductivity. Moreover, the ample chemical and structural freedom of these compounds allows further tuning of the material properties to enhance functionality. It was demonstrated that by tweaking the composition of such compound it was possible to enhance their thermoelectric performance. The main idea was to replace Zn or Cd atoms by Cu, and thereby introduce an extra charge carrier (in this case holes). Such intrinsic doping allowed to increase the electrical conductivity without a detrimental reduction of the Seebeck coefficient, but even more important allow to reduce the thermal conductivity by the generated interstitials. With this in mind, we produced  $\text{Cu}_{2+x}\text{Cd}_{1-x}\text{SnSe}_4$  (Chapter 4) and  $\text{Cu}_{2+x}\text{Zn}_{1-x}\text{GeSe}_4$  (Chapter 5) nanoparticles with different compositions (different x) and tested their thermoelectric performance. Despite the reduction in the electrical conductivity due to the huge interface density of such nanostructured bulk material the overall figure of merit was slightly increased with respect to their bulk analogous thanks to the enormous phonon scattering at the grain boundaries. The results presented in Chapter 4 and 5 were published in *Chemistry of Materials* and in *Journal of the American Chemical Society* respectively in 2012.

### **Block 3: Solution processing approach to produce highly homogenous bulk nanocomposites and their thermoelectric characterization**

---

The highest thermoelectric performance has been reported for multi-phase nanomaterials or nanocomposites, where acoustic impedance mismatches at the interfaces between dissimilar structures boost phonon scattering. One of the most successful methods to produce nanocomposites is based in the spontaneous formation of nanoscale inclusion by controlling the thermal history of solid solution. However, such approach is not versatile in composition and it lacks control over the size, composition and phase of the crystalline domains. Considering the possibilities of solution-processed nanomaterials to overcome such lack of control, two different systems with different nature were analyzed.

In the first system,  $\text{Cu}_2\text{GeSe}_3$  (CGSe) nanoparticles were produced with nanometer scale control over their crystal phases (Chapter 6). By carefully adjusting the nucleation and growth conditions, ordered single-phase orthorhombic or disordered polytypic wurzite-zinc blenda CGSe nanoparticles could be produced. The obtained nanoparticles were compacted into pellets to produce single- and multi- phase nanocomposites and their thermoelectric properties were studied. The most relevant result was the significant lower thermal conductivity of the multi-phase nanocomposite, which resulted into a 2.5 fold increase of the thermoelectric figure of merit when compare with the single phase nanocomposite. The results shown in Chapter 6 were published in *Chemistry of Materials* in 2012.

The second approach studied the possibility to produce highly homogeneous nanocomposites by using core-shell nanostructure as building blocks (Chapter 7).  $\text{PbTe@PbS}$  core-shell nanoparticles were synthesized to produce  $(\text{PbTe})_{1-x}(\text{PbS})_x$  nanocomposites with tuned composition. The structural, chemical and thermoelectric properties of the obtained nanocrystal were carefully studied. Although the figure of merit obtained was lower than the analogous material in bulk, the results were really promising. Figure of merit up to 1.1 were



obtained which represents one of the highest values ever reported for nanomaterials produced by solution-techniques. The results expose in Chapter 7 has been just accepted for publication in *ACS Nano*.

# Resum en Català

El treball desenvolupat durant aquesta tesi doctoral engloba diverses temàtiques que s'han dividit en tres blocs. Cada bloc conté dos capítols. A més a més, com a Capítol 1 s'ha inclòs una introducció general de cadascuna de les temàtiques tractades. En el primer bloc, Capítols 2 i 3, s'estudien diferents síntesis col·loïdals per produir nanopartícules funcionals. En el segon bloc, Capítols 4 i 5, les nanopartícules desenvolupades s'utilitzen per produir materials nanoestructurats en *bulk* a partir del seu assemblatge. Les propietats funcionals d'aquests nanomaterials es caracteritzen també en aquest segon bloc. Com a aplicació paradigmàtica s'ha considerat la termoelectricitat. En l'últim bloc, Capítols 6 i 7, es va un pas més enllà i es dissenyen nanopartícules heterogènies com blocs de construcció per a la producció de nanocompostos amb millor rendiment termoelèctric.

## **Bloc 1: síntesi col·loïdal**

---

Inicialment, es va dur a terme un estudi acurat de la metodologia en síntesi col·loïdal per a la producció de nanomaterials funcionals (Capítols 2 i 3). Es perseguia obtenir els coneixements i habilitats necessàries per preparar nanopartícules col·loïdals que ens permetessin dissenyar nanomaterials en *bulk* amb les propietats adequades per a una determinada aplicació. El primer treball que es va realitzar tenia com a objectiu prioritari obtenir les condicions idònies per produir nanopartícules asimètriques de sulfur de bismut, concretament, *nanorods* (Capítol 2) amb la mínima distribució possible de mida i forma. Variant els paràmetres de reacció (temperatura i temps de creixement), es va aconseguir produir *nanorods* amb diferents longituds i gruixos. Addicionalment, es va desenvolupar un model cinètic de difusió-reacció per explicar el creixement del conjunt de *nanorods*. El model proposat té en compte el creixement de les nanopartícules en la direcció longitudinal

(longitud) i radial (gruix) per separat en funció de la seua energia lliure superficial, la concentració de monòmers i les dimensions del *nanorod*. Els resultats obtinguts i presentats en el Capítol 2 es van publicar a la revista *Journal of Physical Chemistry C* el 2011.

El següent sistema en el que es va treballar pretenia desenvolupar una ruta sintètica per produir nanopartícules quaternàries,  $\text{Cu}_2\text{-II-IV-VI}_4$  (Capítol 3). Les nanopartícules d'aquest tipus de compostos han despertat un gran interès per la seua aplicabilitat en camps diversos: energia solar fotovoltaica, òptica no lineal, termoelectricitat o aïllants topològics. El potencial d'aquestes aplicacions està fortament lligat a les propietats de les nanopartícules: mida, forma i composició. No obstant això, en aquest tipus de compostos hi havia un control molt limitat sobre aquestes propietats. Aquesta carència era deguda a les diferències termodinàmiques i cinètiques entre els diferents elements presents en les nanopartícules. Amb l'objectiu de cobrir aquest buit, es van investigar les condicions necessàries en la nucleació i el creixement de les nanopartícules per tal d'obtenir un bon control sobre la mida, la forma i la composició. A més, es va tenir especial cura en dissenyar un procés de síntesi amb alt rendiment i fàcilment escalable per assegurar la seua rellevància en una possible implementació industrial. Els resultats obtinguts es van publicar a la revista *Crystal Growth and Design* el 2012.

## **Bloc 2: Producció de nanomaterials en bulk a partir de l'assemblament de nanopartícules processades en solució i la seua caracterització termoelèctrica.**

---

Diversos estudis teòrics i experimentals han revelat les prometedores propietats termoelèctriques dels compostos  $\text{Cu}_2\text{XSnY}_4$  ( $X = \text{Zn, Cd}$ ,  $Y = \text{S, Se}$ ). Les seues complexes estructures cristal·logràfiques estan directament associades amb una baixa conductivitat tèrmica. D'altra banda, la gran llibertat química i estructural d'aquests compostos permet ajustar les propietats del material augmentant la seua funcionalitat. Es va demostrar que en ajustar la composició d'aquests compostos era possible millorar el seu rendiment

termoelèctric. L'estratègia consisteix en substituir àtoms de Zn o Cd per Cu, i amb això introduir portadors de càrrega addicionals (en aquest cas forats). Aquest dopatge intrínsec permet augmentar la conductivitat elèctrica del material sense una gran reducció del coeficient Seebeck, i addicionalment permet reduir una mica més la conductivitat tèrmica a causa dels defectes intersticials generats. Amb això en ment juntament amb les tècniques de síntesi desenvolupades en els treballs anteriors (Capítol 3), es va decidir produir nanopartícules de  $\text{Cu}_{2+x}\text{Cd}_{1-x}\text{SnSe}_4$  (Capítol 4) i  $\text{Cu}_{2+x}\text{Zn}_{1-x}\text{GeSe}_4$  (Capítol 5) amb diferents composicions (diferent  $x$ ), compactar-les per a la fabricació del nanomaterial en *bulk* i estudiar-ne el rendiment termoelèctric. Tot i la reducció en la conductivitat elèctrica a causa de l'alta densitat d'interfícies d'aquest material nanoestructurat, la figura de mèrit obtinguda va superar lleugerament la reportada pel seu anàleg en *bulk* gràcies a l'enorme dispersió de fonons en les fronteres de gra. Els resultats presentats en els Capítols 4 i 5 es van publicar en les revistes *Chemistry of Materials* i *Journal of the American Chemical Society*, respectivament, el 2012.

### **Bloc 3: Producció de nanocompostos altament homogenis en *bulk* a partir de l'assemblament de nanopartícules heterogènies processades en solució i la seua caracterització termoelèctrica.**

---

El rendiments termoelèctrics més elevats s'han obtingut per a materials nanoestructurats amb múltiples fases, és a dir, nanocompostos, on la dispersió de fonons es veu altament incrementada a causa de les diferències en les impedàncies acústiques en les interfícies entre les diferents estructures. Un dels mètodes més eficaços per produir nanocompostos es basa en la formació espontània d'inclusions nanomètriques mitjançant el control de la història tèrmica de la solució sòlida. No obstant això, aquest enfocament no és versàtil en la seua composició i no es pot controlar la mida, composició o fase dels dominis cristal·lins. En aquesta darrera part de la tesi es van estudiar les possibilitats de produir nanocompostos a partir de

nanoheteroestructures processades en solució. L'objectiu era utilitzar els coneixements adquirits en els dos blocs anteriors per dissenyar nanocompostos en *bulk* on es pogués tenir una àmplia llibertat en l'elecció de les fases cristal·logràfiques i controlar el mida dels nanocristalls. Amb aquest objectiu en ment es van investigar dos sistemes multifàsics de diferent naturalesa.

En el primer sistema, es van sintetitzar nanopartícules de  $\text{Cu}_2\text{GeSe}_3$  (CGSe) amb diferents fases cristal·lines dins de cada partícula (Capítol 6). Ajustant acuradament les condicions de nucleació i creixement, es va aconseguir produir nanoapartícules amb una sola fase cristal·logràfica ordenada (ortorròmbica) o diverses/vàries fases cristal·logràfiques desordenades (wurzita-zinc blenda). Les nanopartícules obtingudes es van compactar en pastilles per produir nanocompostos amb una única fase o amb múltiples fases i es van estudiar les seues propietats termoelèctriques. El resultat obtingut més rellevant va ser la gran reducció en la conductivitat tèrmica del material nanocompost de múltiples fases gràcies a la qual es va aconseguir un increment de 2.5 vegades en la figura de mèrit respecte del material nanoestructurat d'una única fase. Els resultats mostrats en el Capítol 6 es van publicar en la revista *Chemistry of Materials* el 2012.

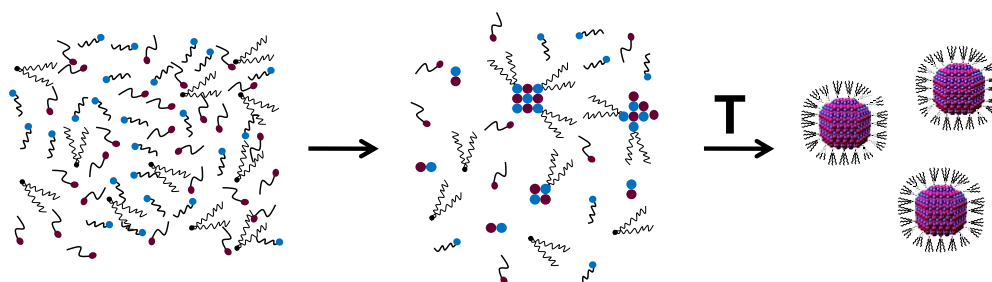
Un segon plantejament va ser estudiar la possibilitat de produir nanocompostos altament homogenis mitjançant l'ús de nanopartícules *core-shell* com a blocs de construcció dels nanocompostos (Capítol 7). Es van sintetitzar nanopartícules *core-shell* de  $\text{PbTe@PbS}$  amb diferents mides del *core* i la *shell* de manera que es poguessin obtenir mitjançant el seu assemblatge nanocompostos de  $(\text{PbTe})_{1-x}(\text{PbS})_x$  amb different composicions. Les propietats químiques, estructurals, i termoelèctriques d'aquests nanocompostos es van estudiar acuradament. A pesar que la figura de mèrit obtinguda va resultar ser inferior a la del material anàleg en *bulk*, els resultats van ser molt prometedors. Es va obtenir una figura de mèrit de 1.1, el que representa un dels valors més alts mai reportats per a nanomaterials produïts en

solució. Els resultats exposats en el Capítol 7 han recentment acceptats per a la seva publicació en la revista *ACS Nano*.



# Chapter 1

## Introduction to block 1: Colloidal synthesis



### 1.1 Colloidal Nanoparticles

---

Colloidal Nanoparticles (NPs) are inorganic particles with nanometric size grown in solution and stabilized by a layer of surfactants attached to their surface. The inorganic core consists of hundreds to a few thousand atoms each and their size ranges from 1 to 100 nm. In this regime, materials possess special properties directly related to their high surface-to-volume ratio, their tiny sizes, and the possible quantum confinement.<sup>1</sup>

The physical properties of NPs are strongly influenced by their relatively high number of weakly bonded surface atoms. One of the best known consequences of this high surface-to-volume ratio is the decrease of the melting temperature with the NP size.<sup>2</sup> Other examples are the higher NPs chemical reactivity,<sup>3,4</sup> and their self-cleaning capability.<sup>5</sup>

When the NP size is of the same magnitude as the wavelength of the electron wave function, quantum confinement effects are observed. Under such circumstances, the density of their electronic states, which control many physical properties, can be easily tuned by



adjusting NP size, shape or composition.<sup>6</sup> New phenomena, such as size dependent band gap<sup>7-10</sup> or shifting of the plasmon resonance<sup>11-14</sup> can take place.

These size-tunable characteristics offer unique opportunities to tailor the materials properties to fulfill a wide variety of applications: i.e. optically transparent layers,<sup>15</sup> thin-film electrodes,<sup>16</sup> superparamagnetic nanoparticles,<sup>17</sup> photodetectors,<sup>18</sup> light-emitting devices,<sup>19, 20</sup> sensors,<sup>21</sup> radio frequency tags, solar cells,<sup>22</sup> thermoelectrics.<sup>23-25</sup>

## 1.2 Colloidal synthesis of NPs

---

Fine control of NP properties is extremely important for further progress in fundamental studies and technological applications.<sup>6</sup> Reproducible synthetic approaches to produce inorganic NPs with uniform shape, size and composition have been extensively studied for over the last two decades.<sup>26, 27</sup>

A reaction system consists of three components: precursors, organic surfactants, and solvents. Typically a colloidal synthetic route involves three consecutive events: nucleation, growth and purification of the NPs.<sup>6, 28, 29</sup> Temporal separation between nucleation and growth is required to produce NPs with a narrow size distribution.<sup>30</sup> The most common method used for such finality is the hot-injection technique,<sup>31</sup> where the precursors are rapidly injected into a hot solvent with the subsequent temperature drop. Although the separation of these two events can be also accomplish by heating-up the reaction mixture. Additionally nucleation and growth should be kinetically balanced, otherwise bulk crystals or molecular species could be produce. The proper balance of these two different processes is usually addressed empirically by searching the good combination of chemicals (precursors, surfactants and solvents) and reaction conditions (injection temperature, reaction temperature and growth time). Among them, surfactants play a key role during NPs formation. Most common surface ligands are long-chained, carbon-based molecule with at least one coordinating functional group. Typical

examples are alkyl phosphonic acids, fatty acids, and amines. The energy with which surfactant molecules adhere to the surface of growing NPs needs to allow a dynamic solvation. Surfactants need to be able to go on and off the NPs surface, controlling in this way the surface accessibility to monomers and thus determining the NP growth rate.<sup>31</sup> Additionally, surfactants determine the NPs solubility, their ability to adhere to a substrate, and their surface charge.

In the following section, a classical nucleation and growth model will be used to describe the processes occurring during colloidal NPs formation. Although this model represents a useful guide to understand such phenomena, its limitations must be mentioned. While the model considers the formation of spherical NP nucleus, nucleation and growth appear to go through a number of discrete, magic-sized clusters.<sup>32, 33</sup> Additionally, the model fails to explain the sensitive relationship between NP growth and the molecular interactions between ligands and solvents. It also fails to describe the crystallographic detail of the NP facets. Advanced studies on the formation of colloidal NPs have proven such deficiencies and have introduced new knowledge to overcome the current hurdles in designing new NPs.<sup>34</sup>

### 1.2.1 Nucleation event

A high energy barrier to spontaneous homogeneous nucleation exists. The free energy change ( $\Delta G$ ) related with nucleation depends on the variation of the chemical potential ( $\Delta\mu$ ) required to convert molecular precursors (monomers) into a crystalline solid (driving energy), and the surface energy ( $\gamma$ ) necessary to overcome the particle/solution interface. Considering spherical particles with radius  $r$ , it can be expressed as

$$\Delta G = \frac{4}{3}\pi r^3 \cdot \Delta\mu + 4\pi r^2 \cdot \gamma$$

The driving energy can be described in terms of the monomer concentration (S). A High concentration of monomers present into the solution is required to overcome the height of the energy activation barrier for nucleation. To produce highly uniform NPs, it is necessary to force a nucleation event and to prevent additional nucleation during the following growth process.<sup>35</sup> The idea is to cause a burst of nucleation which will generate NPs with nearly the same growth histories. Considering the hot-injection as the experimental approach for such goal, a temporal evolution of the reaction temperature and concentration of monomers is presented in figure 1. The injection produces a rapid increase of the monomers concentration in the solution, which is necessary to induce nucleation, and the temporary drop of the solution temperature. Due to the nuclei formation, the monomer concentration is strongly reduced. At this point the NPs concentration reaches a maximum. This point represents the transition between the nucleation and the growth event, after which the number of NPs will either remain constant or decrease depending on the growth mode.<sup>36</sup>

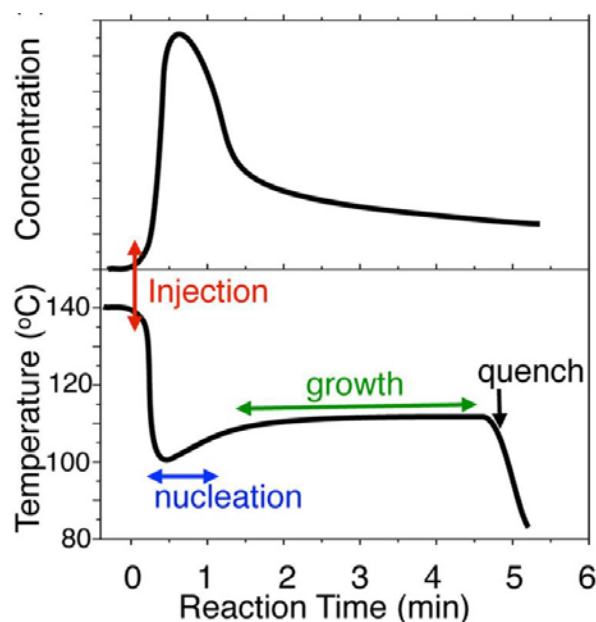


**Figure 1.** Typical concentration and reaction temperature profiles illustrating the temporal separation of the nucleation and growth event.<sup>36</sup>

## 1.2.2 Growth

The NPs growth process can occur in two different modes, ‘focusing’ and ‘defocusing’, depending on the concentration of monomers present in the solution. Figure 2 represents the dependence of the growth rate on the size of the nanoparticle for two different monomer concentrations.

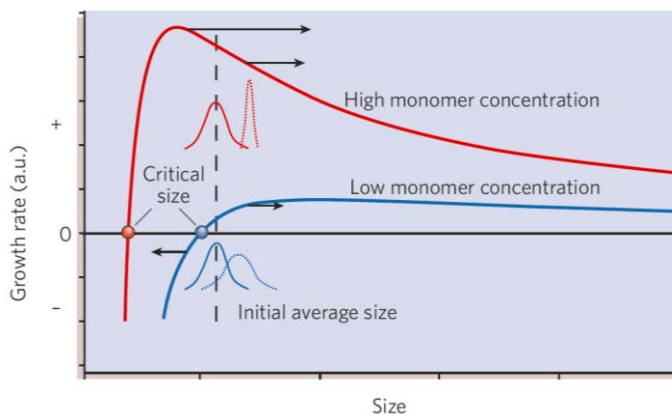


**Figure 2.** Growth rate dependence on the nanoparticle size for low and high concentration of monomers.<sup>31</sup>

Very tiny NPs possess a larger fraction of active surface atoms, which make them highly unstable. As their size increase, the surface-to-volume ratio decreases, and the NPs become more stable and grow. The free energy expressed in the nucleation section predicts the existence of a critical size at which NPs neither grow nor dissolve ( $d\Delta G/dr = 0$ ). The critical size and the growth rates are dependent on the monomer concentration, the molecular volume of the NPs ( $v$ ), the Boltzmann constant ( $k_B$ ); and the temperature (T) by the equation:

$$r_c = 2\gamma v/k_B T \ln S$$

Lower monomer concentrations favor larger critical sizes and lower growth rates. The depletion of monomers due to the NPs growth eventually results in a larger critical size than the average size present and the system enters in the Oswald-ripening regime. In this regime, larger NPs grow at the expenses of the dissolution of smallest ones broadening the size

distribution.<sup>29</sup> However, if the concentration of monomers is kept high enough during the NPs growth, the smaller NPs grow faster than the larger ones, and the size distribution can be focused down.<sup>37</sup> This is known as size focusing which is optimal when the monomer concentration is kept such that the average NPs size is slightly larger than the critical size.<sup>31</sup> The condition to establish the focusing or defocusing regime has been addressed theoretically and proven experimentally for an ensemble of spherical NPs.<sup>38, 39</sup> The model determined two general strategies to obtain narrow size distribution of NP: i) diffusion-controlled regime (controlling the diffusion or mass-transfer coefficient); and ii) increase surface tension at the NP-solvent interface. This model was extended lately for nanorods.<sup>40</sup>

### **1.2.3. Purification of NP**

Once the NPs growth is stopped a purification step is necessary to separate them from the free ligand molecules and the non-reacted monomers. Efficient purification is critical to any future use of the NPs. Moreover, the final properties of the NPs will strongly depend on the purification history.<sup>41, 42</sup> There are several methods to purify the NPs: magnetic separation,<sup>43</sup> selective precipitation,<sup>44 45</sup> filtration/diafiltration,<sup>46</sup> electrophoresis,<sup>47, 48</sup> and density gradient ultracentrifugation<sup>49</sup> are some examples. However, the most common technique for purification of the NP produced by organometallic synthesis is the precipitation/dissolution technique.

### 1.2.4 Shape control

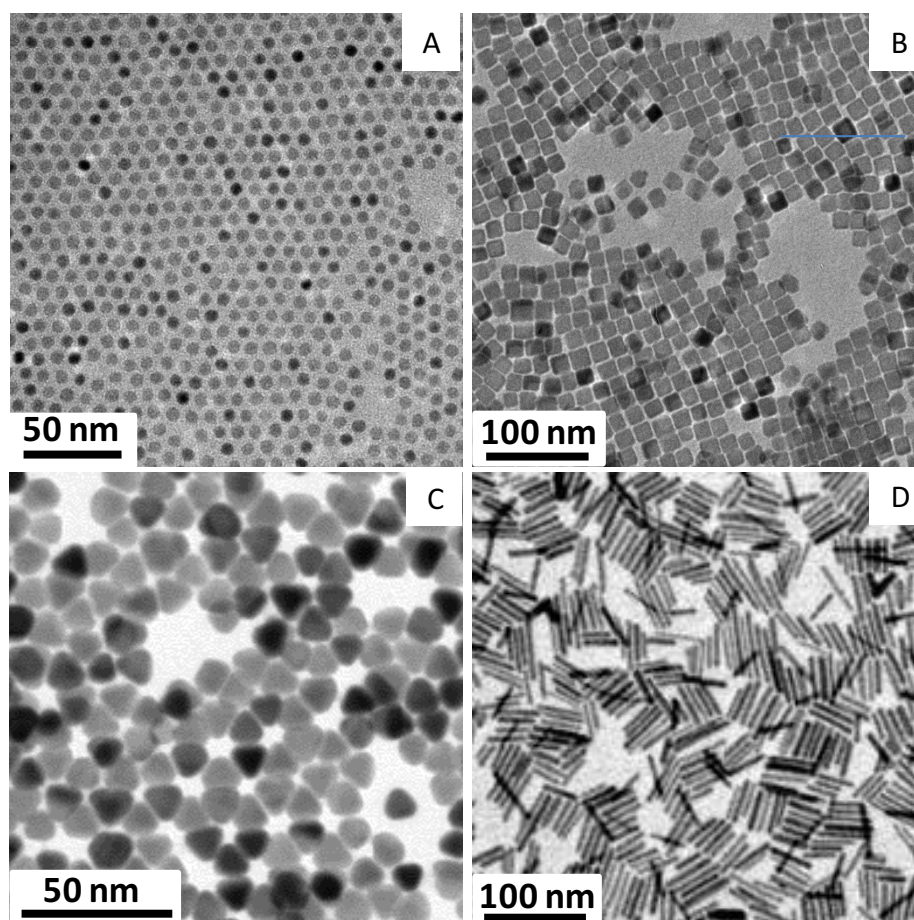


**Figure 3.** Examples of inorganic nanoparticles with different shape and morphologies synthesized by colloidal chemistry: <sup>50</sup> a) PbS spheres; b) PbTe cubes; c) Cu<sub>2</sub>CdSnSe<sub>4</sub> tetrahedrons; d) Bi<sub>2</sub>S<sub>3</sub> nanorods.

The NP shape can be controlled by two different manners. NP can be formed under thermodynamic or kinetic control to yield equilibrium or non-equilibrium shapes. The first approach is based on modifying the NP surface energy. Thermodynamics suggest that the final shape of the NP is determined by the surface free energy of individual crystallographic faces. The final NP shape will correspond to the minimum surface free energy.<sup>51, 52</sup> Although this theory explains most of the morphological evolution of NP, cannot account for the formation of highly anisotropic shapes which are metastable, high energy forms. Such kind of NPs can be only obtained under kinetic control conditions. In a kinetically controlled regime,

high growth rates results in the faster growth of high-energy facets than low-energy facets.<sup>31</sup> By choosing the appropriate surfactants it is possible to block or limit the dynamic solvation on certain facets reducing their growth rate with respect to others.<sup>53-57</sup> Additionally, in the kinetic growth regime, it is possible to create sequences of events to produce more complex shapes such as tetrapods.<sup>58</sup>

Another important approach for the formation of complex NP morphologies is by oriented attachment via dipole-dipole attractions.<sup>59-61</sup> Nanorods, nanowires, nanorings and nanosheets are some examples of the possible morphologies obtained by dipole-mediated alignment. Figure 4, shows a schematic illustration of the formation of a nanosheet by oriented attachment, using as a model PbS NPs.

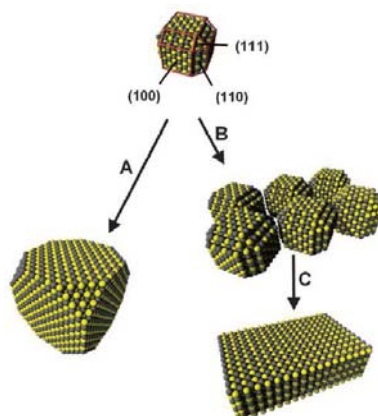


**Figure 4.** schematic illustration of large-particle (A) and sheet formation (B and C) from small PbS quantum dots.<sup>60</sup>

The NPs shape plays a crucial role in determining of their properties.<sup>62</sup> Depending on their dimensionality in the quantum confinement regime NPs can be classified as zero-dimensional (0D; Isotropic spheres, cubes, and polyhedron); 1D (rods and wires); and 2D (disc, prisms, and plates).<sup>63</sup> Figure 5 shows the variation on the density of electronic states versus energy for

bulk material, 2D where the charge are confined along one direction, 1D confined along 2 direction; and 0D confined in all directions.

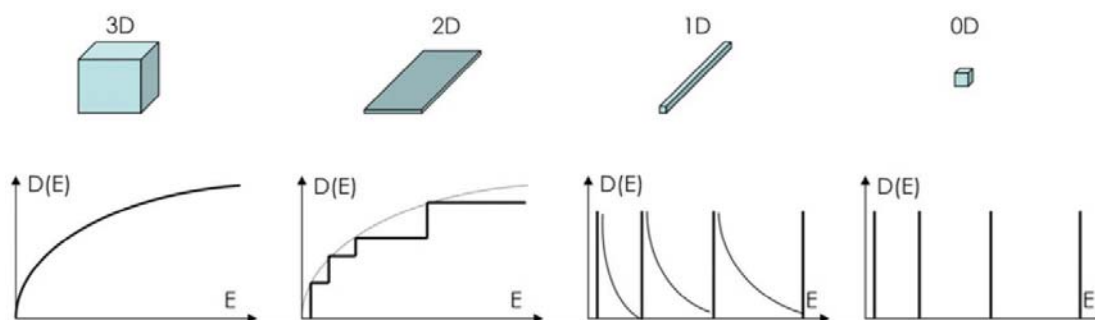


**Figure 5.** Evolution of the density of states function from a bulk (3D) material to a 2D, 1D and 0D.

### 1.2.5 Synthesis of colloidal nanoheterostructures

Colloidal nanoheterostructures are multi-component NPs, consisting of two or more different material sections that are combined through chemical bonding interfaces.<sup>64</sup> One of the most exciting and unique features of colloidal NPs is the possibility to prepare such multi-component nanostructures with a huge degree of freedom of the individual components. Novel functional nanomaterials with synergetic properties could be created by combining materials with different functionalities.<sup>65, 66</sup> The resulting nanoparticles could exhibit distinct physical-chemical properties from those inherent to the individual components, such as enhanced or tunable plasmon scattering<sup>67, 68</sup> or photoluminescence,<sup>69-71</sup> modified magnetic behavior,<sup>72, 73</sup> and improved (photo) catalytic responses<sup>74, 75</sup>, depending on the specific combination. Different nanoheterostructure geometries can be found in the literature, from core-shell nanocrystals to the so-called janus NP. Some examples are shown in the figure 6.



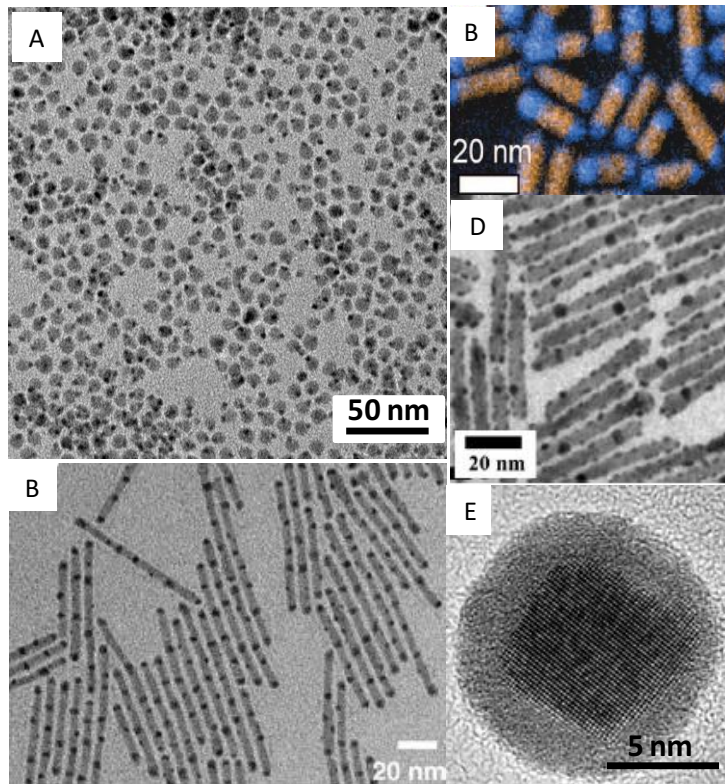
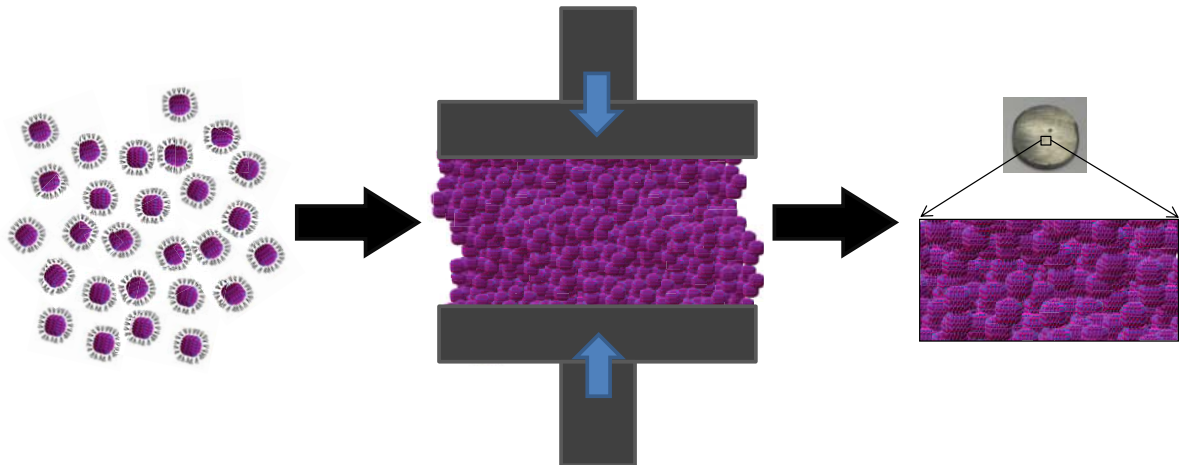


**Figure 6.** FePt-PbTe nanostructures with dumbbell morphologies (A),<sup>50</sup> Color-composite map energy-filtered TEM map binary heterostructures made of  $\text{Cu}_2\text{S}$ -CdS nanorods synthesized by partial  $\text{Cu}^+$  for  $\text{Cd}^{2+}$  cation exchange (B),<sup>76</sup> CdS nanorod with periodic array of  $\text{Ag}_2\text{S}$  domains within their body (C),<sup>77</sup> Au-decorated CdSe@CdS nanorods heterostructures (D);<sup>78</sup> and PbTe@PbS core-shell nanoparticles.<sup>50</sup>

There are several possible methods to synthesize nanoheterostructures. The most common route is to grow a second crystallographic phase onto an existing nucleus of a different material. Synthetic parameters must be carefully chosen to provide the conditions for lower activation energy for nucleation of the second material on the surface of the primary phase than the activation energy for an independent nucleation.

## Introduction to block 2 & 3: Solution processing approach to produce bulk nanomaterials or nanocomposites for thermoelectric application



### 1.3 Macroscopic arrays of nanoparticles

---

The actual active element of most devices will not be individual NPs, but their macroscopic arrays. The step from synthesized NPs to 2D or 3D functional nanomaterials represents the challenge path which scientists and engineers are meant to walk to go from performing fundamental studies to developing real world applications. NPs assemblies find applications in areas such as photonics,<sup>79</sup> electronics,<sup>80</sup> thermoelectrics,<sup>23</sup> photovoltaics<sup>22, 81</sup> and sensing.<sup>82</sup> The ability to tailor size, shape, and compositions of the individual NPs provide means for fine-tuning the bulk nanomaterials properties. Additionally, the behavior of such solids does not only depend on the properties of individual elements, but also on the electronic and optical communication between them, on the interparticle medium, packing density, the nature of interfaces, mutual orientation of NPs, etc.

NPs can be assembled as a disordered (amorphous) solid or as an ordered periodic supercrystal. Amorphous NPs solids are isotropic materials and have only short-range order among the NPs. On the other side, ordered NPs solids are anisotropic materials (superlattices) characterized by 3D periodicity with or without preferential orientation of individual NPs.<sup>6 83,</sup>  
<sup>84</sup> Despite the technological potential of such periodic NPs arrays, the technical challenges of large scale production, reproducibility and control over their structural defects has avoided their implementation in real applications, and remain the subject of fundamental studies.<sup>85-87</sup>

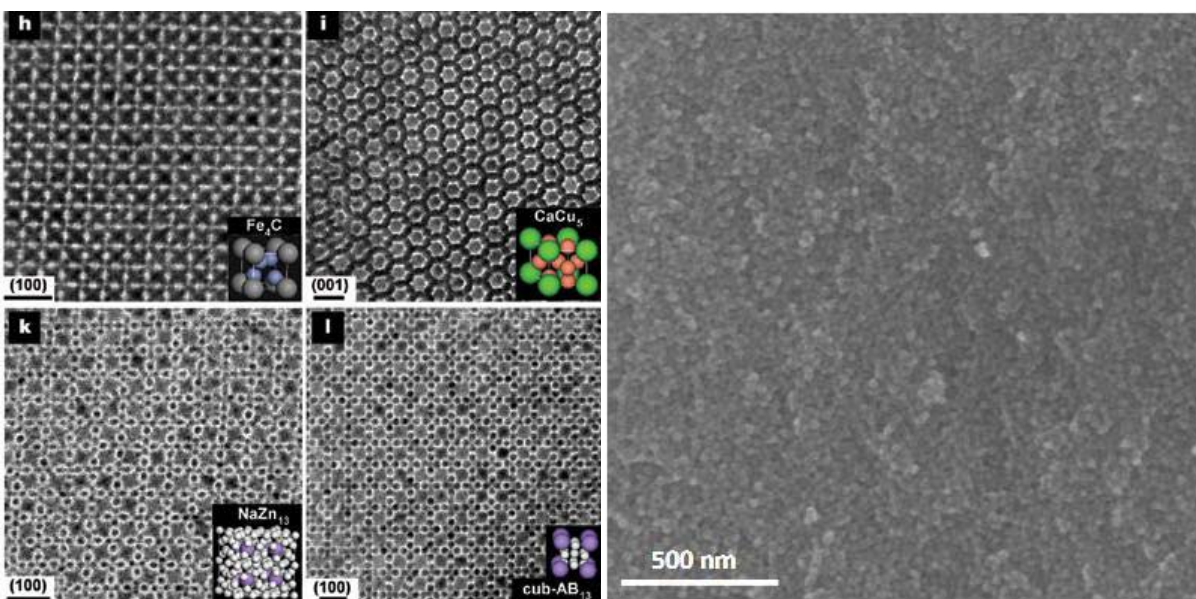


**Figure 7.** (A) Some examples of binary superlattices, self-assembled from different NP, and modeled unit cells of the corresponding 3D structures.<sup>84</sup> (B) An example of a disordered organization of NP, the image correspond to dried powder of  $\text{Cu}_2\text{GeSe}_3$  NP.<sup>50</sup>

The easiest way to produce bulk nanomaterials is to dry out the NPs from solution to form a gel or solid phase. By this method the material formed will be a close packed array of disordered NPs. The aggregation of suspended NPs is the easiest, most inexpensive and scalable processes to produce nanomaterials by the bottom-up assembly of colloidal NPs. Thereby, to date, this is the only feasible process to produce nanostructured materials from colloidal nanoparticles at an industrial scale.

A special mention should be made here to the determining role of surface ligands in NPs solids. Surfactant molecules determine the distance between adjacent NP and the interparticle interactions. Unfortunately, most organic ligands are highly electrically insulating obstructing the charge transport between NPs. Several post-synthesis treatments have been addressed to remove or replace long-chain organic ligands by shorter organic groups or inorganic ligands. An extended list of compounds has been proven already useful: e.g. pyridine,<sup>88, 89</sup> molecular metal chalcogenides complexes (MCC) stabilized by hydrazine,<sup>90</sup> nitrosonium (NOBF<sub>4</sub>),<sup>91</sup> diazonium<sup>91</sup> and trialkyl oxonium;<sup>92</sup> tetrafluoroborate acids (HBF<sub>4</sub>, HPF<sub>6</sub>);<sup>93</sup> ammonium thiocyanate (NH<sub>4</sub>SCN);<sup>94, 95</sup> sulphides like Na<sub>2</sub>S, NH<sub>4</sub>S, and K<sub>2</sub>S;<sup>93, 96, 97</sup> halide anions such as Cl<sup>-</sup>, Br<sup>-</sup> and I<sup>-</sup>.<sup>98-100</sup>

## 1.4 Thermoelectricity

---

Thermoelectricity represents the direct solid-state conversion between thermal and electrical energy. In the current energy scenario, where more than half of the energy produced end up wasted in form of heat (Figure 8),<sup>101</sup> thermoelectric energy conversion constitutes an alternative solution to improve energy efficiency of current industrial and domestic processes. However, their implementation in market application has not been yet widespread due to the low efficiencies of current thermoelectric (TE) devices and the need for expensive materials.

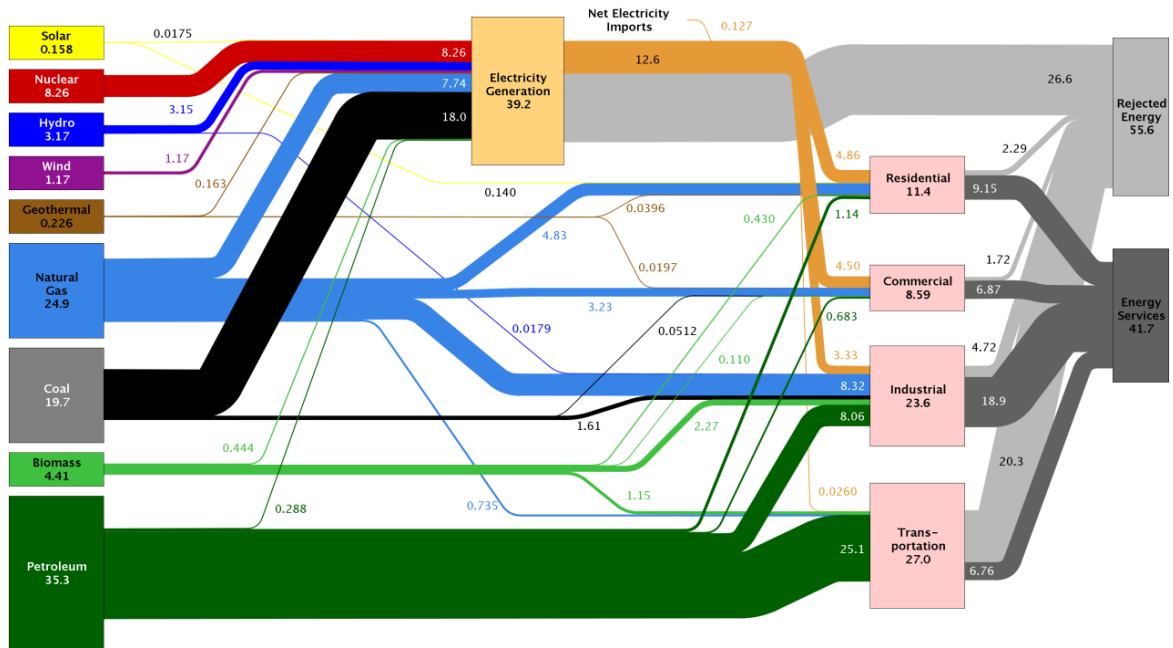


Figure 8. U.S. Energy Flow Use in 2011.<sup>101</sup>

Beside waste heat recovery, the thermoelectric effect can be used for precise temperature control, either by cooling or refrigeration. A heat flow is generated when a potential gradient is applied to a material, the so-called Peltier effect. Thermoelectric convertors operating as Peltier elements could become essential pieces of modern transistor microchips. All semiconductor based electronic devices can solely work appropriately within a narrow temperature window. As the transistor dimensions is been reduced, fan-based cooling devices are no longer a possibility. Additionally, Peltier elements work silently and can be maintenance-free. Thermoelectric materials will play a crucial role in such systems. However, to accomplish this goal there is an urgent need to improve their efficiencies and to find more low cost, abundant and environmental friendly materials.

### 1.4.1 Thermoelectric devices

A TE module is an array of TE couples connected electrically in series and thermally in parallel. A TE couple is composed of a p-type and an n-type material connected electrically in

a looped arrangement (figure 9). Both refrigeration and power generation can be accomplished using the same module.

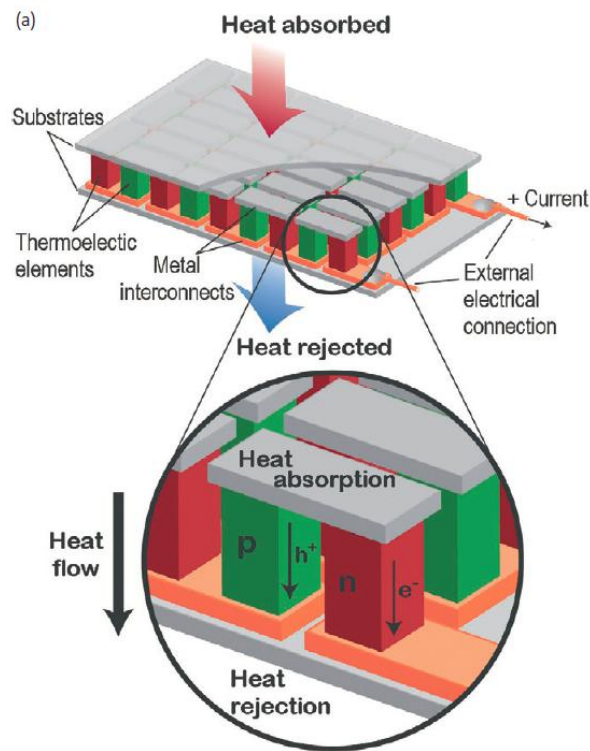


**Figure 9.** TE module showing the direction of charge flow on both cooling or power generation<sup>102</sup>

TE power generation is obtained when one side of the module is heated (cooled) by an external source generating a temperature gradient alongside the two materials (Seebeck effect). This leads toward a kinetic diffusion of the predominant charge carriers to the cold (hot) side. The resulting voltage can be used to drive a current through a load resistance. Conversely, the TE refrigeration is the response of the electrically driven carriers toward one side. The accumulation of charge carriers rise the probability of collisions and the consequently release of heat (Peltier effect).

The TE device performance relies directly on the temperature gradient ( $\Delta T$ ) and an intrinsic material parameter, the so-called thermoelectric figure of merit ( $ZT$ ):

$$ZT = \frac{\sigma S^2}{k} T$$



Where  $S$  is the Seebeck coefficient (also known as thermopower),  $\sigma$  is the electrical conductivity,  $k$  is the thermal conductivity, and  $T$  is the absolute temperature. The efficiency of a TE energy generator producing electricity from a temperature difference  $\Delta T$  is given by equation 2.

$$\eta = \frac{\Delta T}{T_{hot}} \frac{\sqrt{1 + ZT} - 1}{\sqrt{1 + ZT} + \frac{T_{cold}}{T_{hot}}}$$

With  $T_{cold}$  and  $T_{hot}$  being the temperatures at the cold and hot ends respectively. The larger is the  $ZT$ , the more efficient is the TE material. Such increase in efficiency is limited by the second law of thermodynamics up to the Carnot efficiency, which correspond to an infinitely large  $ZT$ . Figure 10 compare the current efficiency for several heat sources (geothermal, industrial waste, solar, nuclear and coal) with the estimated efficiency of a thermoelectric convertor as a function of the working temperatures for different  $ZT$ .<sup>103-105</sup>  $ZT > 2$  are indispensable to produce TE convertors competitive enough to be commercially available.

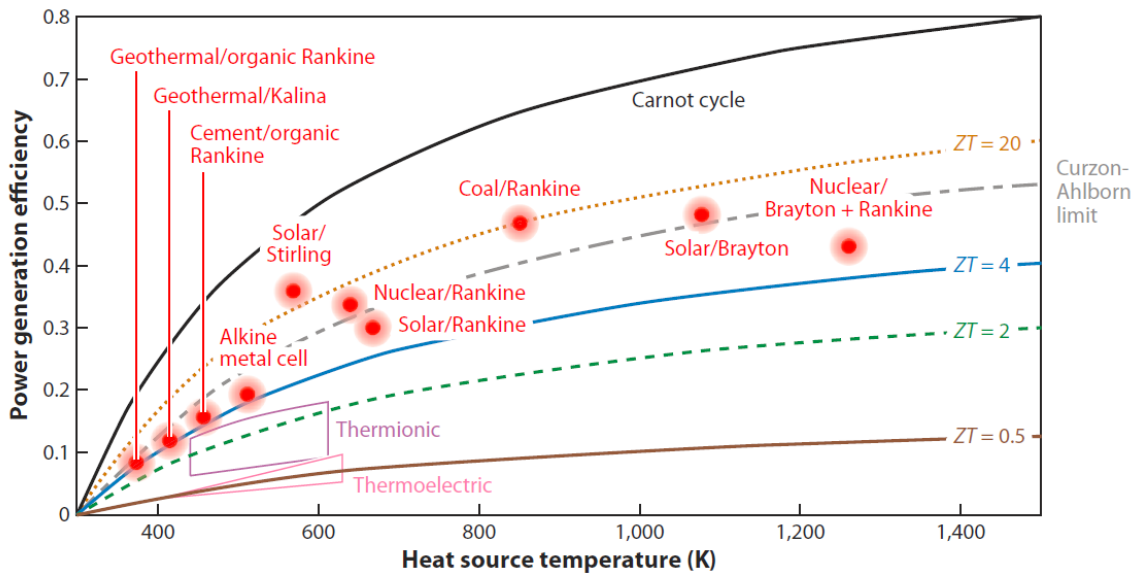


**Figure 10.** Thermoelectric power generation efficiencies versus  $T_{hot}$  ( $T_{cold}=300\text{k}$ ). Efficiencies for conventional mechanical engines and the Carnot limit.<sup>103</sup>

### 1.4.2 Interdependence of the thermoelectric parameter

One of the main problems to increase thermoelectric efficiency is the difficulty to optimize a variety of interdependent properties.  $\sigma$ ,  $S$  and  $k$  are tightly interrelated (figure 11). They all depend on the electronic density of states. Nevertheless, the transport of heat ( $\kappa$ ) is carried by two different elements: charge carriers and phonons. The former, the electronic thermal conductivity ( $k_e$ ), is proportional to  $\sigma$  via the Wiedemann-Franz law. On the hand, the lattice thermal conductivity ( $k_{latt}$ ) depends on the ability of phonons to propagate through the material and it is the only straightforward decoupled property. Most of the successful attempts to increase the TE efficiency are based on the  $k_{latt}$  reduction, namely the reduction of heat transport by phonons.

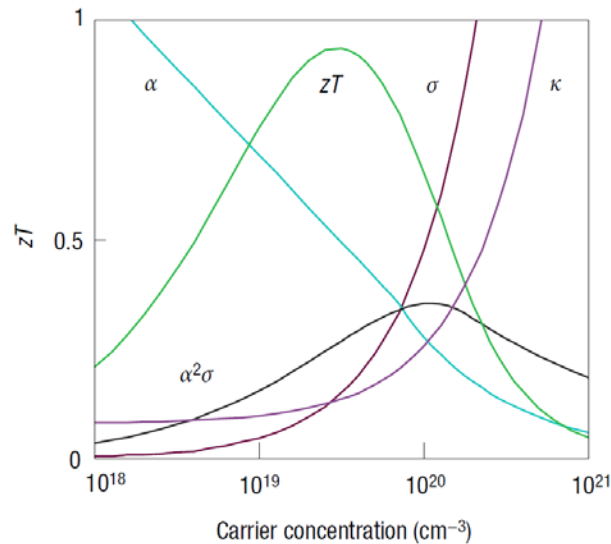


**Figure 11.** Trade-off between electrical conductivity, Seebeck coefficient and thermal conductivity as a function of the free carriers.<sup>102</sup>

Several approach have been investigate with that goal in mind. The first idea was scatter phonons within the unit cell by creating rattling structures, point defects, vacancies or alloying.<sup>106-108</sup> However, such scattering mechanism was proven to be truly effective just for short-wavelength phonons.<sup>109</sup> A different idea was to use materials with complex crystal



structure that allow separating charge from phonon transport, the paradigmatic idea of phonon-glass electron-crystal (PGEC).<sup>110-113</sup> Despite the advance in the bulk-materials approach, the most efficient method used to date to reduce the lattice thermal conductivity is by nanostructuring.<sup>114-117</sup> Nano-grain boundaries introduce an interface scattering mechanism which scatter mid- to long-wavelength phonons.<sup>109, 118</sup>

Figure 12 shows a schematic illustration of the scattering mechanisms as well as the electronic transport of hot and cold electrons.

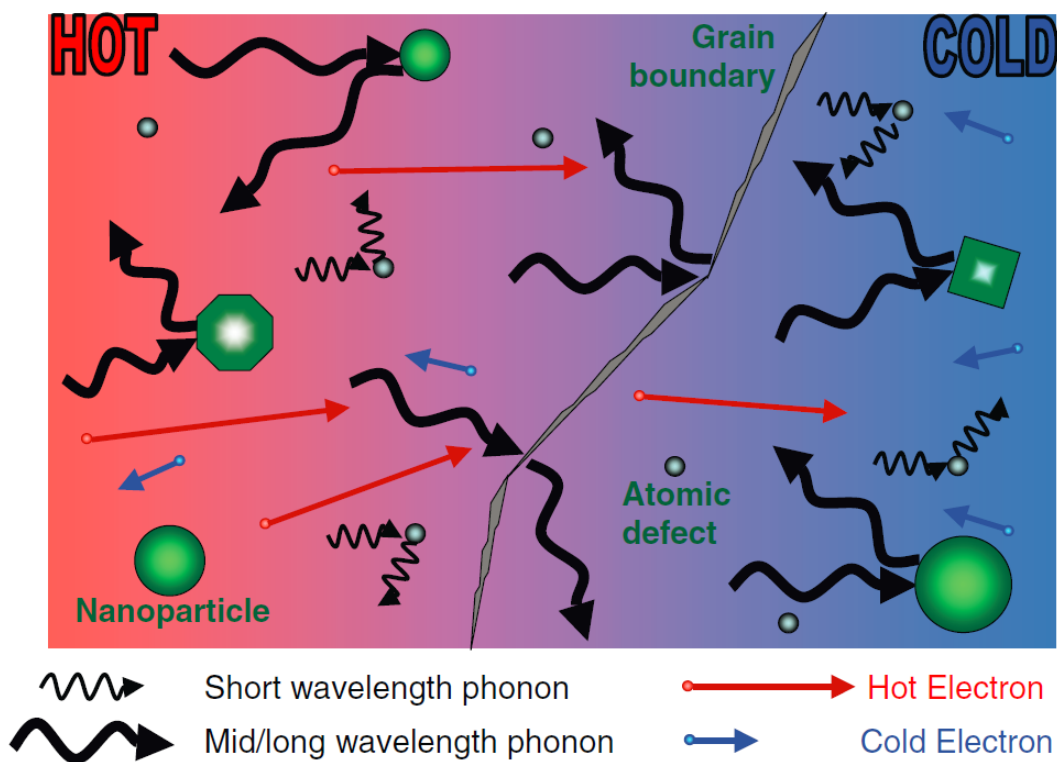


**Figure 12.** Schematic illustration of various phonon mechanisms within a thermoelectric material.<sup>109</sup>

### 1.4.3 Enhancements by nanostructuring

To date, nearly all high figure of merit thermoelectrics are nanostructured. The low-dimensional approach is based in two different ideas: the possibility to partially decouple  $S$  from  $\sigma$  to increase the overall power of factor ( $\sigma S^2$ ) and the introduction of a large density of interfaces to reduce thermal conductivity and increase Seebeck coefficient by the filtering of

low energy carriers at the interface energy barriers. The former idea was introduced theoretically in 1993 by Hicks and Dresselhaus.<sup>119, 120</sup> They predicted that making the size scale of the material comparable to the spatial extend of the electronic wave-function (confining the electrons) would directly result in an increase of the Seebeck coefficient without any reduction of the electrical conductivity by increasing the electronic density of states near the Fermi level. Up to now, quantum confinement has not been yet proven useful to increase the ZT. Although the S was highly enhanced, the reduced electron mobility diminishes the electrical conductivity.

On the other hand, the effect of numerous interfaces to scatter phonons more effectively than electrons<sup>114, 121-124</sup> or to filter out the low-energy electrons at the interfacial energy barriers<sup>125-129</sup> has allowed developing beyond doubt nanostructured materials with enhanced ZT.

#### **1.4.4 Production of bulk nanomaterials**

The best thermoelectric performances have been obtained from thin film nanocomposites produced by complex and expensive techniques such as molecular beam epitaxy.<sup>121, 130</sup> Despite their promising results, these methods are just useful as an experimental proof-of-principle of the potential benefits of nanostructures.<sup>121, 130</sup> Their scale-up challenges and the high cost techniques used for the materials production require the development of more economically feasible alternatives. Different options are being studied to produce large scale quantities of bulk nanostructured materials, e.g. solvothermal/hydrothermal methods,<sup>131</sup> wet-chemical synthesis (colloidal synthesis),<sup>23, 24, 124, 132, 133</sup> nanoprecipitation into solid solution,<sup>114, 134-138</sup> and high energy ball milling.<sup>139</sup>

In this thesis we have explore the opportunities of solution processed nanomaterials to produce economically affordable bulk nanostructured material. One of the main characteristic

of wet-chemical synthesis is the nearly endless possibilities for materials design. As explained in the first section of this introduction, by tuning the reaction parameters or/and changing the chemicals in the solution is possible to produce highly homogeneous nanoparticles with controlled size, shape, composition and phase of crystal domains. No other technology has the potential to produce nanomaterials with a comparable level of control over such parameters. The huge capacity of colloidal synthesis to create new complex materials at the nanoscale introduces into the thermoelectric field the possibility to design new materials that can boost the thermoelectric performance. The importance of controlling the nanograin properties does not end on the promising new thermoelectric performances, it is also important to carry on some fundamental studies that can provide new knowledge to further advances in the field.

## 1.5 References

---

- (1) Goesmann, H.; Feldmann, C., *Angew. Chem. Int. Ed.* **2010**, 49, 1362-1395.
- (2) Buffat, P.; Borel, J. P., *Phys. Rev. A* **1976**, 13, 2287-2298.
- (3) Klabunde, K. J.; Mulukutla, R. S., Chemical and Catalytic Aspects of Nanocrystals. In *Nanoscale Materials in Chemistry*, John Wiley & Sons, Inc.: 2002; pp 223-259.
- (4) Jia, C.-J.; Schuth, F., *Phys. Chem. Chem. Phys.* **2011**, 13, 2457-2487.
- (5) Blossey, R., *Nat. Mater.* **2003**, 2, 301-306.
- (6) Talapin, D. V.; Lee, J.-S.; Kovalenko, M. V.; Shevchenko, E. V., *Chem. Rev.* **2010**, 110, 389-458.
- (7) Brus, L., *J. Phys. Chem.* **1986**, 90, 2555-2560.
- (8) Alivisatos, A. P., *Science* **1996**, 271, 933.
- (9) Alivisatos, A. P.; Harris, A. L.; Levinos, N. J.; Steigerwald, M. L.; Harris, L. E., *J. Chem. Phys.* **1988**, 89, 4001-4011.
- (10) Alivisatos, A. P., *J. Phys. Chem.* **1996**, 100, 13226-13239.
- (11) Eustis, S.; El-Sayed, M. A., *Chem. Soc. Rev.* **2006**, 35, 209-217.
- (12) Link, S.; El-Sayed, M. A., *J. Phys. Chem. B* **1999**, 103, 4212-4217.
- (13) Sherry, L. J.; Chang, S.-H.; Schatz, G. C.; Van Duyne, R. P.; Wiley, B. J.; Xia, Y., *Nano Lett.* **2005**, 5, 2034-2038.
- (14) Mock, J. J.; Barbic, M.; Smith, D. R.; Schultz, D. A.; Schultz, S., *J. Chem. Phys.* **2002**.

- (15) Bittler, K.; Ostertag, W., *Angew. Chem. Int. Ed.* **1980**, 19, 190-196.
- (16) Bühler, G.; Thölmann, D.; Feldmann, C., *Adv. Mater.* **2007**, 19, 2224-2227.
- (17) Sun, S.; Murray, C. B.; Weller, D.; Folks, L.; Moser, A., *Science* **2000**, 287, 1989-1992.
- (18) Tang, J.; Konstantatos, G.; Hinds, S.; Myrskog, S.; Pattantyus-Abraham, A. G.; Clifford, J.; Sargent, E. H., *ACS Nano* **2009**, 3, 331-338.
- (19) Klimov, V. I.; Ivanov, S. A.; Nanda, J.; Achermann, M.; Bezel, I.; McGuire, J. A.; Piryatinski, A., *Nature* **2007**, 447, 441-446.
- (20) Klimov, V. I.; Mikhailovsky, A. A.; Xu, S.; Malko, A.; Hollingsworth, J. A.; Leatherdale, C. A.; Eisler, H.; Bawendi, M. G., *Science* **2000**, 290, 314-317.
- (21) Snee, P. T.; Somers, R. C.; Nair, G.; Zimmer, J. P.; Bawendi, M. G.; Nocera, D. G., *J. Am. Chem. Soc.* **2006**, 128, 13320-13321.
- (22) McDonald, S. A.; Konstantatos, G.; Zhang, S.; Cyr, P. W.; Klem, E. J. D.; Levina, L.; Sargent, E. H., *Nat. Mater.* **2005**, 4, 138-142.
- (23) Scheele, M.; Oeschler, N.; Meier, K.; Kornowski, A.; Klinke, C.; Weller, H., *Adv. Funct. Mater.* **2009**, 19, 3476-3483.
- (24) Ibáñez, M.; Cadavid, D.; Zamani, R.; García-Castelló, N.; Izquierdo-Roca, V.; Li, W.; Fairbrother, A.; Prades, J. D.; Shavel, A.; Arbiol, J.; Pérez-Rodríguez, A.; Morante, J. R.; Cabot, A., *Chem. Mater.* **2012**, 24, 562-570.
- (25) Ibáñez, M.; Zamani, R.; Li, W.; Cadavid, D.; Gorsse, S.; Katcho, N. A.; Shavel, A.; López, A. M.; Morante, J. R.; Arbiol, J.; Cabot, A., *Chem. Mater.* **2012**.
- (26) Park, J.; Joo, J.; Kwon, S. G.; Jang, Y.; Hyeon, T., *Angew. Chem., Int. Ed.* **2007**, 46, 4630-4660.
- (27) Murray, C. B.; Kagan, C. R.; Bawendi, M. G., *Annu. Rev. Mater. Sci.* **2000**, 30, 545-610.
- (28) Rogach, A. L., *Semiconductor Nanocrystal Quantum Dots. Synthesis, Assembly, Spectroscopy and Applications*. SpringerWien: New York, 2008.
- (29) Park, J.; Joo, J.; Kwon, S. G.; Jang, Y.; Hyeon, T., *Angew. Chem. Int. Ed.* **2007**, 46, 4630-4660.
- (30) Shevchenko, E. V.; Talapin, D. V.; Schnablegger, H.; Kornowski, A.; Festin, O.; Svedlindh, P.; Haase, M.; Weller, H., *J. Am. Chem. Soc.* **2003**, 125, 9090-9101.
- (31) Yin, Y.; Alivisatos, A. P., *Nature* **2005**, 437, 664-670.
- (32) Zheng, H.; Claridge, S. A.; Minor, A. M.; Alivisatos, A. P.; Dahmen, U., *Nano Lett.* **2009**, 9, 2460-2465.

- (33) Evans, C. M.; Guo, L.; Peterson, J. J.; Maccagnano-Zacher, S.; Krauss, T. D., *Nano Lett.* **2008**, 8, 2896-2899.
- (34) Abe, S.; Čapek, R. K.; De Geyter, B.; Hens, Z., *ACS Nano* **2012**, 6, 42-53.
- (35) LaMer, V. K.; Dinegar, R. H., *J. Am. Chem. Soc.* **1950**, 72, 4847-4854.
- (36) Hanrath, T., *J. Vac. Sci. Technol. A* **2012**, 30, 030802.
- (37) Peng, X.; Wickham, J.; Alivisatos, A. P., *J. Am. Chem. Soc.* **1998**, 120, 5343-5344.
- (38) Talapin, D. V.; Rogach, A. L.; Haase, M.; Weller, H., *J. Phys. Chem. B* **2001**, 105, 12278-12285.
- (39) Talapin, D. V.; Rogach, A. L.; Shevchenko, E. V.; Kornowski, A.; Haase, M.; Weller, H., *J. Am. Chem. Soc.* **2002**, 124, 5782-5790.
- (40) Ibáñez, M.; Guardia, P.; Shavel, A.; Cadavid, D.; Arbiol, J.; Morante, J. R.; Cabot, A., *J. Phys. Chem. C* **2011**, 115, 7947-7955.
- (41) Kalyuzhny, G.; Murray, R. W., *J. Phys. Chem. B* **2005**, 109, 7012-7021.
- (42) Jia, S.; Banerjee, S.; Herman, I. P., *J. Phys. Chem. C* **2007**, 112, 162-171.
- (43) Yavuz, C. T.; Mayo, J. T.; Yu, W. W.; Prakash, A.; Falkner, J. C.; Yean, S.; Cong, L.; Shipley, H. J.; Kan, A.; Tomson, M.; Natelson, D.; Colvin, V. L., *Science* **2006**, 314, 964-967.
- (44) McLeod, M. C.; Anand, M.; Kitchens, C. L.; Roberts, C. B., *Nano Lett.* **2005**, 5, 461-465.
- (45) Akbulut, O.; Mace, C. R.; Martinez, R. V.; Kumar, A. A.; Nie, Z.; Patton, M. R.; Whitesides, G. M., *Nano Lett.* **2012**, 12, 4060-4064.
- (46) Sweeney, S. F.; Woehrle, G. H.; Hutchison, J. E., *J. Am. Chem. Soc.* **2006**, 128, 3190-3197.
- (47) Hanauer, M.; Pierrat, S.; Zins, I.; Lotz, A.; Sönnichsen, C., *Nano Lett.* **2007**, 7, 2881-2885.
- (48) Bass, J. D.; Ai, X.; Bagabas, A.; Rice, P. M.; Topuria, T.; Scott, J. C.; Alharbi, F. H.; Kim, H.-C.; Song, Q.; Miller, R. D., *Angew. Chem. Int. Ed.* **2011**, 50, 6538-6542.
- (49) Bai, L.; Ma, X.; Liu, J.; Sun, X.; Zhao, D.; Evans, D. G., *J. Am. Chem. Soc.* **2010**, 132, 2333-2337.
- (50) Ibáñez, M.; *et al.*, *Unpublish results* **2009-2013**.
- (51) Kumar, S.; Nann, T., *Small* **2006**, 2, 316-329.
- (52) Biacchi, A. J.; Schaak, R. E., *ACS Nano* **2011**, 5, 8089-8099.
- (53) Burda, C.; Chen, X.; Narayanan, R.; El-Sayed, M. A., *Chem. Rev.* **2005**, 105, 1025-1102.
- (54) Xia, Y.; Xiong, Y.; Lim, B.; Skrabalak, S. E., *Angew. Chem. Int. Ed.* **2009**, 48, 60-103.
- (55) Jiang, Z.-Y.; Kuang, Q.; Xie, Z.-X.; Zheng, L.-S., *Adv. Funct. Mater.* **2010**, 20, 3634-3645.
- (56) Sau, T. K.; Rogach, A. L., *Adv. Mater.* **2010**, 22, 1781-1804.
- (57) Polarz, S., *Adv. Funct. Mater.* **2011**, 21, 3214-3230.

- (58) Manna, L.; Scher, E. C.; Alivisatos, A. P., *J. Am. Chem. Soc.* **2000**, 122, 12700-12706.
- (59) Cho, K.-S.; Talapin, D. V.; Gaschler, W.; Murray, C. B., *J. Am. Chem. Soc.* **2005**, 127, 7140-7147.
- (60) Schliehe, C.; Juarez, B. H.; Pelletier, M.; Jander, S.; Greshnykh, D.; Nagel, M.; Meyer, A.; Foerster, S.; Kornowski, A.; Klinke, C.; Weller, H., *Science* **2010**, 329, 550-553.
- (61) Liao, H.-G.; Cui, L.; Whitlam, S.; Zheng, H., *Science* **2012**, 336, 1011-1014.
- (62) Li, L.-s.; Hu, J.; Yang, W.; Alivisatos, A. P., *Nano Lett.* **2001**, 1, 349-351.
- (63) Jun, Y.-W.; Choi, J.-S.; Cheon, J., *Angew. Chem. Int. Ed.* **2006**, 45, 3414-3439.
- (64) Carbone, L.; Cozzoli, P. D., *Nano Today* **2010**, 5, 449-493.
- (65) Gao, J.; Gu, H.; Xu, B., *Acc. Chem. Res.* **2009**, 42, 1097-1107.
- (66) Jiang, J.; Gu, H.; Shao, H.; Devlin, E.; Papaefthymiou, G. C.; Ying, J. Y., *Adv. Mater.* **2008**, 20, 4403-4407.
- (67) Cortie, M. B.; McDonagh, A. M., *Chem. Rev.* **2011**, 111, 3713-3735.
- (68) Xu, Z.; Hou, Y.; Sun, S., *J. Am. Chem. Soc.* **2007**, 129, 8698-8699.
- (69) Reiss, P.; Bleuse, J.; Pron, A., *Nano Lett.* **2002**, 2, 781-784.
- (70) Li, L.; Daou, T. J.; Texier, I.; Kim Chi, T. T.; Liem, N. Q.; Reiss, P., *Chem. Mater.* **2009**, 21, 2422-2429.
- (71) Reiss, P.; Protière, M.; Li, L., *Small* **2009**, 5, 154-168.
- (72) Lee, J.-S.; Bodnarchuk, M. I.; Shevchenko, E. V.; Talapin, D. V., *J. Am. Chem. Soc.* **2010**, 132, 6382-6391.
- (73) Li, Y.; Zhang, Q.; Nurmikko, A. V.; Sun, S., *Nano Lett.* **2005**, 5, 1689-1692.
- (74) Subramanian, V.; Wolf, E. E.; Kamat, P. V., *J. Am. Chem. Soc.* **2004**, 126, 4943-4950.
- (75) Li, J.; Cushing, S. K.; Bright, J.; Meng, F.; Senty, T. R.; Zheng, P.; Bristow, A. D.; Wu, N., *ACS Catal.* **2013**, 3, 47-51.
- (76) Sadtler, B.; Demchenko, D. O.; Zheng, H.; Hughes, S. M.; Merkle, M. G.; Dahmen, U.; Wang, L.-W.; Alivisatos, A. P., *J. Am. Chem. Soc.* **2009**, 131, 5285-5293.
- (77) Robinson, R. D.; Sadtler, B.; Demchenko, D. O.; Erdonmez, C. K.; Wang, L.-W.; Alivisatos, A. P., *Science* **2007**, 317, 355-358.
- (78) Mokari, T.; Sztrum, C. G.; Salant, A.; Rabani, E.; Banin, U., *Nat. Mater.* **2005**, 4, 855-863.
- (79) Vlasov, Y. A.; Bo, X.-Z.; Sturm, J. C.; Norris, D. J., *Nature* **2001**, 414, 289-293.
- (80) Lee, J.-S.; Kovalenko, M. V.; Huang, J.; Chung, D. S.; Talapin, D. V., *Nat. Nano.* **2011**, 6, 348-352.
- (81) Jiang, C.; Lee, J.-S.; Talapin, D. V., *J. Am. Chem. Soc.* **2012**, 134, 5010-5013.

- (82) Shipway, A. N.; Katz, E.; Willner, I., *ChemPhysChem* **2000**, 1, 18-52.
- (83) Shevchenko, E. V.; Talapin, D. V.; Murray, C. B.; O'Brien, S., *J. Am. Chem. Soc.* **2006**, 128, 3620-3637.
- (84) Shevchenko, E. V.; Talapin, D. V.; Kotov, N. A.; O'Brien, S.; Murray, C. B., *Nature* **2006**, 439, 55-59.
- (85) Bodnarchuk, M. I.; Shevchenko, E. V.; Talapin, D. V., *J. Am. Chem. Soc.* **2011**, 133, 20837-20849.
- (86) Bodnarchuk, M. I.; Kovalenko, M. V.; Heiss, W.; Talapin, D. V., *J. Am. Chem. Soc.* **2010**, 132, 11967-11977.
- (87) Singh, A.; Dickinson, C.; Ryan, K. M., *ACS Nano* **2012**, 6, 3339-3345.
- (88) Ridley, B. A.; Nivi, B.; Jacobson, J. M., *Science* **1999**, 286, 746-749.
- (89) Murray, C. B.; Norris, D. J.; Bawendi, M. G., *J. Am. Chem. Soc.* **1993**, 115, 8706-15.
- (90) Kovalenko, M. V.; Scheele, M.; Talapin, D. V., *Science* **2009**, 324, 1417-1420.
- (91) Dong, A.; Ye, X.; Chen, J.; Kang, Y.; Gordon, T.; Kikkawa, J. M.; Murray, C. B., *J. Am. Chem. Soc.* **2011**, 133, 998-1006.
- (92) Rosen, E. L.; Buonsanti, R.; Llordes, A.; Sawvel, A. M.; Milliron, D. J.; Helms, B. A., *Angew. Chem. Int. Ed.* **2012**, 51, 684-689.
- (93) Nag, A.; Kovalenko, M. V.; Lee, J.-S.; Liu, W.; Spokoyny, B.; Talapin, D. V., *J. Am. Chem. Soc.* **2011**, 133, 10612-10620.
- (94) Fafarman, A. T.; Koh, W.-k.; Diroll, B. T.; Kim, D. K.; Ko, D.-K.; Oh, S. J.; Ye, X.; Doan-Nguyen, V.; Crump, M. R.; Reifsnnyder, D. C.; Murray, C. B.; Kagan, C. R., *J. Am. Chem. Soc.* **2011**, 133, 15753-15761.
- (95) Koh, W.-k.; Saudari, S. R.; Fafarman, A. T.; Kagan, C. R.; Murray, C. B., *Nano Lett.* **2011**, 11, 4764-4767.
- (96) Zhang, H.; Hu, B.; Sun, L.; Hovden, R.; Wise, F. W.; Muller, D. A.; Robinson, R. D., *Nano Lett.* **2011**, 11, 5356-5361.
- (97) Nag, A.; Chung, D. S.; Dolzhenkov, D. S.; Dimitrijevic, N. M.; Chattopadhyay, S.; Shibata, T.; Talapin, D. V., *J. Am. Chem. Soc.* **2012**, 134, 13604-13615.
- (98) Zhitomirsky, D.; Furukawa, M.; Tang, J.; Stadler, P.; Hoogland, S.; Voznyy, O.; Liu, H.; Sargent, E. H., *Adv. Mater.* **2012**, 24, 6181-6185.
- (99) Tang, J.; Kemp, K. W.; Hoogland, S.; Jeong, K. S.; Liu, H.; Levina, L.; Furukawa, M.; Wang, X.; Debnath, R.; Cha, D.; Chou, K. W.; Fischer, A.; Amassian, A.; Asbury, J. B.; Sargent, E. H., *Nat. Mater.* **2011**, 10, 765-771.

- (100) Ning, Z.; Ren, Y.; Hoogland, S.; Voznyy, O.; Levina, L.; Stadler, P.; Lan, X.; Zhitomirsky, D.; Sargent, E. H., *Adv. Mater.* **2012**, 24, 6295-6299.
- (101) Laboratory, L. L. N. <https://flowcharts.llnl.gov/>.
- (102) Snyder, G. J.; Toberer, E. S., *Nat. Mater.* **2008**, 7, 105-114.
- (103) Shakouri, A., *Annu. Rev. Mater. Res.* **2011**, 41, 399-431.
- (104) Volz, S.; Shakouri, A.; Zebarjadi, M., Nanoengineered Materials for Thermoelectric Energy Conversion. In *Thermal Nanosystems and Nanomaterials*, Springer Berlin Heidelberg: 2009; Vol. 118, pp 225-299.
- (105) Vining, C. B., *Nat Mater* **2009**, 8, 83-85.
- (106) Wood, C., *Rep. Prog. Phys.* **1988**, 51, 459.
- (107) Rowe, D. M., *Thermoelectrics Handbook: Macro to Nano*. CRC Press: Boca Raton: FL, 2006.
- (108) Wright, D. A., *Nature* **1958**, 181, 834-834.
- (109) Vineis, C. J.; Shakouri, A.; Majumdar, A.; Kanatzidis, M. G., *Adv. Mater.* **2010**, 22, 3970-3980.
- (110) Snyder, G. J.; Christensen, M.; Nishibori, E.; Caillat, T.; Iversen, B. B., *Nat. Mater.* **2004**, 3, 458-463.
- (111) Nolas, G. S.; Slack, G. A.; Schujman, S. B.; Terry, M. T., Chapter 6 Semiconductor clathrates: A phonon glass electron crystal material with potential for thermoelectric applications. In *Semiconductors and Semimetals*, Elsevier: 2001; Vol. Volume 69, pp 255-300.
- (112) Sales, B. C.; Mandrus, D.; Chakoumakos, B. C.; Keppens, V.; Thompson, J. R., *Phys. Rev. B* **1997**, 56, 15081-15089.
- (113) Nolas, G. S.; Morelli, D. T.; Tritt, T. M., *Annu. Rev. Mater. Res.* **1999**, 29, 89-116.
- (114) Biswas, K.; He, J.; Blum, I. D.; Wu, C.-I.; Hogan, T. P.; Seidman, D. N.; Dravid, V. P.; Kanatzidis, M. G., *Nature* **2012**, 489, 414-418.
- (115) Johnsen, S.; He, J.; Androulakis, J.; Dravid, V. P.; Todorov, I.; Chung, D. Y.; Kanatzidis, M. G., *J. Am. Chem. Soc.* **2011**, 133, 3460-3470.
- (116) Zhao, L.-D.; He, J.; Hao, S.; Wu, C.-I.; Hogan, T. P.; Wolverton, C.; Dravid, V. P.; Kanatzidis, M. G., *J. Am. Chem. Soc.* **2012**.
- (117) Dresselhaus, M. S.; Chen, G.; Tang, M. Y.; Yang, R. G.; Lee, H.; Wang, D. Z.; Ren, Z. F.; Fleurial, J. P.; Gogna, P., *Adv. Mater.* **2007**, 19, 1043-1053.
- (118) Medlin, D. L.; Snyder, G. J., *Adv. Colloid Interface Sci.* **2009**, 14, 226-235.



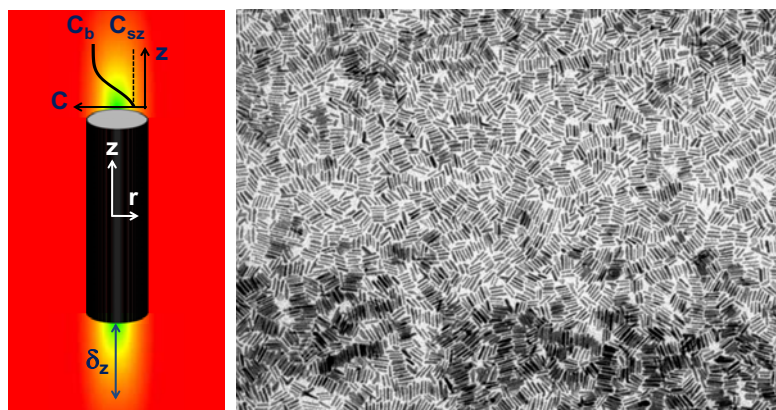
- (119) Hicks, L. D.; Dresselhaus, M. S., *Phys. Rev. B* **1993**, 47, 12727-12731.
- (120) Hicks, L. D.; Dresselhaus, M. S., *Phys. Rev. B* **1993**, 47, 16631-16634.
- (121) Venkatasubramanian, R.; Siivola, E.; Colpitts, T.; O'Quinn, B., *Nature* **2001**, 413, 597-602.
- (122) Boukai, A. I.; Bunimovich, Y.; Tahir-Kheli, J.; Yu, J.-K.; Goddard Iii, W. A.; Heath, J. R., *Nature* **2008**, 451, 168-171.
- (123) Chen, H.-S.; Lo, B.; Hwang, J.-Y.; Chang, G.-Y.; Chen, C.-M.; Tasi, S.-J.; Wang, S.-J. J., *J. Phys. Chem. B* **2004**, 108, 17119-17123.
- (124) Mehta, R. J.; Zhang, Y.; Karthik, C.; Singh, B.; Siegel, R. W.; Borca-Tasciuc, T.; Ramanath, G., *Nat. Mater.* **2012**, 11, 233-240.
- (125) Soni, A.; Shen, Y.; Yin, M.; Zhao, Y.; Yu, L.; Hu, X.; Dong, Z.; Khor, K. A.; Dresselhaus, M. S.; Xiong, Q., *Nano Lett.* **2012**, 12, 4305-4310.
- (126) Liu, M.; Qin, X. Y., *Appl. Phys. Lett.* **2012**, 101, 132103.
- (127) Faleev, S. V.; Léonard, F., *Phys. Rev. B* **2008**, 77, 214304.
- (128) Ko, D.-K.; Kang, Y.; Murray, C. B., *Nano Lett.* **2011**, 11, 2841-2844.
- (129) O'Dwyer, M. F.; Lewis, R. A.; Zhang, C.; Humphrey, T. E., *Phys. Rev. B* **2005**, 72, 205330.
- (130) Harman, T. C.; Taylor, P. J.; Walsh, M. P.; LaForge, B. E., *Science* **2002**, 297, 2229-2232.
- (131) Zhang, Y. H.; Zhu, T. J.; Tu, J. P.; Zhao, X. B., *Mater. Chem. Phys.* **2007**, 103, 484-488.
- (132) Ibáñez, M.; Zamani, R.; Lalonde, A.; Cadavid, D.; Li, W.; Shavel, A.; Arbiol, J.; Morante, J. R.; Gorsse, S.; Snyder, G. J.; Cabot, A., *J. Am. Chem. Soc.* **2012**, 134, 4060-4063.
- (133) Scheele, M.; Oeschler, N.; Veremchuk, I.; Reinsberg, K. G.; Kreuziger, A. M.; Kornowski, A.; Broekaert, J.; Klinke, C.; Weller, H., *ACS Nano* **2010**, 4, 4283-4291.
- (134) Androulakis, J.; Chung, D.-Y.; Su, X.; Zhang, L.; Uher, C.; Hasapis, T. C.; Hatzikraniotis, E.; Paraskevopoulos, K. M.; Kanatzidis, M. G., *Phys. Rev. B* **2011**, 84, 155207.
- (135) Androulakis, J.; Todorov, I.; He, J.; Chung, D.-Y.; Dravid, V.; Kanatzidis, M., *J. Am. Chem. Soc.* **2011**, 133, 10920-10927.
- (136) Biswas, K.; He, J.; Wang, G.; Lo, S.-H.; Uher, C.; Dravid, V. P.; Kanatzidis, M. G., *Energy Environ. Sci.* **2011**, 4, 4675-4684.
- (137) Girard, S. N.; He, J.; Li, C.; Moses, S.; Wang, G.; Uher, C.; Dravid, V. P.; Kanatzidis, M. G., *Nano Lett.* **2010**, 10, 2825-2831.
- (138) Girard, S. N.; He, J.; Zhou, X.; Shoemaker, D.; Jaworski, C. M.; Uher, C.; Dravid, V. P.; Heremans, J. P.; Kanatzidis, M. G., *J. Am. Chem. Soc.* **2011**, 133, 16588-16597.

(139) Sootsman, J. R.; Chung, D. Y.; Kanatzidis, M. G., *Angew. Chem. Int. Ed.* **2009**, 48, 8616-8639.



## Chapter 2

### Growth Kinetics of Asymmetric $\text{Bi}_2\text{S}_3$ Nanocrystals: Size Distribution Focusing in Nanorods



#### 2.1 Abstract

---

The growth kinetics of colloidal  $\text{Bi}_2\text{S}_3$  nanorods was investigated. After nucleation, the length-distribution of the growing  $\text{Bi}_2\text{S}_3$  nanorods narrows with the reaction time until a bimodal length distribution appears. From this critical reaction time on, the smallest nanorods of the ensemble dissolve, feeding with monomer the growth of the largest ones. A comprehensive characterization of the size-distribution evolution of  $\text{Bi}_2\text{S}_3$  nanorods is used here to illustrate the dependences of the anisotropic growth rates of cylindrical nanoparticles on the nanoparticle dimensions and the monomer concentration in solution. With this goal in mind, a diffusion-reaction model is presented to explain the origin of the experimentally obtained length distribution focusing mechanism. The model is able to reproduce the decrease of the growth rate in the nanorod axial direction with both its thickness and length. On the other hand, low lateral reaction rates prevent the nanorod thickness distribution to be focused. In both crystallographic growth directions, a concentration-dependent critical thickness exists,

which discriminates between nanorods with positive growth rates and those dissolving in the reaction solution.

## 2.2 Introduction

---

Colloidal nanocrystals have achieved a great interest because of their intrinsic size-dependent properties and their huge potential as building blocks for solution-processed devices.<sup>11</sup> However, to uncover and fully exploit their size- and shape-dependent optical, magnetic, electronic, thermodynamic and catalytic properties and to assemble them into crystalline superstructures, a precise control over their size, shape and composition is required. With this motivation, during the last 20 years, a huge effort has been put into understanding the nanocrystal nucleation, growth and shape-evolution mechanisms.<sup>2-13</sup>

After nucleation, nanocrystal coarsening is thermodynamically driven by the decrease of its surface free energy. The minimization of its surface free energy also determines the nanocrystal morphology and its equilibrium facets. However, nanocrystals themselves are thermodynamically metastable species compared to bulk crystals. Coarsening would continue indefinitely if a continuous supply of monomer exists. Thus, their size- and shape-distribution are in part kinetically determined.

The evolution of the size distribution of a nanocrystal ensemble is specially influenced by the monomer reaction rate and the monomer concentration and diffusivity in solution. In this framework, three main growth regimes are usually considered: i) Size distribution defocusing, when the nanocrystal growth rate increases with the particle size, thus broadening the size distribution. This growth regime is usually encountered in reaction-controlled growth scenarios, where the growth rate is limited by the monomer reaction rate. Size distribution defocusing is also encountered in the diffusion-controlled growth of small nanoparticles in solutions with low monomer concentrations. In this last scenario, the nanocrystal growth rate

is controlled by the monomer diffusivity and thus, a monomer concentration gradient exists around each nanoparticle; ii) Size-distribution focusing, when the nanocrystal growth rate decreases with the particle size, thus narrowing the size distribution. This growth regime is generally encountered in the diffusion-controlled growth of relative large nanocrystals in solutions containing high concentrations of monomer; iii) Ostwald-ripening, when the larger nanoparticles in the ensemble grow at expenses of the dissolution of the smallest ones, broadening the size distribution. As the solution is depleted of monomer, in both reaction- and diffusion-controlled growth scenarios, the smallest nanocrystals of the ensemble are the first to reach their critical monomer concentration, starting to dissolve while keeping feeding with monomer the growth of the largest ones.

While it is generally agreed that the anisotropic growth of colloidal nanocrystals is kinetically driven,<sup>14-23</sup> the size- and shape-distribution evolution of asymmetric nanocrystals is not so well understood. Three growth stages were previously pointed out to describe the size and shape evolution of an ensemble of CdSe nanorods:<sup>21</sup> i) 1D-growth, when the axial growth rate is much higher than the radial one at high monomer concentration; ii) 3D-growth, when the axial and radial growth rates equilibrate at lower monomer concentration; iii) 1D-to-2D-ripening or intra-particle Ostwald-ripening when, at still lower monomer concentration in solution, the nanorod dissolve in the axial direction to feed its radial growth. A recent diffusion-controlled kinetic model calculated the temporal evolution of the average nanorod length and thickness considering independent kinetic parameters for each, longitudinal and radial growth directions.<sup>24</sup> From a direct adaptation of the growth rate equation previously obtained for spherical particles,<sup>12</sup> but considering different reaction orders for axial and radial growth, this model was able to reproduce the faster axial than radial growth at high monomer concentrations and the gradual transition to a 3D-growth regime when decreasing the monomer concentration in solution. However, the model failed to show the 1D-2D ripening

involving the dissolution of the nanorod in the longitudinal direction and was not able to determine the weight of the specific free energy of each crystallographic plane on the growth and dissolution rates in each crystallographic direction.

In the present work, the growth kinetics of an ensemble of  $\text{Bi}_2\text{S}_3$  nanorods is characterized by analyzing the size distribution of the nanorods formed at different reaction times and at various reaction temperatures. The comparison of the obtained experimental results with the predictions of an activated-complex diffusion-reaction model allows describing the different growth regimes involved in the nanorod growth.

## 2.3 Experimental

---

All reactants were acquired from Sigma-Aldrich and were used without additional purification.  $\text{Bi}_2\text{S}_3$  nanocrystals were obtained by reacting bismuth (III) acetate (99.99+%) or bismuth (III) neodecanoate (technical) with elemental sulfur (99.98%) in a 1-octadecene (90%) solution containing oleic acid (90%) and/or oleylamine (70%).

In a typical  $\text{Bi}_2\text{S}_3$  preparation, 0.26 mmol bismuth acetate and 16 mmol oleic acid were mixed with 20 ml of 1-octadecene in a 3-neck flask. The solution was heated under vacuum to 90 °C and maintained at this temperature during 30 min to remove water and other low-boiling point impurities. Afterwards, an argon atmosphere was introduced and the bismuth-acid solution was heated to the reaction temperature. The sulfur solution was prepared by dissolving 0.03g of elemental sulfur with 6 mmol of oleylamine. This solution was injected through a septum into the heated three-neck flask containing the bismuth precursor solution.

The formation of  $\text{Bi}_2\text{S}_3$  nanostructures could be qualitatively followed by the color change of the mixture from an initial light yellow to the light brown and eventually black color of the solution containing the  $\text{Bi}_2\text{S}_3$  nanoparticles.

To quantitatively monitor the reaction process, aliquots were extracted at successive reaction times after the sulfur injection. Aliquots were rapidly cooled down to quench the nanocrystal growth by dissolving them in toluene. The excess of sulfur and surfactants from the prepared nanocrystal solution was immediately removed by multiple precipitation-dispersion steps using a mixture of ethanol and ethyl acetate for precipitation and toluene for re-dispersion. The size, shape and crystallographic structure of the prepared Bi<sub>2</sub>S<sub>3</sub> nanorods were characterized using transmission electron microscopy (TEM) and high-resolution TEM (HRTEM). For TEM and HRTEM characterization, samples were prepared by placing a drop of the colloidal solution containing the nanoparticles onto a carbon coated copper grid at room temperature and ambient atmosphere. TEM micrographs were obtained using Jeol 1010 microscope, operating at 80 kV. Images were digitally acquired using a MegaviewIII scanning CCD camera with a soft imaging system. The morphology and crystallographic structure of the nanorods were further characterized with atomic resolution by means of HRTEM in a Jeol 2010F field emission gun microscope with a 0.19 nm point to point resolution. 3D atomic supercell modeling was performed by using the Rhodius software package,<sup>25, 26</sup> which allows to create complex atomic models, including nanowire-like structures.<sup>27-29</sup>

## 2.4 Calculations

---

### Derivation of the surface area change with the longitudinal and radial growth and parameters of the growth rate calculation

For a nanorod with a circular cross section of radius  $r$ , length  $z$  and a molar volume  $V_m$ :

$$V = \pi r^2 z = V_m n$$

$$A = A_a + A_r = 2\pi r^2 + 2\pi r z$$



Where  $A_z$  is the area of what we refer as the basal planes of the nanorod and  $A_r$  is the lateral surface area. Then, for a nanorod growing in the radial direction, thus incorporating monomer in the lateral planes:

$$\frac{dA_z}{dn_r} = \frac{dA_z}{dr} \frac{dr}{dn_r} = \frac{2V_m}{z}$$

$$\frac{dA_r}{dn_r} = \frac{dA_r}{dr} \frac{dr}{dn_r} = \frac{V_m}{r}$$

On the other hand, for a nanorod growing in the longitudinal or axial direction, thus incorporating monomer in the basal planes:

$$\frac{dA_z}{dn_z} = \frac{dA_z}{dz} \frac{dz}{dn_z} = 0$$

$$\frac{dA_r}{dn_z} = \frac{dA_r}{dz} \frac{dz}{dn_z} = \frac{2V_m}{r}$$

Then, the chemical potential changes associated to the surface area variation when incorporating a monomer in a lateral plane and a basal plane of a cylindrical particle are:

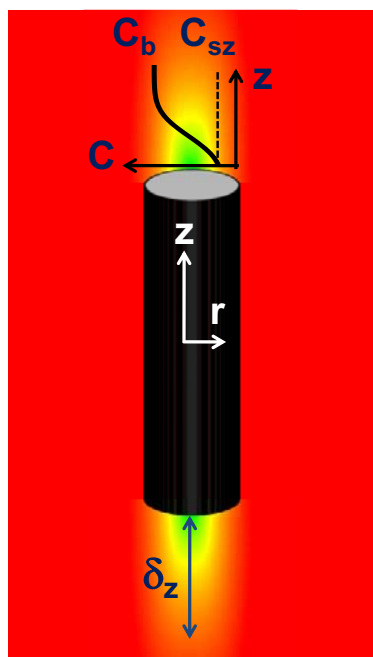
$$\Delta\mu_r = \gamma_z \frac{dA_z}{dn_r} + \gamma_r \frac{dA_r}{dn_r} = V_m \left( \frac{2\gamma_z}{z} + \frac{\gamma_r}{r} \right)$$

$$\Delta\mu_z = \gamma_z \frac{dA_z}{dn_z} + \gamma_r \frac{dA_r}{dn_z} = \frac{2V_m\gamma_r}{r}$$

Where  $V_m$  is the molar volume and  $\gamma_r$  and  $\gamma_z$  are the specific surface energies of the nanorod lateral and basal planes, respectively.

**Table 1.** Parameters used for the growth rate calculation

<b>Parameter</b>	<b>Symbol</b>	<b>Value</b>
Molar volume	$V_m$	$7.6 \times 10^{-5} \text{ m}^3$
Specific lateral surface energy	$\gamma_r$	$0.35 \text{ J m}^{-2}$
Specific basal surface energy	$\gamma_z$	$0.42 \text{ J m}^{-2}$
Reaction rate in infinite basal surface	$k_{gz}^\infty$	$6.4 \times 10^{-6} \text{ m s}^{-1}$
Dissolution rate in infinite basal surface	$k_{dz}^\infty$	$8.4 \times 10^{-8} \text{ mol m}^{-2} \text{ s}^{-1}$
Reaction rate in infinite lateral surface	$k_{gr}^\infty$	$3.8 \times 10^{-7} \text{ m s}^{-1}$
Dissolution rate in infinite lateral surface	$k_{dr}^\infty$	$1.7 \times 10^{-9} \text{ mol m}^{-2} \text{ s}^{-1}$
Temperature	T	450 K
Monomer diffusivity	$D$	$10^{-13} \text{ m}^2 \text{ s}^{-1}$
Thickness of the stagnant layer	$\delta$	$100r^{5/6}z^{5/12}$



$$\frac{dr}{dt} = V_m \left\{ C_b k_{gr}^{\infty} \exp \left[ -\frac{V_m}{2RT} \left( \frac{2\gamma_z}{z} + \frac{\gamma_r}{r} \right) \right] - k_{dr}^{\infty} \exp \left[ \frac{V_m}{2RT} \left( \frac{2\gamma_z}{z} + \frac{\gamma_r}{r} \right) \right] \right\}$$

$$\frac{dz}{dt} = V_m \frac{C_b k_{gz}^{\infty} - k_{dz}^{\infty} \exp \left( \frac{2\gamma_r V_m}{rRT} \right)}{\frac{\delta_z}{D} k_{gz}^{\infty} + \exp \left( \frac{\gamma_r V_m}{rRT} \right)}$$

**Scheme 1.** Schematic representation of the nanorod with the axial monomer diffusion layers.

## 2.5 Results and Discussion

$\text{Bi}_2\text{S}_3$  nanocrystals were obtained by reacting bismuth (III) acetate with elemental sulfur in a heated 1-octadecene solution containing oleic acid and/or oleylamine. In the presence of carboxylic acids, but no amines, initial  $\text{Bi}_2\text{S}_3$  nanorods rapidly evolved into large asymmetric and hierarchical structures, such as nanoribbons, nanoflakes and nanoflowers, analogous to those previously obtained by different methods.<sup>30-35</sup> The presence of amines slowed down the nanocrystal growth rate, but it did not efficiently prevent by itself the aggregation of the nanocrystals. Nanorods with narrow size distributions and high solubilities were obtained by introducing a combination of oleic acid and oleylamine in the reaction solution. In our synthesis conditions, the nanorod size distribution and solubility were optimized with a molar ratio 8:3 between oleic acid and oleylamine. In figures 1a and 1b, representative transmission electron microscopy (TEM) images of the  $\text{Bi}_2\text{S}_3$  nanorods obtained in the presence of oleic acid and oleylamine are shown.

$\text{Bi}_2\text{S}_3$  crystallized in the orthorhombic  $Pbnm$  phase (Bismuthinite, JCPDS file 17-0320), as observed from high resolution TEM (HRTEM) characterization of the nanorods (Figure 1c). In all the synthesis conditions tested, the preferential crystallographic growth direction was the  $[001]$ . TEM characterization of the obtained nanorods at different tilting angles showed them to have elliptical cross sections (Figure 1d). Extensive HRTEM characterization showed the long and short axis of the ellipse to be most probably along the  $[1-10]$  and  $[110]$  directions, respectively. The identified crystallographic orientations are in agreement with previous HRTEM characterization of  $\text{Bi}_2\text{S}_3$  nanowires.<sup>34</sup>

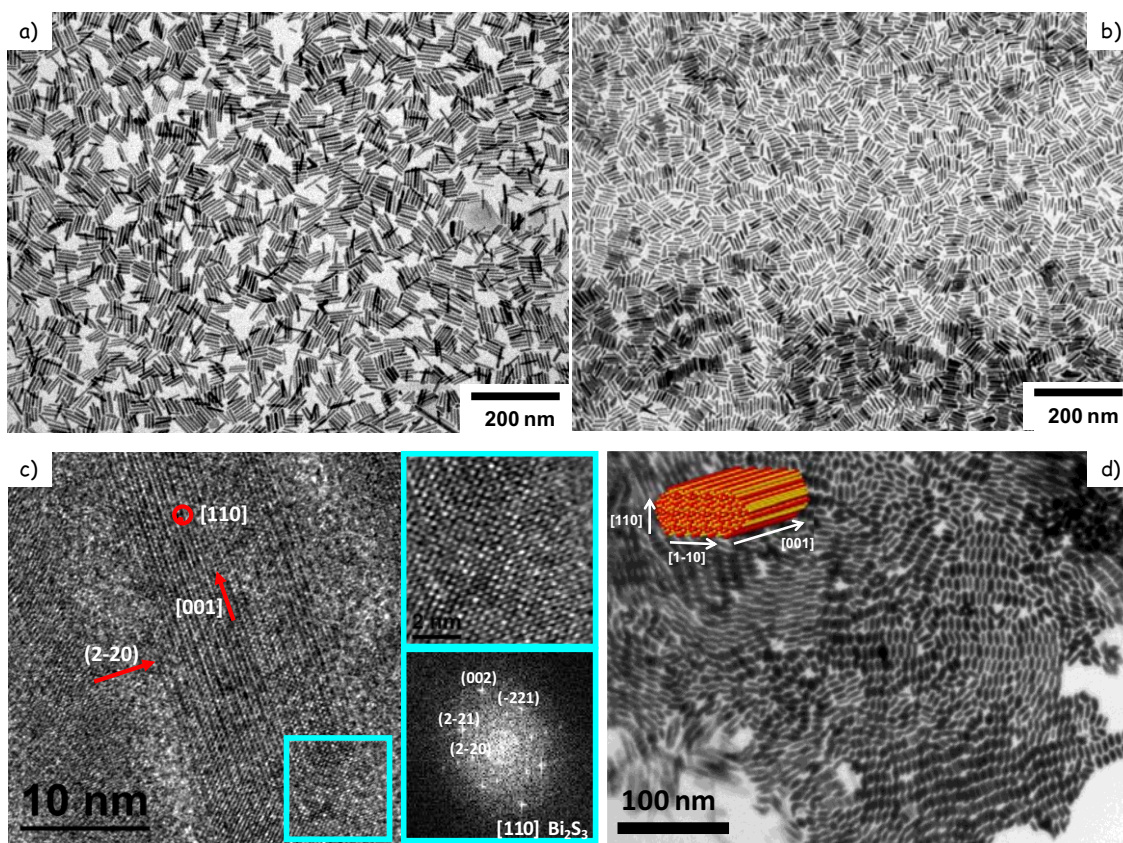


**Figure 1.** (a) and (b) Low-magnification TEM micrograph of  $\text{Bi}_2\text{S}_3$  nanorods obtained after 50 s at 180 °C and 60 s at 170 °C, respectively; (c) Representative High-Resolution TEM micrograph of a single  $\text{Bi}_2\text{S}_3$  nanorod with an indexed fast Fourier transform pattern of the selected area; (d) TEM image of an assembly of  $\text{Bi}_2\text{S}_3$  nanorods observed while tilting the TEM holder 30 degrees. The inset shows a 3D atomic supercell model of the nanorod proposed morphology and crystallographic directions.

The evolution of the nanocrystals ensemble was followed by analyzing, by means of TEM, the size distribution of aliquots extracted at successive reaction times. The whole relevant range of reaction times and temperatures, from 120 °C to 180 °C, was characterized. Figure 2 shows TEM images illustrating the time evolution of the nanorod ensemble for different reaction temperatures. The mean value of the nanorod lengths and widths and the normalized standard deviations of their distributions are plotted in figure 3 and 4, respectively. Due to the ellipsoidal cross section of the nanorods and their tendency to lay down on their largest surface, only the long axis of their elliptical cross section could be systematically measured. Thus, this long axis will be used here as the nanorod width.

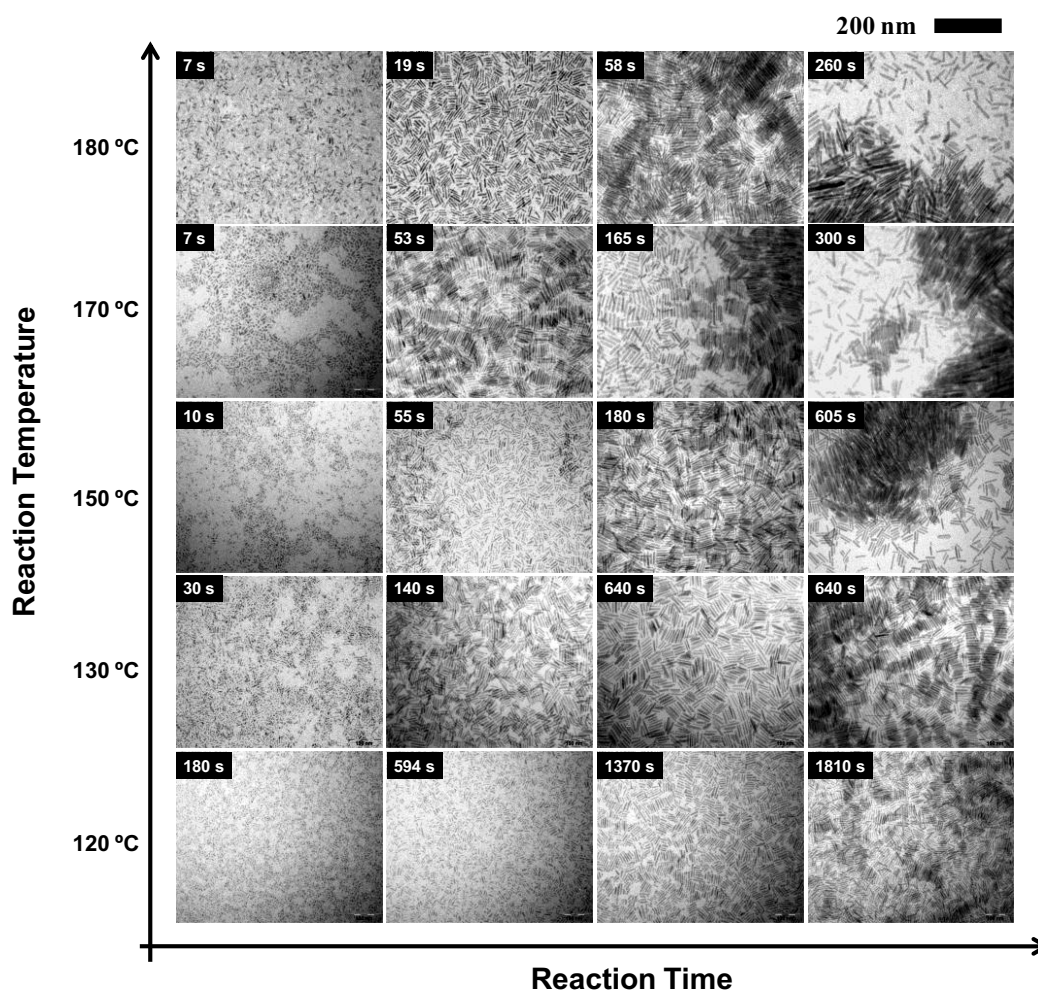


**Figure 2.** TEM images of the ensemble of  $\text{Bi}_2\text{S}_3$  nanorods obtained at different reaction temperatures and after successive reaction times as specified in each image.

Seconds after the oleylamine-sulfur injection into the heated solution containing the Bi precursor, a relatively heterogeneous distribution of  $\text{Bi}_2\text{S}_3$  nanocrystals was obtained. With the reaction time,  $\text{Bi}_2\text{S}_3$  nanocrystals evolved into elongated nanostructures of increasingly higher aspect ratio. The length distribution of the  $\text{Bi}_2\text{S}_3$  nanorods sharpened with the reaction time after nucleation, until a critical temperature-dependent time, when the nanocrystal length distribution became bimodal (Figure 5). From this critical time on, a population of small and highly soluble nanorods was clearly differentiated from a distribution of larger and mostly aggregated nanorods. Figure 5b shows a scanning electron microscopy (SEM) image of the  $\text{Bi}_2\text{S}_3$  nanorods obtained after long reaction times, where the bimodal nanorod distribution is clearly observed. After the critical reaction time, the aspect ratio and the average length of the smallest nanorods decreased, while the standard deviation of their length distribution increased. In parallel, the larger nanorods aggregated. Their aggregation introduced an important experimental error on their size measurement, preventing a reliable assessment of their size distribution standard deviation. While the measurement of the nanorods width has associated a larger relative experimental error, a nanorod width increase with the reaction time until the critical temperature-dependent moment is clearly inferred from the experimental results. However, no width distribution focusing was detected.

Notice that, both the growth and dissolution rates increased with the reaction temperature, while the critical reaction time decreased. The average nanorod length obtained just before the development of the bimodal size distribution also increased with the reaction temperature. From a technological point of view, the reaction temperature should be selected based on the required nanorod length, while the reaction time should be set equal to the critical time, when the narrowest size distribution is obtained.

To interpret the size-distribution evolution of the nanorods ensemble, a diffusion-reaction kinetic model based on the activated complex theory previously reported by D. V. Talapin et

al.<sup>3</sup> for spherical nanocrystals was developed. Our model considers the nanocrystal growth rates in the longitudinal and radial directions separately, and evaluates them as a function of each surface free energy, the monomer concentration and the nanorod dimensions.

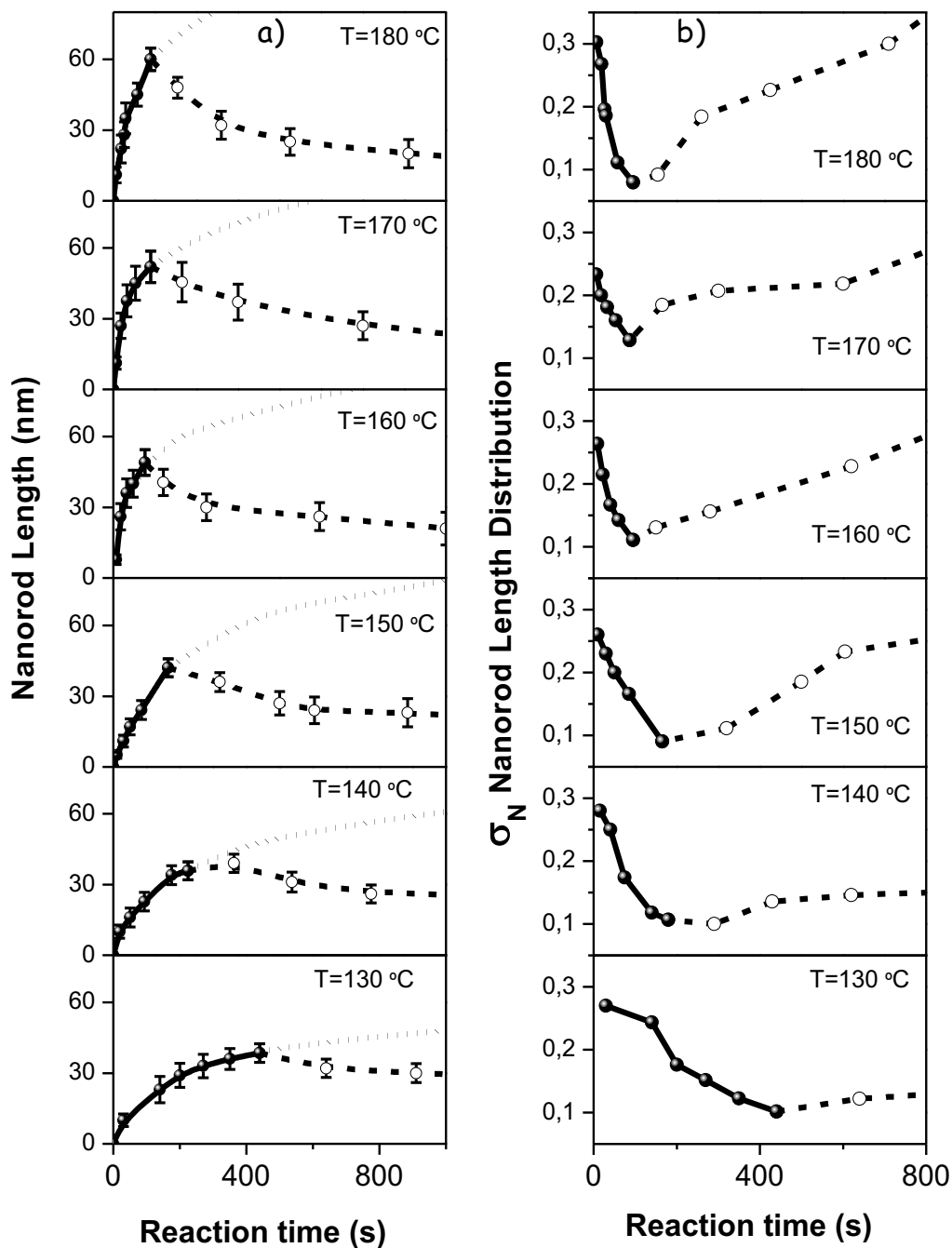


**Figure 3.** Average value (a) and normalized standard deviation (b) of the length distribution of the ensemble of  $\text{Bi}_2\text{S}_3$  nanorods obtained at different reaction temperatures and after successive reaction times.

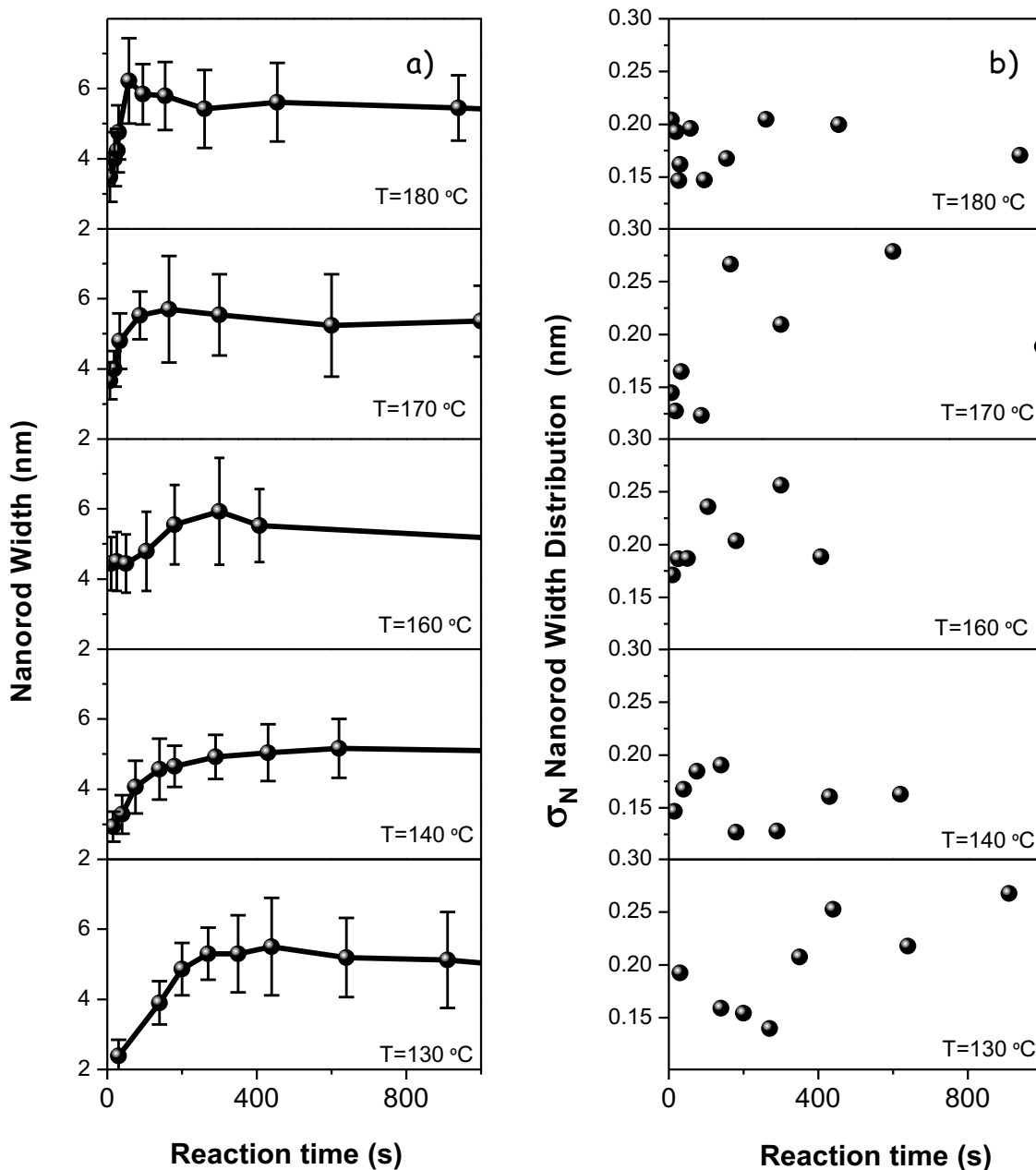


**Figure 4.** Average value (a) and normalized standard deviation (b) of the long width distribution of the ensemble of  $\text{Bi}_2\text{S}_3$  nanorods obtained at different reaction temperatures and after successive reaction times.

Notice that, as defined by D. V. Talapin et al., the term “monomer” generally refers to any molecular precursor participating in the reversible act of adding/removing a molecular unit to a nanoparticle in the reaction vessel.<sup>3</sup> For simplification, we consider here only one monomer



type, but obviously multiple precursors having different activation energies may participate in the reaction. In general, the monomer with the lowest-concentration and/or the larger activation energies and/or the slowest diffusing will limit the nanoparticle growth rate. Thus the present theory can be used to model the asymmetric growth not only of elemental nanoparticles, but also of those having binary, ternary or quaternary composition.

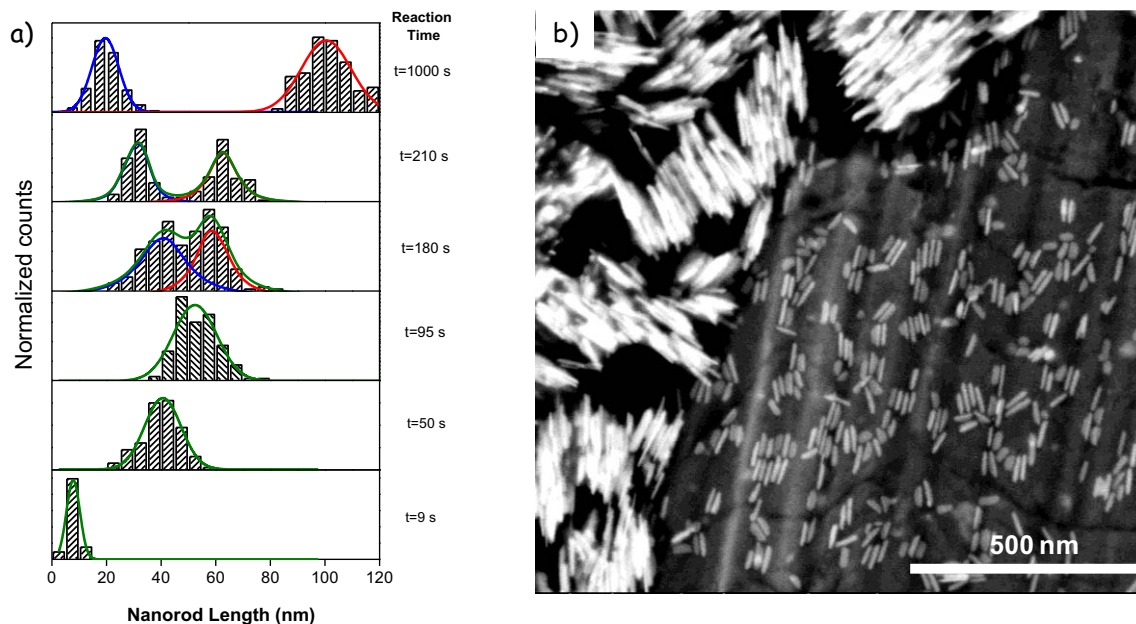


**Figure 5.** (a) Evolution of the  $\text{Bi}_2\text{S}_3$  nanorod length distribution obtained at  $160^\circ\text{C}$ ; (b) SEM image of the ensemble of  $\text{Bi}_2\text{S}_3$  nanorods obtained at  $180^\circ\text{C}$  after 120 s reaction time, where the bimodal nanorod length distribution is evident.

In the activated complex theory, the monomer incorporation/desorption into/from the nanocrystal surface takes place through an energy barrier, which depends on the change of surface free energy associated to the reaction:

$$E_g = \Delta\mu_{c\infty} + \alpha\gamma \frac{dA}{dn} = E_{g\infty} + \alpha\gamma \frac{dA}{dn} \quad (1)$$

$$E_d = \Delta\mu_{c\infty} + \Delta\mu_{\infty} - (1 - \alpha)\gamma \frac{dA}{dn} = E_{d\infty} - (1 - \alpha)\gamma \frac{dA}{dn} \quad (2)$$

Where  $E_g$  and  $E_d$  are the energy barriers for nanocrystal growth and dissolution, respectively;  $\Delta\mu_{c\infty}$  is the complex activation energy associated to the incorporation of a monomer into an infinite crystal;  $\Delta\mu_{\infty}$  is the change of chemical potential between the free monomer in solution and the monomer incorporated in an infinite crystal surface;  $E_{g\infty}$  and  $E_{d\infty}$  are the activation energies for growth and dissolution of an infinite crystal;  $\alpha$  is the transfer coefficient, which determines the ratio of the barrier change with the variation of the surface chemical potential;  $\gamma$  is the specific surface energy; and  $dA/dn$  is the surface area variation with the incorporation of monomer. In figure 6a a schematic representation of the energy levels and chemical potential variations is shown.

The chemical potential change associated to the surface area variation when incorporating a monomer in a lateral plane and in what we will refer as the basal planes of a cylindrical particle are:

$$\Delta\mu_r = \gamma_z \frac{dA_z}{dn_r} + \gamma_r \frac{dA_r}{dn_r} = V_m \left( \frac{2\gamma_z}{z} + \frac{\gamma_r}{r} \right) \quad (3)$$

$$\Delta\mu_z = \gamma_z \frac{dA_z}{dn_z} + \gamma_r \frac{dA_r}{dn_z} = \frac{2V_m\gamma_r}{r} \quad (4)$$

here  $V_m$  is the molar volume and  $\gamma_r$  and  $\gamma_z$  are the specific surface energies of the nanorod lateral and basal planes, respectively.

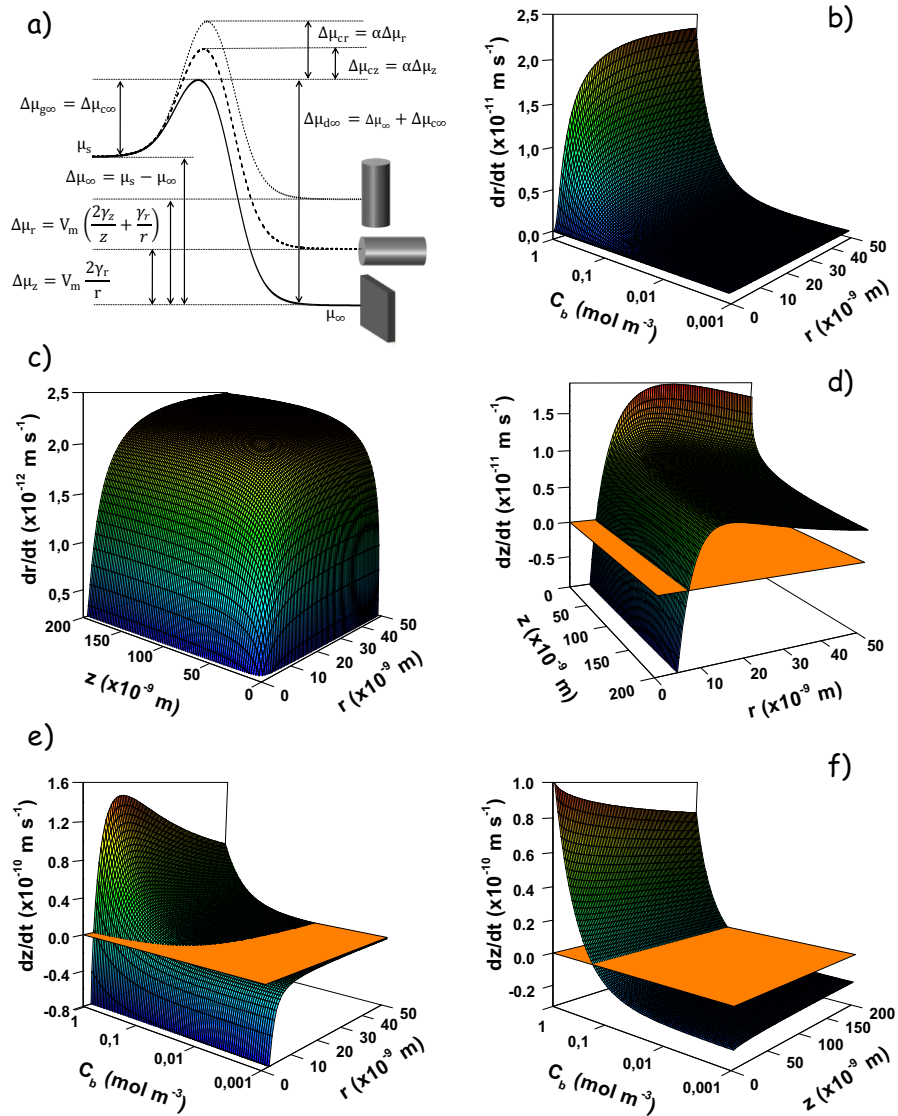


**Figure 7.** (a) Schematic representation of the chemical potential changes associated to the incorporation of monomer from solution into the basal and lateral nanorod planes and into an infinite crystal surface; (b) Radial growth rate for a 50 nm nanorod vs monomer concentration and nanorod radius; (c) Radial growth rate vs nanorod radius and length in a solution containing  $0.1 \text{ mol}\cdot\text{m}^{-3}$  of monomer; (d) Axial growth rate vs nanorod radius and length in a solution containing  $0.06 \text{ mol}\cdot\text{m}^{-3}$  of monomer; (e) Axial growth rate for a 50 nm long nanorod vs nanorod radius and monomer concentration; (f) Axial growth rate for a 5 nm thick nanorod vs nanorod length and monomer concentration. Growth rates were calculated using the parameters detailed in the calculations section.

Notice how the change of chemical potential associated to the nanorod growth on the radial direction decreases with both, its length and radius. However, the change of chemical potential associated to the nanorod growth in the longitudinal direction does not depend on its length, but only on its radius, as there is no variation on the basal surface area with the axial growth. Therefore, the axial growth is energetically favored over the radial one only while the nanostructure aspect ratio is smaller than twice the ratio between the basal and lateral specific surface energies. For larger aspect ratios, the energy toll paid to incorporate a monomer in the lateral planes is lower than the required to incorporate a monomer in the basal planes, thus the radial growth is energetically favored over the longitudinal one:

$$\frac{\Delta\mu_r}{\Delta\mu_z} = \frac{\gamma_z r}{\gamma_r z} + \frac{1}{2} = \begin{cases} > 1 & \text{if } \frac{z}{r} < \frac{2\gamma_z}{\gamma_r} \\ < 1 & \text{if } \frac{z}{r} > \frac{2\gamma_z}{\gamma_r} \end{cases} \quad (5)$$

Considering the surface free energies previously calculated for the bare basal and lateral crystallographic planes,<sup>35</sup> a critical aspect ratio of 2.4 is obtained. However, it should be taken into account that the intrinsic differential of surface free energies can be modified by the presence of surfactants selectively adhered to specific crystal facets.<sup>9</sup> The higher aspect ratios obtained for Bi<sub>2</sub>S<sub>3</sub> in the present and previous works may be explained by a more efficient surfactant surface coverage of the lateral planes than the basal ones, lowering their surface free energy ratio. Furthermore, the probable selective passivation of the lateral planes would reduce the lateral reaction sites density, lowering its reaction rate.

The nanocrystal growth rate is obtained from the balance between the flux of monomer incorporating and dissociating into/from each surface. It is considered here that the monomer incorporation rate is first-order with the monomer concentration next to the nanorod surface ( $C_s$ ), while the dissolution rate is independent of  $C_s$ . Then, expressing the rate constants of the

growth/dissolution reactions in the Arrhenius form and taking  $\alpha = 0.5$ , the total flux of monomer reacting/dissociating at the lateral surface becomes:

$$\begin{aligned}
 J_r &= J_{gr} + J_{dr} = 2\pi r z (C_{sr} k_{gr} - k_{dr}) \\
 &= 2\pi r z \left\{ C_{sr} k_{gr}^{\infty} \exp \left[ -\frac{V_m}{2RT} \left( \frac{2\gamma_z}{z} + \frac{\gamma_l}{r} \right) \right] - k_{dr}^{\infty} \exp \left[ \frac{V_m}{2RT} \left( \frac{2\gamma_z}{z} + \frac{\gamma_r}{r} \right) \right] \right\}
 \end{aligned} \tag{6}$$

where  $k_{gr}^{\infty}$  and  $k_{dr}^{\infty}$  are the growth and dissolution rates at an infinite radial crystal surface, which take into account the density of reaction sites.

The total monomer flux reacting at the lateral nanorod surface is related to the radius variation by means of:

$$J_r = \frac{2\pi r z}{V_m} \frac{dr}{dt} \tag{7}$$

Then, considering a reaction-limited radial growth, in view of the very low radial reaction rates experimentally obtained:

$$\frac{dr}{dt} = V_m \left\{ C_b k_{gr}^{\infty} \exp \left[ -\frac{V_m}{2RT} \left( \frac{2\gamma_z}{z} + \frac{\gamma_r}{r} \right) \right] - k_{dr}^{\infty} \exp \left[ \frac{V_m}{2RT} \left( \frac{2\gamma_z}{z} + \frac{\gamma_r}{r} \right) \right] \right\} \tag{8}$$

where the monomer concentration at the particle surface is considered equal to that in solution,  $C_b$ .

In figure 6b and 6c, the radial growth rate vs the monomer concentration and the nanorod dimensions is plotted. Growth rate values were obtained considering previously calculated surface free energies and the reaction rates obtained from the fitting of the experimental results reported here (Calculations section). Notice how the radial growth rate monotonically increases with both the nanorod length and radius. Therefore, no thickness-distribution focusing exists. Nanorods grow thicker at a faster rate the thicker and longer they get. At the same time, the

radial growth rate monotonically decreases with the monomer concentration. Thus, a thickness- and length-dependent critical concentration exists, at which rods start to laterally dissolve:

$$C_{b0r} = \frac{k_{dr}^{\infty}}{k_{gr}^{\infty}} \exp \left[ \frac{V_m}{RT} \left( \frac{2\gamma_z}{z} + \frac{\gamma_r}{r} \right) \right] \quad (9)$$

As expected, the thinnest and shortest nanorods start to laterally dissolve at higher concentrations than the thickest and longest ones. Thus, at low enough monomer concentrations, the lateral growth may enter into an Oswald-ripening regime. In this regime, the thinnest and shortest nanorods laterally dissolve, releasing monomer into the solution, which is used by the thickest and longest nanorods to continue growing.

On the other hand, considering  $\alpha = 0.5$ , the flux of monomer reacting/dissociating at each basal plane is:

$$\begin{aligned} J_z &= J_{gz} + J_{dz} = \pi r^2 (C_{sz} k_{gz} - k_{dz}) \\ &= \pi r^2 \left\{ C_{sz} k_{gz}^{\infty} \exp \left[ -\frac{\gamma_r V_m}{rRT} \right] - k_{dz}^{\infty} \exp \left[ \frac{\gamma_r V_m}{rRT} \right] \right\} \end{aligned} \quad (10)$$

which is related to its length variation by:

$$J_z = \frac{\pi r^2}{V_m} \frac{dz}{dt} \quad (11)$$

Because at high monomer concentrations the nanoparticle growth in the axial direction takes place at relatively high rates, the possibility of a diffusion-limited axial growth rate must be considered. It is also assumed here that no redistribution of monomers takes place between different nanocrystal surface planes; i.e. monomer reacting at the nanorod basal planes reach them by diffusion from the solution and not by surface diffusion from the nanorod lateral planes. In this scenario, the longitudinal growth rate is proportional to the monomer flux in the axial

direction at the nanorod basal planes, which is related to the monomer concentration gradient by Fick's first law:

$$J_z = \pi r^2 D \frac{\partial C}{\partial z} \quad (12)$$

where D is the diffusivity constant of the monomer in solution.

Apparently, neither the monomer concentration gradient nor the monomer flux at the nanorod basal planes depends on the nanorod length,  $z$ . However, they are explicitly influenced by its thickness. In order to obtain an analytical solution, two related major approximations need to be considered: i) The monomer concentration is homogeneous across the whole basal plane. This is a reasonable approximation because, while it is evident that the monomer concentration profile and hence the thickness of its diffusion layer and the monomer flux have a radial distribution across the basal plane, monomers will redistribute along the basal surfaces to result in a homogeneous nanorod longitudinal growth, as experimentally observed. ii) The monomer flux in the axial direction is constant through the whole diffusion layer. This approximation neglects part of the dependence of the diffusion layer thickness on the nanorod radius. The consequences of this omission will be qualitatively discussed below.

Under these approximations, the integration of eq. 12 through the whole diffusion layer of average thickness  $\delta_z(r)$  results in an average value of the monomer flux reaching each basal plane given by:

$$J_z = \frac{\pi r^2}{\delta_z} D (C_b - C_{sz}) \quad (13)$$

Then, from eqs 10 and 13:

$$C_{sz} = \frac{DC_b + \delta_z k_{dz}^{\infty} \exp\left[\frac{\gamma_r V_m}{rRT}\right]}{D + \delta_z k_{gz}^{\infty} \exp\left[-\frac{\gamma_r V_m}{rRT}\right]} \quad (14)$$

and from eq., 13 and 14:

$$\frac{dz}{dt} = V_m \frac{C_b k_{gz}^\infty - k_{dz}^\infty \exp\left(\frac{2\gamma_r V_m}{rRT}\right)}{\frac{\delta_z}{D} k_{gz}^\infty + \exp\left(\frac{\gamma_r V_m}{rRT}\right)} \quad (15)$$

The longitudinal growth rate depends on the nanorod thickness in a similar way spherical crystals do on their radius,<sup>3</sup> except for the presence of  $\delta_z$  instead of  $r$  in the denominator sum.

While the longitudinal growth rate does not apparently vary with the nanorod length, it does depend on the thickness of the diffusion layer,  $\delta_z$ , which is tied to the particle size in two ways:

i) Since there is a lateral diffusion of monomer inside the diffusion layer, the monomer concentration profile at the nanorod basal planes varies with the nanorod thickness,. In this way, the thickness of the diffusion layer increases with the nanorod radius; ii) The thickness of the diffusion layer is strongly influenced by the relative solid-liquid velocity, i.e. the degree of agitation of the system and the nanocrystal Brownian movement, which depends on its size.<sup>36, 37</sup>

For static nanoparticles in solution, very large stagnant layers could be maintained. However, usually nanocrystals growth takes place in vigorously agitated and heated solutions. While forced convection has a major role on the micro and macroscopic homogenization of the solution, which is a key factor to obtain a homogeneous nucleation, Brownian motion controls the mass transfer in solution at the nanometer scale. In this regime, and for spherical particles, the dependence of the diffusion layer thickness on the particle volume was approximated by the semitheoretical equation:<sup>37</sup>

$$\delta = \frac{2^{1/6}}{3^{1/12} \theta} \left(\frac{D^2 \nu}{d_0}\right)^{1/6} \left(\frac{\pi^{5/3} d}{kT}\right)^{1/4} V^{5/12} \quad (16)$$

where  $V$  is the particle volume,  $\nu$  is the fluid viscosity and  $d$  and  $d_0$  are the particle and fluid densities, respectively. In the nanometer size range, the thickness of the diffusion layer was found to be of the same order of magnitude as the particle dimensions and to vary almost linearly



with the radius:  $\delta \sim r^{5/4}$ .<sup>37</sup> While this equation was obtained for spherical particles, a similar dependence on the nanoparticle volume can be considered for nanorods. Then, taking into account the dependence of the nanorod volume on its radius and length the following dependence of the thickness of the diffusion layer on the nanorod geometrical parameters can be assumed:

$$\delta = ar^{2b}z^b \quad (17)$$

with  $b \sim 5/12$

Then, we can rewrite eq 15 as:

$$\frac{dz}{dt} = V_m \frac{C_b k_{gz}^\infty - k_{dz}^\infty \exp\left(\frac{2\gamma_r V_m}{rRT}\right)}{\frac{a k_{gz}^\infty}{D} r^{2b} z^b + \exp\left(\frac{\gamma_r V_m}{rRT}\right)} \quad (18)$$

In figure 6d, the growth rate in the axial direction vs  $r$  and  $z$  is plotted. Notice that the dependence of the axial growth rate on the radius follows a similar trend as that obtained for spherical nanoparticles. The longitudinal growth rate decreases with the nanorod thickness only for thick enough nanorods, but monotonically with the nanorod length. Thus, for high enough monomer concentrations, the nanorods length-distribution narrows with the reaction time. The driving force behind such length-distribution focusing is the increase of the diffusion layer thickness with the particle volume due to a slow down of the particle Brownian motion. Although not considered in the equation, the nanorod axial growth also has associated an increase of the diffusion layer thickness at the nanorod basal planes through the reduction of the monomer lateral diffusion. This is a second way in which, at high enough monomer concentration, the longitudinal growth rate decreases with the nanorod thickness.

As the reaction proceeds and nanocrystals coarsen, the solution becomes depleted of monomer. At a critical monomer concentration:

$$C_{b0z} = \frac{k_{dz}^{\infty}}{k_{gz}^{\infty}} \exp\left(\frac{2\gamma_r V_m}{rRT}\right) \quad (19)$$

the axial growth enters into an Ostwald-ripening regime. Interestingly, the critical monomer concentration for axial growth does not depend on the nanorod length but only on its thickness (Figures 6e and 6f). Thus, the first nanorods starting to dissolve from their basal planes when the monomer concentration is reduced are not the shortest ones, but the thinnest ones.

Comparing the critical monomer concentration for radial and axial growth, the critical aspect ratio determining if the nanorod dissolution takes place first from the basal or lateral planes is given by:

$$\frac{C_{b0z}}{C_{b0r}} = \frac{k_{dz}^{\infty} k_{gr}^{\infty}}{k_{dr}^{\infty} k_{gz}^{\infty}} \exp\left[\frac{V_m}{RT} \left(\frac{\gamma_r}{r} - \frac{2\gamma_z}{z}\right)\right] \quad (20)$$

Considering the experimental growth rates and the approximated critical monomer concentrations obtained for Bi<sub>2</sub>S<sub>3</sub> nanorods:

$$\frac{k_{dz}^{\infty}k_{gr}^{\infty}}{k_{dr}^{\infty}k_{gz}^{\infty}} \sim 3 \quad (21)$$

Then, for all physically meaningful parameters and dimensions:  $C_{b0z} > C_{b0r}$ , and thus nanorods start to dissolve always from the basal planes, as experimentally observed. The nanorod dissolution in the axial direction may continue feeding its radial growth in a particular case of intraparticle Oswald ripening. While no evidences of intraparticle Oswald ripening were obtained here, it is evident from the present study that the monomer released from the dissolution of the smallest nanorods contributed to the growth of the larger ones in a classical interparticle Oswald-ripening scenario.

Note finally that, for identical reaction rate ratios for growth and dissolution in infinite basal and lateral surfaces, the critical nanorod aspect ratio determining the preferential dissolution direction is the same that determines the energetically favored growth direction (Eq. 6). Large enough aspect ratio nanorods start to dissolve at higher critical monomer concentrations from their basal planes than from their lateral ones, but lower aspect ratio nanorods start to dissolve first from their lateral surfaces.

In all cases, the dissolution rate increases when decreasing the length and/or radius of the nanorod. Then, while the length-distribution focuses with the nanorod growth, it defocus with the nanorod dissolution, as it was experimentally observed (Figure 3b).

The presented model explains most of the experimental trends observed for the size distribution evolution not only of  $\text{Bi}_2\text{S}_3$  nanorods, but also of other asymmetric nanostructures, such as CdSe nanorods,<sup>21</sup> previously reported. However, the present model hardly explains the striking experimental observation of the bimodal length distribution obtained for  $\text{Bi}_2\text{S}_3$  at the late reaction stage. Because the critical monomer concentration for nanorod dissolution in the axial direction

does not depend on its length, but only on its thickness, it is possible to imagine an ensemble of nanorods with a particularly enough length and thickness distribution such that would evolve into a bimodal length distribution. However, it would be difficult to explain how such a particular combination of length and thickness distributions would have been obtained in first place. Thus, an alternative mechanism outside the presented model may be required to understand the evolution of the length distribution into bimodal. A possible explanation is the formation of larger nanorods from the oriented attachment of the smaller ones. Such aggregation would introduce the tilting point needed at the critical time to split the nanorod ensemble into two size distributions. Nevertheless, no definitive evidence of such oriented attachment was experimentally obtained.

## 2.6 Conclusions

---

In summary, we detailed the evolution of an ensemble of colloidal Bi<sub>2</sub>S<sub>3</sub> nanorods. After nucleation, Bi<sub>2</sub>S<sub>3</sub> nanorods grow in a length-distribution focusing regime until the monomer concentration in solution is reduced to a critical value. At this critical temperature-dependent reaction time, the system enters into an Ostwald-ripening growth regime where the smallest nanorods start to axially dissolve to feed the growth of the largest ones. At this point, a clearly differentiated bimodal length distribution appears. A diffusion-reaction model for the growth of nanocrystals with cylindrical shape predicts the length-distribution focusing to be directed by the nanorod thickness and the total volume of the particle. The much slower radial growth is not subjected to a focusing mechanism. The model further predicts that the Ostwald ripening length growth regime is controlled not by the nanorod length but by its thickness.

## 2.7 References

---

- (1) Talapin, D. V.; Lee, J.-S.; Kovalenko, M. V.; Shevchenko, E. V., *Chem. Rev.* **2010**, 110, 389-458.
- (2) Talapin, D. V.; Rogach, A. L.; Shevchenko, E. V.; Kornowski, A.; Haase, M.; Weller, H., *J. Am. Chem. Soc.* **2002**, 124, 5782-5790.
- (3) Talapin, D. V.; Rogach, A. L.; Haase, M.; Weller, H., *J. Phys. Chem. B* **2001**, 105, 12278-12285.
- (4) Park, J.; Joo, J.; Kwon, S. G.; Jang, Y.; Hyeon, T., *Angew. Chem. Int. Ed.* **2007**, 46, 4630-4660.
- (5) Shevchenko, E. V.; Talapin, D. V.; Schnablegger, H.; Kornowski, A.; Festin, Ö.; Svedlindh, P.; Haase, M.; Weller, H., *J. Am. Chem. Soc.* **2003**, 125, 9090-9101.
- (6) Peng, X. G.; Wickham, J.; Alivisatos, A. P., *J. Am. Chem. Soc.* **1998**, 120, 5343-5344.
- (7) Bullen, C. R.; Mulvaney, P., *Nano Lett.* **2004**, 4, 2303-2307.
- (8) Peng, Z. A.; Peng, X., *J. Am. Chem. Soc.* **2002**, 124, 3343-3353.
- (9) Manna, L.; Wang, Cingolani, R.; Alivisatos, A. P., *J. Phys. Chem. C* **2005**, 109, 6183-6192.

- (10) Barnard, A. S., *Rep. Prog. Phys.* **2010**, 73, 086502.
- (11) Sugimoto, T., *Encycl. Surf. Colloid Sci.* **2006**, 1, 4257-4270.
- (12) Sugimoto, T., *Adv. Colloid Interface Sci.* **1987**, 28, 65-108.
- (13) Mullin, J. W., *Crystallization, 3rd ed.* Butterworth-Heinemann: Oxford: 1997.
- (14) Peng, X., *Adv. Mater.* **2003**, 15, 459-463.
- (15) Barnard, A. S.; Zapol, P., *J. Phys. Chem.* **2004**, 121, 4276-4283.
- (16) Kumar, S.; Nann, T., *Small* **2006**, 2, 316-329.
- (17) Jun, Y.-W.; Choi, J.-S.; Cheon, J., *Angew. Chem. Int. Ed.* **2006**, 45, 3414-3439.
- (18) Marks, L. D., *Rep. Prog. Phys.* **1994**, 57, 603.
- (19) Yin, Y.; Alivisatos, A. P., *Nature* **2005**, 437, 664-670.
- (20) Peng, X.; Manna, L.; Yang, W.; Wickham, J.; Scher, E.; Kadavanich, A.; Alivisatos, A. P., *Nature* **2000**, 404, 59-61.
- (21) Peng, Z. A.; Peng, X., *J. Am. Chem. Soc.* **2001**, 123, 1389-1395.
- (22) Manna, L.; Scher, E. C.; Alivisatos, A. P., *J. Am. Chem. Soc.* **2000**, 122, 12700-12706.
- (23) Kanaras, A. G.; Sönnichsen, C.; Liu, H.; Alivisatos, A. P., *Nano Lett.* **2005**, 5, 2164-2167.
- (24) Xu, X.; Liu, F.; Yu, K.; Huang, W.; Peng, B.; Wei, W., *ChemPhysChem* **2007**, 8, 703-711.
- (25) Bernal, S.; Botana, F. J.; Calvino, J. J.; López-Cartes, C.; Pérez-Omil, J. A.; Rodríguez-Izquierdo, J. M., *Ultramicroscopy* **1998**, 72, 135-164.
- (26) Pérez-Omil, J. A. University of Cádiz, Cádiz, 1994.
- (27) Arbiol, J.; Cirera, A.; Peiro, F.; Cornet, A.; Morante, J. R.; Delgado, J. J.; Calvino, J. J., *Appl. Phys. Lett.* **2002**, 80, 329-331.
- (28) Arbiol, J.; Fontcuberta i Morral, A.; Estradé, S.; Peirò, F.; Kalache, B.; Roca i Cabarrocas, P.; Morante, J. R., *J. Appl. Phys.* **2008**, 104, 064312-7.
- (29) Uccelli, E.; Arbiol, J.; Morante, J. R.; Fontcuberta i Morral, A., *ACS Nano* **2010**, 4, 5985-5993.
- (30) Liu, Z.; Peng, S.; Xie, Q.; Hu, Z.; Yang, Y.; Zhang, S.; Qian, Y., *Adv. Mater.* **2003**, 15, 936-940.
- (31) Tang, J.; Alivisatos, A. P., *Nano Lett.* **2006**, 6, 2701-2706.
- (32) Liu, Z.; Liang, J.; Li, S.; Peng, S.; Qian, Y., *Chem. Eur. J.* **2004**, 10, 634-640.
- (33) Jiang, J.; Yu, S.-H.; Yao, W.-T.; Ge, H.; Zhang, G.-Z., *Chem. Mater.* **2005**, 17, 6094-6100.
- (34) Sigman, M. B.; Korgel, B. A., *Chem. Mater.* **2005**, 17, 1655-1660.

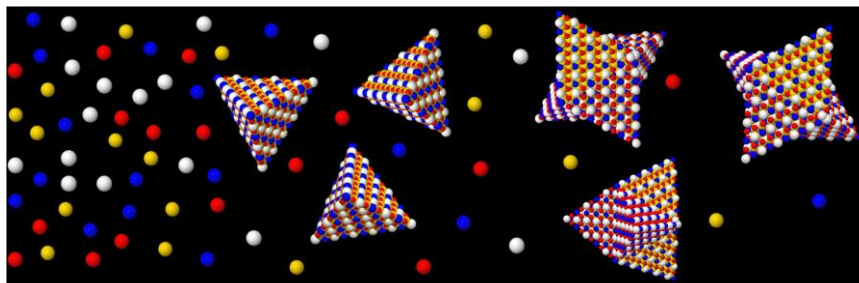
- (35) Wang, Y.; Chen, J.; Wang, P.; Chen, L.; Chen, Y.-B.; Wu, L.-M., *J. Phys. Chem. C* **2009**, 113, 16009-16014.
- (36) Shiau, L.-D.; Lu, Y.-F., *J. Phys. Chem.* **2009**, 130, 094105.
- (37) Sugimoto, T., *AIChE J.* **1978**, 24, 1125-1127.





# Chapter 3

## Extending the nanocrystal synthesis control to quaternary compositions



### 3.1 Abstract

---

The ample chemical and structural freedom of quaternary compounds permits engineering materials that fulfill the requirements of a wide variety of applications. In this work, the mechanisms to achieve unprecedented size, shape and composition control in quaternary nanocrystals are detailed. The described procedure allows obtaining tetrahedral and penta-tetrahedral quaternary nanocrystals with tuned size distributions and controlled compositions from a plethora of I<sub>2</sub>-II-IV-VI<sub>4</sub> semiconductors.

## 3.2 Introduction

---

Colloidal synthesis routes have proven successful in obtaining elemental and binary nanocrystals with controlled size and shape distributions. One step beyond that, the production of ternary and quaternary nanocrystals with precisely controlled characteristics remains a challenge. Owing to their recognized interest, significant efforts are currently underway to accomplish this step-change in the potential of solution-processing methods to produce functional nanomaterials. These efforts pay off with the strong added value that ternary and quaternary compositions bring in.

The numerous possibilities for chemical substitutions and structural modifications in quaternary materials allow significant range in tuning their fundamental chemical and physical properties.<sup>1-4</sup> For instance, compositional control in these quaternary semiconductors offers an accessible method to tune their valence balance, thereby adjusting their Fermi level. This intrinsic doping strategy to control the semiconductor electronic properties is especially interesting in the bottom-up processing of nanomaterials, where the introduction of extrinsic dopants has not proven significantly feasible. Such ample chemical and structural freedom, permits engineering quaternary chalcogenides, potentially made of abundant and non-toxic elements, to fulfill the requirements of a wide variety of applications. As an example,  $\text{Cu}_2\text{ZnSn}(\text{S},\text{Se})_4$  having a direct band gap in the visible spectrum and a high absorption coefficient, has recently attracted much attention in the field of photovoltaics as alternative absorber materials to CdTe and  $\text{Cu}(\text{In},\text{Ga})\text{Se}_2$ .<sup>5-7</sup> On the other hand, some quaternary diamond-like chalcogenides has been proven excellent thermoelectric materials because of their layered structures and intrinsically low lattice thermal conductivities.<sup>8,9</sup> Quaternary  $\text{I}_2\text{-II-IV-VI}_4$  semiconductors are also excellent

candidates for non-linear optic applications.<sup>10</sup> Furthermore, some of these compounds has been very recently demonstrated to be topological insulators with large nontrivial band gaps.<sup>11, 12</sup>

A few reports have already detailed successful preliminary synthesis procedures to obtain particularly interesting quaternary nanostructured chalcogenides:  $\text{Cu}_2\text{ZnSnS}_4$ <sup>13,14</sup> and  $\text{Cu}_2\text{ZnSnSe}_4$ .<sup>6</sup> However, the complexity of the thermodynamics and kinetics of nucleation and growth of such complex structures has resulted up to now in irregular shapes and broad size distributions. The very limited control over the size, geometry and composition of the nanocrystals previously obtained precludes a systematic investigation of their fundamental properties and limits their range of potential applications. Moreover, the synthesis of nanocrystals of new potentially useful quaternary chalcogenides, e.g.  $\text{Cu}_2\text{CdGeSe}_4$  and  $\text{Cu}_2\text{ZnGeSe}_4$ , has not yet been attempted.

In the present work, the mechanisms to achieve unprecedented size, shape and composition control in quaternary  $\text{I}_2\text{-II-IV-VI}_4$  nanocrystals are detailed. While the presented procedures are illustrated using  $\text{Cu}_2\text{CdSnSe}_4$  nanocrystals as the prototypical system, this synthetic route is proven successful for the production of a plethora of other quaternary chalcogenide nanoparticles. Furthermore, in the present approach particular care was taken in designing a cost-effective and up-scalable process to assure its relevance in a future industrial implementation. The potential for large scale synthesis is demonstrated by producing grams of quaternary nanocrystals with preserved exceptionally narrow size distributions and controlled morphologies.

### 3.3 Experimental

---

*Synthesis.* Metal complexes were prepared by dissolving the metal salts or oxides in hexadecylamine (HDA, 90% Aldrich) in the presence of small amounts of alkylphosphonic acids at 200 °C. In a typical synthesis for  $\text{Cu}_2\text{CdSnSe}_4$  or  $\text{Cu}_2\text{CdGeSe}_4$ , 0.50 mmol  $\text{CuCl}$  (97%,

Aldrich), 0.25 mmol CdO (99.999%, Aldrich), 0.25 mmol SnCl<sub>4</sub>·5H<sub>2</sub>O (98%, Across) or 0.5 mmol GeCl<sub>4</sub> (99.9999%, Strem), 1-7 mM HDA, 0.1 mmol of n-octadecyl phosphonic (ODPA, PCI Synthesis) acid and 10 ml octadecene (90%, Aldrich) were placed in a four-neck flask and heated up to 200 °C under argon flow until all precursors were completely dissolved. The resultant solution was maintained at 200 °C for one additional hour to ensure removal of water and oxygen. At this point, the solution was heated up to the reaction temperature. Separately, a 0.8 M selenium solution was prepared under argon by dissolving selenium dioxide (99.8%, Strem) in octadecene at 180 °C. 4 mL of the precursor Se solution were injected into the heated solution containing the metal complexes. Subsequently to the injection, the solution dropped around 30 °C and gradually recovered to the injection temperature. The solution was kept in this temperature range for 5 min to allow the nanoparticles growth. Finally, the flask was rapidly cooled down to room temperature. To prevent aggregation and ensure long-term solution stability, the weakly bonded HDA on the nanoparticles surface was replaced with a carboxylic acid by injecting 3 ml of oleic acid (OA, ≥99%, Aldrich) into the mixture during the cooling step at about 70 °C. The nanoparticles were isolated from the crude solution by centrifugation at 4000 rpm. Further purification was performed by multiple precipitation and re-dispersion cycles using chloroform as a solvent and 2-propanol as the precipitating agent. In the case of Cu<sub>2</sub>ZnSnSe<sub>4</sub>, or Cu<sub>2</sub>ZnSnSe<sub>4</sub>, the same protocol was used with slight variations. To promote the incorporation of zinc into the structure, the amount of ZnO (99.9%, Aldrich) was increased to 0.5 mmol. Besides, 0.1 mmol of a shorter phosphonic acid, n-tetradecylphosphonic acid (TDPA, PCI Synthesis) was used, and the reaction temperature was increased to 295 °C.

The synthesis procedure was scaled up by the straightforward increase of the amounts of all precursor, surfactant and solvent. Keeping the exact same concentration of each compound, the

potential for nanocrystal production of the presented procedure was raised to the gram-per-batch scale.

To quantitatively monitor the reaction process, aliquots were extracted at successive reaction times after the precursor injection. Aliquots were rapidly cooled down to quench the nanocrystal growth by dissolving them in toluene. The excess of unreacted precursors and surfactants from the prepared nanocrystal solution was immediately removed by multiple precipitation-dispersion steps using 2-propanol for precipitation and chloroform for re-dispersion.

*Measurements.* For XRD characterization, a Bruker D8 Advance diffractometer with Cu K $\alpha$ 1 radiation ( $\lambda = 1.5406 \text{ \AA}$ ) was used. Field emission scanning electron microscopy images used to characterize the morphology of the resulting materials were obtained using a FEI Nova Nanosem 230.

For TEM and HRTEM characterization, samples were prepared by placing a drop of the colloidal solution containing the nanoparticles onto a carbon coated copper grid at room temperature and ambient atmosphere. TEM micrographs were obtained using Jeol 1010 microscope, operating at 80 kV. Images were digitally acquired using a MegaviewIII scanning CCD camera with a soft imaging system. The morphology and crystallographic structure of the nanoparticles were further characterized with atomic resolution by means of HRTEM in a Jeol 2010F field emission gun microscope with a 0.19 nm point to point resolution. 3D atomic supercell modeling was performed by using the Rhodius software package,<sup>15, 16</sup> which allows creating complex atomic models, including nanowire-like structures.<sup>17-19</sup>

The materials chemical composition was analyzed both by EDX and EELS. Energy Dispersive X-ray (EDX) spectroscopy analyses were performed on an Oxford INCA detector coupled to a Jeol J2100 TEM microscope. In the case of electron energy loss spectroscopy (EELS) analyses,

they were performed on a GATAN GIF 2001 detector coupled to a Jeol 2010F field emission TEM microscope operated on scanning TEM (STEM) mode.

### 3.4 Results and Discussion

---

Quaternary nanocrystals were prepared by reacting metal-amine and metal-phosphonic acid complexes with an excess of selenium. In a typical synthesis, 0.50 mmol CuCl, 0.25 mmol CdO, 0.25 mmol SnCl<sub>4</sub>·5H<sub>2</sub>O, 1 mM HDA, 0.1 mmol of n-octadecyl phosphonic acid and 10 ml octadecene were heated up to 200 °C under argon flow until all precursors were completely dissolved. The resultant solution was maintained at 200 °C for one additional hour to ensure removal of water and oxygen. At this point, the solution was heated up to 285 °C. Separately, a 0.8 M selenium solution was prepared under argon by dissolving selenium dioxide in octadecene at 180 °C. 4 mL of the precursor Se solution were injected into the heated solution containing the metal complexes. Subsequently to the injection, the solution dropped around 30 °C and gradually recovered to the injection temperature. The solution was kept in this temperature range for 5 min to allow the nanoparticles growth. Figure 1 shows the shape and size evolution of the obtained nanocrystals. For this study, several aliquots were extracted from the reacting solution at different times. At the very early stage of the nanocrystals growth, spherical nanoparticles with a narrow size distribution were formed (Fig 1A). The crystallographic and chemical analysis of these initially nucleated spherical nanoparticles revealed Cu<sub>2-x</sub>Se with the Berzelianite cubic structure (JCPDS 01-088-2043; S.G.: Fm3-m).<sup>20</sup> During the first reaction minute, a progressive change of the nanoparticles morphology, from spherical to tetrahedral, was observed (Figure 1B). The spherical-to-tetrahedral geometry transformation was accompanied by the incorporation of the group II and IV elements in the crystal structure. EDX and ICP measurements allowed following the evolution of the nanoparticles composition with the reaction time (Figure 2). Sn ions clearly

incorporated to the CCTSe structure at earlier reaction times and lower temperatures than Cd. Cd-poor CCTSe with a stannite crystal structure (JCPDS 01-070-0831, S.G.: I-42m)<sup>21</sup> was obtained after 1 minute reaction. The stoichiometric composition was obtained after 2 minutes of reaction time (Figure 2). Single particle HRTEM-EDX and EELS analysis<sup>6</sup> confirmed both, that all nanoparticles contained all four elements and that the four elements were homogeneously distributed within each nanocrystal. The different reaction kinetics of the I, II and IV elements with Se, allowed adjusting the nanocrystals composition in a broad range by just controlling the reaction time and the initial concentration of precursors in solution.

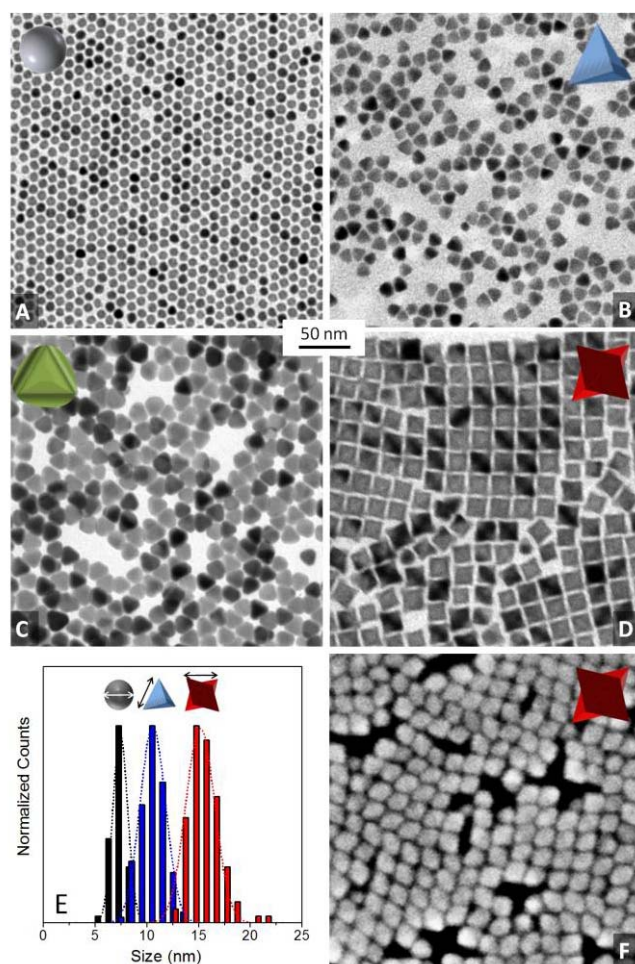


**Figure 1.** A)-D) TEM images of the nanocrystals obtained at different reaction times at 285 °C: 10 s (A); 1 min (B); 2 min (C); 5 min (D). E) Size distribution histograms from the nanoparticles obtained after 10 s, 1 min and 5 min. F) SEM image of the  $\text{Cu}_2\text{CdSnSe}_4$  nanocrystals obtained after 5 minutes at 285 °C.

The presence of alkylphosphonic acids was observed to be critical in controlling the nanoparticle composition. Alkylphosphonic acids are known to strongly interact with  $\text{Cd}^{2+}$  and  $\text{Zn}^{2+}$  ions to form complexes.<sup>22, 23</sup> These complexes allow a high degree of control over the size and shape of II-VI semiconductors. With no phosphonic acid in solution, the composition of the obtained  $\text{I}_2\text{-II-IV-VI}_4$  nanocrystals was generally deficient in the II ion. This experimental observation points towards a higher reactivity of a II-alkylphosphonic acid than the equivalent amine complex. For the quaternary chalcogenides produced here, the best results were obtained in the presence of octadecyl or tetradecylphosphonic acids.

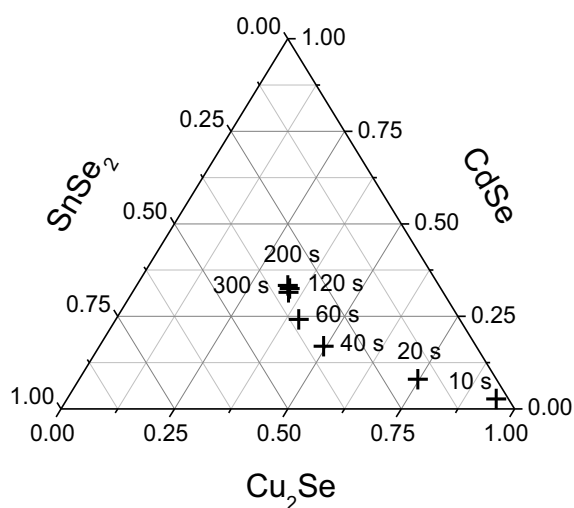


**Figure 2.** Ternary diagram showing the evolution of the  $\text{Cu}_2\text{CdSnSe}_4$  nanocrystals composition with the reaction time.

During the next few minutes of reaction, the tetrahedral quaternary nanocrystals grew into highly monodisperse penta-tetrahedral nanoparticles (Figure 1C-F). A more detailed illustration of the obtained penta-tetrahedron and their multiple orientations is shown in figure 3. In the same figure, HRTEM images and atomic 3D models obtained by using the Rhodius software package are displayed.<sup>15</sup> The four facets of the tetrahedrons correspond to the  $\{112\}$  family planes in the CCTSe tetragonal (S.G.: I-42m) structure.<sup>21</sup> HRTEM characterization showed the five



tetrahedrons composing the penta-tetrahedron to have crystallographic continuity. The size of the crystal domains estimated from the fitting of the XRD patterns confirmed this result.

We believe the epitaxial growth of four additional tetrahedrons on the facets of a fifth one to be the most probable mechanism of formation of such penta-tetrahedral nanocrystals. Owing to the dilated time of nanocrystal growth, we believe the penta-tetrahedron growth was most probably accompanied by the dissolution of the smallest tetrahedral crystals, in a classical Ostwald ripening scenario. However, the possibility of an oriented attachment mechanism having a role on the penta-tetrahedron formation cannot be ruled out from our experimental results. In this regard, occasionally obtained polydispersed samples showed the coexistence of both, tetrahedral and penta-tetrahedral nanoparticles, which could be understood as an intermediate state of the nanoparticle self-assembling process. An animated movie showing the 3D atomic modelling of the formation of these penta-tetrahedral nanostructures can be found elsewhere.<sup>24</sup> Proof of the quality of the final products yielded by this approach came from observations of spontaneous self-assembly of the nanocrystals produced (Figures 1F). Best assemblies were obtained with penta-tetrahedral particles, although the tetrahedral geometry has potentially higher packing densities.

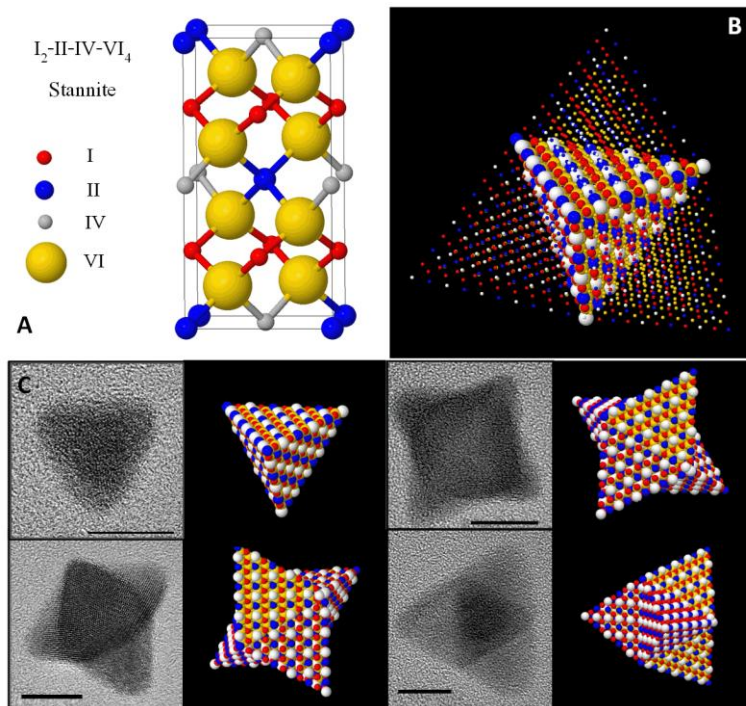


**Figure 3.** A) Crystal structure of the stannite  $\text{Cu}_2\text{CdSnSe}_4$  compound. B) Stannite penta-tetrahedron model showing the organization and orientation of the 5-composing tetrahedron with crystallographic continuity. An animated movie showing the 3D atomic modeling of the formation of these penta-tetrahedral nanostructures can be found elsewhere.<sup>24</sup> C) HRTEM images and models of the  $\text{Cu}_2\text{CdSnSe}_4$  stannite tetrahedron and penta-tetrahedron with different orientations. Scale bars = 10 nm.

Alkylamines were proven as the shape-directing ligands. The tetrahedral shape of the nanoparticles obtained, with  $\{112\}$  terminated facets suggested a preferential binding of the amine groups to these facets. Alkylamines were used to dissolve the metal salt or oxide, yielding metal-amine complexes. For the materials produced in this work, the best results were obtained using hexadecylamine (HDA) as the complexation agent. The concentration of alkylamines played a key role in the thermodynamic control of the nanoparticle growth. In figure 4, TEM images are shown of the CCTSe nanocrystals obtained with different amine concentrations in solution. The products obtained after two different reaction times were analyzed to illustrate the amine influence on the size distribution of both, the initially formed tetrahedrons (figure 4A) and the final penta-tetrahedral (figure 4B) nanoparticles. In figures 4C and 4D, the size distribution

histograms obtained from the measurement of several hundreds of tetrahedral and pentatetrahedral particles are displayed. Particle size distributions with no more than 5% dispersions were systematically obtained. The square of the average particle size obtained from the statistical analysis of these results was plotted as a function of the inverse of the amine concentration in figure 4E. A lineal dependence of the average tetrahedral nanoparticle surface area with the inverse of the HDA concentration was experimentally obtained. This lineal dependence was preserved for the pentatetrahedral particles. These experimental observations illustrate the important role of HDA in dynamically controlling the thermodynamic equilibrium existing between the ions at the particle surface and those in solution. An increase of the alkylamine concentration in solution allows a more efficient surface coverage of smaller nanoparticles, thus reducing their total surface energy. Then, higher alkylamine concentrations shift the equilibrium of chemical potentials towards the stabilization of nanoparticle ensembles with reduced average sizes. In this way, the amount of HDA added to the solution allowed an effective control of the nanoparticle size in the range from 5 to 20 nm for the tetrahedral particles, and from 10 to 30 nm for the pentatetrahedral ones.

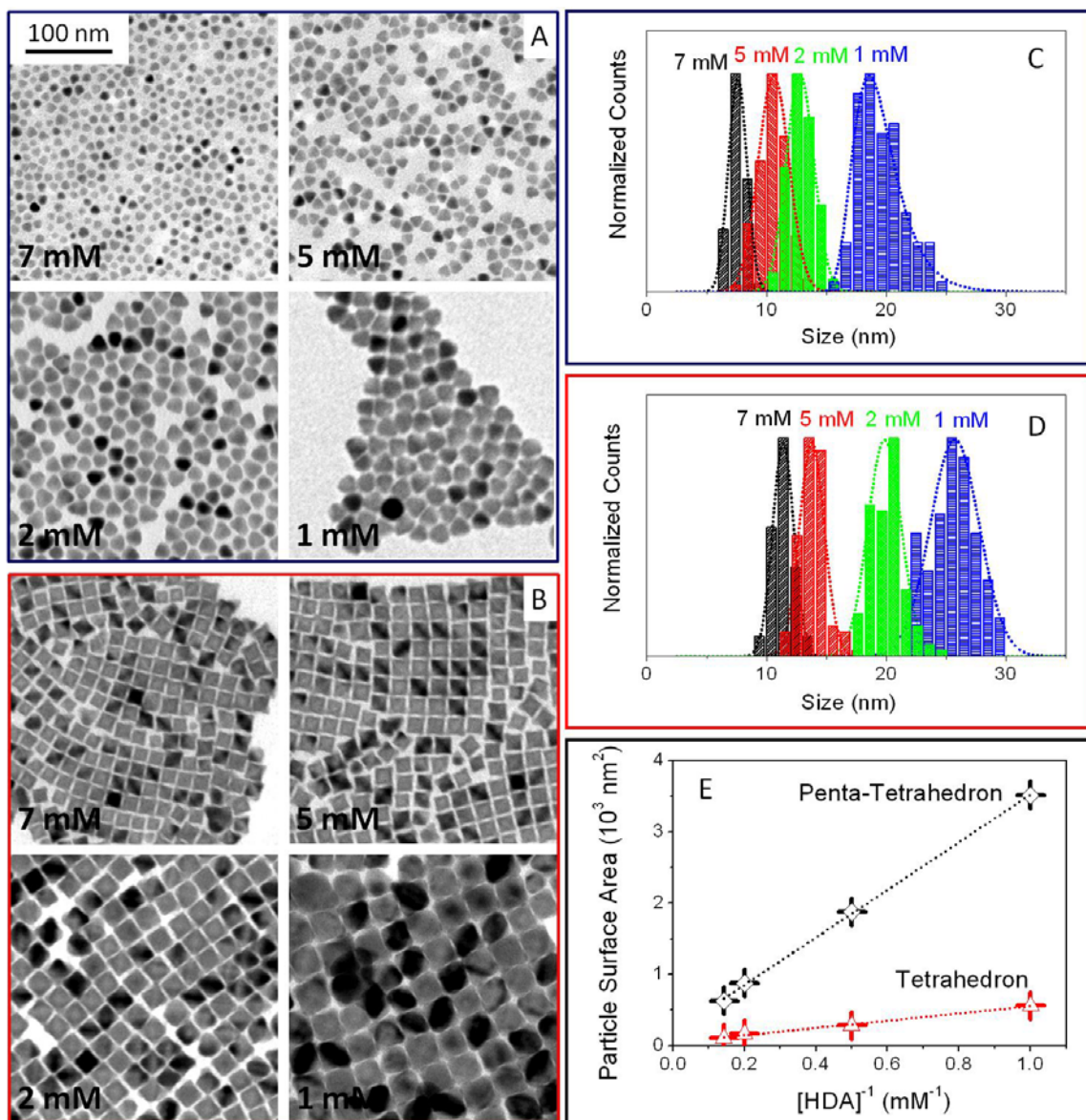


**Figure 4.** A) - B) TEM images of the tetrahedral (A) and penta- tetrahedral (B)  $\text{Cu}_2\text{CdSnSe}_4$  nanocrystals obtained at 285 °C using different concentrations of hexadecylamine: from 1 mM to 7 mM. C) – D) Size distribution of the tetrahedral (C) and penta- tetrahedral (D) nanocrystals displayed in (A) and (B). E) Estimated average surface area per particle as a function of the hexadecylamine concentration.

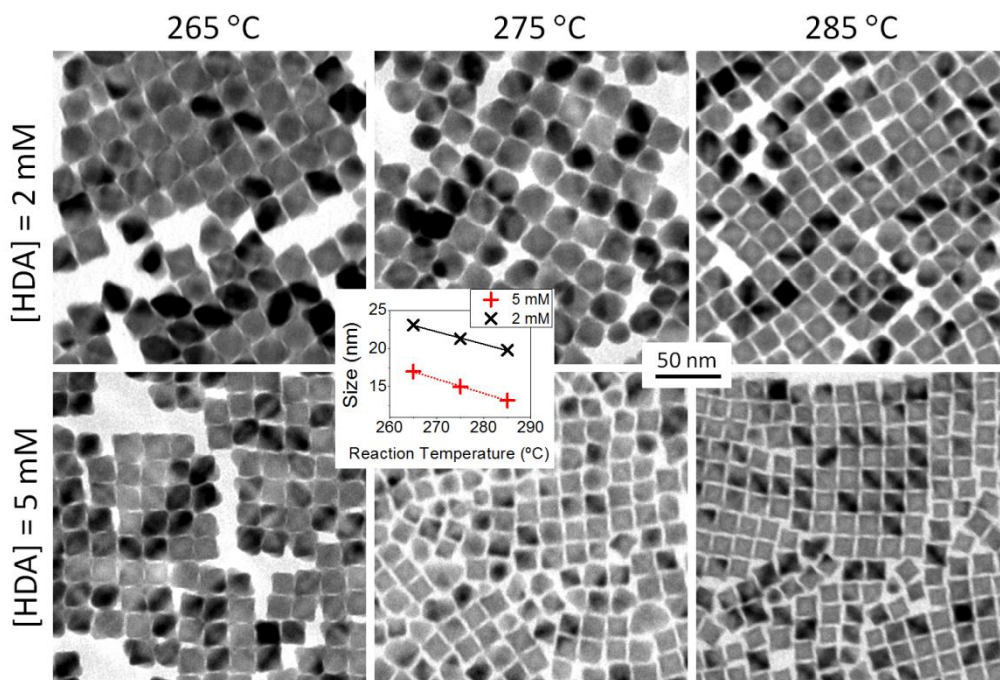


**Figure 5.** TEM images of the  $\text{Cu}_2\text{CdSnSe}_4$  nanocrystals obtained at different reaction temperatures, 265, 275 and 285 °C, from left to right. Top (bottom) images correspond to the nanocrystals obtained using 2 mM (5 mM) of hexadecylamine in solution.

While the nanoparticle shape and size was in part thermodynamically controlled by the presence of alkylamines, the nucleation kinetics also played an important role in determining the size of the final nanoparticles produced. Figure 5 displays TEM images of the nanocrystals obtained at different reaction temperatures and at two different amine concentrations in solution. These experimental results demonstrate that a reduction of the precursor injection temperature resulted in an increase of the particle size. This expected observation can be explained by the reduction of the number of nucleation events taking place at lower temperatures. The reduction of the nucleus concentration directly translates into higher amounts of monomer per particle, which results in an extension of the crystal growth regime.

To demonstrate the versatility of the presented procedure to obtain different  $\text{I}_2\text{-II-IV-VI}_4$  nanocrystals with narrow size and shape distributions, nanoparticles with the quaternary



compositions  $\text{Cu}_2\text{ZnSnSe}_4$ ,  $\text{Cu}_2\text{ZnGeSe}_4$  and  $\text{Cu}_2\text{CdGeSe}_4$  were produced. Figure 6 shows TEM micrograph and XRD patterns of the nanoparticles obtained by the presented synthetic procedure. To probe the potential of the presented procedure for the large-scale production of highly monodisperse nanocrystals, figure 6D displays a TEM image of the CCTSe nanoparticles obtained in a gram-per-batch scale. The inset shows the nanopowder obtained after drying the CCTSe nanocrystals produced in a scaled-up batch.

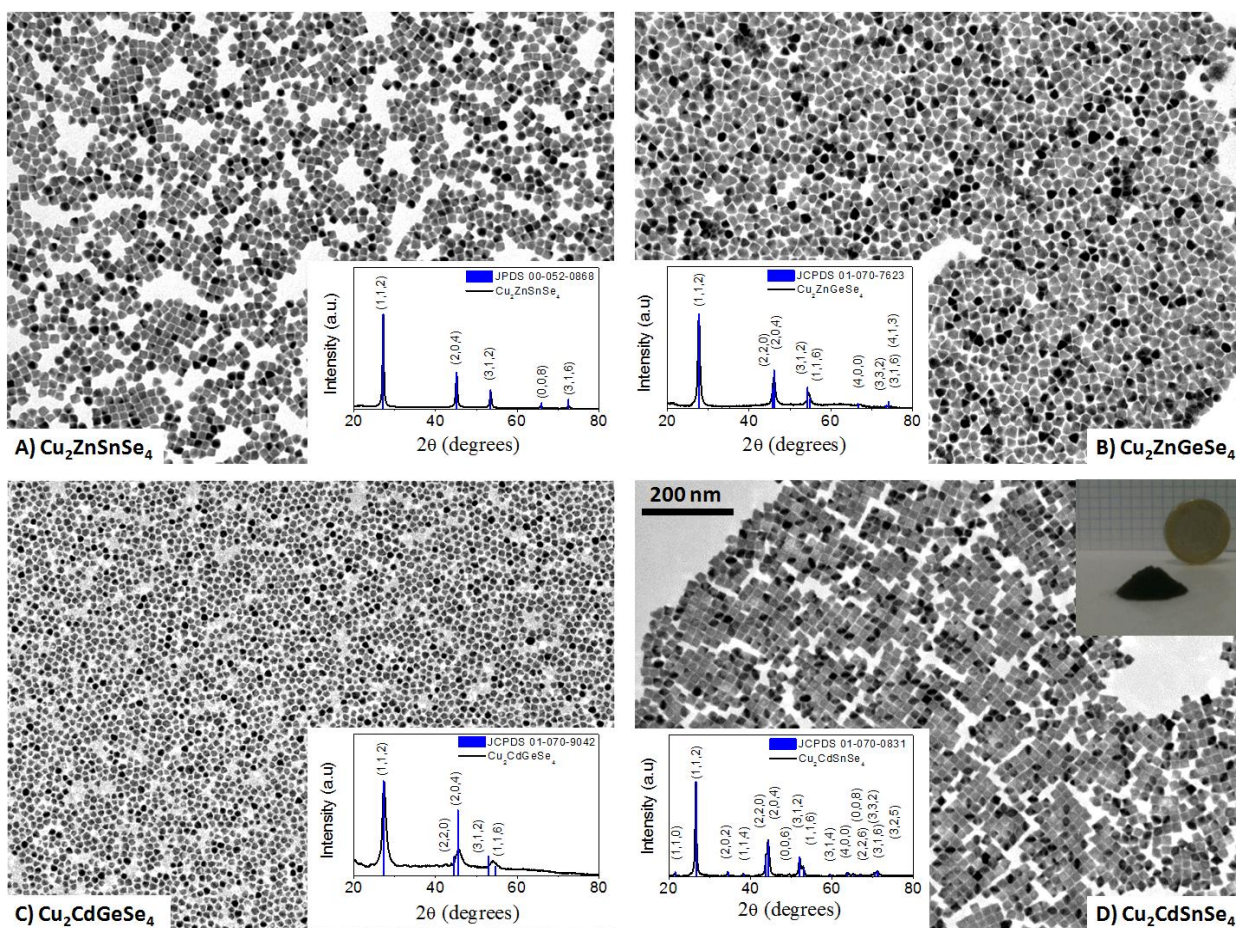


**Figure 6.** TEM images and XRD patterns of  $\text{Cu}_2\text{ZnSnSe}_4$ ,  $\text{Cu}_2\text{ZnGeSe}_4$ ,  $\text{Cu}_2\text{CdGeSe}_4$ , and  $\text{Cu}_2\text{CdSnSe}_4$  nanocrystals obtained by the synthesis procedure detailed in the present work. The TEM image of  $\text{Cu}_2\text{CdSnSe}_4$  nanocrystals corresponds to the nanoparticles obtained from a gram-scale synthesis. An inset shows the  $\text{Cu}_2\text{CdSnSe}_4$  nanopowder obtained from the scaled-up synthesis procedure.

### 3.5 Conclusions

---

In summary, the preparation of quaternary nanocrystals with an unprecedented control over their size, shape and composition was demonstrated. The detailed procedure allowed obtaining tetrahedral and penta-tetrahedral I<sub>2</sub>-II-IV-VI<sub>4</sub> nanocrystals with narrow size distributions. The average particle size could be tuned in the range from 5 to 30 nm by two independent parameters: i) the concentration of amine in solution; and ii) the nucleation temperature. The different reaction kinetics of the various elements composing the nanocrystal allowed adjusting the nanocrystals composition by controlling the reaction time and the precursors' concentrations. In this regard, the formation of metal-alkylphosphonic acids was considered key to reach the stoichiometric compositions. At the same time, alkylamines were shown to be valid capping agents to thermodynamically control the morphology and size of such complex quaternary structures. The potential of the detailed procedure was illustrated using Cu<sub>2</sub>CdSnSe<sub>4</sub> as the prototypical system. However, similar reaction conditions and synthetic parameters allowed producing other I<sub>2</sub>-II-IV-VI<sub>4</sub> nanocrystals with tight size and shape distributions. The unprecedented degree of control over the size and shape of the obtained quaternary nanocrystals will facilitate systematic investigations of the relationship between their performance and the underlying nanometric processes. It will also open a broad avenue for new applications of quaternary materials with precisely tuned functional properties.

### 3.6 References

---

- (1) Sevik, C.; Çağın, T., *Phys. Rev. B* **2010**, 82, 045202.
- (2) Matsushita, H.; Maeda, T.; Katsui, A.; Takizawa, T., *J. Cryst. Growth* **2000**, 208, 416-422.
- (3) Chen, S.; Gong, X. G.; Walsh, A.; Wei, S.-H., *Phys. Rev. B* **2009**, 79, 165211.
- (4) Matsushita, H.; Ichikawa, T.; Katsui, A., *J. Mater. Sci.* **2005**, 40, 2003-2005.

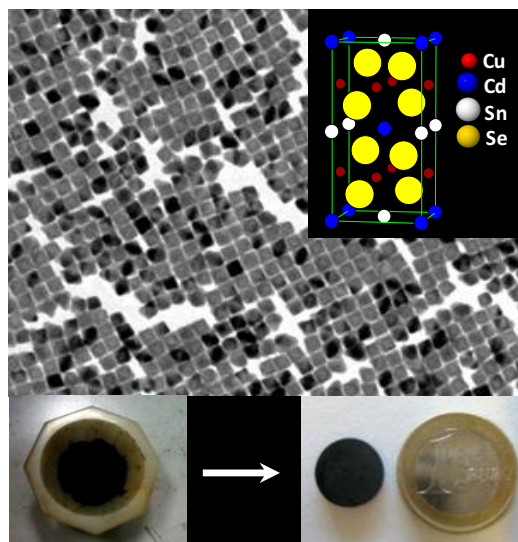
- (5) Guo, Q.; Ford, G. M.; Yang, W.-C.; Walker, B. C.; Stach, E. A.; Hillhouse, H. W.; Agrawal, R., *J. Am. Chem. Soc.* **2010**, 132, 17384-17386.
- (6) Shavel, A.; Arbiol, J.; Cabot, A., *J. Am. Chem. Soc.* **2010**, 132, 4514-4515.
- (7) Mitzi, D. B.; Gunawan, O.; Todorov, T. K.; Wang, K.; Guha, S., *Sol. Energ. Mat. Sol. C.* **2011**, 95, 1421-1436.
- (8) Liu, M.-L.; Chen, I. W.; Huang, F.-Q.; Chen, L.-D., *Adv. Mater.* **2009**, 21, 3808-3812.
- (9) Ibáñez, M.; Cadavid, D.; Zamani, R.; García-Castelló, N.; Izquierdo-Roca, V.; Li, W.; Fairbrother, A.; Prades, J. D.; Shavel, A.; Arbiol, J.; Pérez-Rodríguez, A.; Morante, J. R.; Cabot, A., *Chem. Mater.* **2012**, 24, 562-570.
- (10) Samanta, L. K.; Bhar, G. C., *Phys. Status Solidi A* **1977**, 41, 331-337.
- (11) Wang, Y. J.; Lin, H.; Tanmoy, D.; Hasan, M. Z.; Bansil, A., *New J. Phys.* **2011**, 13, 085017.
- (12) Chen, S.; Gong, X. G.; Duan, C.-G.; Zhu, Z.-Q.; Chu, J.-H.; Walsh, A.; Yao, Y.-G.; Ma, J.; Wei, S.-H., *Phys. Rev. B* **2011**, 83, 245202.
- (13) Guo, Q.; Hillhouse, H. W.; Agrawal, R., *J. Am. Chem. Soc.* **2009**, 131, 11672-11673.
- (14) Chane-Ching, J. Y.; Gillorin, A.; Zaberca, O.; Balocchi, A.; Marie, X., *Chem. Comm.* **2011**, 47, 5229-5231.
- (15) Bernal, S.; Botana, F. J.; Calvino, J. J.; López-Cartes, C.; Pérez-Omil, J. A.; Rodríguez-Izquierdo, J. M., *Ultramicroscopy* **1998**, 72, 135-164.
- (16) Pérez-Omil, J. A. University of Cádiz, Cádiz, 1994.
- (17) Arbiol, J.; Cirera, A.; Peiro, F.; Cornet, A.; Morante, J. R.; Delgado, J. J.; Calvino, J. J., *Appl. Phys. Lett.* **2002**, 80, 329-331.
- (18) Arbiol, J.; Fontcuberta i Morral, A.; Estradé, S.; Peirò, F.; Kalache, B.; Roca i Cabarrocas, P.; Morante, J. R., *J. Appl. Phys.* **2008**, 104, 064312-7.
- (19) Uccelli, E.; Arbiol, J.; Morante, J. R.; Fontcuberta i Morral, A., *ACS Nano* **2010**, 4, 5985-5993.
- (20) Davey, W. P., *Phys. Rev.* **1923**, 21, 143-161.
- (21) Olekseyuk, I. D.; Gulay, L. D.; Dydchak, I. V.; Piskach, L. V.; Parasyuk, O. V.; Marchuk, O. V., *J. Alloys Compd.* **2002**, 340, 141-145.
- (22) Liu, H.; Owen, J. S.; Alivisatos, A. P., *J Am Chem Soc* **2007**, 129, 305-312.
- (23) Owen, J. S.; Park, J.; Trudeau, P.-E.; Alivisatos, A. P., *J Am Chem Soc* **2008**, 130, 12279-12281.



(24) <http://www.icmab.es/gaen/research/157.html>.

# Chapter 4

## Composition control and Thermoelectric Properties of Quaternary Chalcogenide Nanocrystals: The Case of Stannite $\text{Cu}_2\text{CdSnSe}_4$



### 4.1 Abstract

---

A high-yield and upscalable colloidal synthesis route for the production of quaternary I<sub>2</sub>-II-IV-VI<sub>4</sub> nanocrystals, and particularly stannite  $\text{Cu}_{2+x}\text{Cd}_{1-x}\text{SnSe}_4$ , with narrow size distribution and precisely controlled composition is presented. It is also shown here how the diversity of valences in the constituent elements allows an effective control of their electrical conductivity through the adjustment of the cation ratios. At the same time, while the crystallographic complexity of quaternary chalcogenides is associated with intrinsically low thermal conductivities, the reduction of the lattice dimensions to the nanoscale further reduces the materials thermal conductivity. In

the specific case of the stannite crystal structure, a convenient slab distribution of the valence band maximum states permits a partial decoupling of the p-type electrical conductivity from both the Seebeck coefficient and the thermal conductivity. Combining these features, we demonstrate how an initial optimization of the nanocrystals Cd:Cu ratio allowed us to obtain low-temperature solution-processed materials with ZT values up to 0.71 at 685 K.

## 4.2 Introduction

---

Thermoelectrics, allowing the solid-state conversion between thermal and electrical energy, have long been considered a very attractive technology for cooling and waste heat recovery. However, the low conversion efficiencies of actual thermoelectric devices have prevented them from entering in most of their potential application markets. Over the last 15 years, advances in the fields of materials science and nanotechnology have restored an intense interest for such an energy conversion technology. Today's main strategy to produce materials with high thermoelectric figures of merit is to trigger phonon scattering at multiple length scales without disturbing the charge carrier transport.<sup>1-9</sup> The goal is to minimize the lattice thermal conductivity in highly electrically conductive materials; the so-called electron-crystal phonon-glass paradigm. This strategy is implemented by two main approaches: i) the scattering of phonons at the atomic length scale by the synthesis of complex crystal phases that include 1D phonon scattering centers, such as vacancies or rattling atoms,<sup>4</sup> and/or 2D layered crystallographic structures;<sup>5</sup> ii) the scattering of phonons at the 1-100 nm scale by reducing the crystal domain dimensions to the nanoscale.<sup>6-9</sup> An additional advantage of the confinement of the lattice dimensions to the nanometer scale is the potential decoupling of the Seebeck coefficient from electrical conductivity.<sup>10, 11</sup> In this regard, the increase of the electronic density of states near the Fermi level in quantum confined nanostructures have been predicted to enhance the Seebeck

coefficient.<sup>9, 12, 13</sup> At the same time, energy filtering at nanocrystal interfaces may further enhance the thermopower of nanostructured material by selectively scattering low energy charge carriers.<sup>14-17</sup>

In this scenario, colloidal synthesis routes are particularly well suited for the production of thermoelectric materials. Solution-processing methods have a high potential for the production of low-cost, high-yield, large-scale, high-output and shape-adaptable devices. Moreover, bottom-up approaches allow to directly obtain materials with reduced crystal domain size and controlled geometry.<sup>18-20</sup> In this regard, while the fabrication of solar cells from solution-processed semiconductors generally has the downside of requiring a thermal treatment to crystallize the absorbent layers, the huge interface densities of the solution-processed nanocrystalline materials represent an advantage in the thermoelectrics field.<sup>21-23</sup>

Some quaternary chalcogenides and in particular  $I_2-II-IV-VI_4$  adamantines have the required attributes to be potentially excellent thermoelectric materials. Not only the complex structures of these quaternary compounds are associated with intrinsically low thermal conductivities, but also their different cationic valences provide a means of controlling their Fermi level by adjusting their cation ratios.<sup>24-28</sup> Besides, some  $I_2-II-IV-VI_4$  adamantines crystallizing in the stannite phase are characterized by a convenient structure layering, which allows decoupling the electrical conductivity from both the thermal conductivity and the Seebeck coefficient.<sup>24-29</sup> This is the same motivation behind the use of Zintl compounds as thermoelectric materials.<sup>30</sup>

We present here a novel colloidal synthetic route to prepare quaternary  $I_2-II-IV-VI_4$  adamantine nanocrystals, with unprecedented narrow size distributions and exceptional control over their composition. We took particular care in designing a scalable process to assure its relevance in a future industrial implementation. The synthetic route presented here was used for the preparation

of several grams of nanocrystals of the quaternary chalcogenide  $\text{Cu}_{2+x}\text{Cd}_{1-x}\text{SnSe}_4$  (CCTSe), which is a p-type semiconductor with a 0.98 eV band gap and crystallizes in the stannite phase.<sup>24, 3124,31</sup> The results from the characterization of the electrical and thermoelectric properties of these materials are also presented here.

### 4.3 Experimental Section

---

*Chemicals.* Copper (I) chloride (reagent grade, 97%), Cadmium Oxide (99.999%), 1-octadecene (ODE, 90%), oleic acid (OA, tech. 90%), hexadecylamine (HDA, tech. 90%) and tetrachloroethylene (TCE, spectrophotometric grade, 99%) were purchased from Aldrich. Tin (IV) chloride pentahydrate (98%) was purchased from Across. Selenium (IV) oxide (99.8%) was purchased from Strem. n-Octadecylphosphonic acid was purchased from PCI Synthesis. Chloroform, isopropanol and ethanol were of analytical grade and obtained from various sources. All chemicals were used as received without further purification.

All syntheses were carried out using standard airless techniques: a vacuum/dry argon gas Schlenk line was used for the synthesis and an argon glove-box for storing and handling air and moisture-sensitive chemicals.

*Synthesis of  $\text{Cu}_2\text{CdSnSe}_4$  NCs.* Copper (I) chloride (50 mg, 0.5 mmol), Cadmium oxide (33 mg, 0.25mmol), Tin (IV) chloride pentahydrate (88mg, 0.25 mmol), hexadecylamine (1230 mg, 5mM), n-Octadecylphosphonic acid (33mg, 0.1mmol) were dissolved in 10 ml ODE. The solution was heated under argon flow to 200 °C and maintained at this temperature during 1h to remove water and other low-boiling point impurities. Afterwards, the mixture was heated to the reaction temperature (285 °C). The selenium solution was obtained by dissolving selenium (IV) oxide in 1-octadecene under argon atmosphere at 180 °C. The selenium solution (4 mL, 3 mM)

was rapidly injected through a septum into the reaction flask. Following the injection, the temperature dropped to around 260 °C and then slowly recovered to 285 °C. The solution was kept at a temperature between 260 and 285 °C for 5 min and then quickly cooled down. The formation of CCTSe could be qualitatively followed by the color change of the mixture from an initial light yellow to green and eventually black color of the solution containing the CCTSe nanocrystals. 3 mL of oleic acid were added to the mixture during the cooling at ~70 °C to replace the weakly bonded HDA. The crude solution was mixed with 10 ml of chloroform and sonicated at 50 °C for 5 minutes. The CCTSe nanoparticles were isolated by centrifugation at 4000 rpm during 5 minutes. The black precipitate was redispersed in chloroform (~20 ml) and sonicated again at 50 °C for 5 minutes. . Then the product was additionally precipitated by adding isopropanol (~10 ml) and centrifuging. The nanocrystals were redispersed in chloroform (~5 ml) and stored in an Ar filled glove-box.

The same synthesis procedure was scaled up for the production of a few grams of nanoparticles. In the scaled-up synthesis, 6 times larger amounts of all precursor, surfactant and solvent were used. Washed nanocrystals were dried out from solution under argon atmosphere. Afterward, the nanocrystals were heated to 500 °C for 2 hours under an Ar flow inside a tube furnace. The material resulting from few scaled-up syntheses was pressed into pellets under a load of 5 tons at room temperature (13 mm diameter; 2 mm thickness). The density obtained by this methods was close to 85%.

*Thermoelectric Characterization.* The samples used to measure the electrical conductivity and the Seebeck coefficient were rectangular parallelepipeds of about 10x12x1 mm<sup>3</sup>. The Seebeck coefficient was measured by using a static DC method. Electrical resistivity data were obtained by a standard four-probe method. Both Seebeck coefficient and electrical resistivity were

measured simultaneously in a LSR-3 LINSEIS system in the range between room temperature up to 700 K, under helium atmosphere.

For thermal conductivity measurements, two pellets (13 mm in diameter and 2 mm thick) were used. Thermal conductivity was measured by means of the transient plane source method (TPS), using a Hot Disk Thermal Constants Analyzer system, in the range between room temperature up to 700 K, under N<sub>2</sub> atmosphere.

*Computational details.* For the ab initio calculations, we used the SIESTA<sup>32</sup> code which combines density functional theory (DFT), normconserving pseudopotentials, and local basis set functions. We used the generalized gradient approximations (GGA) with the Perdew, Burke, and Ernzerhof (PBE) parameterization.<sup>33</sup> For all the atoms, double  $\zeta$  local basis set with polarization was used. Well converged densities of states and orbital distributions were obtained with a real space mesh cut-off of 250 Ryd and Monkhorst–Pack sets larger than  $5 \times 5 \times 3$ . Experimental HRTEM lattice parameters were used to build all crystal models. Atomic positions were determined by performing structural relaxations using conjugate gradient minimization of the energy, until the forces on all the atoms were smaller than  $0.04 \text{ eV \AA}^{-2}$ . In the relaxation of the models, lattice dimensions were kept constant (in accordance with the experimental values) and no constraints were imposed on the atomic positions within the supercell.

To model the Cu substitution in the Cd sites of  $\text{Cu}_{2+x}\text{Cd}_{1-x}\text{SnSe}_4$ , a  $2 \times 1 \times 2$  supercell based on the unit cell of the stannite structure was constructed. Such a supercell contained 8 Cd atoms, which allowed us to study different substitution degrees, ranging from  $x = 0$  to  $x = 1$  in steps of  $\Delta x = 0.125$ . In order to rule out any influence of the different substitution localization, up to four different configurations were considered at each  $x$  value, when possible. Additionally, to discard any artifact related to the limitations of DFT concerning the energy band gap, the displacement of

the Fermi level was measured with respect two different features of the band structure: the valence band maximum (VBM) and the conduction band minimum (CBM).

#### **4.4 Results and Discussion**

---

Figure 1 shows representative TEM and SEM images of the obtained nanocrystals. The synthesis procedure here detailed yielded CCTSe nanocrystals with very narrow size distributions, which easily self-assembled in 2D superlattices when supported on carbon grids or silicon substrates for TEM or SEM characterization. The average size of the nanoparticles shown in figure 1 was  $15 \pm 2$  nm (inset Fig. 1). The good control on the particle size achieved by this synthetic route allowed us to obtain nanocrystals with similar sizes for all the compositions tested in the present work. In this way, we can presume that the influence of the crystal domain size on the thermoelectric characteristics will be similar for all the materials here analyzed.



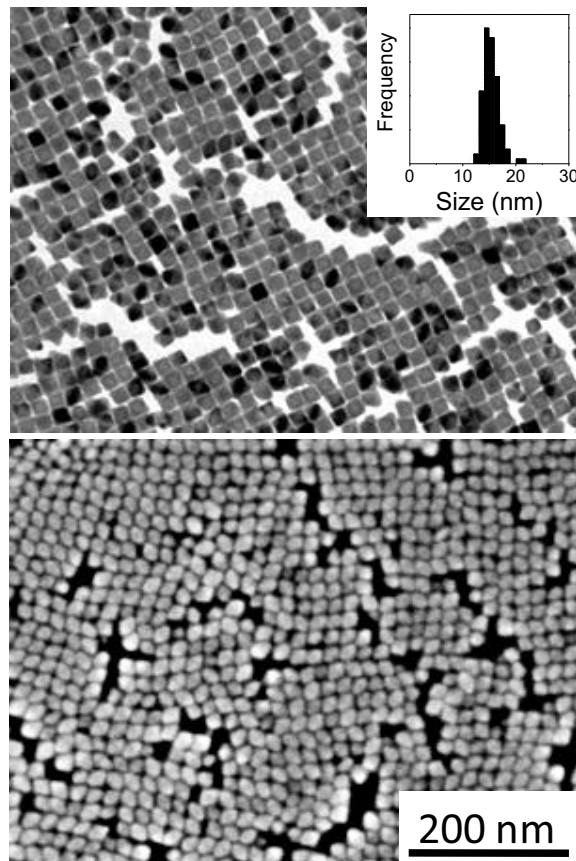


**Figure 1.** Representative TEM and SEM images of the CCTSe nanocrystals obtained after 5 minutes of reaction at 285 °C. Inset shows a histogram of the nanoparticles size distribution.

Figure 2 resumes the results obtained from the HRTEM, EDX, XRD and UV-vis characterization of the nanocrystals obtained at different growth times. These set of characterization techniques revealed the compositional evolution of the nanoparticles with the reaction time: upon injection,  $\text{Cu}_{2-x}\text{Se}$  spherical nanocrystals with the Berzelianite cubic structure (JCPDS 01-088-2043; S.G.:  $\text{Fm}\bar{3}\text{-m}$ )<sup>34</sup> rapidly nucleated as shown by XRD, HRTEM and the characteristic plasmon observed in the UV-vis spectra (Figure 2A-D and 2I). The high amounts of selenium detected by the EDX analysis were attributed to the presence of complexes of this element on the surface of the nanocrystals (Figure 2D). It should be pointed out here, that the

purification of these first-formed  $\text{Cu}_{2-x}\text{Se}$  nanocrystals was not an easy task due to the large amount of unreacted complexes covering the nanoparticles.

During the first few minutes of reaction, Sn and Cd ions gradually entered into the nanocrystal structure, extending the unit cell along the c-axis into the double supercell characteristic of the stannite structure (JCPDS 01-070-0831, S.G.: I-42m, Figure 2G).<sup>35</sup> After 5 minutes of reaction at 285 °C, the obtained nanoparticles already had the stoichiometric chemical composition:  $\text{Cu}_2\text{CdSnSe}_4$  (Figure 2E-H). Inductively Coupled Plasma-Atomic Emission Spectroscopy analysis confirmed these results. Single particle EDX and EELS analysis confirmed all the elements to be homogeneously distributed within each particle and showed no compositional variation from particle to particle within each sample (Figure 2J).

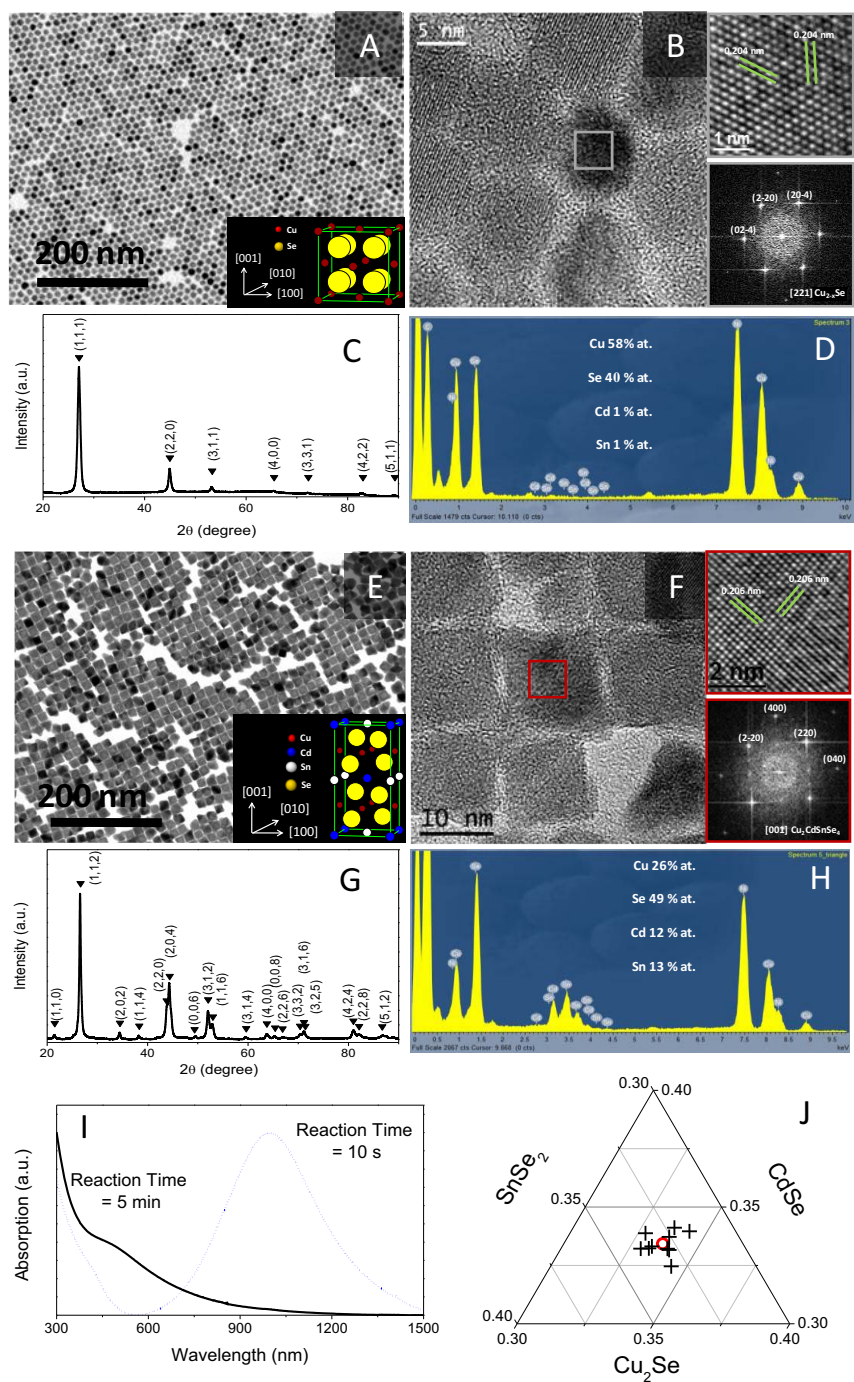


**Figure 2.** TEM and HRTEM images, XRD patterns and EDX spectra of the nanocrystals obtained after 10 s reaction time (A)-(D) and 5 minutes of reaction at 285 °C (E)-(H). I) UV-vis spectra of the nanocrystals obtained after 10 s and after 5 minutes reaction time at 285 °C. Notice the plasmon peak in the UV-vis spectra of the nanoparticles obtained after 10 s reaction time, which can be identified with that of  $\text{Cu}_{2-x}\text{Se}$ .<sup>36</sup> J) Ternary diagram showing the typical distribution of single particle compositions obtained after 5 minute reaction time at 285 °C.

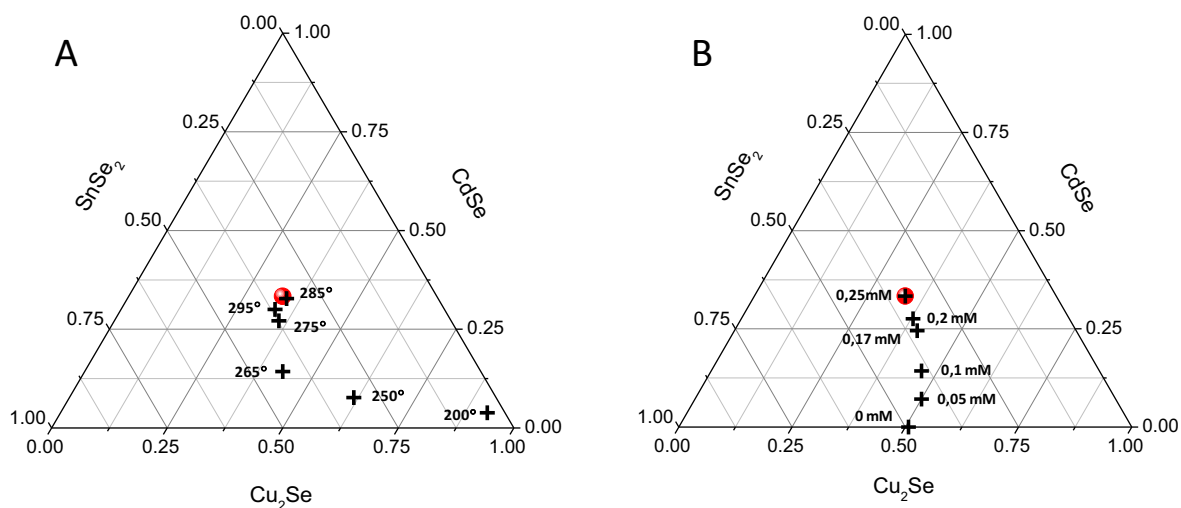


**Figure 3.** Ternary diagrams of the composition of the nanocrystals obtained after 5 min reaction times at different reaction temperatures (A) and at 285 °C using different Cd precursor concentration (B)

Lower reaction temperatures extended the time spread needed for the complete incorporation of Cd and Sn ions inside the CCTSe crystal structure. Thus, at a fixed reaction time, the evolution of the nanoparticles composition with the reaction temperature followed a trend parallel to that observed when varying the reaction time at a fixed temperature. Figure 3 shows a ternary diagram with the nanocrystals composition obtained after 5 minutes of reaction at different temperatures. Sn ions clearly incorporated to the CCTSe structure at earlier reaction times and lower temperatures than Cd. After 5 minutes of reaction time, the Sn incorporation was completed at 265 °C and above. Temperatures below 250 °C were not sufficient to promote either the Sn or Cd inclusion into the lattice, thus  $\text{Cu}_2\text{Se}$  nanoparticles were consistently obtained at all reaction times. The complete incorporation of the appropriate amount of Cd required temperatures above 280 °C. It should be pointed out that in the presence of HDA as the unique surfactant, it was not possible to reach the  $\text{Cu}_2\text{CdSnSe}_4$  composition, with the maximum concentration of Cd introduced 20 % below the stoichiometric values were obtained:

$\text{Cu}_{2.2}\text{Cd}_{0.8}\text{SnSe}_4$ . Conveniently, we found out that the presence of alkylphosphonic acids significantly promoted the Cd incorporation into the lattice. The best results were obtained when introducing 0.1 mmol of ODPA into the initial reaction solution.

The different reaction kinetics of Cu, Sn and Cd with Se allowed us to adjust the nanoparticle composition inside a relatively wide range by tuning the precursors concentration, the amount of ODPA and the reaction time and temperature. The synthetic procedure reported here was easily up-scalable, while conserving the compositional control and excellent size and shape distributions. At the same time, the high yield of the procedure allowed an efficient production of the relatively large amounts of nanoparticles required for their proper characterization.

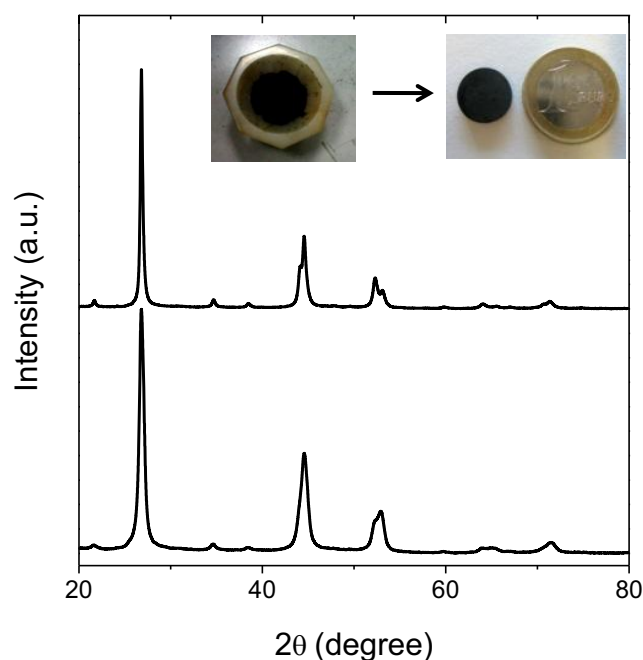


**Figure 4.** XRD patterns of a  $\text{Cu}_2\text{CdSnSe}_4$  sample before (bottom pattern) and after (top pattern) the thermal treatment at 500 °C during 2 h in an Ar flow. The fitting of the pattern allowed calculating an increase of the crystal domain size by a factor 1.8, from 16 nm to 29 nm. Inset shows the black powder obtained after cleaning and drying the nanocrystals and one of the pellets measured.

For thermoelectric characterization, roughly 5 grams of nanoparticles of each composition tested were prepared. The nanocrystals were thoroughly washed by multiple precipitation and re-dispersion steps, until they were not soluble anymore. The cleaned and dried nanoparticles were pressed into 13 mm pellets by applying 5 tons of force with a hydraulic press (Inset Figure 4). Then the materials were heated to 500 °C in an N<sub>2</sub> flow atmosphere and maintained at this temperature for 2 hours to remove all the remaining organics. The concentration of residual carbon in the final materials was less than 1 %, as determined by elemental analysis. During this thermal treatment, the crystal domain size typically increased a factor 1.8, from 16 to 29 nm, but no change of crystallographic structure or composition was caused as observed by XRD and EDX (Figure 4). Figure 5A and 5B shows the XRD and Raman spectra of the pellets obtained from pressing and sintering at 500 °C materials with different composition. No new crystal phase was noticed after sintering. When replacing Cd by Cu, the XRD peaks clearly shifted in accordance with the change of the lattice parameters (Figure 5C). This shift was maintained after the sintering treatment and no phase segregation was observed. Notice also how the multiple peaks at around 44 and 52 degrees, characteristic of the stannite structure, fused into the single peak of the spharelite Cu<sub>2</sub>SnSe<sub>3</sub> when reducing the Cd concentration within the nanoparticles. At the same time, the Raman spectrum characteristic of the CCTS structure gradually evolved into that of Cu<sub>2</sub>SnSe<sub>3</sub>. No secondary phases could be detected either by Raman spectroscopy. However, at temperatures above 550 °C, some of the materials with higher degrees of Cd by Cu substitution were not stable and segregated into CCTSe and Cu<sub>2</sub>Se phases. Therefore the thermoelectric characterization of the materials was limited to the temperature range extending from room temperature to 450 °C. The shape and size distribution of the nanocrystals having different compositions did not significantly change as appreciated in figure 5D.

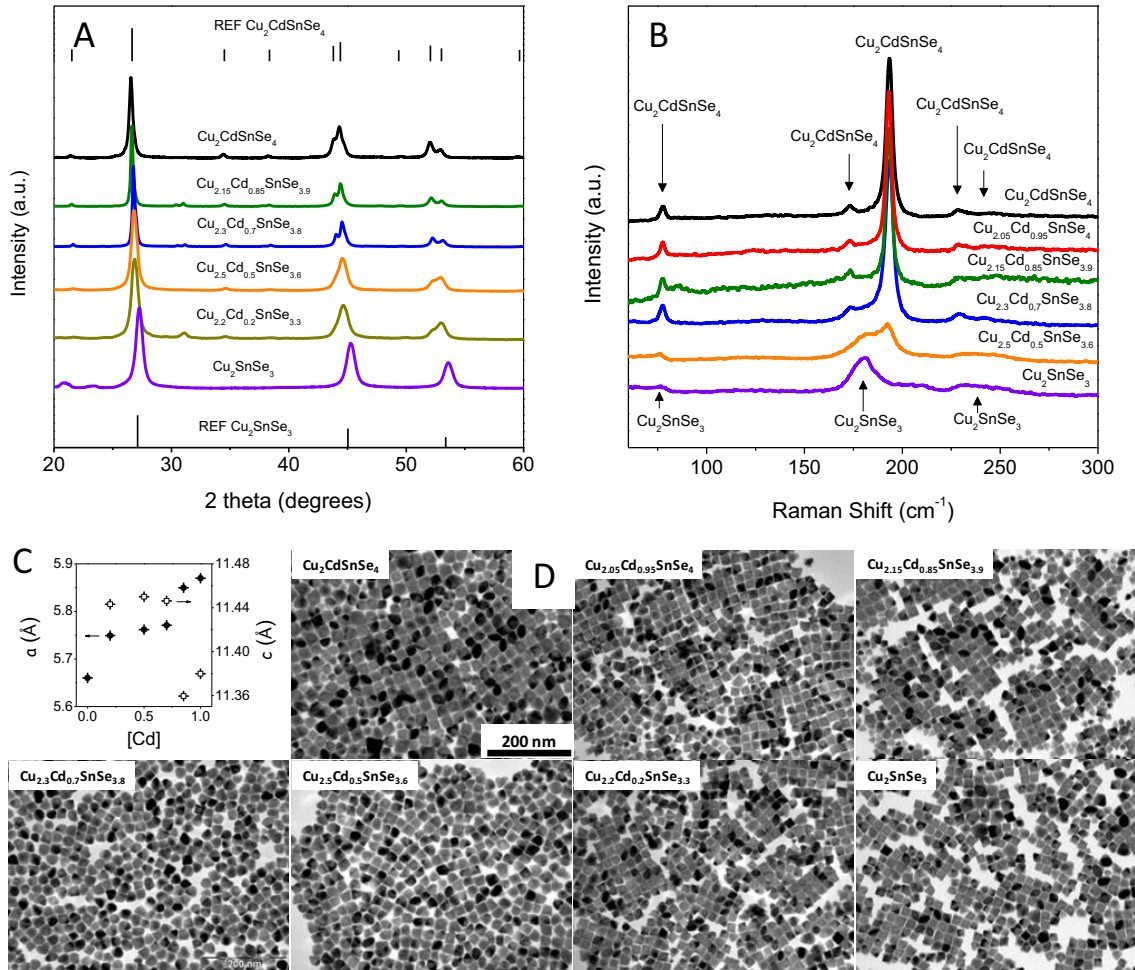
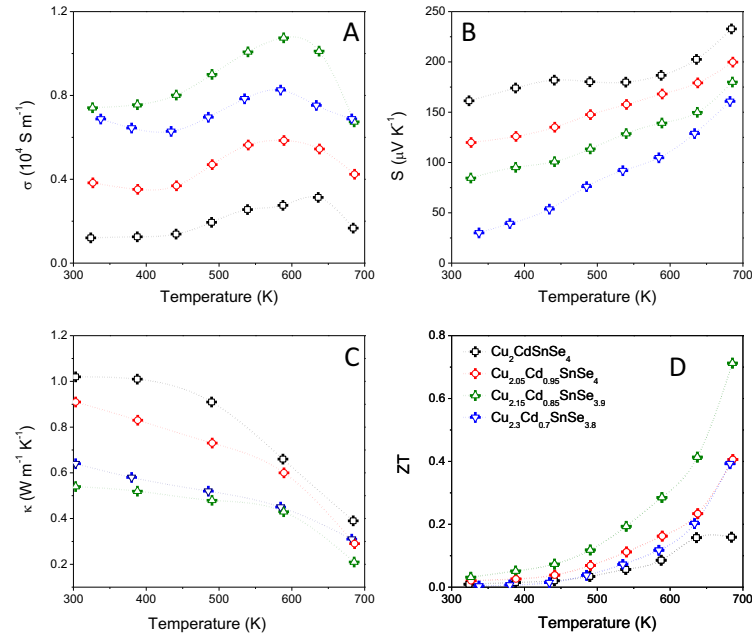


**Figure 5.** XRD patterns (A) and Raman spectra (B) of the annealed (500 °C, 2h, Ar flow) Cu<sub>2+x</sub>Cd<sub>1-x</sub>SnSe<sub>4</sub> nanocrystals with 0 ≤ x ≤ 1. C) Lattice parameters calculated from the fitting of the XRD patterns considering a tetragonal structure for all the compositions [Cd] > 0. D) Representative TEM images of the characterized materials.

Figure 6 shows the electrical conductivity, Seebeck coefficient, thermal conductivity, and thermoelectric figure of merit ( $ZT = S^2 \sigma T / \kappa$ ) of a series of 4 CCTSe samples having similar particle size but different compositions. The relatively high electrical conductivities obtained from the thermally treated samples pointed toward the complete removal of surfactants. The electrical conductivity increased with the Cu concentration from Cu<sub>2</sub>CdSnSe<sub>4</sub> to

$\text{Cu}_{2.15}\text{Cd}_{0.85}\text{SnSe}_{3.9}$  (Figure 6A). Our experimental evidence suggests that higher levels of Cd by Cu substitution did not further improve the electrical conductivity, as shown for the  $\text{Cu}_{2.3}\text{Cd}_{0.7}\text{SnSe}_{3.8}$  sample.

As expected, the Seebeck coefficient followed an opposite trend to that obtained for the electrical conductivity, as it decreased with the Cu content for the whole measured range (Figure 6B). In figure 6C, the thermal conductivity is plotted as a function of the temperature for the same series of 4 samples. Remarkably, the thermal conductivity of all the materials tested was exceptionally low. Both the intrinsic complexity of the crystallographic structure and the large density of crystallographic interfaces contributed to an efficient phonon scattering. The thermal conductivity further decreased with the levels of Cd by Cu substitution from  $\text{Cu}_2\text{CdSnSe}_4$  to  $\text{Cu}_{2.05}\text{Cd}_{0.95}\text{SnSe}_4$  and to  $\text{Cu}_{2.15}\text{Cd}_{0.85}\text{SnSe}_{3.9}$ , but it increased with higher substitution levels.



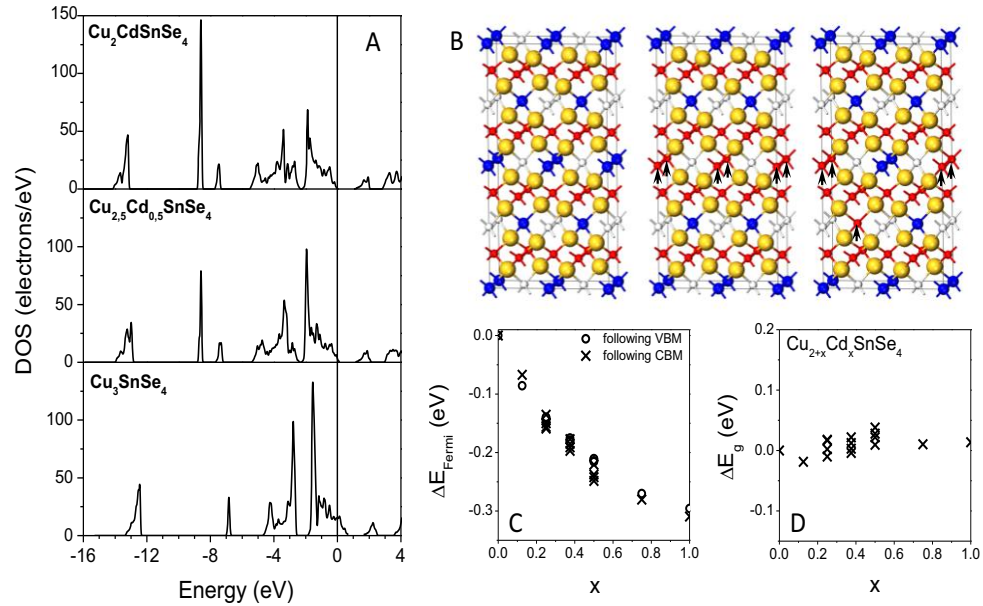
**Figure 6.** Electrical conductivity (A), Seebeck coefficient (B), thermal conductivity (C) and figure of merit (D) of nanocrystals with the following compositions:  $\text{Cu}_2\text{CdSnSe}_4$  (squares),  $\text{Cu}_{2.05}\text{Cd}_{0.95}\text{SnSe}_4$  (circles),  $\text{Cu}_{2.15}\text{Cd}_{0.85}\text{SnSe}_4$  (triangles),  $\text{Cu}_{2.3}\text{Cd}_{0.7}\text{SnSe}_{3.7}$  (inverted triangles).



Figure 6D shows the calculated dependence of the figure of merit with the temperature. In the range tested, ZT values were observed to continuously increase with the temperature. The maximum ZT value was obtained with  $\text{Cu}_{2.15}\text{Cd}_{0.85}\text{SnSe}_{3.9}$  nanoparticles. This material reached a ZT up to 0.71 at 685 K. In a previous characterization of this material in bulk form electrical conductivities a factor 2 higher were obtained.<sup>24</sup> At the same time, slightly higher Seebeck coefficients were measured for these materials. However the thermal conductivities obtained with the nanocrystalline materials here characterized are a factor 2.5 lower, what finally equilibrates the ZT values obtained for this material in bulk and nanocrystalline forms. Notice that a systematic optimization was not carried out here in attempt to maximize the ZT value. We strongly believe the nanocrystal parameters can be further optimized to obtain even larger figures of merit. It should be also pointed out here, that the pellets obtained had relatively low densities of the order or an 85 %. A further densification of the material by means of hot pressing or other sintering techniques could yield improved electrical conductivities and possibly higher Seebeck coefficients, while thermal conductivities could remain low due to the high density of interfaces.

*Ab initio* density of states calculations were performed for our materials to clarify the mechanisms behind the variation of the thermoelectric properties with the nanocrystal composition. In order to rule out any influence of the different substitution localization, up to four different configurations were considered at each x value. Additionally, to discard any artifact related to the limitations of density functional theory (DFT) concerning the energy band gap, the displacement of the Fermi level was measured with respect two different features of the band structure: the valence band maximum (VBM) and the conduction band minimum (CBM). Our density of states calculations consistently revealed a gradual downshift of the Fermi level towards the valence band when replacing Cd by Cu ions (figure 7). The Fermi level shift reached up to

0.3 eV, clearly entering inside the CCTSe valence band at high substitution levels. In contrast, the variation of the band gap with the ion replacement obtained from our calculations was very small (Figure 7D). Different substitution configurations or measurement references did not vary significantly any of these conclusions



**Figure 7.** A) Total density of states for  $\text{Cu}_2\text{CdSnSe}_4$ ,  $\text{Cu}_{2.5}\text{Cd}_{0.5}\text{SnSe}_4$  and  $\text{Cu}_3\text{SnSe}_4$ . The scissors operator was applied in all graphics to match with the experimental band gap of 0.96 eV. B) Original configuration ( $\text{Cu}_2\text{CdSnSe}_4$ ) and two different possible configurations for  $x=0.25$  ( $\text{Cu}_{2.25}\text{Cd}_{0.75}\text{SnSe}_4$ ). Arrows point at the substituted ions. C) Fermi level shift with the level of Cd by Cu substitution. Crosses and circles show the Fermi level shift calculated from the valence band maximum and the conduction band minimum, respectively. Different localizations of the substituted ions were considered. D) Variation of the band gap energy with the level of Cd by Cu substitution.

The compositional control in ternary and quaternary semiconductors thus offers an accessible method to tune their valence balance and adjust their Fermi level. This intrinsic doping strategy to control the semiconductor electronic properties is especially interesting in the bottom-up processing of nanocrystals, where the introduction of extrinsic dopants is hardly feasible.

However, a limit exist on the amount of Cd(II) ions that can be substituted by Cu(I) without modifying the Sn and Se content in CCTS nanoparticles. When significantly increasing the Cu/Cd ratio, a decrease of the selenium concentration within the nanoparticles was consistently obtained. These selenium vacancies balanced the valences of the nanocrystal's constituent elements. It is also possible that some of the Cd ions were replaced not by Cu but by Sn ions, thus capturing two of the holes.

Therefore, the initial correlation between the increase of the electrical conductivity and the copper concentration obtained in CZTSe nanocrystals was associated to an intrinsic doping effect caused by the substitution of Cd(II) by Cu(I). On the other hand, the saturation of the electrical conductivities obtained at high substitution levels needs to be attributed to the charge compensation by the creation of Se vacancies and/or Cd by Sn substitution.

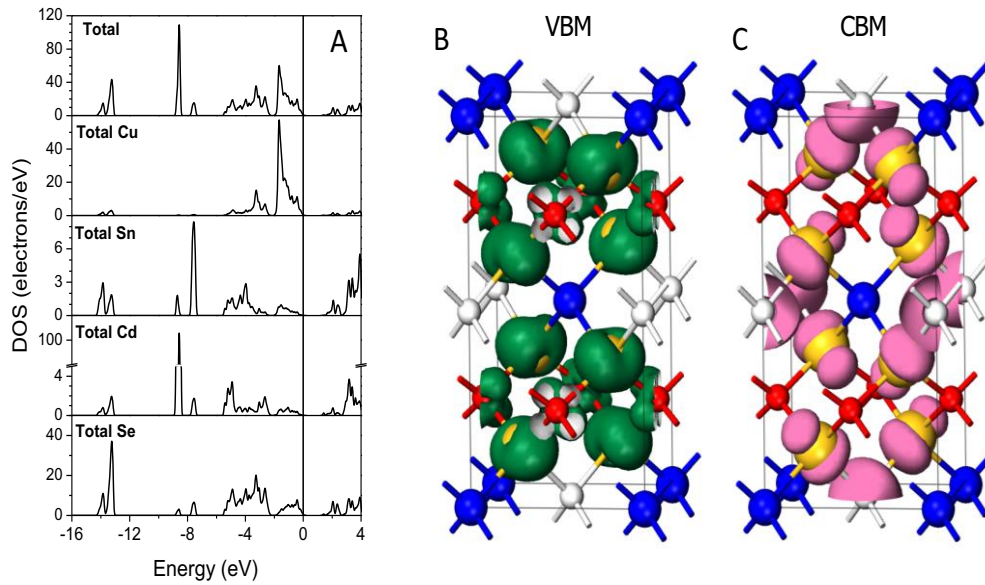


**Figure 8.** A) Total density of states and projected densities corresponding to the different elements within the  $\text{Cu}_2\text{CdSnSe}_4$  compound. B) Localization of the orbitals contributing to the valence band maximum. C) Localization of the orbitals contributing to the conduction band minimum.

In figure 8A, the contribution of each element to the total CCTSe density of states is shown. The main contribution to the VBM comes from Cu. Figures 8B and 8C show the localization of the states contributing to the VBM and those contributing to the CBM, respectively. Notice how, in such a quaternary crystal structure, the states contributing to the electrical conductivity are strongly localized in Cu-Se slabs (hybridization of Cu3d Se4p orbitals). On the other hand, Cd and Sn introduce deep levels inside the valence band, thus not contributing to the electrical conductivity. Therefore, CCTSe may be regarded as composed of tetrahedral [Cu<sub>2</sub>-Se<sub>4</sub>] electrically conductive slabs separated by tetrahedral [Cd-Sn-Se<sub>4</sub>] electrically insulating slabs.<sup>24</sup> The localization of the conductive bands in slabs preserves the hole mobilities from being influenced by the crystal structure complexity, thus permitting the concurrence of relatively low thermal conductivities and high electrical conductivities. At the same time, the states contributing to the CBM, mostly associated to Se, are distributed across the whole unit cell. Hence, electron mobilities are potentially perturbed by the whole cell complexity. Such differential influence of the crystal structure on each charge carrier type should result in relatively high hole-to-electron mobility ratios, which partially explains the material's high Seebeck coefficient.

Conveniently, the disorder introduced when substituting Cd by Cu ions localizes in the non-conducting Cd-Sn slabs. Thus a partial substitution of Cd by Cu should not significantly perturb the hole mobility. However, large substitution levels may have the contrary effect. Excess amounts of Cu could extend the conducting slabs through the whole unit cell and reduce the average hole mobilities.

On the other hand, the disorder introduced by a small level of Cd by Cu substitution increases the phonon scattering and consequently decreases the material's thermal conductivity. The decrease of thermal conductivity correlated with the increase of the Cu concentration

experimentally obtained in the series of samples here studied needs to be attributed to this effect. However, large degrees of substitution result in a homogenization of the slab composition, removing structural complexity and phonon scattering centers, thus increasing the materials thermal conductivity, as observed for the sample with a higher degree of substitution.

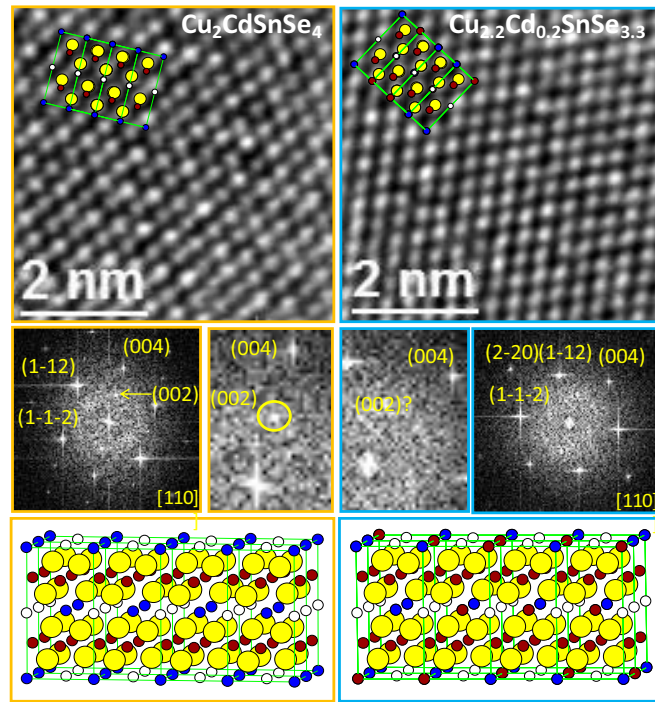


**Figure 9.** HRTEM images and power spectrum analysis of  $\text{Cu}_2\text{CdSnSe}_4$  (left) and  $\text{Cu}_{2.2}\text{Cd}_{0.2}\text{SnSe}_{3.3}$  (right) nanocrystals. Note the alternation of lines of spots with different brightness obtained from the  $\text{Cu}_2\text{CdSnSe}_4$  superstructure, which are not perceptible with the  $\text{Cu}_{2.2}\text{Cd}_{0.2}\text{SnSe}_{3.3}$  compound.

This change of the structural disorder with the Cd-to-Cu ratio is clearly seen by HRTEM characterization of nanocrystals with extreme levels of Cd by Cu substitution. Figure 9 shows the HRTEM images of a  $\text{Cu}_2\text{CdSnSe}_4$  nanocrystal and that of a nanocrystal with a composition:  $\text{Cu}_{2.2}\text{Cd}_{0.2}\text{SnSe}_{3.3}$ . Brighter and dimmer lines of spots were clearly seen from HRTEM images of  $\text{Cu}_2\text{CdSnSe}_4$  nanocrystals. Their power spectrum showed the presence of a bright spot on the (002) corresponding frequency, unequivocally revealing the formation of the superstructure with

two distinguished tetrahedral units in the c-axis:  $[\text{Cu}_2\text{Se}_4]$  and  $[\text{SnCdSe}_4]$ . On the other hand, in the  $\text{Cu}_{2.2}\text{Cd}_{0.2}\text{SnSe}_{3.3}$  nanocrystals, the superstructure and the revealing (002) plane frequency were vanished and no difference of spot contrast in the c-axis were observed, demonstrating the intermixing of the different elements in the tetrahedral units.

## 4.5 Conclusions

---

In summary, CCTSe nanocrystals with narrow size and shape distributions and controlled compositions were prepared by means of a high-yield and easily up-scalable colloidal synthesis route. Because of their structural complexity and many degrees of freedom, these quaternary chalcogenides have an extraordinary potential for thermoelectric energy conversion. By adjusting the Cu-to-Cd ratio, the electrical conductivity of the prepared materials could be increased, while its thermal conductivity was simultaneously reduced. Even with a coarse initial parameter screening for the best thermoelectric properties, we already obtained materials with ZT values up to 0.71. We believe a more systematic optimization of the material parameters may increase their ZT significantly further.

## 4.6 References

---

- (1) Snyder, G. J.; Toberer, E. S., *Nat. Mater.* **2008**, 7, 105-114.
- (2) Dresselhaus, M. S.; Chen, G.; Tang, M. Y.; Yang, R. G.; Lee, H.; Wang, D. Z.; Ren, Z. F.; Fleurial, J. P.; Gogna, P., *Adv. Mater.* **2007**, 19, 1043-1053.
- (3) Rowe, D. M., *Thermoelectrics Handbook: Macro to Nano*. CRC Press: Boca Raton: FL, 2006.
- (4) Feldman, J. L.; Singh, D. J.; Mazin, I. I.; Mandrus, D.; Sales, B. C., *Phys. Rev. B* **2000**, 61, R9209-R9212.
- (5) Gascoin, F.; Ottensmann, S.; Stark, D.; Haïle, S. M.; Snyder, G. J., *Adv. Funct. Mater.* **2005**, 15, 1860-1864.

- (6) Vineis, C. J.; Shakouri, A.; Majumdar, A.; Kanatzidis, M. G., *Adv. Mater.* **2010**, 22, 3970-3980.
- (7) Vaqueiro, P.; Powell, A. V., *J. Mater. Chem.* **2010**, 20, 9577-9584.
- (8) Bux, S. K.; Fleurial, J.-P.; Kaner, R. B., *Chem. Commun.* **2010**, 46, 8311-8324.
- (9) Szczech, J. R.; Higgins, J. M.; Jin, S., *J. Mater. Chem.* **2011**, 21, 4037-4055.
- (10) Hicks, L. D.; Dresselhaus, M. S., *Phys. Rev. B* **1993**, 47, 12727-12731.
- (11) Vashaee, D.; Shakouri, A., *Phys. Rev. Lett.* **2004**, 92, 106103.
- (12) Wang, R. Y.; Feser, J. P.; Lee, J.-S.; Talapin, D. V.; Segalman, R.; Majumdar, A., *Nano Lett.* **2008**, 8, 2283-2288.
- (13) Cornett, J. E.; Rabin, O., *Appl. Phys. Lett.* **2011**, 98, 182104.
- (14) Minnich, A. J.; Dresselhaus, M. S.; Ren, Z. F.; Chen, G., *Energy Environ. Sci.* **2009**, 2, 466-479.
- (15) Heremans, J. P.; Thrush, C. M.; Morelli, D. T., *Phys. Rev. B* **2004**, 70, 115334.
- (16) Martin, J.; Wang, L.; Chen, L.; Nolas, G. S., *Phys. Rev. B* **2009**, 79, 115311.
- (17) Popescu, A.; Woods, L. M.; Martin, J.; Nolas, G. S., *Phys. Rev. B* **2009**, 79, 205302.
- (18) Ibáñez, M.; Guardia, P.; Shavel, A.; Cadavid, D.; Arbiol, J.; Morante, J. R.; Cabot, A., *J. Phys. Chem. C* **2011**, 115, 7947-7955.
- (19) Li, W.; Shavel, A.; Guzman, R.; Rubio-Garcia, J.; Flox, C.; Fan, J.; Cadavid, D.; Ibáñez, M.; Arbiol, J.; Morante, J. R.; Cabot, A., *Chem. Commun.* **2011**, 47, 10332-10334.
- (20) Shavel, A.; Arbiol, J.; Cabot, A., *J. Am. Chem. Soc.* **2010**, 132, 4514-4515.
- (21) Scheele, M.; Oeschler, N.; Meier, K.; Kornowski, A.; Klinke, C.; Weller, H., *Adv. Funct. Mater.* **2009**, 19, 3476-3483.
- (22) Prasher, R., *Phys. Rev. B* **2006**, 74, 165413.
- (23) Kovalenko, M. V.; Spokoyny, B.; Lee, J. S.; Scheele, M.; Weber, A.; Perera, S.; Landry, D.; Talapin, D. V., *J. Am. Chem. Soc.* **2010**, 132, 6686-6695.
- (24) Liu, M.-L.; Chen, I. W.; Huang, F.-Q.; Chen, L.-D., *Adv. Mater.* **2009**, 21, 3808-3812.
- (25) Shi, X. Y.; Huang, F. Q.; Liu, M. L.; Chen, L. D., *Appl. Phys. Lett.* **2009**, 94, 122103.
- (26) Liu, M. L.; Huang, F. Q.; Chen, L. D.; Chen, I. W., *Appl. Phys. Lett.* **2009**, 94, 202103.
- (27) Sevik, C.; Cagin, T., *Appl. Phys. Lett.* **2009**, 95, 112105.
- (28) Schorr, S., *Thin Solid Films* **2007**, 515, 5985-5991.

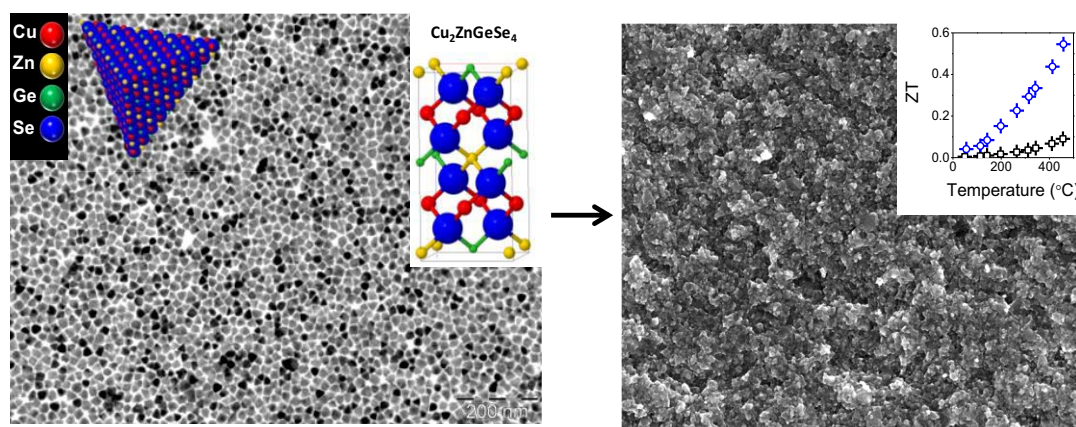
- (29) Fan, F.-J.; Yu, B.; Wang, Y.-X.; Zhu, Y.-L.; Liu, X.-J.; Yu, S.-H.; Ren, Z., *J. Am. Chem. Soc.* **2011**, 133, 15910-15913.
- (30) Toberer, E. S.; May, A. F.; Snyder, G. J., *Chem. Mater.* **2009**, 22, 624-634.
- (31) Sevik, C.; Çağın, T., *Phys. Rev. B* **2010**, 82, 045202.
- (32) José, M. S.; Emilio, A.; Julian, D. G.; Alberto, G.; Javier, J.; Pablo, O.; Daniel, S.-P., *J. Phys.: Condens. Matter* **2002**, 14, 2745.
- (33) Perdew, J. P.; Burke, K.; Ernzerhof, M., *Phys. Rev. Lett.* **1996**, 77, 3865-3868.
- (34) Davey, W. P., *Phys. Rev.* **1923**, 21, 143-161.
- (35) Olekseyuk, I. D.; Gulay, L. D.; Dydchak, I. V.; Piskach, L. V.; Parasyuk, O. V.; Marchuk, O. V., *J. Alloys Compd.* **2002**, 340, 141-145.
- (36) Deka, S.; Genovese, A.; Zhang, Y.; Miszta, K.; Bertoni, G.; Krahne, R.; Giannini, C.; Manna, L., *J. Am. Chem. Soc.* **2010**, 132, 8912-8914.





# Chapter 5

## Cu<sub>2</sub>ZnGeSe<sub>4</sub> Nanocrystals: Synthesis and Thermoelectric Properties



### 5.1 Abstract

A synthetic route to produce Cu<sub>2</sub>ZnGeSe<sub>4</sub> nanocrystals with narrow size distributions and controlled composition is presented. These nanocrystals were used to produce densely packed nanomaterials by hot-pressing. From the characterization of the thermoelectric properties of these nanomaterials, Cu<sub>2</sub>ZnGeSe<sub>4</sub> is demonstrated to show excellent thermoelectric properties. A very preliminary adjustment of the nanocrystals composition has already reached a figure of merit up to 0.55 at 450 °C.

## 5.2 Introduction

---

The ample chemical and structural freedom of quaternary diamond-like chalcogenides allows their use in multiple applications, such as photovoltaics,<sup>1, 2</sup> non-linear optics,<sup>3</sup> thermoelectrics<sup>4-6</sup> and even as topological insulators, as recently demonstrated.<sup>7, 8</sup> In particular, in the field of photovoltaics, copper-based quaternary diamond-like semiconductors of the family  $I_2-II-IV-VI_4$  have recently gained a great deal of attention as alternative absorber materials to CdTe and  $Cu(In,Ga)Se_2$ . The possibility to engineer quaternary semiconductors made of relatively low cost, abundant and non-toxic elements having an optimum direct band gap has drawn a high interest in the preparation and characterization of these class of materials, and particularly  $Cu_2ZnSn(S,Se)_4$ .<sup>1, 2, 9, 10</sup>

On the other hand, the complexity of the crystallographic structures of quaternary compounds is associated with intrinsically low thermal conductivities. In addition, the control of their composition allows for the tuning of their charge carrier concentration. Moreover, in the particular case of compositionally layered structures, such as stannite, high electrical conductivities can coexist with large Seebeck coefficients and intrinsically low thermal conductivities. Thus, these quaternary compounds are also potentially excellent thermoelectric materials.<sup>4, 5, 11</sup>

While in photovoltaics the reduction of the lattice dimensions to the nanoscale allows for the low-cost solution processing of devices, in the thermoelectrics field, nanostructuring further allows improvement of their efficiency.<sup>12, 13</sup> Mainly, the reduction of the crystal domains to the nanoscale introduces a high density of phonon scattering centers, which reduce the materials thermal conductivity and enhance its thermoelectric figure of merit.

$\text{Cu}_2\text{ZnGeSe}_4$  (CZGS) is a p-type semiconductor with a direct band gap between 1.21 and 1.63 eV, as determined experimentally and theoretically.<sup>14-17</sup> Its ideal band gap makes it an alternative indium- and cadmium-free absorber material for photovoltaics.<sup>17-19</sup> CZGS crystallizes in a non-centered tetragonal structure with space group  $I-42m$ .<sup>20-22</sup> Its quaternary nature, variety of ionic valences, and particular crystallographic structure suggest CZGS will be characterized by intrinsically low thermal conductivities and potentially high electrical conductivities and Seebeck coefficients. This combination of properties qualifies CZGS as a potentially outstanding thermoelectric material.

In this communication, a synthetic route to produce CZGS nanoparticles with narrow size distributions and controlled composition is presented. This is the first presented synthetic route to produce CZGS nanocrystals. Furthermore, the potential of CZGS as thermoelectric material is demonstrated by characterizing the thermoelectric properties of CZGS nanocrystals with two different compositions.

### **5.3 Experimental**

---

*Chemicals:* Copper (I) chloride (reagent grade, 97%), Zinc Oxide (99.9%), 1-octadecene (ODE, 90%), oleic acid (OA,  $\geq 99\%$ ), hexadecylamine (HDA, tech. 90%) were purchased from Aldrich. Germanium (IV) chloride (99.9999 %) and Selenium (IV) oxide (99.8%) was purchased from Strem. n-Tetradecylphosphonic acid was purchased from PCI Synthesis. Chloroform, isopropanol and ethanol were of analytical grade and obtained from various sources. All chemicals were used as received without further purification.

All synthesis were carried out using standard airless techniques: a vacuum/dry argon gas Schlenk line was used for the synthesis and a argon glove-box for storing and handling air and moisture-sensitive chemicals.

*Selenium solution:* Selenium (IV) oxide (6.67g, 60mmol) was dissolved under argon atmosphere at 190° in 75ml of 1-octadecene. The mixture was stirred additionally at 190 °C for 5 hours to obtain a perfectly clear brownish orange solution.

*Synthesis of Cu<sub>2</sub>ZnGeSe<sub>4</sub> NCs:* Copper (I) chloride (50 mg, 0.50 mmol), Zinc oxide (41 mg, 0.50 mmol), hexadecylamine (242-1694 mg, 1-7mM), n-Tetradecylphosphonic acid (33mg, 0.1mmol) were dissolved in 10 ml ODE. The solution was heated under argon flow to 200 °C and maintained at this temperature during 1h to remove water and other low-boiling point impurities. Afterwards, the mixture was cooled down to 150 °C and Germanium (IV) chloride (54 mg, 0.50 mmol) dissolved in dried ODE was injected. Following the Ge injection we observe a clear blueish solution. The solution is kept at this temperature for an additional 30minuts and finally heated to the reaction temperature. The selenium solution (4mL, 3mM) was rapidly injected through a septum into the reaction flask. In order to reduce the dropping in the temperature, selenium solution was previously heated up at 180 °C. Following the injection, the temperature dropped to around 260 °C and then slowly recovered to 295 °C. The solution was kept at a temperature between 260 and 295 °C for 5 min and then quickly cooled down. The formation of Cu<sub>2</sub>ZnGeSe<sub>4</sub> could be qualitatively followed by the color change of the mixture from an initial light yellow to green and eventually black color of the solution containing the Cu<sub>2</sub>ZnGeSe<sub>4</sub> NCs. 3 mL of oleic acid were added to the mixture during the cooling at ~70 °C to replace the weakly bound HDA. The crude solution was mixed with 10 ml of chloroform and sonicate for 5 minutes. The Cu<sub>2</sub>ZnGeSe<sub>4</sub> nanoparticles were isolated by centrifugation at 4000 rpm during 5 minutes.

The black precipitate was redispersed in chloroform (~20 ml) and sonicate for 5 minutes. Then the product was additionally precipitated by adding isopropanol (~10 ml) and centrifuging. The NCs were redispersed in chloroform (~5 ml) and stored for further use.

*Preparation of Pellets:* The same synthesis procedure was scaled up for the production of a few grams of nanoparticles. In the scaled-up synthesis procedure, 6 times larger amounts of all precursor, surfactant and solvent were used. The nanocrystals were thoroughly washed by multiple precipitation and re-dispersion steps. The final nanoparticles could not be redispersed in organic solvents, proving the high degree of surfactant removal. Washed nanocrystals were dried out from solution under argon atmosphere. Afterward, the nanocrystals were heated to 500 °C for 1 hour under an Ar flow inside a tube furnace. The annealed nanoparticles were ground into fine powder and then hot pressed under a pressure of 40 MPa at 500 °C for 5 min into 12 mm pellets. The hot pressing was carried out in a Rapid Hot Press (RHP) system. In this system, the heat is provided by an induction coil operated in the RF range applied directly to a graphite die acting as a susceptor. This set up configuration allows increasing temperature at a similar rate than Spark Plasma Sintering (SPS). However, during RHP only the die body is heated inside the induction coil enabling faster cooling of the die and chamber. In our conditions, we increase temperature from room temperature to 500 °C in around 3 minutes under a load of 40 MPa. The density of the pressed pellets was in the range 92-96 % of theoretical value, measured by weight/volume.

*Electrical conductivity and Thermopower Measurements:* The Seebeck coefficient was measured by using a static DC method. Electrical resistivity data were obtained by standard four-probe method. Both Seebeck coefficient and electrical resistivity were measured simultaneously

by using LSR-3 equipment (LINSEIS) in the range between room temperature up to 450 °C, under helium atmosphere.

*Thermal diffusivity measurement:* Thermal conductivity measurements were obtained from flash diffusivity measurements, using the mass density and the Dulong-Petit approximation for the specific heat capacity ( $C_p = 0.34 \text{ J}\cdot\text{g}^{-1}\text{K}^{-1}$ ). The thermal conductivity was calculated as  $\kappa = DC_p d$ , where  $D$  is the thermal diffusivity,  $C_p$  is the heat capacity, and  $d$  is the density.

## 5.4 Results and Discussion

---

CZGS nanoparticles were prepared by reacting metal complexes with an excess of selenium in octadecene. In a typical synthesis, 0.50 mmol CuCl, 0.50 mmol of ZnO, 0.25 mmol of GeCl<sub>4</sub>, 5 mM hexadecylamine, 0.1 mmol of n-tetradecylphosphonic acid and 10 ml octadecene were placed in a four-neck flask and heated up to 200 °C under argon flow. Separately, a 0.8 M selenium solution was prepared under argon by dissolving selenium dioxide in octadecene at 180 °C. 4 mL of the precursor Se solution were injected into the heated solution containing the metal complexes at 295 °C. The solution was kept at this temperature for 5 min to allow the nanoparticles growth. Finally, the flask was rapidly cooled down to room temperature.

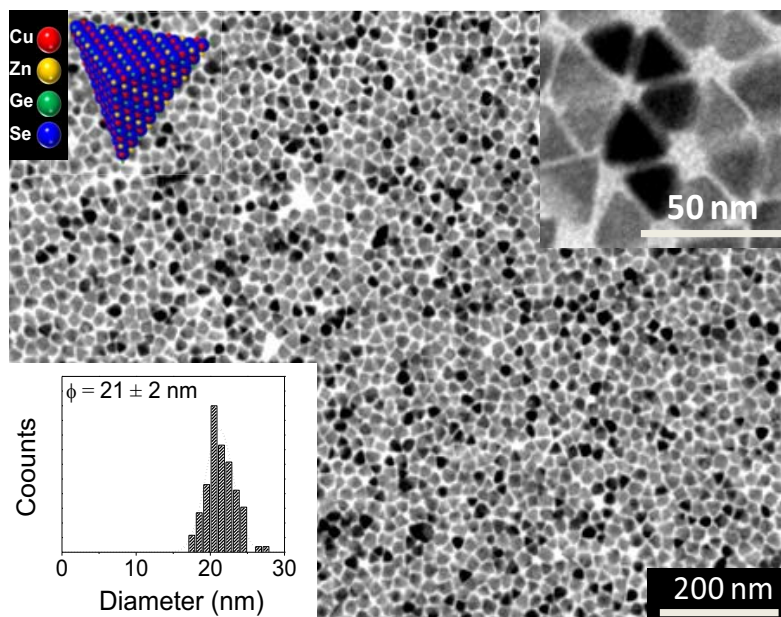


**Figure 1.** Representative TEM micrograph of the CZGS nanoparticles produced. Insets show an atomic model of the tetrahedral particle, a higher magnification TEM micrograph and the histogram with the measured particle size distribution.

Figure 1 shows a representative TEM micrograph of the CZGSe nanoparticles produced by the procedure detailed here. Narrow size distributions, with dispersions below a 10%, were systematically obtained. The prepared nanocrystals typically showed tetragonal geometries (Figure 1, insets). The average nanoparticle size could be controlled by the reaction time and temperature in the range from 10 to 25 nm. Because of the particular kinetics of reaction of the different elements with selenium, we were unable to produce smaller nanocrystals with the stoichiometric composition.

As determined by energy dispersive x-ray spectroscopy (EDX) and confirmed by inductively coupled plasma spectrometry (ICP) analysis, the overall composition of the initially formed nanocrystals was very rich in Cu and Se and very poor in Zn and Ge. A few minutes of reaction time were necessary to obtain nanocrystals with the stoichiometric composition. Single particle chemical analysis, performed by electron energy loss spectroscopy (EELS), confirmed the



nanoparticles obtained after 10 s of reaction to be mostly composed of Cu and Se (Figure 2A). It should be pointed out that the purification of these initial nanocrystals was not an easy task due to the large amount of unreacted complexes in the solution. This explains the relatively large concentration of Zn and Ge detected by EELS outside the particles. After longer reaction time, single particle analyses proved the presence of all four elements within each nanocrystal in the correct composition. It was further confirmed that the 4 elements were homogeneously distributed throughout the nanocrystal (Figure 2B). HRTEM analysis of the nanocrystals verified their tetragonal structure with lateral facets corresponding to {112} planes (Figure 2C).

The different reaction kinetics of Cu, Zn and Ge with Se allow for the adjustment of the nanoparticle composition inside a relatively wide range by controlling the reaction time and temperature and by adjusting the concentration of the different elements in the precursor solution. Figure 2E shows a ternary diagram with the composition distribution of two samples with different global composition:  $\text{Cu}_2\text{ZnGeSe}_4$  and  $\text{Cu}_{2.15}\text{Zn}_{0.85}\text{GeSe}_{3.9}$ . In the same graph, the average value of the single particle analysis is also indicated. This is in good agreement with SEM-EDX, EELS and ICP analysis performed.

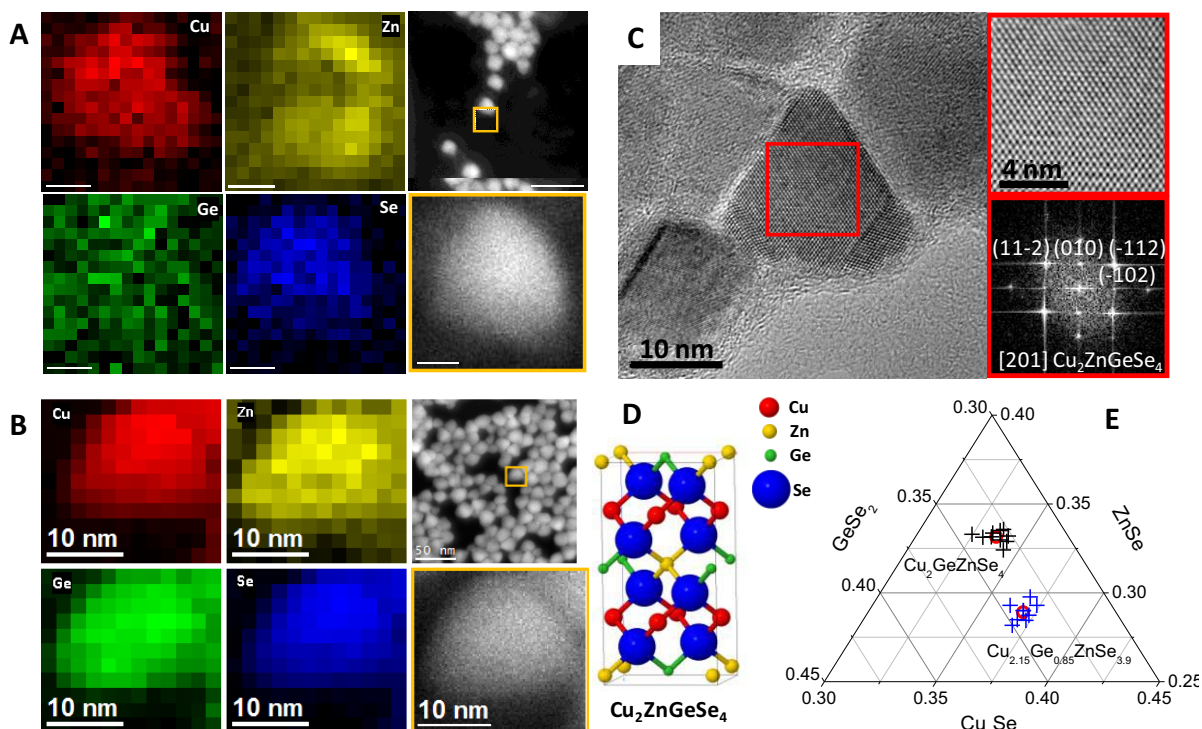
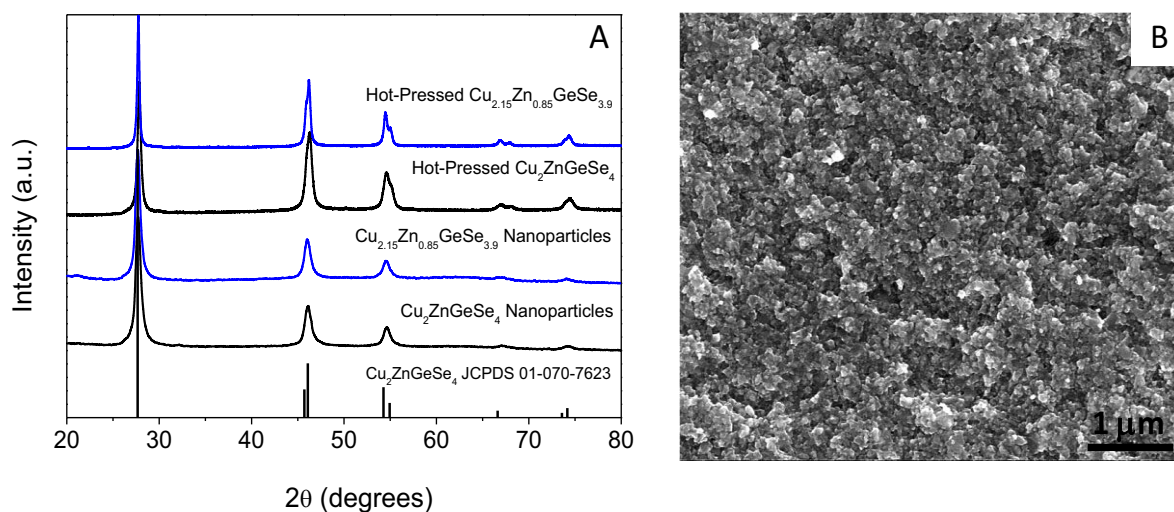


Figure 2. A), B) HAADF image of a few and single nanoparticles and Cu, Zn, Ge and Se compositional maps of the same single particle obtained after 10 s (A) and 5 minutes reaction times (B). C) HRTEM image and power spectrum analysis of a  $\text{Cu}_2\text{ZnGeSe}_4$  nanoparticle. D) Scheme of the tetragonal structure of CZGS. E) Ternary diagrams with the composition of single nanoparticles obtained by HRTEM-EDX. The red circle shows the average value of the single particle analysis, which is in good agreement with SEM-EDX, EELS and ICP analysis.

Figure 3 shows the XRD patterns of the obtained nanocrystals. Patterns resemble those of a tetragonal-symmetry structure with  $I4_2m$  space group (JCPDS 01-070-7623).<sup>21</sup> No secondary phases were detected either in the stoichiometric or the copper-rich sample  $\text{Cu}_{2.15}\text{Zn}_{0.85}\text{GeSe}_{3.9}$ .



**Figure 3.** A) X-ray diffraction pattern of the  $\text{Cu}_2\text{ZnGeSe}_4$  and  $\text{Cu}_{2.15}\text{Zn}_{0.85}\text{GeSe}_{3.9}$  nanoparticles before and after hot-pressing. As a reference, the JCPDS 01-070-7623 pattern corresponding to the tetragonal CZGS phase (S.G. I-42m) is also plotted. B) SEM image of the nanomaterial obtained after hot-pressing.

The high yield of the previously detailed synthetic route allowed scaling up the procedure to the production of grams of nanocrystals with similarly narrow size distributions and controlled compositions. For thermoelectric characterization, roughly 2 grams of nanoparticles of each of the two compositions tested were prepared. The nanocrystals were thoroughly washed by multiple precipitation and re-dispersion steps. The final nanoparticles could not be re-dispersed in organic solvents, proving the high degree of surfactant removal. Washed nanocrystals were dried out from solution under argon atmosphere. To completely remove remaining residual organic ligands, the nanocrystals were heated to 500 °C for 1 hour under an Ar flow inside a tube furnace. The annealed nanoparticles were ground into a fine powder. This nanopowder was hot pressed under Ar atmosphere at 40 MPa and 500 °C for 5 min. The density of the 12 mm pellets obtained was in the range 92-96 %, as calculated from their weight and volume.

Figure 3B shows an SEM image of the material obtained after hot pressing. The crystal domain size increased roughly a factor 1.7 with the annealing and the hot-pressing treatment, as calculated from the fitting of the XRD patterns. In the particular case of the materials used for thermoelectric characterization, the average crystal domain size increased from 15 to 26 nm. No change of composition was obtained with the annealing treatment. The final residual carbon content within the annealed materials was estimated to be in the range from 0.5 and 1% from elemental analysis.

Figure 4 shows the electrical conductivity, Seebeck coefficient, thermal conductivity and calculated figure of merit of  $\text{Cu}_2\text{ZnGeSe}_4$  and  $\text{Cu}_{2.15}\text{Zn}_{0.85}\text{GeSe}_{3.9}$ . Thermal conductivity measurements were obtained from flash diffusivity measurements, using the material's mass density and the Dulong-Petit approximation for its specific heat capacity ( $C_p = 0.34 \text{ J}\cdot\text{g}^{-1}\text{K}^{-1}$ ). The thermal conductivity was calculated as  $\kappa = DC_p d$ , where  $D$  is the thermal diffusivity,  $C_p$  is the heat capacity, and  $d$  is the density.

The relatively high electrical conductivities obtained suggest complete removal of surfactants. The electrical conductivity increased with the partial replacement of Zn by Cu ions as expected by their different valences. In this regard, it should be highlighted how the compositional control in these quaternary semiconductors offers an accessible method to tune their carrier concentration. This intrinsic doping strategy is especially appealing in the bottom-up processing of nanomaterials, where the introduction of extrinsic dopants is not an easy task.

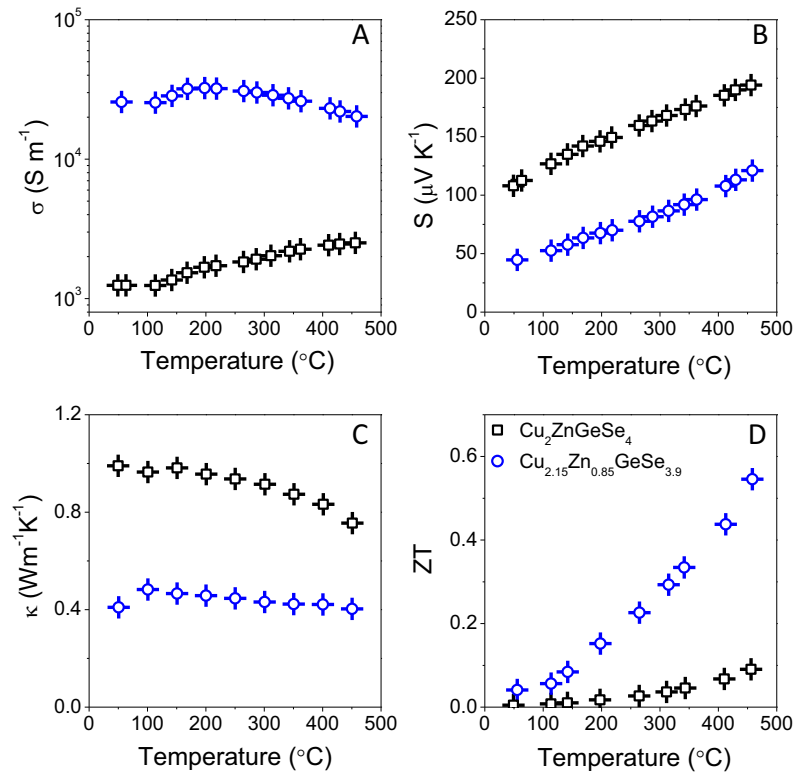


**Figure 4.** Electrical conductivity (A), Seebeck coefficient (B), thermal conductivity (C) and figure of merit (D) of CZGS nanomaterials with the following compositions:  $\text{Cu}_2\text{ZnGeSe}_4$  (black squares),  $\text{Cu}_{2.15}\text{Zn}_{0.85}\text{GeSe}_{3.9}$  (blue circles).

As expected for a heavily doped semiconductor, the Seebeck coefficient followed an opposite trend than the electrical conductivity. Lower Seebeck coefficients were obtained for the materials with a partial substitution of Zn by Cu ions as this should increase the concentration of holes in the valence band. Finally, the sample with a partial substitution of Zn by Cu showed lower thermal conductivity. This lower thermal conductivity is in part associated to the higher degree of disorder introduced in the structure with the Zn by Cu replacement. However, fine microstructural differences between the two nanomaterials having different compositions may also play a significant role.

The final ZT values obtained were higher for the  $\text{Cu}_{2.15}\text{Zn}_{0.85}\text{GeSe}_{3.9}$  than the  $\text{Cu}_2\text{ZnGeSe}_4$  owing to the improved electrical conductivities and the reduced thermal conductivities of the former. The best ZT value obtained from this very preliminary composition screening was 0.55 at 450 °C.

## 5.5 Conclusions

---

In summary, we have detailed a synthetic procedure to produce CZGS nanocrystals with narrow size distribution and controlled compositions. Furthermore, the thermoelectric properties of the nanomaterials obtained after carefully washing the nanocrystals and hot-pressing them into pellets was characterized. By partial replacement of Zn by Cu ions, the materials electrical conductivity could be substantially increased and ZT values up to 0.55 were demonstrated. A further optimization of the materials parameters and processing methods could result in materials with higher ZT values. While the CZGS nanocrystals presented here show promising thermoelectric properties, we also envisage their potential use as absorber materials in solution-processed solar cells and in other applications, such as topological insulators.

## 5.6 References

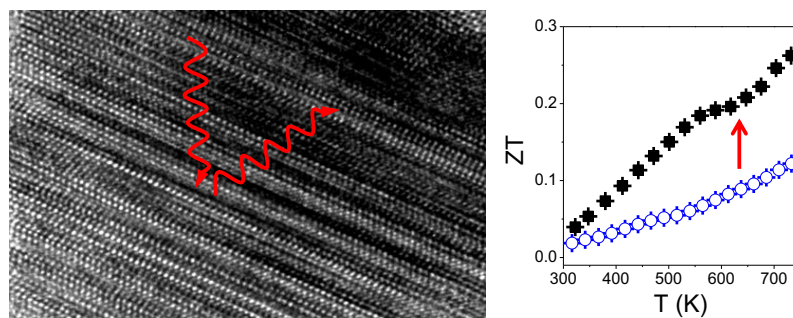
---

- (1) Guo, Q.; Ford, G. M.; Yang, W.-C.; Walker, B. C.; Stach, E. A.; Hillhouse, H. W.; Agrawal, R., *J. Am. Chem. Soc.* **2010**, 132, 17384-17386.
- (2) Mitzi, D. B.; Gunawan, O.; Todorov, T. K.; Wang, K.; Guha, S., *Sol. Energ. Mat. Sol. C.* **2011**, 95, 1421-1436.
- (3) Samanta, L. K.; Bhar, G. C., *Phys. Status Solidi A* **1977**, 41, 331-337.
- (4) Liu, M.-L.; Chen, I. W.; Huang, F.-Q.; Chen, L.-D., *Adv. Mater.* **2009**, 21, 3808-3812.

- (5) Ibáñez, M.; Cadavid, D.; Zamani, R.; García-Castelló, N.; Izquierdo-Roca, V.; Li, W.; Fairbrother, A.; Prades, J. D.; Shavel, A.; Arbiol, J.; Pérez-Rodríguez, A.; Morante, J. R.; Cabot, A., *Chem. Mater.* **2012**, 24, 562-570.
- (6) Fan, F.-J.; Yu, B.; Wang, Y.-X.; Zhu, Y.-L.; Liu, X.-J.; Yu, S.-H.; Ren, Z., *J. Am. Chem. Soc.* **2011**, 133, 15910-15913.
- (7) Wang, Y. J.; Lin, H.; Tanmoy, D.; Hasan, M. Z.; Bansil, A., *New J. Phys.* **2011**, 13, 085017.
- (8) Chen, S.; Gong, X. G.; Duan, C.-G.; Zhu, Z.-Q.; Chu, J.-H.; Walsh, A.; Yao, Y.-G.; Ma, J.; Wei, S.-H., *Phys. Rev. B* **2011**, 83, 245202.
- (9) Shavel, A.; Arbiol, J.; Cabot, A., *J. Am. Chem. Soc.* **2010**, 132, 4514-4515.
- (10) Shavel, A.; Cadavid, D.; Ibáñez, M.; Carrete, A.; Cabot, A., *J. Am. Chem. Soc.* **2012**, 134, 1438-1441.
- (11) Davydyuk, G. Y.; Parasyuk, O. V.; Romanyuk, Y. E.; Semenyuk, S. A.; Zaremba, V. I.; Piskach, L. V.; KozioÅ., J. J.; Halka, V. O., *J. Alloys Compd.* **2002**, 339, 40-45.
- (12) Snyder, G. J.; Toberer, E. S., *Nat. Mater.* **2008**, 7, 105-114.
- (13) Vineis, C. J.; Shakouri, A.; Majumdar, A.; Kanatzidis, M. G., *Adv. Mater.* **2010**, 22, 3970-3980.
- (14) Schleich, D. M.; Wold, A., *Mater. Res. Bull.* **1977**, 12, 111-114.
- (15) Lee, C.; Kim, C.-D., *J. Korean Phys. Soc.* **2000**, 37, 364.
- (16) Matsushita, H.; Ichikawa, T.; Katsui, A., *J. Mater. Sci.* **2005**, 40, 2003-2005.
- (17) Chen, S.; Gong, X. G.; Walsh, A.; Wei, S.-H., *Phys. Rev. B* **2009**, 79, 165211.
- (18) Matsushita, H.; Ochiai, T.; Katsui, A., *J. Cryst. Growth* **2005**, 275, e995-e999.
- (19) Nakamura, S.; Maeda, T.; Wada, T., *Jpn. J. Appl. Phys.* **2010**, 49, 121203.
- (20) Romanyuk, Y. E.; Parasyuk, O. V., *J. Alloys Compd.* **2003**, 348, 195-202.
- (21) Parasyuk, O. V.; Gulay, L. D.; Romanyuk, Y. E.; Piskach, L. V., *J. Alloys Compd.* **2001**, 329, 202-207.
- (22) Doverspike, K.; Dwight, K.; Wold, A., *Chem. Mater.* **1990**, 2, 194-197.

# Chapter 6

## Crystallographic Control at the Nanoscale to Enhance Functionality: Polytypic $\text{Cu}_2\text{GeSe}_3$ Nanoparticles as Thermoelectric Materials



### 6.1 Abstract

---

The potential to control the composition and crystal phase at the nanometer scale enable the production of nanocrystalline materials with enhanced functionalities and new applications. In the present work, we detail a novel colloidal synthesis route to prepare nanoparticles of the ternary semiconductor  $\text{Cu}_2\text{GeSe}_3$  (CGSe) with nanometer scale control over their crystal phases. We also demonstrate the structural effect on the thermoelectric properties of bottom-up prepared CGSe nanomaterials. By carefully adjusting the nucleation and growth temperatures, pure orthorhombic CGSe nanoparticles with cationic order or polytypic CGSe nanoparticles with disordered cation positions can be produced. In this second type of nanoparticles, a high density of twins can be created to periodically change the atomic planes stacking, forming a hexagonal wurtzite CGSe phase. The high yield of the synthetic routes here reported allows the production



of single-phase and multi-phase CGSe nanoparticles in the gram scale, which permits the characterization of the thermoelectric properties of these materials. Reduced thermal conductivities and a related 2.5 fold increase of the thermoelectric figure of merit for multi-phase nanomaterials when compared with pure-phase CGSe are systematically obtained. These results are discussed in terms of the density and efficiency of phonon scattering centers in both types of materials.

## 6.2 Introduction

---

The numerous possibilities for chemical substitutions and structural modifications of ternary and quaternary chalcogenides allow a significant degree of engineering their fundamental chemical and physical properties, including band-gap and carrier concentration.<sup>1-3</sup> Besides, the possibility of tailoring the material properties by the preparation of metastable crystallographic phases has recently generated a great deal of attention. Special mention deserves the metastable wurzite phases recently identified in many compounds and particularly in some copper-based ternary and quaternary semiconductors.<sup>4-7</sup>

A particularly attractive ternary chalcogenide is  $\text{Cu}_2\text{GeSe}_3$  (CGSe). CGSe is a p-type semiconductor with a direct band-gap in the IR ( $E_g = 0.78$  eV).<sup>8, 9</sup> It has a low melting temperature (770 °C), a relatively low density ( $\rho=5.6$  g/cm<sup>3</sup>)<sup>10</sup> and a high refraction index,  $n\sim 3.2$ .<sup>8, 9, 11</sup> Different crystal structures have been described for this compound: cubic (zinc-blende-like),<sup>12</sup> tetragonal chalcopyrite<sup>13-15</sup> and orthorhombic with space group Imm2.<sup>16, 17</sup> CGSe has a thermal expansion coefficient of  $8.4 \times 10^{-6}$  K<sup>-1</sup>, a heat capacity of about  $0.34$  Jg<sup>-1</sup>K<sup>-1</sup>, and a relatively low thermal conductivity of  $2.4$  Wm<sup>-1</sup>K<sup>-1</sup> at 300 K.<sup>11, 18</sup> These properties makes it a promising thermoelectric material.<sup>19-21</sup>

One main strategy to increase the figure of merit of thermoelectric materials is to decrease their thermal conductivity by promoting phonon scattering. This goal can be achieved by reducing the size of the crystal domains to the nanoscale.<sup>22-27</sup> In this direction, the ball-milling of crystalline ingots into a nanopowder and its posterior reconsolidation into bulk nanomaterials by hot-pressing or spark-plasma-sintering is the most usual approach in single phase materials. Nevertheless, higher thermoelectric figures of merit have been obtained with multiphase nanomaterials or nanocomposites, where acoustic impedance mismatches at the interfaces between dissimilar structures boost phonon scattering.<sup>22-24, 28</sup> Nanocomposites can be obtained by the spontaneous formation of nanoscale inclusions when cooling down solid solutions in a controlled manner. This is an excellent approach, but it lacks of high composition versatility and of an extensive control over the size, composition and phase of the nanocrystalline domains.

In this scenario, bottom-up approaches based on solution-processed nanoparticles are especially well suited to produce nanocomposites with high level of control over the size, phase and composition of the crystallographic nanodomains. The availability of colloidal nanocrystals with tuned properties allows producing nanocomposites by simply mixing controlled ratios of nanoparticles with different phases and/or compositions. To ensure more homogeneous distributions of the two phases at the nanometer scale, colloidal nanoheterostructures become even a more suitable candidate for bottom-up nanocomposite processing.<sup>29, 30</sup> Nevertheless, while a-priori nanocomposites have associated low thermal conductivities, the charge carriers sign and concentration of the constituent materials need to be carefully matched in order not to significantly reduce the electrical conductivity and Seebeck coefficient of the final compound. In this scenario, nanocomposites with homogenous compositions but multiple crystal structure may have associated important advantages.

In this work, the first synthetic route to prepare highly monodisperse CGSe nanoparticles is presented. By controlling the synthesis parameters, single-phase CGSe nanoparticles or multi-phase polytypic CGSe nanoparticles were prepared. The high yield of the synthetic route detailed here allowed the production of dense nanocrystalline materials from the bottom-up assembly and posterior sintering of the prepared nanoparticle building blocks. These nanocrystalline materials were further used to characterize the thermoelectric properties of nanocrystalline CGSe and to demonstrate the strong improvement over the thermoelectric properties that the control of the crystallographic phase at the nanometer scale can provide.

### 6.3 Experimental Section

---

*Chemicals;* Copper (I) chloride (reagent grade, 97 %), 1-octadecene (ODE, 90 %), oleic acid (OA,  $\geq 99$  %), hexadecylamine (HDA, tech. 90 %) were purchased from Aldrich. Germanium (IV) chloride (99.9999 %) and Selenium (IV) oxide (99.8 %) were purchased from Strem. Chloroform, isopropanol and ethanol were of analytical grade and obtained from various sources. All chemicals were used as received without further purification. All syntheses were carried out using standard airless techniques: a vacuum/dry argon gas Schlenk line was used for the syntheses and an argon glove-box for storing and handling air and moisture-sensitive chemicals.

*Selenium solution (ODE:Se):* Selenium (IV) oxide (8.87 g, 80 mmol) was dissolved under argon atmosphere at 180 °C in 100 mL of ODE. The mixture was additionally stirred at 180 °C for 5 h to obtain a perfectly clear brownish orange solution.

*Cu<sub>2</sub>GeSe<sub>3</sub> nanoparticles:* Copper (I) chloride (50 mg, 0.50 mmol) and HDA (726 mg, 3 mM) were dissolved in 10 ml ODE. The solution was heated under argon flow to 200 °C and maintained at this temperature during 1 h to remove water and other low-boiling point impurities.

Afterwards, the mixture was cooled down to 120 °C and Germanium (IV) chloride (54 mg, 0.25 mmol) dissolved in dried 0.50 mL of ODE was injected. Then, the solution was heated to the reaction temperature. The ODE:Se (4 mL, 3 mM) was rapidly injected through a septum into the reaction flask. In order to reduce the temperature drop with the injection, the selenium solution was previously heated up at 180 °C. Following the injection, the temperature dropped by around 30 °C and then slowly recovered to the set value. The solution was allowed to react for 7 min and afterwards was quickly cooled down. The formation of CGSe could be qualitatively followed by the color change of the mixture from an initial light yellow to green and eventually to the black color of the solution containing CGSe nanoparticles. 3 ml of OA were added to the mixture during the cooling step, at ~70 °C, to replace the weakly bound HDA. The crude solution was mixed with 10 ml of chloroform and sonicated for 5 minutes. The CGSe nanoparticles were isolated by centrifugation at 4000 rpm during 3 minutes. The black precipitate was redispersed in chloroform (~ 20 ml) and sonicated for 5 minutes. Then the product was additionally precipitated by adding isopropanol (~ 10 ml) and centrifuging. The nanoparticles were re-dispersed in chloroform (~ 5 ml) and stored until their posterior use.

*Cu<sub>2</sub>GeSe<sub>3</sub> nanocrystalline pellets:* The same synthesis procedure was scaled up for the production of nanoparticles at the gram scale. In the up-scaled synthesis procedure, 6 times larger amounts of all precursor, surfactant and solvent were used. The obtained CGSe nanoparticles were thoroughly washed by multiple precipitation and re-dispersion steps, until they could not be re-dispersed in organic solvents. At this point, most of the surfactants initially used to control the nanoparticle size, shape and solubility had been already removed. The washed nanoparticles were dried under argon atmosphere. Afterward, the nanoparticles were heated to 500 °C for 2 hour

under an Ar flow inside a tube furnace. The annealed nanoparticles were ground into a fine nanopowder and then pressed into 10 mm pellets under a pressure of 2 tones for 5 min at room temperature. The relative density of the pressed disks was in the range 82-87 % of their theoretical value, measured by weight/volume.

*Electrical conductivity and thermopower measurements:* The Seebeck coefficient was measured using a static DC method. Electrical conductivity data were obtained by standard four-probe method. Both Seebeck coefficient and electrical conductivity were measured simultaneously using a LINSEIS LSR-3 system. Measurements were carried out under helium atmosphere in the temperature range from 50 to 450 °C.

*Thermal diffusivity measurement:* Thermal conductivities were calculated from flash diffusivity measurements, using the mass density and the Dulong-Petit approximation for the specific heat capacity ( $C_p = 0.34 \text{ J}\cdot\text{g}^{-1}\text{K}^{-1}$ ). The thermal conductivity was calculated as  $\kappa = DC_p d$ , where  $D$  is the thermal diffusivity,  $C_p$  is the heat capacity, and  $d$  is the density.

*Transmission electron microscopy and x-ray diffraction:* The chemical and structural characterization of the nanoparticles was carried out by transmission electron microscopy (TEM), high resolution TEM (HRTEM), electron energy loss spectroscopy (EELS), and 3D atomic supercell modeling. HRTEM images were obtained using a Jeol 2010F field emission gun microscope with a 0.19 nm point-to-point resolution at 200 keV with an embedded Gatan Image Filter (GIF) for EELS analyses. Images were analyzed by means of Gatan Digital Micrograph software. In addition, 3D atomic supercell modeling was performed by using the Rhodius software package<sup>31</sup>, which allows to create complex atomic models of nanostructures.<sup>32, 33</sup> The

powder x-ray diffraction (XRD) patterns were obtained with Cu  $K_{\alpha}$  ( $\lambda = 1.5406 \text{ \AA}$ ) radiation in a reflexion geometry on a Bruker D8 operating at 40 kV and 40 mA.

## 6.4 Results and Discussion

CGSe nanoparticles were prepared by reacting metal-amine complexes with an excess of selenium in ODE. In a typical procedure, 0.50 mmol CuCl, 3 mM HDA, and 10 ml ODE were placed in a four-neck flask and heated up to 200 °C under argon flow until all precursors were dissolved. Afterwards, the solution was cooled to 120 °C and 0.25 mmol of GeCl<sub>4</sub> in 0.5 ml of ODE were injected. Then the solution was heated up to 300 °C. At this temperature, 4 mL of a 0.8 M Se solution were injected. Nanoparticles were allowed to grow for 7 min before rapidly cooling down.

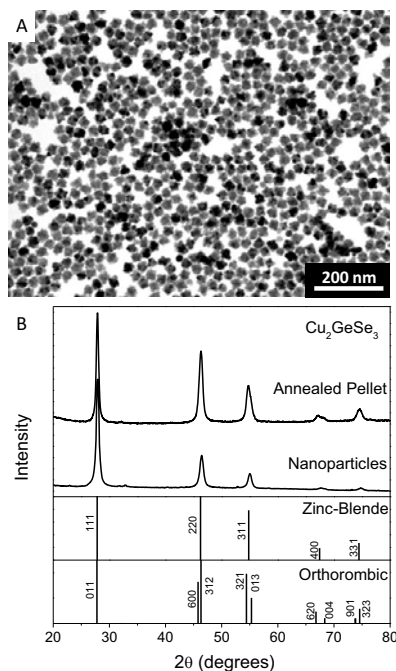


**Figure 1.** A) Representative TEM micrograph of Cu<sub>2</sub>GeSe<sub>3</sub> nanoparticles obtained at 300 °C. B) X-ray diffraction pattern of the nanoparticles and an annealed pellet. Cubic (JCPDS 04-005-4184) and orthorhombic (JCPDS 04-008-8914) patterns are also plotted for reference.

Figure 1A shows a representative TEM micrograph of the CGSe nanoparticles prepared by the described synthetic route. Narrow size distributions systematically characterized the CGSe nanoparticles obtained. The irregular shapes and the different contrasts within each particle observed by TEM clearly pointed out their polycrystalline nature. HRTEM characterization showed the nanoparticles to contain multiple twin defects (Figure 2A), which were at the origin of the nanoparticles polycrystallinity. XRD analysis suggested the CGSe nanoparticles to have either an orthorhombic (OTR, space group  $Imm2$ ) or a cubic zinc-blende (ZB, s.g.:  $F-43m$ ) crystal structure (Figure 1B). The broadening associated to the small size of the crystallographic domains made the differentiation between these two phases not straightforward. However, the double peak at around  $68^\circ$  suggested the CGSe to have an OTR crystallographic structure.

Average crystal domain sizes calculated from the fitting of the XRD patterns using Scherrer's equation were systematically lower than the average nanoparticle sizes measured by TEM. This is consistent with the polycrystalline nature of the nanoparticles.

Single nanoparticle chemical analyses performed by EELS and EDX confirmed the presence and homogeneous distribution of all three elements within each nanoparticle in the  $Cu_2GeSe_3$  stoichiometric composition (Figure 2B). At the same time, the same composition was obtained from all the nanoparticles analyzed.

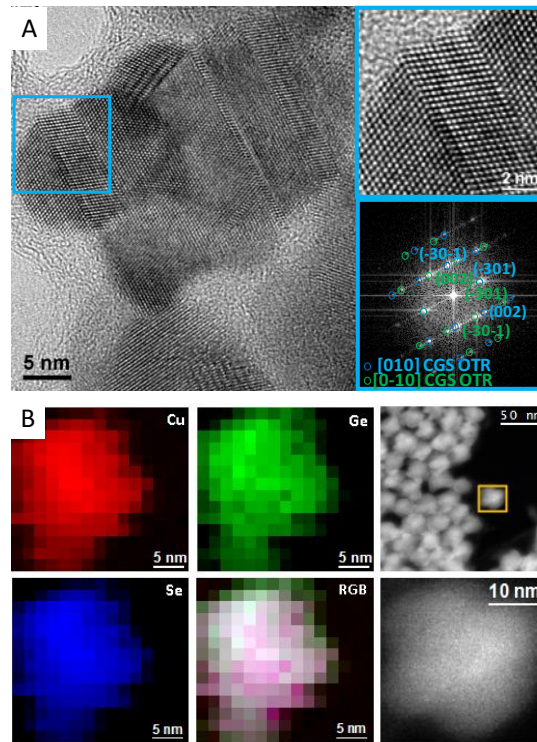


**Figure 2.** A) HRTEM micrograph, detail of a twinned segment and power spectrum analysis of a polycrystalline  $\text{Cu}_2\text{GeSe}_3$  nanoparticle. B) HAADF image of a few and a single particle, and Cu, Ge and Se compositional EELS maps of the same  $\text{Cu}_2\text{GeSe}_3$  nanoparticle.

It has been previously reported by several researchers that  $\text{Cu}_2\text{GeSe}_3$  undergoes a phase transformation caused by site-exchange order/disorder near its melting temperature. The high temperature phase is the disordered face-centered cubic (fcc) ZB structure while the low temperature structure is the ordered OTR phase. At the same time, as the Ge content is increased in  $\text{Cu}_2\text{Ge}_{1+x}\text{Se}_3$ , a structural phase transition takes place, resulting in the conversion of the OTR cell to the fcc structure with a unit cell parameter of  $\sim 0.555$  nm ( $a=b=c$ ). The relationship between both phases corresponds to multiplying the a-axis of the orthorhombic cell by  $(2)^{1/2}/3$  and the b axis by  $(2)^{1/2}$ . The c-axis remains the same in both structures aside from a small expansion. However, the OTR phase should present crystallographically ordered cations and



anions on their respective sites,<sup>19</sup> showing the following cell parameters:  $a = 1.186$  nm,  $b = 0.396$  nm, and  $c = 0.5485$  nm (OTR, s.g.: *Imm2*).<sup>2, 7</sup>

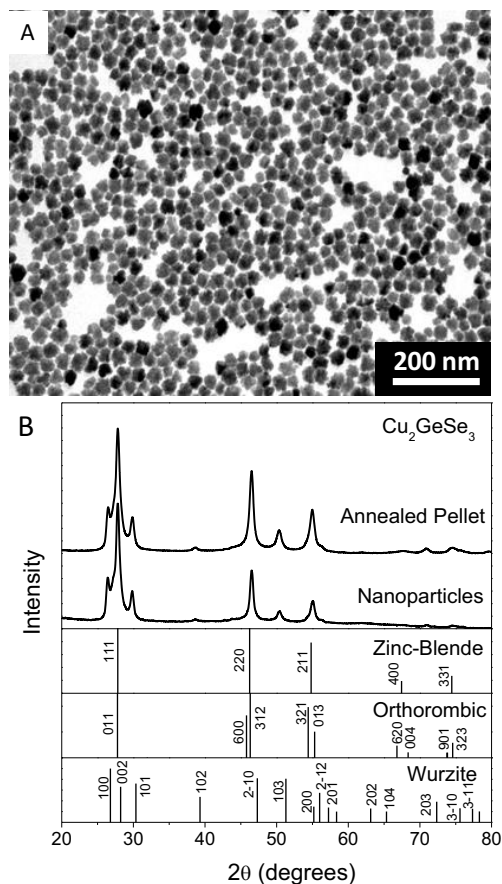


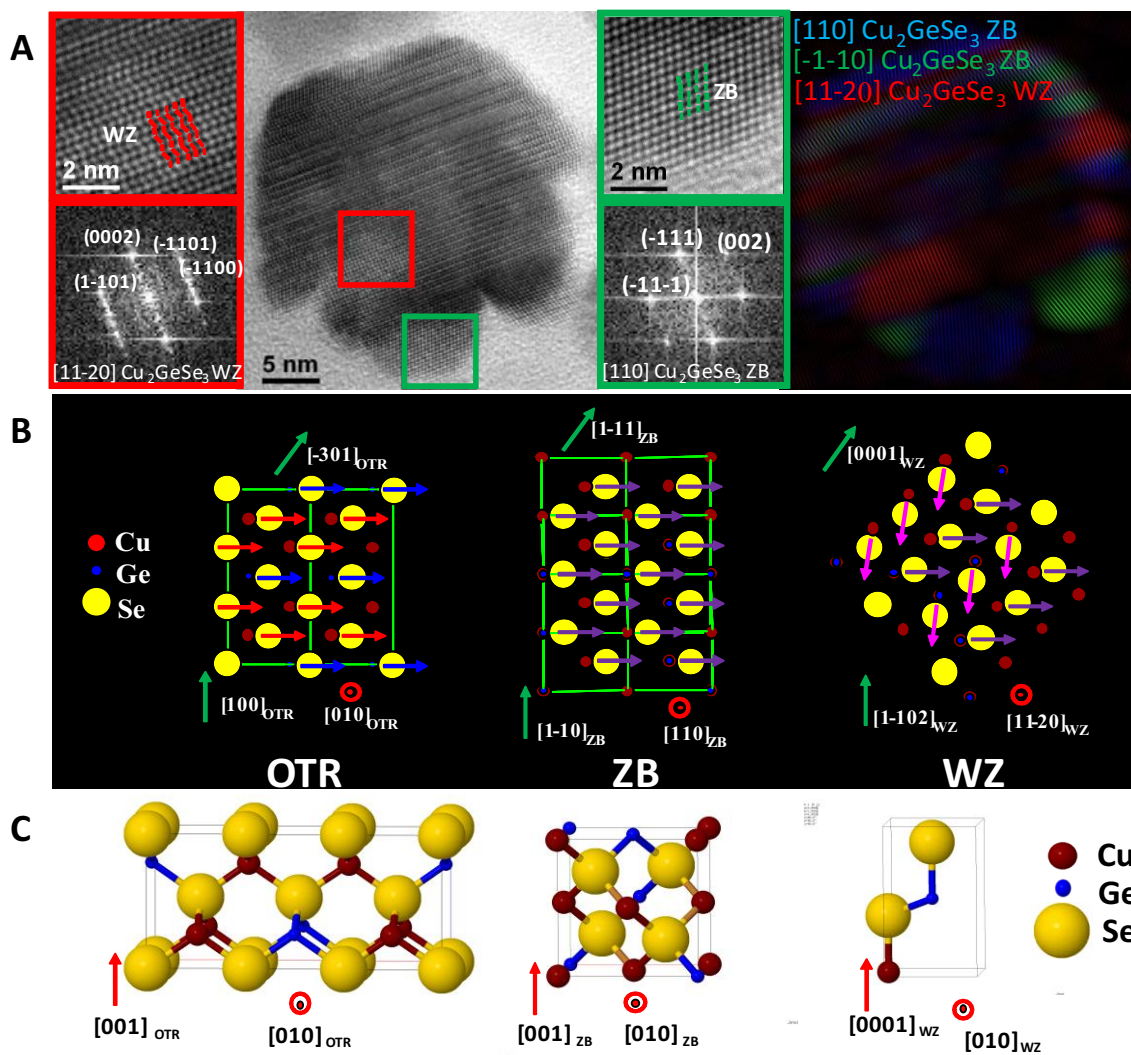
**Figure 3.** A) Representative TEM micrograph of the nanoparticles obtained at 285 °C. B) X-ray diffraction pattern of the nanoparticles and an annealed pellet. As a reference, the cubic (JCPDS 04-005-4184), orthorhombic (JCPDS 04-008-8914) and the simulated wurtzite patterns are also plotted.

When reducing the nucleation temperatures below 300 °C, nanoparticles with a higher degree of cation disorder were obtained. In figure 3A a representative TEM micrograph of the nanoparticles obtained at 285 °C is shown. These nanoparticles conserved both the narrow size distribution and the polycrystallinity characterizing the products obtained at 300 °C. However, when reducing the temperature for nanoparticle growth below 300 °C the more disordered ZB

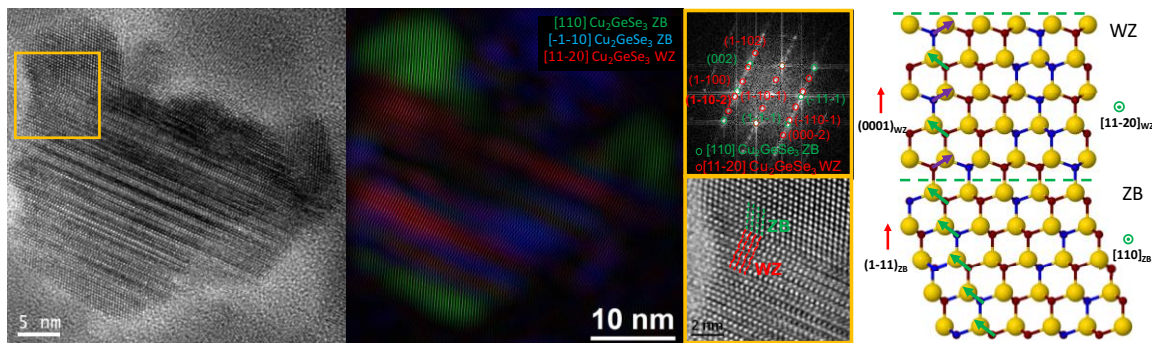
structure was obtained instead of the ordered OTR one (Figure 3B). At the same time, a higher density of defects was created and a new crystallographic phase appeared intermixed with ZB (Figure 3B, 4A). HRTEM characterization allowed us to determine the spatial distribution of the crystal phases within the nanoparticles. The obtained nanoparticles were formed by a central core and a few ZB crystal domains distributed around it in an anisotropic manner. Figure 4A shows a crystal phase color map of a single CGSe nanoparticle. At its core, many twin-like defects were identified. The high density of twins periodically changed the atomic planes stacking. Similar twinning has been observed in other semiconductor nanoparticles and nanowires.<sup>34-37</sup> As none of the CGSe structures in literature matched the phases resulting from the periodic twinning, we assumed the existence of a new polytype (Figure 4B). In order to create the new structure we took as a model a similar twin-induced phase transformation reported in other semiconductors.<sup>34-37</sup> Following the same crystal ratio as in previous calculations, we created a new crystal cell polytype with the hexagonal wurtzite (WZ) structure (S.G.: P63/mc).<sup>38</sup> The new cell perfectly matched the polytype structure found in the CGSe nanoparticles. Notice that in our model, Ge atoms were considered substitutional on the Cu sites, and they were randomly distributed without cation ordering.

The three phases, ZB, OTR and WZ are intimately related and create a kind of dumbbell system similar to that found in III-V and group IV semiconductors in their cubic and hexagonal polytypes, ZB and WZ, respectively. In figure 4B, a scheme of the crystal relationship between the related phases is shown. To understand these crystal structures, it is useful to consider the dumbbell unit composed of a cation (Cu or Ge) and an anion (Se) as the minimum repeatable unit.<sup>39</sup> These dumbbell units are oriented in parallel on the (600) planes in the OTR structure and on the (2-20) planes in the ZB one. In the cubic ZB structure, Cu and Ge are randomly distributed

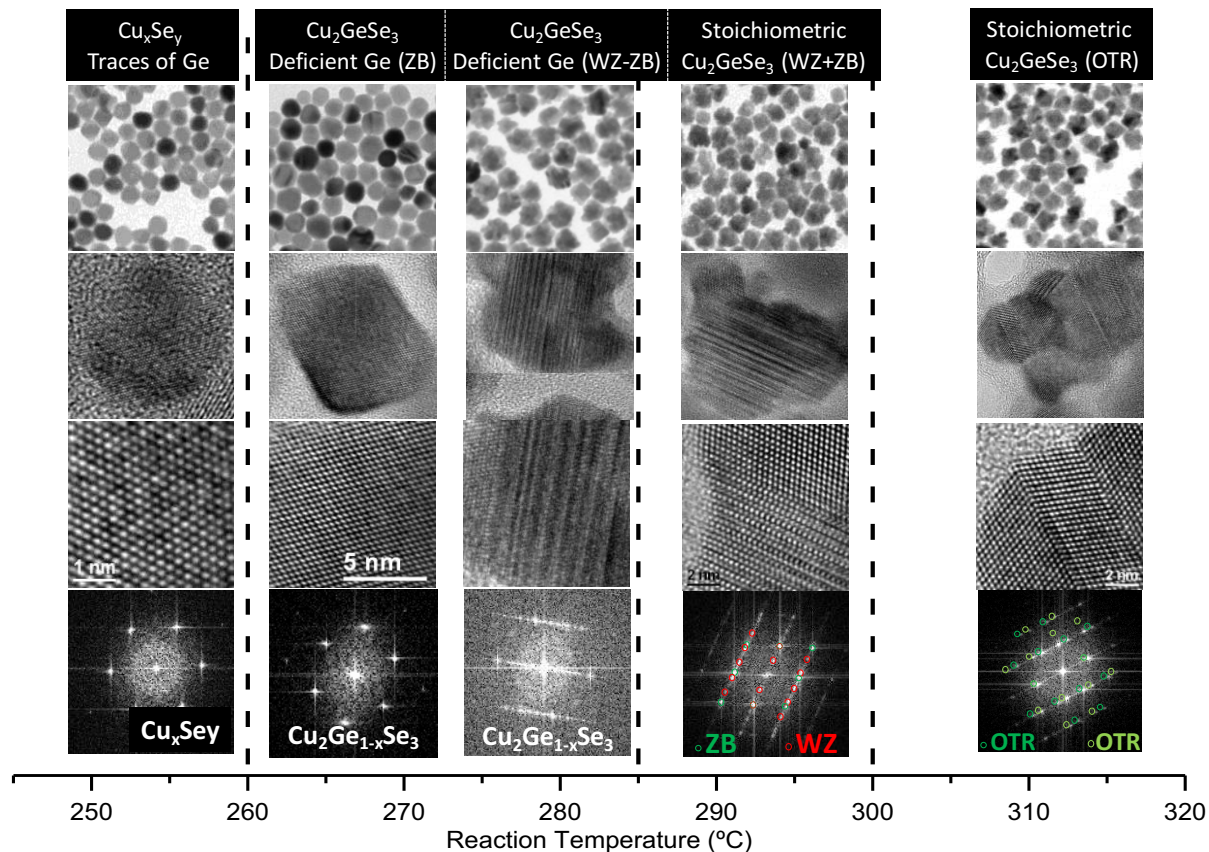
in the cationic positions, with occupation factors 2/3 and 1/3 for Cu and Ge, respectively. However, in the OTR phase cations are ordered along the (200) planes, meaning that all the cation positions in every plane are occupied by the same element, following an ordered sequence of two (200)<sub>OTR</sub> planes with Cu cations plus one (200)<sub>OTR</sub> plane with Ge cations. Red arrows on the OTR phase scheme are pointing the dumbbell orientation on the Cu cation (200)<sub>OTR</sub> planes, while the blue arrows point the dumbbell orientation on the Ge cations. In the case of the ZB structure, as the cations are randomly distributed, arrows have been painted in purple (blue and red mixture). These structures have a strong polarity, with Cu-Ge pointing up and Se down (or vice-versa). The OTR and ZB structures have an *abcabc* stacking along the (30-1)<sub>OTR</sub> or (1-11)<sub>ZB</sub> planes, while the WZ presents an *ababab* stacking on the (0001) planes. The presence of a twin defect in the OTR or ZB structure (corresponding to a 180° rotation of the structure along the (30-1)<sub>OTR</sub> or (1-11)<sub>ZB</sub> axes) may form one monolayer of WZ. Then several consecutive twins create the pure hexagonal phase (WZ polytype).<sup>31-34</sup> The epitaxial relationship between the 3 phases is as follows: (30-1)[010]<sub>OTR</sub> // (1-11)[110]<sub>ZB</sub> // (0001)[11-20]<sub>WZ</sub>. Figure 5 shows the change in the atomic stacking when moving from the ZB structure to the WZ phase.



**Figure 4.** A) HRTEM micrograph of a  $\text{Cu}_2\text{GeSe}_3$  nanoparticle, with details of the WZ (red squared) and ZB (green squared) areas and respective power spectra analyses. On the right a crystal phase color map is shown. B) Scheme of the crystal relationship between OTR, ZB and WZ phases. C) Unit cell of the different phases.



**Figure 5.** A) HRTEM micrograph of a polycrystalline nanoparticle, detail of the atomic stacking change when moving from the ZB to the WZ phase and phase color map of the WZ-ZB interfaces. B) Two-dimensional representation of a WZ and ZB interface.



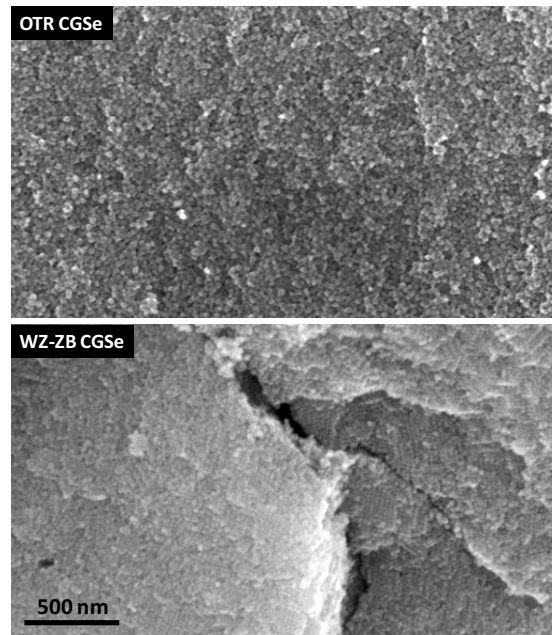
**Figure 6.** Scheme of the crystallographic phase and composition of the Cu-Ge-Se nanoparticles obtained at different temperatures.

Figure 6 schematically summarizes the phase and composition of the nanoparticles that can be obtained at different reaction temperatures. Temperatures below 260 °C result in  $\text{Cu}_x\text{Se}_y$  nanoparticles with traces of Ge. As the temperature is increased, the incorporation of Ge atoms into the crystal structure also increases, producing twin like defects and creating regions where the high density and periodicity of the twins change the atomic planes stacking. Consequently, most of the resulting nanoparticles intermix the new WZ phase with the ZB. Only at 285 °C and

above stoichiometric compositions could be obtained. In the 285-300 °C range the stoichiometric CGSe nanoparticles presented a polycrystalline multiphase WZ-ZB structure. At temperatures above 300 °C, stoichiometric and polycrystalline CGSe nanoparticles were produced. At these higher temperatures, cations are organized within the structure and single-phase OTR nanoparticles could be obtained.

For thermoelectric characterization, roughly 4 grams of OTR and WZ-ZB CGSe nanoparticles were prepared. The nanoparticles were thoroughly washed by multiple precipitation and re-dispersion steps. The purified nanoparticles were heated to 500 °C in an Ar flow atmosphere and maintained at this temperature for 2 hours. The annealed materials were pressed into 10 mm pellets by applying 2 tons of force with a hydraulic press. The annealed nanoparticles conserved their crystallographic phases as observed from the XRD patterns (Figures 1B and 3B). From the SEM analysis of the OTR and WZ-ZB nanocrystalline materials the growth of the crystal domains during thermal treatment was imperceptible (Figure 7). The fitting of the XRD patterns did not allow detecting an improvement of the crystalline structure, and therefore a crystal domain growth. Such a negligible crystal growth rate was in part associated with the residual surfactants covering the nanoparticles before annealing. These organics were slowly decomposed and removed by the argon flow during thermal treatment. The small quantities of carbon that remain after organics decomposition could also inhibit crystal growth. This residual carbon content of the final material was measured to be approximately 1% by elemental analysis. At the same time, the polycrystallinity of the CGSe nanoparticles produced could play an important role on the crystal growth control, as the same thermal process resulted in a 1.5 fold crystal domain increase in similar compounds obtained from single crystal nanoparticles.<sup>1</sup>





**Figure 7.** SEM images of the annealed pellets: orthorhombic  $\text{Cu}_2\text{GeSe}_3$  (top) and wurtzite-zinc-blende  $\text{Cu}_2\text{GeSe}_3$  (bottom).

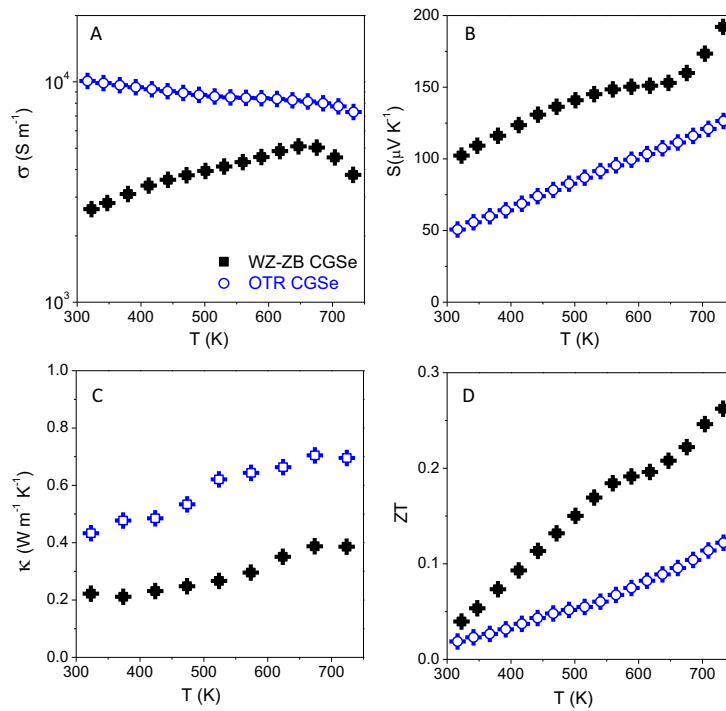


**Figure 8.** Electrical conductivity (A), Seebeck coefficient (B), thermal conductivity (C) and figure of merit (D) of WZ-ZB CGSe (■) and OTR CGSe (○) bulk nanostructured materials.

To accurately compare the thermoelectric properties of the two CGSe nanomaterials, single-phase OTR and multi-phase WZ-ZB CGSe, special attention was paid to produce OTR and WZ-ZB nanoparticles with identical composition ( $\text{Cu}_2\text{GeSe}_3$ ) and size distribution ( $30 \pm 3$  nm) and pellets with similar densities (82 %).

The electrical conductivity, Seebeck coefficient, thermal conductivity and the resulting thermoelectric figure of merit of the CGSe nanocrystalline samples are displayed in Figure 8. The electrical conductivity of the WZ-ZB nanocomposites was slightly lower than that of pure OTR nanomaterials. These slightly lower electrical conductivities may be associated with small band offsets between the WZ and ZB phases, which may promote charge carrier scattering. In this direction, band offsets below 0.1 eV have been previously estimated between WZ and ZB phases in direct band gap semiconductors.<sup>40, 41</sup>

The lower electrical conductivities of the WZ-ZB nanocrystalline sample when compared with those of pure OTR were compensated by larger Seebeck coefficients in the former (Figure 8B). Interestingly, the thermal conductivities of WZ-ZB nanocrystalline pellets were significantly lower than those of pure OTR materials. We attributed such thermal conductivity differences to the distinct crystal structure of the nanomaterials. In addition to the coherent and incoherent interfaces present at the grain boundaries in both nanocrystalline materials, which efficiently scatter long and middle wavelength phonons, we believe that the high density of heterojunctions in the WZ-ZB material can further extend phonon scattering to shorter wavelength (Figure 9). At the same time, phonon scattering at heterojunctions may be more efficient than in homojunctions due to mismatches in the acoustic impedances.<sup>22-24, 28</sup> Additionally, it must be also taken into account, that the CGSe WZ and ZB crystallographic structures here produced had a random cation distribution. Such disorder certainly produced alloying scattering which also strongly



contributed to hamper the propagation of short wavelength phonons. These hypotheses and their repercussions in the thermal conductivity of the nanocomposites need further investigation since there is a lack of understanding in the heat transfer in such crystallographically complex systems.

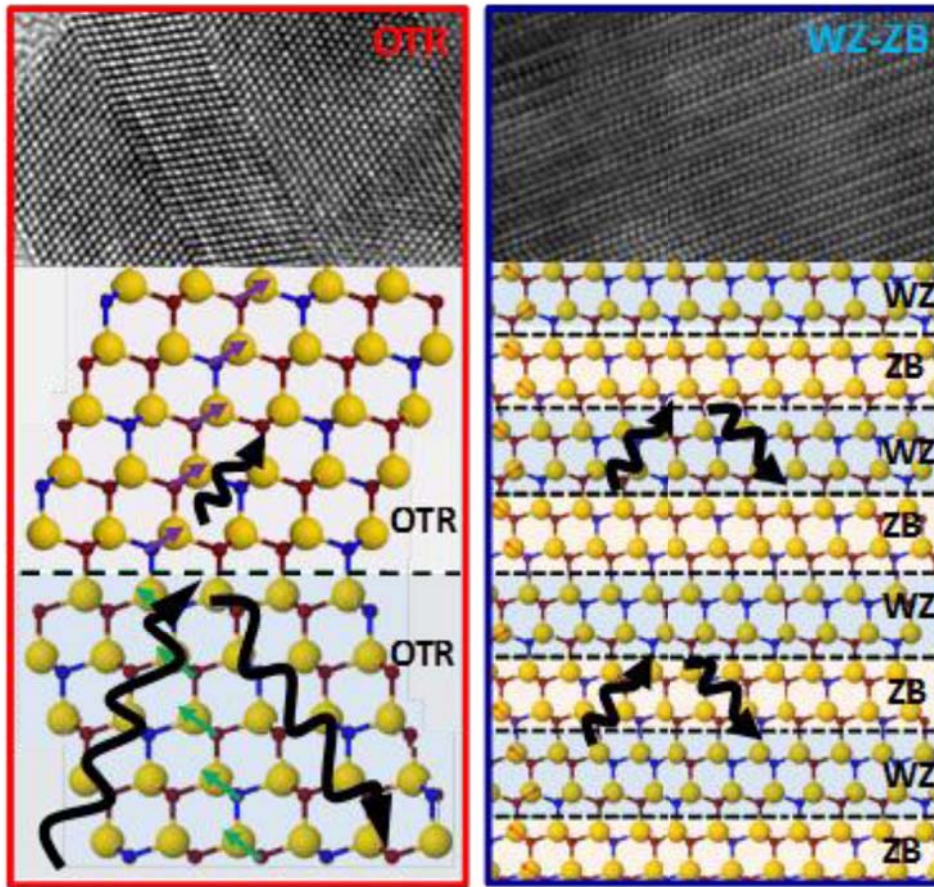


**Figure 9.** Schematic diagram illustrating the different phonon scattering mechanisms in the single-phase nanomaterial and in the multi-phase nanocomposite.

As a result of the higher phonon scattering and lower thermal conductivities in CGSe nanocomposites, a 2.5 fold increase on the thermoelectric figures of merit was obtained for the multi-phase WZ-ZB nanocrystalline material when compared with the single-phase OTR sample. At the same time, the thermoelectric figure of merit measured for the WZ-ZB nanocomposite

represented a 50 % increase over the values obtained for undoped bulk CGSe.<sup>21,30</sup> It should be finally pointed out that the nanoparticles composition has yet to be adjusted to optimize the material carrier concentration. Combining the multi-phase WZ-ZB structure with the proper doping significantly higher thermoelectric figures of merit are expected.

## 6.5 Conclusions

---

In summary, the first solution phase synthesis of CGSe nanoparticles was described. This synthetic procedure allowed obtaining ordered single-phase OTR or disordered polytypic WZ-ZB CGSe nanoparticles. These materials were used to show how bulk nanocrystalline materials obtained from multi-phase nanoparticles result in lower thermal conductivities and higher ZT values than those obtained from single-phase nanoparticles. This case exemplifies the potential of the crystallographic phase control at the nanoscale to enhance nanomaterials functionalities.

## 6.6 References

---

- (1) Ibáñez, M.; Cadavid, D.; Zamani, R.; García-Castelló, N.; Izquierdo-Roca, V.; Li, W.; Fairbrother, A.; Prades, J. D.; Shavel, A.; Arbiol, J.; Pérez-Rodríguez, A.; Morante, J. R.; Cabot, A., *Chem. Mater.* **2012**, 24, 562-570.
- (2) Ibáñez, M.; Zamani, R.; Li, W.; Shavel, A.; Arbiol, J.; Morante, J. R.; Cabot, A., *Cryst. Growth Des.* **2012**, 12, 1085-1090.
- (3) Ibáñez, M.; Zamani, R.; Lalonde, A.; Cadavid, D.; Li, W.; Shavel, A.; Arbiol, J.; Morante, J. R.; Gorsse, S.; Snyder, G. J.; Cabot, A., *J. Am. Chem. Soc.* **2012**, 134, 4060-4063.
- (4) Singh, A.; Geaney, H.; Laffir, F.; Ryan, K. M., *J. Am. Chem. Soc.* **2012**, 134, 2910-2913.
- (5) Norako, M. E.; Brutchey, R. L., *Chem. Mater.* **2010**, 22, 1613-1615.
- (6) Norako, M. E.; Franzman, M. A.; Brutchey, R. L., *Chem. Mater.* **2009**, 21, 4299-4304.
- (7) Norako, M. E.; Greaney, M. J.; Brutchey, R. L., *J. Am. Chem. Soc.* **2012**, 134, 23-26.
- (8) Marcano, G.; Nieves, L., *J. Appl. Phys.* **2000**, 87, 1284-1286.

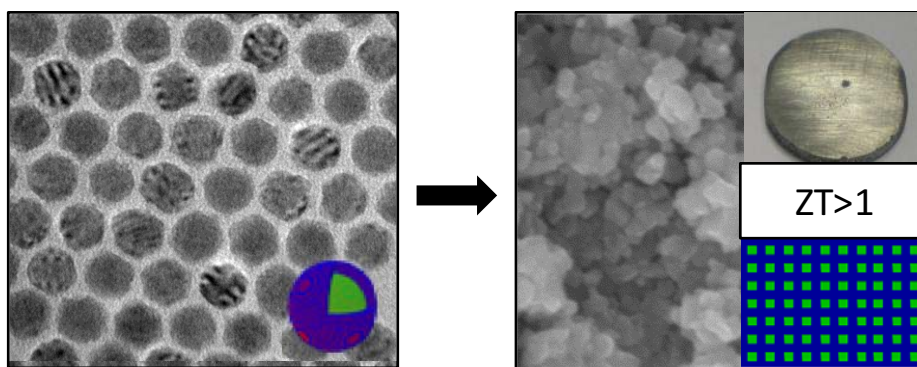
- (9) Echeverría, R.; Nieves, L.; Marcano, G., *Phys. Stat. Sol. (b)* **2000**, 220, 285-288.
- (10) Berger, L. I.; Prochukhan, V. D., *Ternary diamond-like Semiconductors*. Consultants Bureau: New York, 1969.
- (11) Marcano, G.; Márquez, R., *J. Phys. Chem. Solids* **2003**, 64, 1725-1727.
- (12) Palatnik, L. S.; Koshkin, V. M.; Galchinetskii, L. P.; Kolesnikov, V. I.; Komnik, Y. F., *Fiz. Tverd. Tela* **1962**, 4.
- (13) Rivet, J., *Ann. Chim.* **1965**, 10.
- (14) Hanh, H., *Naturwissenschaften* **1966**, 53.
- (15) Sharma, B. B.; Singh, H., *J. Solid State Chem.* **1974**, 11, 285-293.
- (16) Parthé, E.; Garin, J., *Monatsh. Chem.* **1971**, 102.
- (17) Marcano, G.; Rincón, C.; Marín, G.; Delgado, G. E.; Mora, A. J.; Herrera-Pérez, J. L.; Mendoza-Álvarez, J. G.; Rodríguez, P., *Solid State Commun.* **2008**, 146, 65-68.
- (18) Berger, L. I.; Balanevskaya, A. E., *Fiz. Tverd. Tela.* **1964**, 6.
- (19) Cho, J. Y.; Shi, X.; Salvador, J. R.; Yang, J.; Wang, H., *J. Appl. Phys.* **2010**, 108, 073713.
- (20) Endo, S.; Sudo, I.; Irie, T., *Jpn. J. Appl. Phys.* **1971**, 10.
- (21) Cho, J. Y.; Shi, X.; Salvador, J. R.; Meisner, G. P.; Yang, J.; Wang, H.; Wereszczak, A. A.; Zhou, X.; Uher, C., *Phys. Rev. B* **2011**, 84, 085207.
- (22) Zebarjadi, M.; Esfarjani, K.; Dresselhaus, M. S.; Ren, Z. F.; Chen, G., *Energ. Environ. Sci.* **2012**, 5, 5147-5162.
- (23) Vineis, C. J.; Shakouri, A.; Majumdar, A.; Kanatzidis, M. G., *Adv. Mater.* **2010**, 22, 3970-3980.
- (24) Szczech, J. R.; Higgins, J. M.; Jin, S., *J. Mater. Chem.* **2011**, 21, 4037-4055.
- (25) Scheele, M.; Oeschler, N.; Veremchuk, I.; Reinsberg, K. G.; Kreuziger, A. M.; Kornowski, A.; Broekaert, J.; Klinke, C.; Weller, H., *ACS Nano* **2010**, 4, 4283-4291.
- (26) Gorsse, S.; Bauer Pereira, P.; Decourt, R.; Sellier, E., *Chem. Mater.* **2010**, 22, 988-993.
- (27) Gorsse, S.; Bellanger, P.; Brechet, Y.; Sellier, E.; Umarji, A.; Ail, U.; Decourt, R., *Acta Mater.* **2011**, 59, 7425-7437.
- (28) Cahill, D. G.; Ford, W. K.; Goodson, K. E.; Mahan, G. D.; Majumdar, A.; Maris, H. J.; Merlin, R.; Phillpot, S. R., *J. Appl. Phys.* **2003**, 93, 793-818.

- (29) Scheele, M.; Oeschler, N.; Veremchuk, I.; Peters, S. O.; Littig, A.; Kornowski, A.; Klinke, C.; Weller, H., *ACS Nano* **2011**, *5*, 8541-8551.
- (30) Mehta, R. J.; Karthik, C.; Singh, B.; Teki, R.; Borca-Tasciuc, T.; Ramanath, G., *ACS Nano* **2010**, *4*, 5055-5060.
- (31) Bernal, S.; Botana, F. J.; Calvino, J. J.; López-Cartes, C.; Pérez-Omil, J. A.; Rodríguez-Izquierdo, J. M., *Ultramicroscopy* **1998**, *72*, 135-164.
- (32) Uccelli, E.; Arbiol, J.; Morante, J. R.; Fontcuberta i Morral, A., *ACS Nano* **2010**, *4*, 5985-5993.
- (33) Arbiol, J.; Cirera, A.; Peiro, F.; Cornet, A.; Morante, J. R.; Delgado, J. J.; Calvino, J. J., *Appl. Phys. Lett.* **2002**, *80*, 329-331.
- (34) Arbiol, J.; Fontcuberta i Morral, A.; Estradé, S.; Peiró, F.; Kalache, B.; Roca i Cabarrocas, P.; Morante, J. R., *J. Appl. Phys.* **2008**, *104*, 064312-7.
- (35) Conesa-Boj, S.; Zardo, I.; Estradé, S.; Wei, L.; Jean Alet, P.; Roca i Cabarrocas, P.; Morante, J. R.; Peiró, F.; Morral, A. F. i.; Arbiol, J., *Cryst. Growth Des.* **2010**, *10*, 1534-1543.
- (36) Algra, R. E.; Verheijen, M. A.; Borgstrom, M. T.; Feiner, L.-F.; Immink, G.; van Enkevort, W. J. P.; Vlieg, E.; Bakkers, E. P. A. M., *Nature* **2008**, *456*, 369-372.
- (37) Arbiol, J.; Estradé, S.; Prades, J. D.; Cirera, A.; Furtmayr, F.; Stark, C.; Laufer, A.; Stutzmann, M.; Eickhoff, M.; Gass, M. H.; Bleloch, A. L.; Peiró, F.; Morante, J. R., *Nanotechnology* **2009**, *20*, 145704.
- (38) Cell parameters of the new hexagonal wurtzite-like crystal cell: (S.G: P63/mc, N. w. a. b. n. c. n. a.
- (39) de la Mata, M.; Magen, C.; Gazquez, J.; Utama, M. I. B.; Heiss, M.; Lopatin, S.; Furtmayr, F.; Fernández-Rojas, C. J.; Peng, B.; Morante, J. R.; Rurali, R.; Eickhoff, M.; Fontcuberta i Morral, A.; Xiong, Q.; Arbiol, J., *Nano Lett.* **2012**, *12*, 2579-2586.
- (40) Murayama, M.; Nakayama, T., *Phys. Rev. B* **1994**, *49*.
- (41) Yeh, C.-Y.; Wei, S.-H.; Zunger, A., *Phys. Rev. B* **1994**, *50*, 2715-2718.



# Chapter 7

## Core-shell nanoparticles as building blocks for the bottom-up production of functional nanocomposites: PbTe-PbS thermoelectric properties



### 7.1 Abstract

---

The bottom-up assembly of nanocrystals provides access to a three-dimensional composition control at the nanoscale not attainable by any other technology. In particular, colloidal nanoheterostructures, with intrinsic multi-phase organization, are especially appealing building blocks for the bottom-up production of nanocomposites. In the present work, we use PbTe-PbS as the model material system and thermoelectricity as the paradigmatic application to investigate the potential of the bottom-up assembly of core-shell nanoparticles to produce functional nanocomposites. With this goal in mind, a rapid, high-yield and scalable colloidal synthetic route

to prepare grams of PbTe@PbS core-shell nanoparticles with unprecedented narrow size distributions and exceptional composition control is detailed. PbTe@PbS nanoparticles were used as building blocks for the bottom-up production of PbTe-PbS nanocomposites with tuned composition. In such PbTe-PbS nanocomposites, synergistic nanocrystal doping effects result in up to 10-fold higher electrical conductivities than in pure PbTe and PbS nanomaterials. At the same time, the acoustic impedance mismatch between PbTe and PbS phases and a partial phase alloying provide PbTe-PbS nanocomposites with strongly reduced thermal conductivities. As a result, record thermoelectric figures of merit  $ZT \sim 1.1$  were obtained from undoped PbTe and PbS phases. These high  $ZT$  values probe the potential of the proposed processes to produce efficient functional nanomaterials with programmable properties.

## 7.2 Introduction

---

To control material properties and to understand mechanism and phenomena at the atomic scale are two main ambitious goals of current research and development of advanced functional materials. One step above that, industrial innovation requires the development of cost-effective processes able to transform this control and understanding into optimized or novel products. In this context, the bottom-up assembly of nanoparticles (NP) offers a unique potential not only to perform fundamental studies with precisely controlled material parameters, but also to produce artificial materials with functional properties by design in a cost-effective manner. In this scenario, the outstanding degree of control over size, shape, phase and composition that colloidal synthesis methods have achieved makes colloidal NPs particularly suitable building blocks to prepare functional nanomaterials.<sup>1-6</sup> At the same time, the advantageous processability, low

synthesis temperatures, large production rates and high production yields of solution-processing methods offer unpaired opportunities to fabricate low-cost devices.

An especially attractive application for nanomaterials and nanotechnology researchers and developers is thermoelectricity. Thermoelectric energy conversion comprises two very appealing attributes: an enormous potential for economical and social impact, and the need for material control at the nanoscale to exploit this potential. Thermoelectric energy conversion devices have an ample range of current and potential applications; from precise temperature control in countless areas to energy harvesting for autonomous sensing devices and waste heat recovery from industrial and domestic processes. However, in spite of their broad range of applications and their unique advantages, thermoelectric devices are banned from multiple potential markets because of their relatively low efficiencies. Nanomaterials may have the key to open these markets to thermoelectricity. To date, nearly all high figure of merit thermoelectrics are nanostructured.<sup>7-9</sup> The confinement of the lattice dimensions to the nanometer scale allows improving thermoelectrics efficiency by promoting phonon scattering at crystal interfaces. At the same time, the selective scattering of the low energy charge carriers at crystal interfaces provides a path towards higher Seebeck coefficients.<sup>10-13</sup>

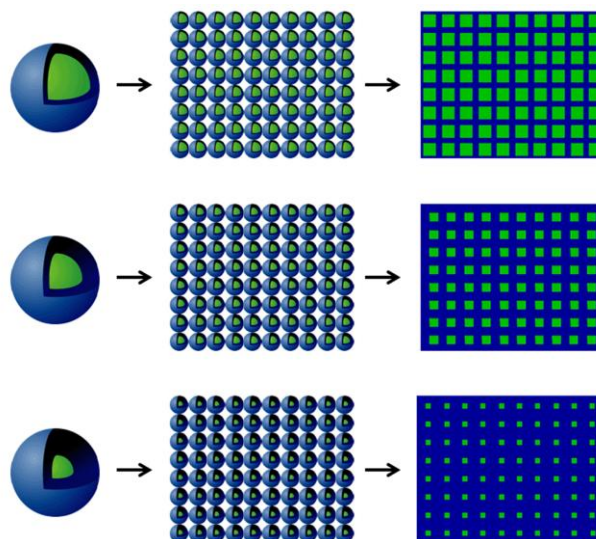
Record thermoelectric figures of merit, up to  $ZT=2.4$ , have been reported for superlattices produced by thin film technologies such as molecular beam epitaxy.<sup>14,15</sup> However, because of their very low growth rates and material yields, such vacuum-based bottom-up processing technologies are neither particularly low-cost nor versatile for large scale production. These processes do not allow the production of nanocomposites in bulk form either. Recently, cost-effective and scalable methods suitable to produce high efficiency thermoelectric nanocomposites have been developed. They are based on the spontaneous formation of nanoscale inclusions by



controlling the thermal history of solid solutions.<sup>16-18</sup> PbTe-PbS nanocomposites are one of the best performing thermoelectric materials obtained by this method.<sup>18-23</sup> However, while such an approach is excellent in particular systems, it is not versatile in composition and it lacks control over the size, composition and phase of the nanocrystalline domains.

The bottom-up assembly of nanocrystal building blocks is becoming a serious alternative to produce thermoelectric nanomaterials.<sup>24-33</sup> No other technology has the potential to produce nanomaterial with a comparable level of control over the size, shape, composition and phase of the crystal domains at the nanoscale.<sup>34-40</sup> In this scenario, nanoheterostructures are particularly interesting building blocks, as they allow producing highly homogeneous bulk nanocomposites in an easier manner. The availability of such multiphase building blocks provides unprecedented degrees of experimental freedom to create nanocomposites with programmed properties. The rational design and engineering of such bottom-up assembled nanocomposites will allow developing the next generation of energy conversion and storage devices having enhanced performances and lower costs.

We aim to demonstrate the potential of the bottom-up assembly of nanoheterostructures to produce bulk nanocomposites with enhanced functional properties. In particular, we target the use PbTe@PbS core-shell NPs to produce PbTe-PbS nanocomposites with high thermoelectric figures of merit. With this goal in mind, we present here a rapid, high-yield and scalable colloidal synthetic route to prepare PbTe@PbS NPs with unprecedented narrow size distributions and exceptional control over their composition. PbTe@PbS core-shell NPs obtained by this method were used to produce  $(\text{PbTe})_{1-x}(\text{PbS})_x$  nanocomposites with tuned composition (Scheme 1). The structural, chemical and thermoelectric properties of the obtained nanocomposites are presented and discussed.



**Scheme 1.** Steps for the production of nanocomposites from the bottom-up assembly of core-shell nanoparticles with different shell thicknesses: i) core-shell nanoparticle preparation; ii) nanoparticle assembly; and iii) annealing to produce a dense nanocomposite.

### 7.3 Experimental

---

*Chemicals.* Lead (II) Oxide (99.9%), oleic acid (OA, tech. 90%), 1-octadecene (ODE, 90%), tellurium shots (99.999%), Thioacetamide (ACS reagent  $\geq 99.0\%$ ), Hexamethyldisilathiane ( $\text{TMS}_2\text{S}$ , synthesis grade) and N,N-Dimethylformamide (DMF,  $\geq 99\%$ ) were purchased from Aldrich. Tri-*n*-octylphosphine (TOP, 97%) was purchased from Strem. Methanol, acetone, hexane, chloroform, and ethanol were of analytical grade and obtained from various sources. All chemicals were used as received without further purification. All syntheses were carried out using standard airless techniques: a vacuum/dry argon gas Schlenk line was used for the synthesis and an argon glove-box for storing and handling air and moisture-sensitive chemicals.

*Preparation of PbS NPs.* A modified approach of that used by Hines et al.<sup>41</sup> was used for the preparation of PbS nanocrystals. Lead (II) oxide (2.94 g, 12 mM) and oleic acid (90 ml, 48 mM)

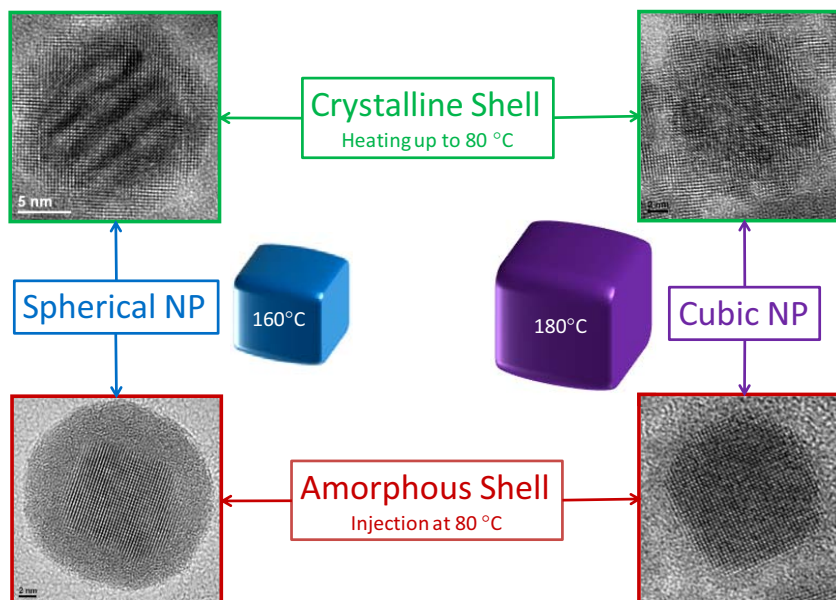
were dissolved in 90 ml ODE. This mixture was degassed at RT and 100 °C for 0.5 h each to form lead oleate complex. Afterwards, the clear transparent solution was flashed with argon and heated up to the reaction temperature (135°C). At this temperature, 1,26 mL of TMS<sub>2</sub>S dissolved in 40m L of ODE was rapidly injected under argon gas flow. For the crystal growth the reaction mixture was kept for 3 more min and then quickly cooled down to room temperature using a water bath.

*Preparation of PbTe NPs.* A modified approach of that used by Murphy et al.<sup>42</sup> was used for the preparation of PbTe nanocrystals. In a typical procedure, PbO (2.94 g, 12 mM) and OA (13.32 g, 4.75 mM) were dissolved in 90 ml ODE. This mixture was degassed at RT and 100 °C for 0.5 h each to form a lead oleate complex. The solution was flushed with Ar and temperature was raised up to 190 °C. Afterwards 2 ml of 1 M TOP:Te were rapidly injected. The reaction mixture was maintained between 160 °C – 180 °C for 3 minutes and then quickly cooled down to room temperature using a water bath. At this point an aliquot was extracted to analyze the PbTe morphology.

*Preparation of PbTe@PbS NPs with a crystalline PbS shell.* Once the crude solution was at room temperature, 114 mg of thioacetamide dissolved in 6 mL of DMF were added into the flask. The NPs solution containing the sulfur precursor was heated up 80 °C at 1.7 °C/min and maintained at this temperature for 30 min. After cooling to room temperature, the NPs were precipitated by centrifugation.

*Preparation of PbTe@PbS NPs with an amorphous PbS shell.* In this case, the cooling procedure of the PbTe NPs crude solution was stop at 80 °C, then the sulfur precursor (114 mg of Thioacetamide dissolved in 6 mL of DMF) was injected. The NPs solution containing the sulfur

precursor was maintain at 80 °C for an additional 5 minutes. After cooling to room temperature, the NPs were precipitated by centrifugation.



**Scheme 2.** Scheme summarizing the synthetic results in terms of crystallinity and shape.

*Preparation of PbTe-PbS nanocomposites.* Washed NPs were dried out under Ar atmosphere. Afterward, the nanocrystals were heated to 500 °C for 2 hours under an Ar flow inside a tube furnace. The resulting material was pressed into pellets (10 mm diameter; 1 mm thickness) under a load of 2 tons at room temperature.

*Structural Characterization.* The samples were analyzed by means of HRTEM in a Jeol 2010F field emission gun microscope operated at 200 kV. Nanoparticle core-shell atomic models were created by using the Rhodius software,<sup>43</sup> widely used to model NW complex nanostructures.<sup>44-46</sup>

*Thermoelectric Characterization.* The samples used to measure the electrical conductivity and the Seebeck coefficient were rectangular parallelepipeds of about 10x13x1 mm<sup>3</sup>. The Seebeck coefficient was measured using a static DC method. Electrical resistivity data were obtained by

standard four-probe method. Both Seebeck coefficient and electrical resistivity were measured simultaneously in a LSR-3 LINSEIS system in the range between room temperature up to 700 K, under helium atmosphere. The temperature dependence of the heat capacity was measured by a relaxation method using a Quantum Design physical properties measurement system (PPMS). Thermal conductivity measurements were obtained from flash diffusivity measurements in a Netzsch LFA-457 Microflash.

*Porosity correction* An estimation of the electrical and thermal conductivity that would be measured from a 100 % dense sample can be obtained using a Maxwell-Eucken expression:<sup>28, 47, 48</sup>

$$X_{100} = X_P \frac{1 + \beta P}{1 - P}$$

Where  $X_{100}$  is the electrical or thermal conductivity in the 100 % dense medium,  $P$  is the porosity degree in the range between 0 and 1, and  $\beta$  is an empirical parameter related to the pore geometry, which we fixed to 2.<sup>48</sup> Notice that the thermoelectric figure of merit  $ZT$  is not modified by this correction because the porosity effect on the electrical and thermal conductivities compensate each other.

## 7.4 Results and Discussion

---

### *PbTe@PbS nanoparticles*

Colloidal synthetic strategies to produce nanoheterostructures are generally highly elaborated.<sup>34, 38, 49-65</sup> To date, most colloidal synthetic routes to produce core-shell nanoparticles are based on two-pot processes not well suited for production scale up. Moreover, most previous efforts to prepare core-shell NPs were focused on the production of shells just thick enough to passivate the core surface and improve photoluminescence or provide biocompatibility.

We aimed at the development of scalable synthetic routes suitable for the production of nanoheterostructures and bulk nanocomposites in an industrially relevant manner. For this purpose, we designed a one-pot two-step procedure to prepare core-shell NPs at multi-gram scale. The one-pot procedure facilitates up-scaling, maximizes production yield, and minimizes the processing time and the number of purification steps. An additional advantage of one-pot processes is that they allow minimizing the core oxidation.

Our one-pot two-step procedure to prepare PbTe@PbS NPs is as follows. In a first step, PbTe NPs were prepared by reacting Pb oleate with TOP:Te in octadecene. Figure 1 shows representative transmission electron microscopy (TEM) micrographs of the cubic PbTe NPs produced in two different 1 g batches. In spite of the relatively high production scale, particle size distributions with exceptional low dispersions, < 10 %, were systematically obtained (Figure 1 insets). In a second step, without purifying or exposing the PbTe NPs to air, the sulfur precursor was added to the crude solution containing the PbTe NPs at room temperature. Then, the temperature was gradually increased to 80 °C at 1.7 °C/min. We found that heating rates, reaction temperatures and sulfur source reactivity determined the mechanism of formation of the PbS shell. Large precursor reactivities or high reaction temperatures promoted the Te replacement by S within the PbTe core or the nucleation of independent PbS crystals. Reaction conditions had to be carefully adjusted to promote the PbS shell growth on the PbTe core surface. A solution of thioacetamide in dimethylformamide was proven to be the most effective S source for PbS shell growth. Figure 2A shows a representative TEM micrograph of the PbTe@PbS core-shell NPs produced. The detailed procedure systematically yielded core-shell NPs with narrow size distributions, < 10 % (Figure 2A inset). It must be pointed out that all the NPs characterized and shown in the present work were obtained from relatively large scale synthesis, producing up to 1-

1.5 g of material in a single pot. More details on the materials synthesis can be found in the experimental section.

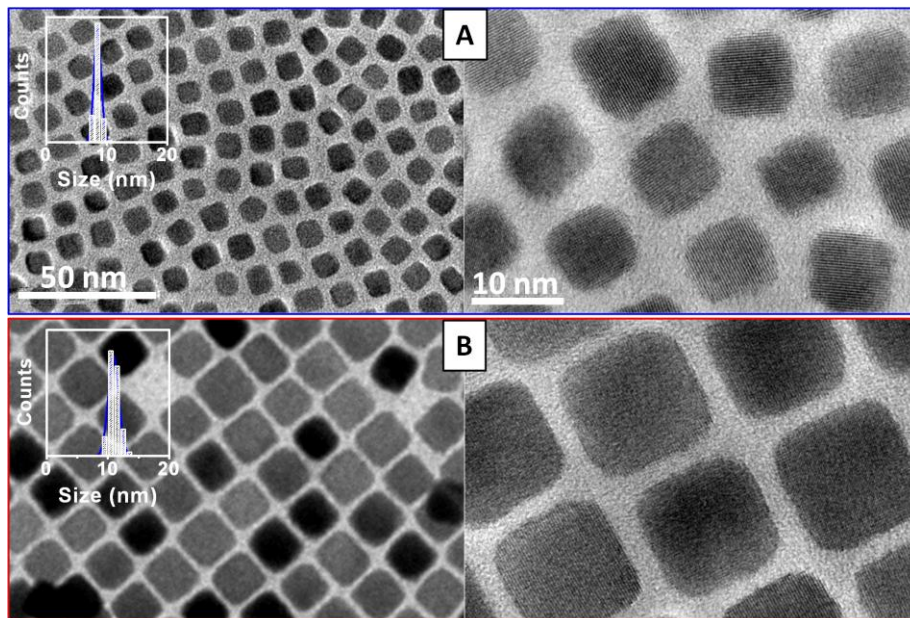


**Figure 1.** TEM micrographs of two batches of PbTe nanoparticles having average sizes of  $8.5 \pm 0.7$  nm (A) and  $11 \pm 1$  nm (B). Insets display the histograms with the particle size distributions

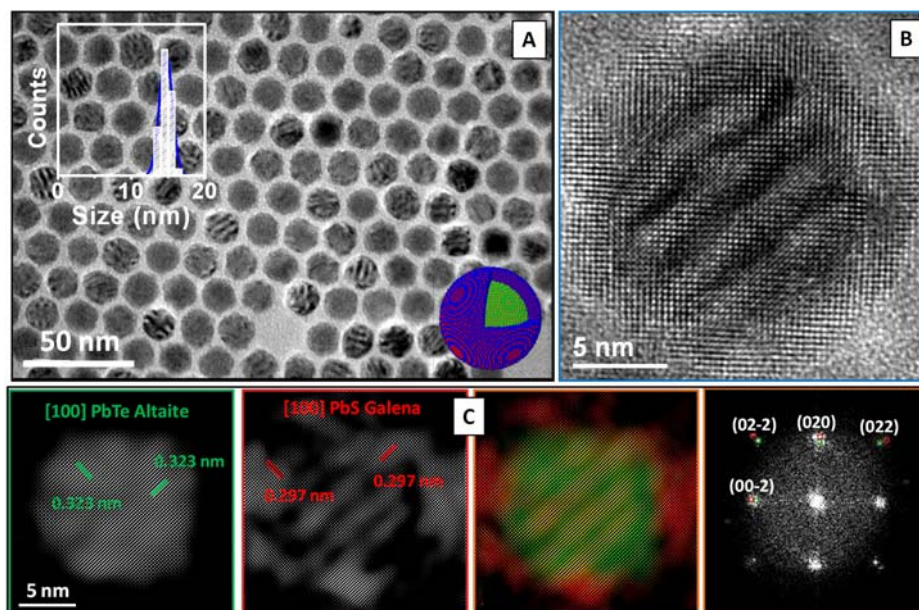


**Figure 2.** A) TEM micrograph of  $(\text{PbTe})_{0.28} @ (\text{PbS})_{0.72}$  core-shell nanoparticles with crystalline PbS shells. Inset displays the histogram of the particle size distribution. B) HRTEM micrograph of a

(PbTe)<sub>0.28</sub>@(PbS)<sub>0.72</sub> core-shell nanoparticle. C) Power spectrum analysis of the same (PbTe)<sub>0.28</sub>@(PbS)<sub>0.72</sub> nanoparticle and PbTe and PbS crystallographic color maps.

High-resolution TEM (HRTEM) micrographs revealed cores and shells produced by this method to be single crystalline (Figure 2B). Double points marked by red and green circles in the power spectrum analysis (FFT) resulted from the shell and core lattices, respectively (Figure 2C). Core and shell had the same crystal structure (S.G.: Fm3m) with identical positions of the atoms in the unit cell but different cell parameters. The lattices spacing shown in Figure 2C correspond to the (200) planes in altaite PbTe (0.323 nm, JCDP: 00-038-1435) and galena PbS (0.297 nm, JCDP: 00-005-0592). The coexistence of both crystal structures was confirmed by x-ray diffraction (XRD). Figure 3 displays the XRD patterns of the (PbTe)<sub>1-x</sub>@(PbS)<sub>x</sub> (x=0, 0.32, 0.40, 0.49, 0.72, 1) NPs with crystalline PbS shells produced. No evidences of alloying, oxidation or the presence of a PbTe<sub>y</sub>S<sub>1-y</sub> interface layer could be obtained by either HRTEM or XRD.

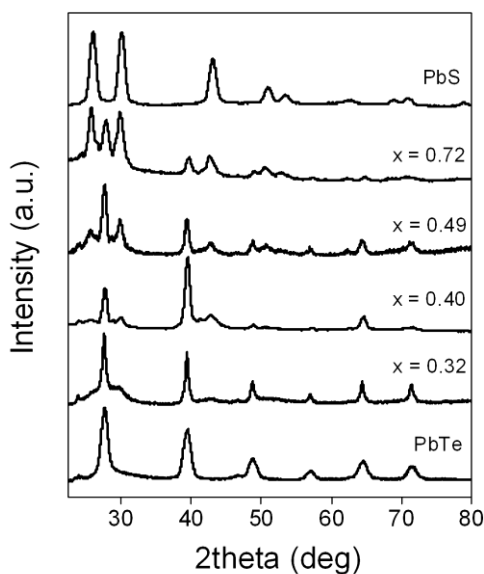


**Figure 3.** XRD patterns of (PbTe)<sub>1-x</sub>@(PbS)<sub>x</sub> core-shell nanoparticles with x=0, 0.32, 0.40, 0.49, 0.72 and 1.



TEM micrographs of the core-shell NPs showed variable contrasts within each NP. A range of different contrast patterns was observed. We attributed these contrast variations to different Moirée patterns produced depending on the NP orientation with respect to the electron beam. Moirée patterns allowed us to characterize in more detail the crystal interface between the core and shell lattices in PbTe@PbS NPs. Moirée patterns depend on the mismatch between cell parameters, the relative orientation between the two superimposed lattices and between the lattices and the electron beam. Figure 4 displays experimental and simulated HRTEM images of NPs with different Moirée patterns. Circular-like patterns (Figure 4A) are characteristic of Moirée fringes occurring along both x and y axes when the NPs are perfectly oriented along the [100] zone axis. This is quite improbable due to the random distribution of the NPs when lying on the carbon grid and thus few NPs showed such circular patterns. Most NPs were characterized by stripe-like Moirée fringes (Figure 4 B, C, D). Stripe-like patterns are generally associated to the superposition of two lattices with the same cell parameter in one direction and a slight difference in another. However, stripe-like patterns were explained here by the slight rotation of the NP from the exact zone axis. Figure 4B shows the experimental and simulated core-shell NP rotated 2° along the [010] axis from [100] view direction, and Figure 4C the same but with 5° rotations. Figure 4D shows the result of rotating 2° along [010] and 2° along [001]. From a thoroughly analysis of the Moirée fringes of a large number of PbTe@PbS NPs, we concluded that all the cores and shell lattices had the same epitaxial relationship:  $(010)[100]_{\text{PbTe}}// (010)[100]_{\text{PbS}}$ .

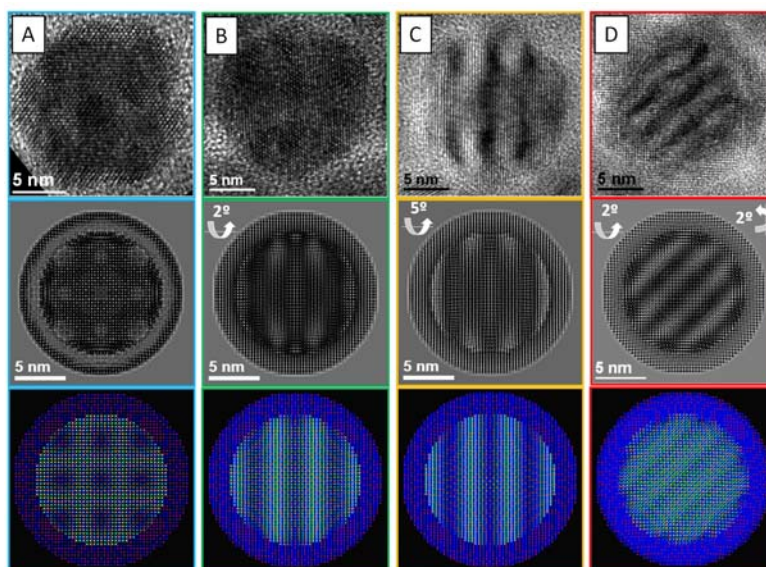


**Figure 4.** Experimental images, simulated HRTEM micrographs, and atomic models of various PbTe@PbS core-shell nanoparticles showing varied Moiré fringes associated to different orientations with respect to the [100] zone axis.

The shell crystallinity could be controlled by varying the reaction kinetics during shell formation. PbTe@PbS core-shell NPs with amorphous PbS shells were produced by boosting PbS nucleation at multiple PbTe surface sites when injecting the S precursor at relatively high temperatures: 80 °C (Figure 5, Supporting information, SI, Figure S1). Additionally, the shape of the PbTe@PbS NPs was controlled by adjusting the degree of faceting of the PbTe core and the thickness of the shell. Small PbTe cores were quasi cubic with slightly rounded corners. The growth of thick PbS shells on the surface of such rounded PbTe nanocrystals resulted in spherical core-shell NPs (Figures 3, 5). In contrast, the growth of relatively thin PbS shells on the surface of larger and highly faceted PbTe cores resulted in quasi-cubic PbTe@PbS NPs (Figure 6). Figure S2 displays a scheme summarizing the synthetic results in terms of crystallinity and shape.

Most important, the developed method allowed us to produce core-shell NPs with large shell thickness (> 5 nm) and an independent control over the NP size and composition. Having in mind

their posterior thermoelectric characterization, we produced a set of  $(\text{PbTe})_{1-x}@\text{(PbS)}_x$  NPs with identical size but different PbTe/PbS ratios. To accomplish this goal, we synthesized PbTe cores with different diameters by varying the PbTe growth temperature between 160 °C and 190 °C but maintaining the same amounts of Pb oleate and surfactants from batch to batch. Thus, large/small PbTe cores obtained at high/low temperatures involved small/large amounts of Pb oleate left in solution to react with S in the second step. In this way, we limited the shell growth by the concentration of Pb monomer, obtaining core-shell NPs with the same diameter for all compositions. Figure 7 displays representative TEM micrograph of the set of  $(\text{PbTe})_{1-x}@\text{(PbS)}_x$  NPs produced.

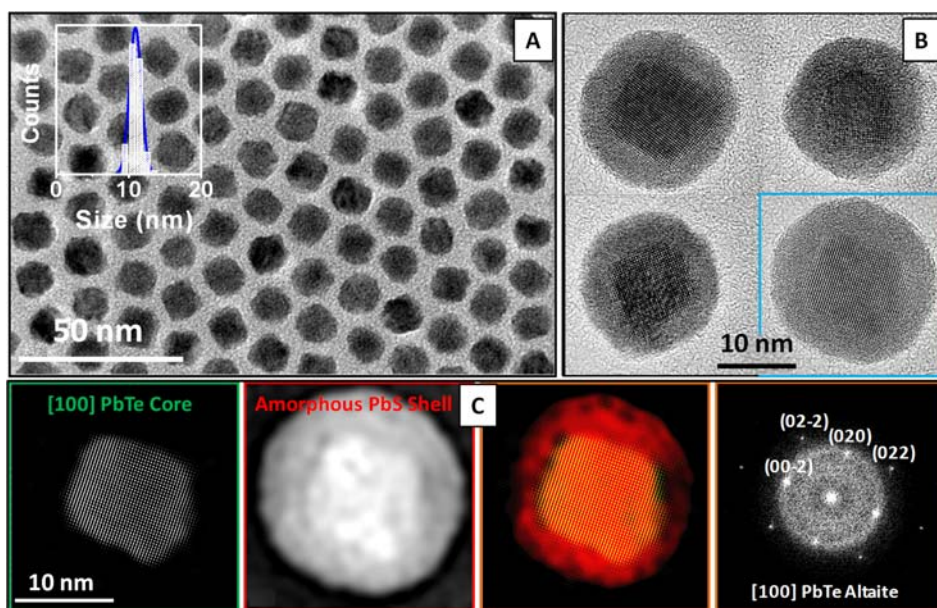


**Figure 5.** A) TEM micrograph of  $(\text{PbTe})_{0.25}@\text{(PbS)}_{0.75}$  core-shell nanoparticles having amorphous PbS shells. Inset displays the histogram of the particle size distribution. B) HRTEM micrograph of few  $(\text{PbTe})_{0.25}@\text{(PbS)}_{0.75}$  core-shell nanoparticles. C) Power spectrum analysis of a  $(\text{PbTe})_{0.25}@\text{(PbS)}_{0.75}$  nanoparticle and PbTe and PbS crystallographic color maps.

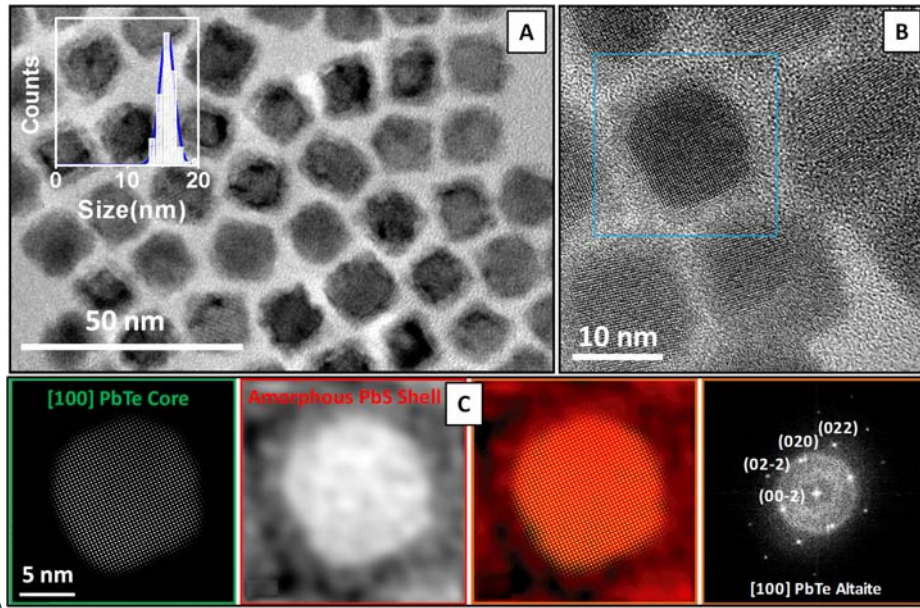


**Figure 6.** A) TEM micrograph of  $(\text{PbTe})_{0.6} @ (\text{PbS})_{0.4}$  core-shell nanoparticles with quasi-cubic shapes. Inset displays the histogram of the particle size distribution. B) HRTEM micrograph of few  $(\text{PbTe})_{0.6} @ (\text{PbS})_{0.4}$  core-shell nanoparticles. C) Power spectrum analysis of a  $(\text{PbTe})_{0.60} @ (\text{PbS})_{0.40}$  nanoparticle and PbTe and PbS crystallographic color maps.

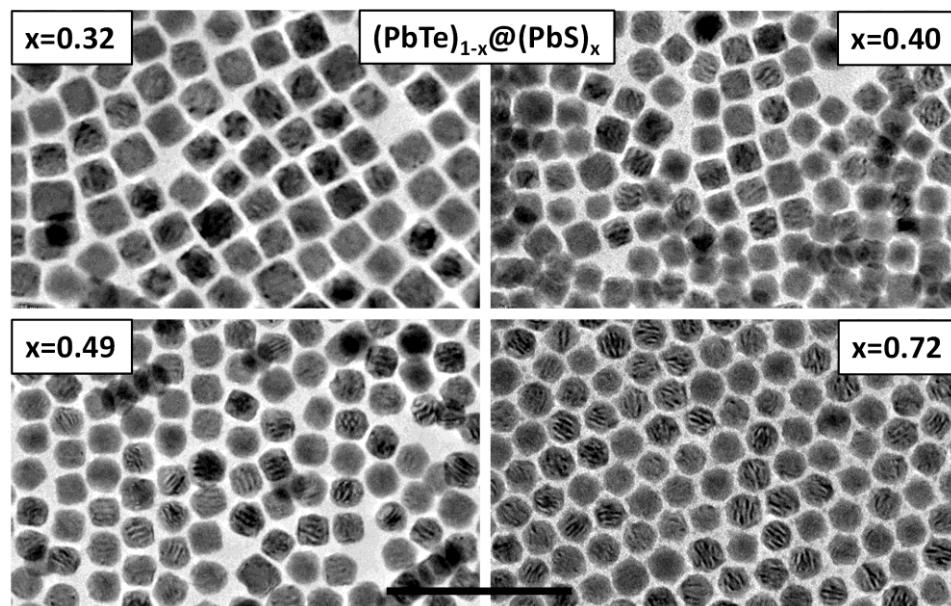


**Figure 7.** TEM micrographs of the  $(\text{PbTe})_{1-x} @ (\text{PbS})_x$  nanoparticles used for thermoelectric characterization. Scale bar corresponds to 100 nm.

### *PbTe-PbS nanocomposite formation*

The set of PbTe@PbS core-shell NPs with similar overall size but different PbTe/PbS ratios displayed in Figure 7 was used to produce a set of  $(\text{PbTe})_{1-x}(\text{PbS})_x$  nanocomposites with  $x = 0.32, 0.40, 0.49$  and  $0.72$ . As references, we also produced pure PbTe and PbS nanomaterials from the processing of PbTe ( $11.2 \pm 1.0$  nm) and PbS ( $6.1 \pm 0.4$  nm) NPs (Figures S3 and S4). Once prepared,  $(\text{PbTe})_{1-x} @ (\text{PbS})_x$  ( $x = 0, 0.32, 0.40, 0.49, 0.72, 1$ ) NPs were purified by multiple precipitation and redispersion steps until no re-dispersion was possible. At this point, most of the organic ligands used to control the size and shape of the NPs during synthesis had been removed. Purified  $(\text{PbTe})_{1-x} @ (\text{PbS})_x$  NPs were dried under vacuum to obtain a dark-gray nanopowder. This nanopowder was annealed at  $500$  °C for 1 h under a dry argon flow to completely remove residual organics. Elemental analysis showed the presence of approximated 1 % of carbon in the annealed materials. The annealed nanopowders were pressed under 2 tons of force at room temperature to produce dense  $(\text{PbTe})_{1-x}(\text{PbS})_x$  pellets. The obtained nanocrystalline pellets were silver-metallic in appearance and had relative densities of 80 %. Table 1 summarizes the basic characteristics of the  $(\text{PbTe})_{1-x}(\text{PbS})_x$  nanocomposites produced.

The characterization of the annealing effect on the nanocomposite structure was both challenging but also necessary to understand the thermoelectric performance of the obtained materials. As proven by SEM-EDX and HRTEM (Figure 8), the composition of the final nanomaterials was highly homogeneous at the micrometer scale but contained a uniform distribution of compositional inhomogeneities at the nanometer scale. HRTEM analysis of the nanocomposites showed them to contain PbS and PbTe crystal nanodomains with sizes in the range 10-20 nm (Figure 8).



**Table 1.** Reaction temperature ( $T_R$ ), PbTe average core size (d), PbTe@PbS average nanoparticle size (D), chalcogen molar content (Te, S), sulfur content in the Te-rich phase (y) and Te content in the S-rich phase (z).

$(\text{PbTe})_{1-x}(\text{PbS})_x$ x	$T_R$ (°C)	PbTe d (nm)	PbTe@PbS D (nm)	Chalcogen content (%)		$\text{PbTe}_y\text{S}_{1-y}$ y	$\text{PbS}_z\text{Te}_{1-z}$ z
				Te	S	y	z
0	190	$11.2 \pm 1.0$	$11.2 \pm 1.0$	100	0	1	0
0.32	190	$11.1 \pm 1.0$	$14.4 \pm 2.1$	68.2	31.8	0.96	0.98
0.40	180	$10.2 \pm 0.8$	$14.2 \pm 1.9$	60.2	39.8	0.93	0.99
0.49	170	$9.4 \pm 0.9$	$14.3 \pm 2.0$	51.4	48.6	0.92	0.99
0.72	160	$8.5 \pm 0.7$	$14.1 \pm 2.0$	27.8	72.2	0.90	1
1	135	0	$6.1 \pm 0.4$	0	100	0	1

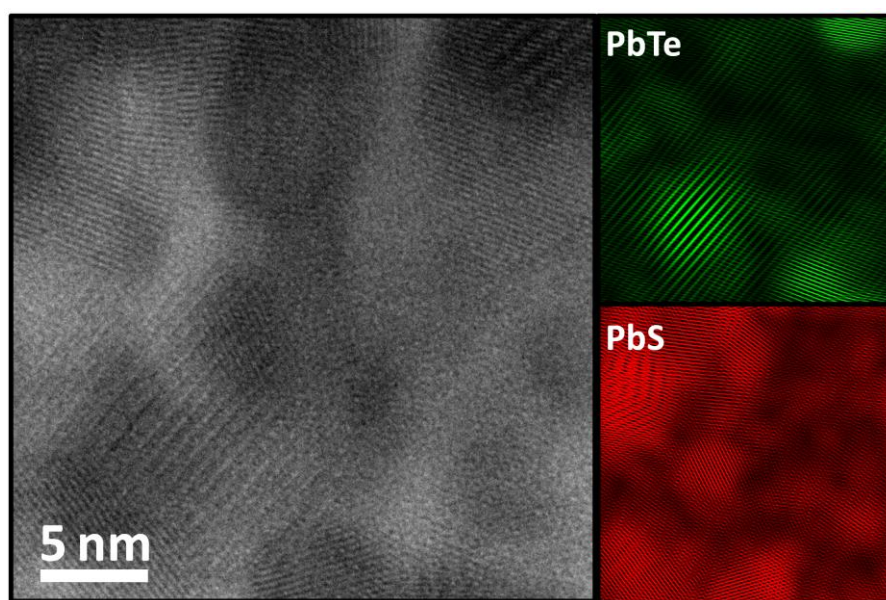


**Figure 8.** HRTEM micrograph and color crystallographic maps of  $(\text{PbTe})_{0.28}(\text{PbS})_{0.72}$  nanocomposite: PbTe = green; PbS = red.

Figure 9 displays the XRD patterns of the set of  $(\text{PbTe})_{1-x}(\text{PbS})_x$  nanomaterials studied. After the annealing treatment, reflections from PbTe and PbS phases still dominated the XRD patterns. However, two new weak crystallographic reflections were observed. The new XRD peaks were identified as the (101) and (110) plane reflections of PbO. Surprisingly, the presence of PbO was observed in all samples except pure PbTe. A significant amount of oxygen is usually observed at the surface of PbTe NPs when exposed to air even during very short periods of time.<sup>27, 66, 67</sup> Therefore, we tentatively associated the absence of the PbO phase reflections from the pure PbTe nanomaterial to the amorphous nature of the thin oxide layer potentially formed. The reason for the distinct crystallinity of the formed oxide over PbS and PbTe surfaces can be found in the different surface termination of the NPs prepared. On the one hand, the surface of cubic or quasi-cubic PbTe nanocrystals was saturated with Te.<sup>68</sup> Oxidation of such Te-rich surfaces results in the formation of  $\text{PbTeO}_3$ .<sup>69, 70</sup> Since no evidence for such a crystal structure was obtained by XRD or HRTEM, we speculate that such oxide layer was amorphous or very thin. On the other hand, the surface of spherical PbS NPs as those obtained here is Pb-rich due to the preferential bonding of oleic acid to Pb sites.<sup>71, 72</sup> The oxidation of the Pb-rich surface of PbS NPs most probably proceeded via the direct formation of PbO, which crystallized during the thermal treatment.

While nanocomposites produced here conserved both PbTe and PbS diffraction patterns after the thermal treatment, we observed a slight shift of the PbTe and PbS reflections towards higher and lower angles, respectively. These shifts were associated to a partial alloying during annealing. The refined lattice parameters calculated from the XRD data are plotted as a function of the PbS content in Figure 10. Smaller lattice parameters were obtained when increasing the PbS concentration in  $(\text{PbTe})_{1-x}(\text{PbS})_x$  nanocomposites. Figure 10 displays the lattice parameter trend considering the Vegard's law for a complete solid solution. Following the Vegard's Law,

the alloying ratio for both, PbTe-rich and PbS-rich phases was calculated (Table 1). This alloying was limited to a 10 % in the Te-rich phase and to a 2 % in the S rich phase. This is consistent with the very limited miscibility of the PbTe-PbS system.<sup>23, 73-75</sup>

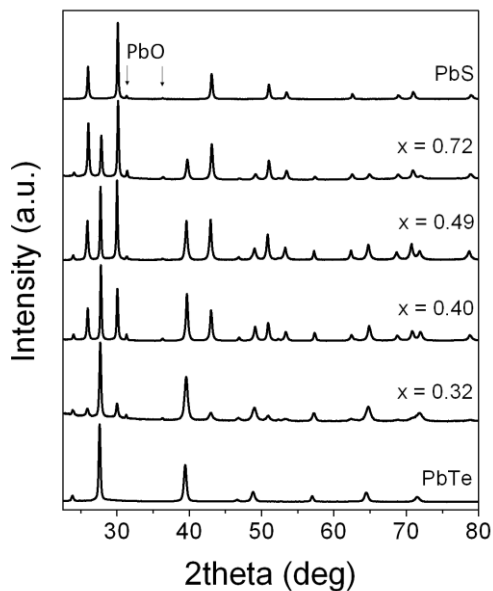


**Figure 9.** XRD patterns of the  $(\text{PbTe})_{1-x}(\text{PbS})_x$  ( $x=0, 0.32, 0.40, 0.49, 0.72, 1$ ) nanomaterials.

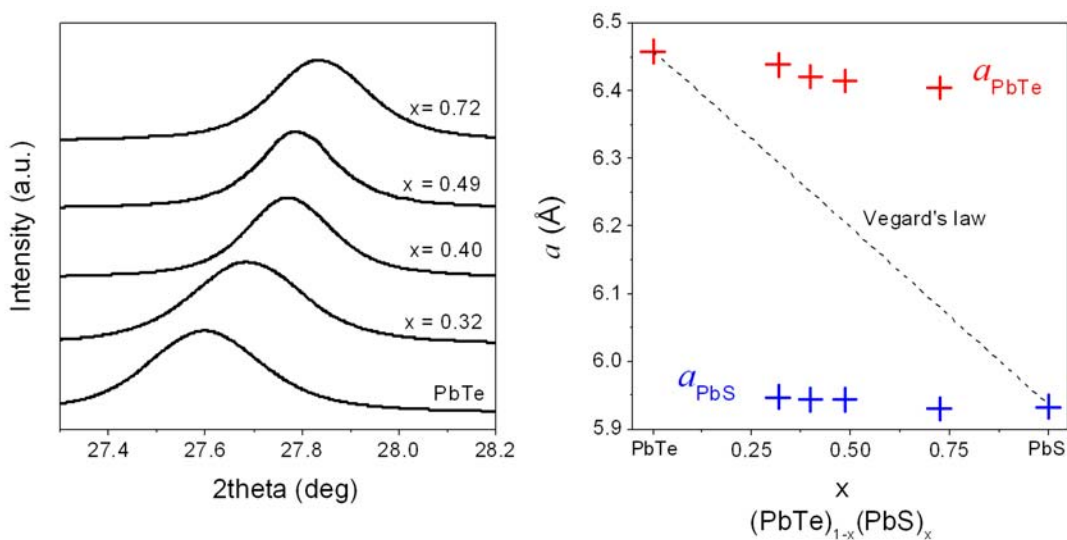


**Figure 10.** XRD patterns and calculated lattice parameters for PbTe- and PbS-rich phases as a function of the  $(\text{PbTe})_{1-x}(\text{PbS})_x$  nanomaterial composition.



### Thermoelectric properties

We characterized the electrical conductivity ( $\sigma$ ), Seebeck coefficient (S) and thermal conductivity ( $\kappa$ ) of the  $(\text{PbTe})_{1-x}(\text{PbS})_x$  ( $x=0, 0.32, 0.40, 0.49, 0.72, 1$ ) nanomaterials in the temperature range from 320 to 710 K. Table 2 summarizes the thermoelectric properties of  $(\text{PbTe})_{1-x}(\text{PbS})_x$  nanomaterials at 320 K and 710 K.

**Table 2.** Activation energy for electrical transport in the low temperature range ( $E_a$ ), electrical conductivity ( $\sigma$ ), thermopower (S), porosity-corrected thermal conductivity ( $\kappa^*$ ) and thermoelectric figure of merit ( $ZT=T\sigma S^2/\kappa$ ) of  $(\text{PbTe})_{1-x}(\text{PbS})_x$  nanomaterials.

$(\text{PbTe})_{1-x}(\text{PbS})_x$	$E_a$ (meV)	$\sigma$ ( $\text{S m}^{-1}$ )		S ( $\mu\text{V K}^{-1}$ )		$\kappa^*$ ( $\text{W m}^{-1} \text{K}^{-1}$ )		ZT	
		320 K	710 K	320 K	710 K	320 K	710 K	320 K	710 K
0	83	55	2370	362	-270	2.2	1.20	$10^{-3}$	0.18
0.32	78	51	5510	184	-247	1.8	1.15	$10^{-4}$	0.37
0.40	81	9.0	4380	1	-259	1.5	0.91	$10^{-4}$	0.34
0.49	75	76	7730	-89	-232	0.85	0.61	$10^{-4}$	0.86
0.72	71	12	12530	-89	-185	0.69	0.53	$10^{-4}$	1.03
1	66	260	1180	-279	-306	1.2	0.77	$10^{-2}$	0.18

*Electrical conductivity and Seebeck coefficient.* Figure 11 displays the electrical conductivity and Seebeck coefficient of  $(\text{PbTe})_{1-x}(\text{PbS})_x$  nanomaterials. The evolution of the electrical conductivity with temperature clearly indicated that charge carrier scattering at grain boundaries and crystal interfaces played a dominant role.<sup>13, 27</sup> Electrical conductivities activated through a

surface energy barrier ( $E_a$ ) can be expressed as follows:<sup>76</sup>  $\sigma \propto T^{-1/2} \exp\left(-\frac{E_a}{kT}\right)$ . The results from the fitting of this equation to our experimental data in the low temperature range ( $T < 400$  K) are displayed in Table 2. The highest activation energy  $E_a = 83$  meV was obtained for pure PbTe. This value is in the range of activation energies previously measured for this material ( $60 \text{ meV} < E_a < 140 \text{ meV}$ ).<sup>27,13</sup> The energy barrier decreased with the PbS content within the  $(\text{PbTe})_{1-x}(\text{PbS})_x$  nanocomposites (Figure 12). Pure PbS nanomaterials displayed the lowest energy barriers  $E_a = 66$  meV.

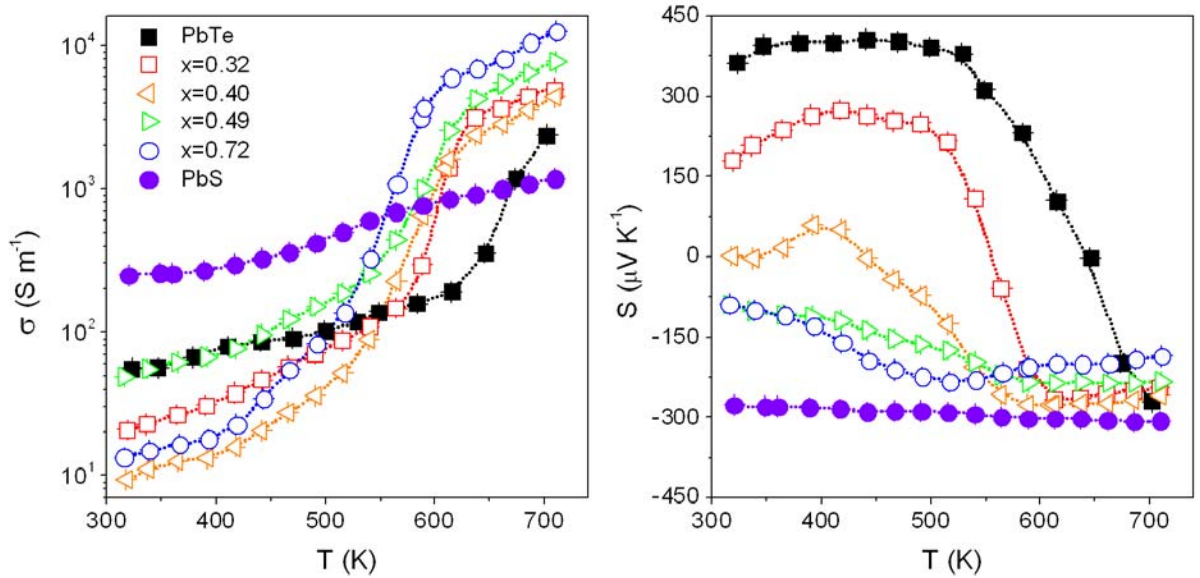


**Figure 11.** Electrical conductivity ( $\sigma$ ) and Seebeck coefficient ( $S$ ) for  $(\text{PbTe})_{1-x}(\text{PbS})_x$  nanomaterials.

In the low temperature regime, majority carriers in PbTe and PbS had opposite signs. While PbTe displayed p-type conductivity, PbS had an n-type character. When both phases were intermixed within  $(\text{PbTe})_{1-x}(\text{PbS})_x$  nanocomposites, holes from PbTe and electrons from PbS compensated each other resulting in lower electrical conductivities and lower absolute Seebeck coefficients than those of pure PbTe and PbS nanomaterials. In this low temperature range,

charge transport was dominated by holes in  $(\text{PbTe})_{1-x}(\text{PbS})_x$  nanocomposites with  $x \leq 0.4$  and by electrons in  $(\text{PbTe})_{1-x}(\text{PbS})_x$  nanocomposites with higher PbS contents ( $x > 0.4$ ).

In nanomaterials with energy activated charge carrier mobilities, the increase of the average carrier kinetic energy with temperature eventually enables charge carriers to overcome the potential barrier. At this temperature, electrical conductivity is largely enhanced. In pure PbTe the boost of electrical conductivity was accompanied by an inversion of the majority carriers charge sign (Figure 11). At around 520 K a strong decrease of the Seebeck coefficient, from positive to negative values, starts to take place in PbTe. This is associated to an increasingly higher density of electrons participating in the charge transport within this material. At around 650 K the electron contribution to the Seebeck coefficient compensated the hole contribution. Negative Seebeck coefficients were obtained at higher temperatures. In  $(\text{PbTe})_{1-x}(\text{PbS})_x$  nanocomposites, charge carrier compensation occurred at lower temperatures. For  $(\text{PbTe})_{0.68}(\text{PbS})_{0.32}$ , the sign inversion in the Seebeck coefficient took place at around 550 K and for  $(\text{PbTe})_{0.6}(\text{PbS})_{0.4}$  at just 450 K. In  $(\text{PbTe})_{1-x}(\text{PbS})_x$  with  $x > 0.4$  a step change of the Seebeck coefficient towards more negative values was also obtained at this temperature range. This sign inversion or step change in the Seebeck coefficient was accompanied by an increase in electrical conductivity in the temperature range from 450 K to 650 K for all nanocomposites.

At relatively high temperature ( $T > 650$  K), both PbTe and PbS displayed n-type conductivity. In this regime a synergistic contribution of the majority charge carriers of both phases was observed and much higher electrical conductivities were obtained for nanocomposites than for pure PbTe and PbS nanomaterials. In the high temperature regime measured, the electrical conductivity of  $(\text{PbTe})_{1-x}(\text{PbS})_x$  nanocomposites increased with the PbS content. The highest electrical conductivities were obtained for  $(\text{PbTe})_{0.28}(\text{PbS})_{0.72}$ . For this material electrical

conductivities up to 10-fold larger than PbS were measured. Without intentional doping of any of the two phases,  $(\text{PbTe})_{0.28}(\text{PbS})_{0.72}$  reached electrical conductivities up to  $1.2 \cdot 10^4 \text{ S m}^{-1}$ . This value is just slightly lower than that reported by S. Johnsen et al. for 0.033 %  $\text{PbCl}_2$ -doped  $\text{PbS}_{0.84}\text{Te}_{0.16}$  nanomaterials obtained through thermodynamic phase segregation:  $\sim 2 \cdot 10^4 \text{ S m}^{-1}$  at 700 K.<sup>77</sup>

While in the present work PbTe and PbS phases were not intentionally doped, a doping-like effect occurred when mixing both semiconductors at the nanometer scale.<sup>38-40</sup> This nanocrystal-based doping translated into larger electrical conductivities but slightly lower absolute values of the Seebeck coefficient (Figures 11, 12).

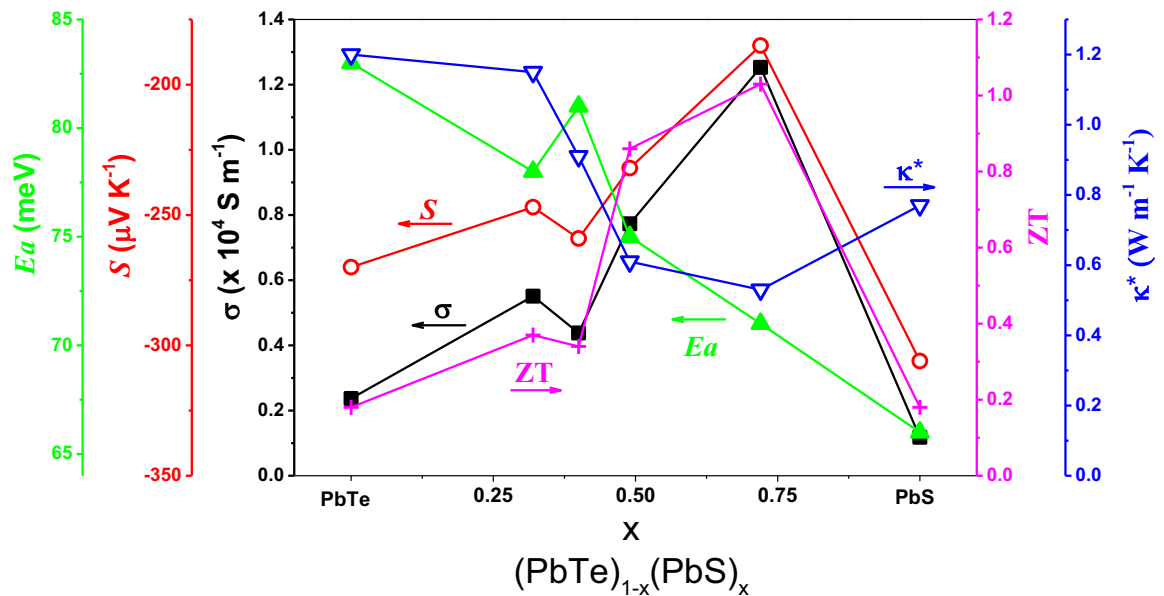


**Figure 12.** Electrical conductivity ( $\sigma$ ), Seebeck coefficient ( $S$ ), porosity-corrected thermal conductivity ( $\kappa^*$ ) and thermoelectric figure of merit ( $ZT$ ) at 710 K and activation energy for electrical transport in the low temperature range ( $E_a$ ), as a function of the PbS concentration in  $(\text{PbTe})_{1-x}(\text{PbS})_x$  nanomaterials.

*Thermal conductivity.* Thermal conductivity values were calculated from thermal diffusivities obtained using flash diffusivity measurements. In nanomaterials, when calculating thermal

conductivity from thermal diffusivity data, the surface contribution to the molar heat capacity needs to be taken into account.<sup>78</sup> Heat capacities were measured by a relaxation method. As expected, the experimental heat capacity values obtained from  $(\text{PbTe})_{1-x}(\text{PbS})_x$  nanomaterials significantly exceeded the Dulong-Petit approximation (Figure 13A). However, surprisingly lower heat capacity values were obtained for nanocomposites when compared to pure nanomaterials. The thermal conductivities calculated from experimental heat capacities are displayed in figure 13. Very low thermal conductivities were obtained for all the nanomaterials characterized. These low thermal conductivity values were in part associated to the material porosity. The porosity contribution could be roughly estimated and removed from the calculated thermal conductivities using Maxwell-Eucken's equation (experimental section).<sup>47, 48</sup> Figure 13 (B and C) displays the porosity corrected thermal conductivities ( $\kappa^*$ ). Taking into account the intrinsic character of the two material components, the electronic contribution to the thermal conductivity ( $\kappa_{\text{el}}^*$ ) was calculated using the Wiedemann-Franz (WF) law assuming the nondegenerated limit for the Lorenz number ( $1.5 \times 10^{-8} \text{ W } \Omega \text{ K}^{-2}$ ).<sup>18, 21, 79, 80</sup>

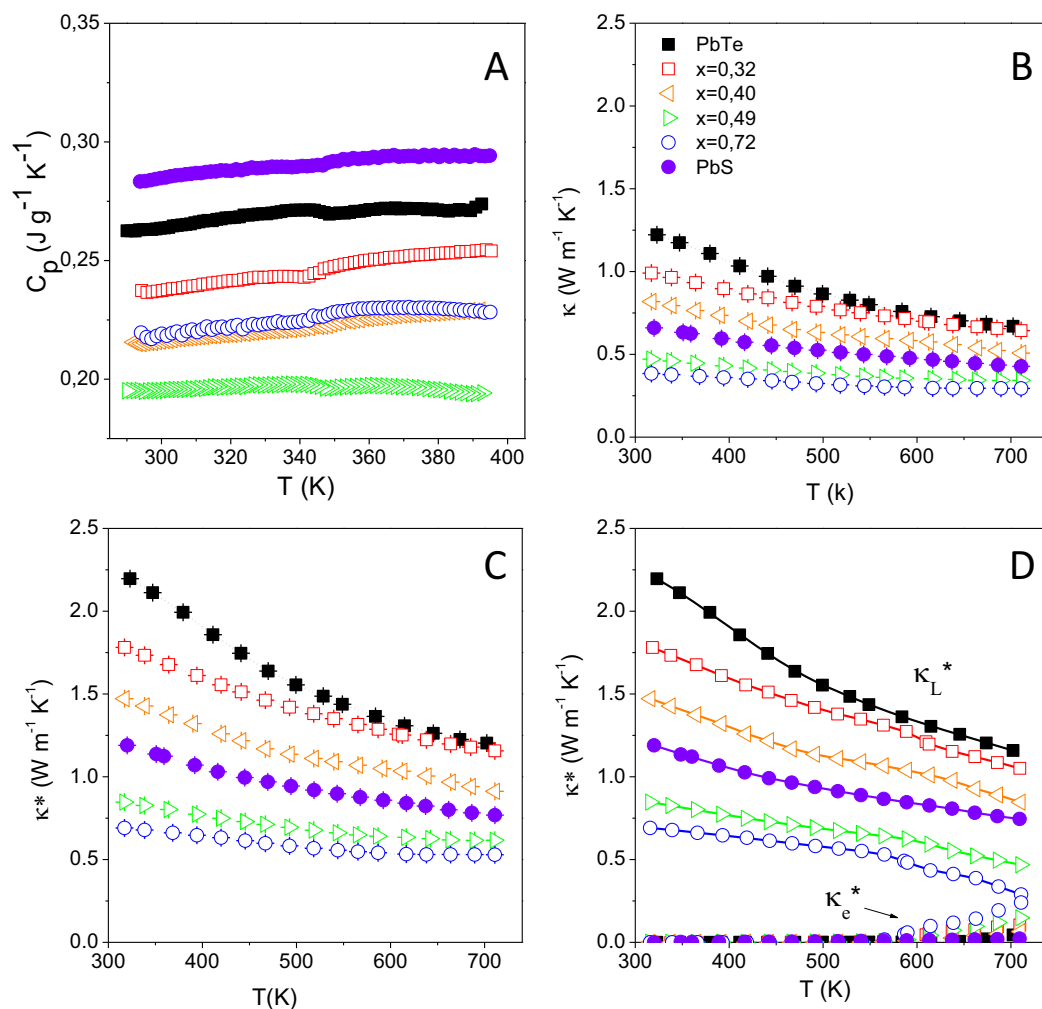


**Figure 13.** Heat Capacity (A), Thermal conductivity (B) and porosity-corrected thermal conductivity (C); and lattice and electronic contribution to the corrected thermal conductivity (D) of  $(\text{PbTe})_{1-x}(\text{PbS})_x$  nanomaterials.

After porosity correction, thermal conductivities were still exceptionally low.<sup>18, 77</sup> The thermal conductivity of the pure PbTe nanomaterial was 1.2 W/mK at 700 K. Thermal conductivity monotonically decreased with the concentration of PbS in  $(\text{PbTe})_{1-x}(\text{PbS})_x$  nanocomposites (Figure 12). The lowest thermal conductivity,  $0.53 \text{ Wm}^{-1}\text{k}^{-1}$ , was obtained for  $(\text{PbTe})_{0.28}(\text{PbS})_{0.72}$  at 710 K. Slightly higher thermal conductivities were obtained for PbS:  $0.77 \text{ Wm}^{-1}\text{k}^{-1}$  at 709 K.

This value still represents a strong reduction with respect to the  $1.5 \text{ W m}^{-1} \text{ K}^{-1}$  at 730 K reported for bulk PbS.

The very low thermal conductivities obtained were associated to the efficient scattering of phonons at the high density of grain boundaries and crystal interfaces within the  $(\text{PbTe})_{1-x}(\text{PbS})_x$  nanomaterials. In nanocomposites, phonon scattering was further enhanced by the acoustic impedance mismatch between PbTe and PbS phases. The incoherent-nature of interfaces in bottom-up assembled nanocomposites additionally enhanced phonon scattering efficiency. Another parameter that may contribute to phonon scattering within the produced  $(\text{PbTe})_{1-x}(\text{PbS})_x$  nanocomposites is the partial phase alloying detected. Alloying or replacement of Te by S ions in PbTe and of S by Te ions in PbS introduced high densities of point defects. Taking into account the large difference in size between Te and S ions, such replacement may effectively scatter short wavelength phonons and thus contribute to further reduce the nanocomposite thermal conductivity. Phase alloying was stronger the larger the concentration of sulfur in the nanocomposite. This experimental observation partially explains the decrease of thermal conductivity with the increase of the PbS content.

*Thermoelectric figure of merit.* Figure 14 displays the thermoelectric figure of merit calculated for the different  $(\text{PbTe})_{1-x}(\text{PbS})_x$  nanomaterials. The maximum ZT value for pure PbTe and PbS nanostructured material obtained were 0.18 at 700 K. A similar thermoelectric figure of merit was reported for undoped bulk PbS.<sup>21</sup> Nanocomposites obtained from core-shell NPs were characterized by figures of merit substantially higher than those of pure PbTe and PbS nanomaterials. From the compositions studied here, the nanocomposite with the largest figure of merit was  $(\text{PbTe})_{0.28}(\text{PbS})_{0.72}$ . For this nanocomposite a figure of merit ZT up to 1.07 at 700 K

was calculated. The larger figures of merit obtained for nanocomposites when compared to pure nanomaterials were attributed to two main effects: i) a synergic effect between the charge carriers of each phase resulted in nanocomposites with electrical conductivities up to one order of magnitude higher than pure materials; ii) enhanced phonon scattering at multiple length scales provided nanocomposites with significantly lower thermal conductivities.

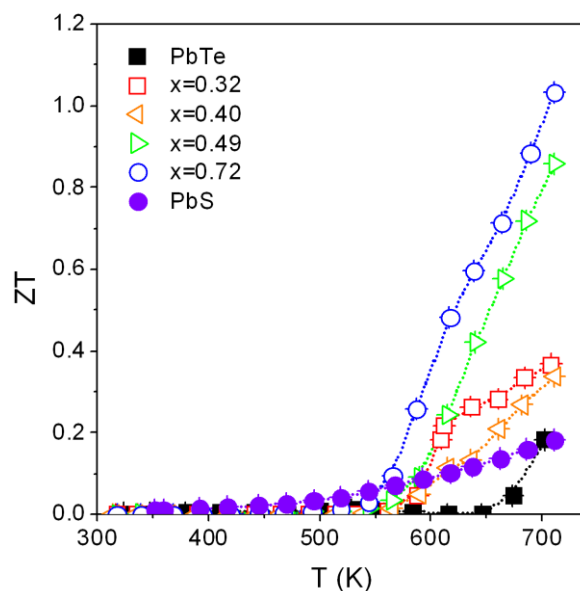


**Figure 14.** Thermoelectric figure of merit (ZT) of  $(\text{PbTe})_{1-x}(\text{PbS})_x$  nanomaterials.

Nanomaterials stability and measurement reproducibility are major concerns, particularly in bottom-up assembled nanocomposites. We tested the thermoelectric performance stability of the nanocomposites by measuring the materials thermoelectric properties multiple times in different days. Figure 15 displays data obtained from measuring the thermoelectric properties of  $(\text{PbTe})_{0.28}(\text{PbS})_{0.72}$  four times. We observed that after the first measurement higher electrical conductivities and Seebeck coefficients and lower thermal conductivities were obtained in the low temperature range. After the second measurement, thermoelectric properties remained



unchanged. We hypothesize that changes between the first and next cycles may have its origin in a slight loss of sulfur.<sup>81</sup> At above 500 K small amounts of S may leave the PbS surface during the measurement. The result of such migration is a slight increase of the free electrons concentration and thus of the electrical conductivity. The concentration of sulfur in the surface may be stabilized after the first measurement as further measurements did not show appreciable changes neither at high or low temperatures. It must be pointed out that such potential sulfur loss was not detected by ICP or EDX.

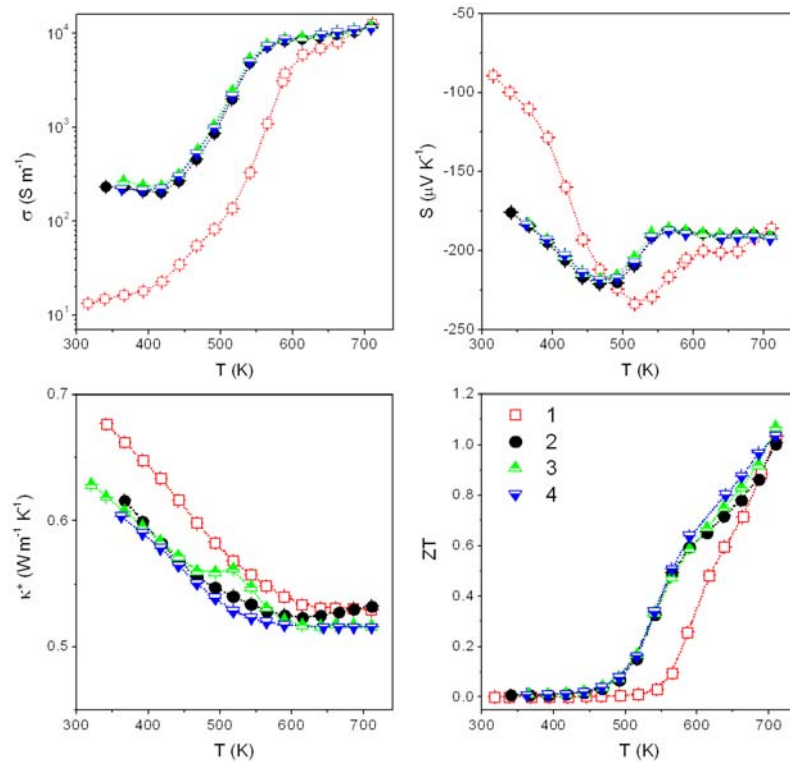


**Figure 15.** Multiple measurements of the electrical conductivity ( $\sigma$ ), thermopower (S), porosity-corrected thermal conductivity ( $\kappa^*$ ) and thermoelectric figure of merit (ZT) from the same  $(\text{PbTe})_{0.28}(\text{PbS})_{0.72}$  pellet.

## 7.5 Conclusions

---

A rapid, high-yield and scalable colloidal synthetic route to prepare PbTe@PbS core-shell NPs with unprecedented narrow size distributions and exceptional control over their composition was presented.  $(\text{PbTe})_{1-x}(\text{PbS})_x$  nanocomposites obtained from the bottom-up assembly of  $(\text{PbTe})_{1-x}@\text{(PbS)}_x$  NPs were highly homogeneous at the micron scale but contained a high distribution of nanoscale inhomogeneities. These  $(\text{PbTe})_{1-x}(\text{PbS})_x$  nanocomposites were characterized by higher electrical conductivities and lower thermal conductivities than pure PbTe and PbS nanomaterials. We associated the higher electrical conductivities to a nanocrystal-based doping effect. The lower thermal conductivities were explained by the acoustic impedance mismatch between PbTe and PbS phases, the incoherent-nature of interfaces and the partial phase alloying. As a result, we obtained nanocomposites with thermoelectric figures of merit much higher than pure PbTe and PbS nanomaterials.

The design and engineering of nanocomposites by the bottom-up assembly of colloidal building blocks is a very recent research field. A lot of effort is still needed to optimize and completely understand the performance and properties of the nanomaterials produced by this method. However, the high thermoelectric figures of merit obtained here serve as an example of the potential of the proposed processes to produce high-performing nanomaterials. It also allows establishing the bottom-up assembly of colloidal NPs as a serious approach to produce functional nanocomposites with unprecedented and unparallel control over materials phase and composition at the nanometer scale.

## 7.6 References

---

- (1) Yin, Y.; Alivisatos, A. P., *Nature* **2005**, 437, 664-670.

- (2) Talapin, D. V.; Lee, J.-S.; Kovalenko, M. V.; Shevchenko, E. V., *Chem. Rev.* **2010**, 110, 389-458.
- (3) Ibáñez, M.; Zamani, R.; Li, W.; Shavel, A.; Arbiol, J.; Morante, J. R.; Cabot, A., *Cryst. Growth Des.* **2012**, 12, 1085-1090.
- (4) Li, W.; Shavel, A.; Guzman, R.; Rubio-Garcia, J.; Flox, C.; Fan, J.; Cadavid, D.; Ibáñez, M.; Arbiol, J.; Morante, J. R.; Cabot, A., *Chem. Commun.* **2011**, 47, 10332-10334.
- (5) Ibáñez, M.; Guardia, P.; Shavel, A.; Cadavid, D.; Arbiol, J.; Morante, J. R.; Cabot, A., *J. Phys. Chem. C* **2011**, 115, 7947-7955.
- (6) Jun, Y.-W.; Choi, J.-S.; Cheon, J., *Angew. Chem. Int. Ed.* **2006**, 45, 3414-3439.
- (7) Hicks, L. D.; Dresselhaus, M. S., *Phys. Rev. B* **1993**, 47, 12727-12731.
- (8) Hicks, L. D.; Harman, T. C.; Dresselhaus, M. S., *Applied Physics Letters* **1993**, 63, 3230-3232.
- (9) Humphrey, T. E.; Linke, H., *Phys. Rev. Lett.* **2005**, 94, 096601.
- (10) Zide, J. M. O.; Vashaee, D.; Bian, Z. X.; Zeng, G.; Bowers, J. E.; Shakouri, A.; Gossard, A. C., *Phys. Rev. B* **2006**, 74, 205335.
- (11) Vashaee, D.; Shakouri, A., *Phys. Rev. Lett.* **2004**, 92, 106103.
- (12) Faleev, S. V.; Léonard, F., *Phys. Rev. B* **2008**, 77, 214304.
- (13) Martin, J.; Wang, L.; Chen, L.; Nolas, G. S., *Phys. Rev. B* **2009**, 79, 115311.
- (14) Harman, T. C.; Taylor, P. J.; Walsh, M. P.; LaForge, B. E., *Science* **2002**, 297, 2229-2232.
- (15) Venkatasubramanian, R.; Siivola, E.; Colpitts, T.; O'Quinn, B., *Nature* **2001**, 413, 597-602.
- (16) Pei, Y.; Lensch-Falk, J.; Toberer, E. S.; Medlin, D. L.; Snyder, G. J., *Adv. Funct. Mater.* **2010**, 21, 241-249.
- (17) Biswas, K.; He, J.; Wang, G.; Lo, S.-H.; Uher, C.; Dravid, V. P.; Kanatzidis, M. G., *Energy Environ. Sci.* **2011**, 4, 4675-4684.
- (18) Girard, S. N.; He, J.; Zhou, X.; Shoemaker, D.; Jaworski, C. M.; Uher, C.; Dravid, V. P.; Heremans, J. P.; Kanatzidis, M. G., *J. Am. Chem. Soc.* **2011**, 133, 16588-16597.
- (19) Androulakis, J.; Lin, C.-H.; Kong, H.-J.; Uher, C.; Wu, C.-I.; Hogan, T.; Cook, B. A.; Caillat, T.; Paraskevopoulos, K. M.; Kanatzidis, M. G., *J. Am. Chem. Soc.* **2007**, 129, 9780-9788.
- (20) Girard, S. N.; He, J.; Li, C.; Moses, S.; Wang, G.; Uher, C.; Dravid, V. P.; Kanatzidis, M. G., *Nano Letters* **2010**, 10, 2825-2831.

- (21) Zhao, L.-D.; Lo, S.-H.; He, J.; Li, H.; Biswas, K.; Androulakis, J.; Wu, C.-I.; Hogan, T. P.; Chung, D.-Y.; Dravid, V. P.; Kanatzidis, M. G., *J. Am. Chem. Soc.* **2011**, 133, 20476-20487.
- (22) Zhao, L.-D.; He, J.; Wu, C.-I.; Hogan, T. P.; Zhou, X.; Uher, C.; Dravid, V. P.; Kanatzidis, M. G., *J. Am. Chem. Soc.* **2012**, 134, 7902-7912.
- (23) Girard, S. N.; Schmidt-Rohr, K.; Chasapis, T. C.; Hatzikraniotis, E.; Njegic, B.; Levin, E. M.; Rawal, A.; Paraskevopoulos, K. M.; Kanatzidis, M. G., *Adv. Funct. Mater.* **2012**, n/a-n/a.
- (24) Mehta, R. J.; Zhang, Y.; Karthik, C.; Singh, B.; Siegel, R. W.; Borca-Tasciuc, T.; Ramanath, G., *Nat. Mater.* **2012**, 11, 233-240.
- (25) Kovalenko, M. V.; Spokoyny, B.; Lee, J. S.; Scheele, M.; Weber, A.; Perera, S.; Landry, D.; Talapin, D. V., *J. Am. Chem. Soc.* **2010**, 132, 6686-6695.
- (26) Scheele, M.; Oeschler, N.; Meier, K.; Kornowski, A.; Klinke, C.; Weller, H., *Adv. Funct. Mater.* **2009**, 19, 3476-3483.
- (27) Scheele, M.; Oeschler, N.; Veremchuk, I.; Peters, S. O.; Littig, A.; Kornowski, A.; Klinke, C.; Weller, H., *ACS Nano* **2011**, 5, 8541-8551.
- (28) Scheele, M.; Oeschler, N.; Veremchuk, I.; Reinsberg, K. G.; Kreuziger, A. M.; Kornowski, A.; Broekaert, J.; Klinke, C.; Weller, H., *ACS Nano* **2010**, 4, 4283-4291.
- (29) Ibáñez, M.; Zamani, R.; Lalonde, A.; Cadavid, D.; Li, W.; Shavel, A.; Arbiol, J.; Morante, J. R.; Gorsse, S.; Snyder, G. J.; Cabot, A., *J. Am. Chem. Soc.* **2012**, 134, 4060-4063.
- (30) Ibáñez, M.; Zamani, R.; Li, W.; Cadavid, D.; Gorsse, S.; Katcho, N. A.; Shavel, A.; López, A. M.; Morante, J. R.; Arbiol, J.; Cabot, A., *Chem. Mater.* **2012**, 24, 4615-4622.
- (31) Ibáñez, M.; Cadavid, D.; Zamani, R.; García-Castelló, N.; Izquierdo-Roca, V.; Li, W.; Fairbrother, A.; Prades, J. D.; Shavel, A.; Arbiol, J.; Pérez-Rodríguez, A.; Morante, J. R.; Cabot, A., *Chem. Mater.* **2012**, 24, 562-570.
- (32) Ibáñez, M.; Cadavid, D.; Anselmi Tamburini, U.; Zamani, R.; Gorsse, S.; Li, W.; Shavel, A.; López, A. M.; Morante, J. R.; Arbiol, J.; Cabot, A., *J. Mater. Chem. A* **2013**, 1, 1421.
- (33) Cadavid, D.; Ibáñez, M.; Gorsse, S.; López, A. M.; Cirera, A.; Morante, J.; Cabot, A., *J. Nanopart. Res.* **2012**, 14, 1-10.
- (34) Lee, J.-S.; Bodnarchuk, M. I.; Shevchenko, E. V.; Talapin, D. V., *J. Am. Chem. Soc.* **2010**, 132, 6382-6391.
- (35) Lee, J.-S.; Shevchenko, E. V.; Talapin, D. V., *J. Am. Chem. Soc.* **2008**, 130, 9673-9675.

- (36) Shevchenko, E. V.; Ringler, M.; Schwemer, A.; Talapin, D. V.; Klar, T. A.; Rogach, A. L.; Feldmann, J.; Alivisatos, A. P., *J. Am. Chem. Soc.* **2008**, 130, 3274-3275.
- (37) Talapin, D. V.; Shevchenko, E. V.; Bodnarchuk, M. I.; Ye, X.; Chen, J.; Murray, C. B., *Nature* **2009**, 461, 964-967.
- (38) Urban, J. J.; Talapin, D. V.; Shevchenko, E. V.; Kagan, C. R.; Murray, C. B., *Nat. Mater.* **2007**, 6, 115-121.
- (39) Hanrath, T., *J. Vac. Sci. Technol. A* **2012**, 30, 030802.
- (40) Ko, D.-K.; Urban, J. J.; Murray, C. B., *Nano Lett.* **2010**, 10, 1842-1847.
- (41) Hines, M. A.; Scholes, G. D., *Adv. Mater.* **2003**, 15, 1844-1849.
- (42) Murphy, J. E.; Beard, M. C.; Norman, A. G.; Ahrenkiel, S. P.; Johnson, J. C.; Yu, P.; Mičić, O. I.; Ellingson, R. J.; Nozik, A. J., *J. Am. Chem. Soc.* **2006**, 128, 3241-3247.
- (43) Bernal, S.; Botana, F. J.; Calvino, J. J.; López-Cartes, C.; Pérez-Omil, J. A.; Rodríguez-Izquierdo, J. M., *Ultramicroscopy* **1998**, 72, 135-164.
- (44) Arbiol, J.; Cirera, A.; Peiro, F.; Cornet, A.; Morante, J. R.; Delgado, J. J.; Calvino, J. J., *Appl. Phys. Lett.* **2002**, 80, 329-331.
- (45) Uccelli, E.; Arbiol, J.; Morante, J. R.; Fontcuberta i Morral, A., *ACS Nano* **2010**, 4, 5985-5993.
- (46) Arbiol, J.; Magen, C.; Becker, P.; Jacopin, G.; Chernikov, A.; Schafer, S.; Furtmayr, F.; Tchernycheva, M.; Rigutti, L.; Teubert, J.; Chatterjee, S.; Morante, J. R.; Eickhoff, M., *Nanoscale* **2012**, 4, 7517-7524.
- (47) Yang, L.; Wu, J. S.; Zhang, L. T., *J. Alloys Compd.* **2004**, 364, 83-88.
- (48) Adachi, J.; Kurosaki, K.; Uno, M.; Yamanaka, S., *J. Alloys Compd.* **2007**, 432, 7-10.
- (49) Reiss, P.; Bleuse, J.; Pron, A., *Nano Lett.* **2002**, 2, 781-784.
- (50) Peng, X.; Schlamp, M. C.; Kadavanich, A. V.; Alivisatos, A. P., *J. Am. Chem. Soc.* **1997**, 119, 7019-7029.
- (51) Chalkidou, A.; Simeonidis, K.; Angelakeris, M.; Samaras, T.; Martinez-Boubeta, C.; Balcells, L.; Papazisis, K.; Dendrinou-Samara, C.; Kalogirou, O., *J. Magn. Magn. Mater.* **2011**, 323, 775-780.
- (52) Gerion, D.; Pinaud, F.; Williams, S. C.; Parak, W. J.; Zanchet, D.; Weiss, S.; Alivisatos, A. P., *J. Phys. Chem. B* **2001**, 105, 8861-8871.

- (53) Wise, F. W., *Acc. Chem. Res.* **2000**, 33, 773-780.
- (54) Talapin, D. V.; Murray, C. B., *Science* **2005**, 310, 86-89.
- (55) Konstantatos, G.; Howard, I.; Fischer, A.; Hoogland, S.; Clifford, J.; Klem, E.; Levina, L.; Sargent, E. H., *Nature* **2006**, 442, 180-183.
- (56) McDonald, S. A.; Konstantatos, G.; Zhang, S.; Cyr, P. W.; Klem, E. J. D.; Levina, L.; Sargent, E. H., *Nat. Mater.* **2005**, 4, 138-142.
- (57) Choi, J. J.; Lim, Y.-F.; Santiago-Berrios, M. E. B.; Oh, M.; Hyun, B.-R.; Sun, L.; Bartnik, A. C.; Goedhart, A.; Malliaras, G. G.; Abruña, H. c. D.; Wise, F. W.; Hanrath, T., *Nano Lett.* **2009**, 9, 3749-3755.
- (58) Pattantyus-Abraham, A. G.; Kramer, I. J.; Barkhouse, A. R.; Wang, X.; Konstantatos, G.; Debnath, R.; Levina, L.; Raabe, I.; Nazeeruddin, M. K.; Grätzell, M.; Sargent, E. H., *ACS Nano* **2010**, 4, 3374-3380.
- (59) Ma, W.; Luther, J. M.; Zheng, H.; Wu, Y.; Alivisatos, A. P., *Nano Lett.* **2009**, 9, 1699-1703.
- (60) Tang, J.; Liu, H.; Zhitomirsky, D.; Hoogland, S.; Wang, X.; Furukawa, M.; Levina, L.; Sargent, E. H., *Nano Lett.* **2012**, 12, 4889-4894.
- (61) Koleilat, G. I.; Levina, L.; Shukla, H.; Myrskog, S. H.; Hinds, S.; Pattantyus-Abraham, A. G.; Sargent, E. H., *ACS Nano* **2008**, 2, 833-840.
- (62) Luther, J. M.; Law, M.; Beard, M. C.; Song, Q.; Reese, M. O.; Ellingson, R. J.; Nozik, A. J., *Nano Lett.* **2008**, 8, 3488-3492.
- (63) Hoogland, S.; Sukhovatkin, V.; Howard, I.; Cauchi, S.; Levina, L.; Sargent, E. H., *Opt. Express* **2006**, 14, 3273-3281.
- (64) Michalet, X.; Pinaud, F. F.; Bentolila, L. A.; Tsay, J. M.; Doose, S.; Li, J. J.; Sundaresan, G.; Wu, A. M.; Gambhir, S. S.; Weiss, S., *Science* **2005**, 307, 538-544.
- (65) Gill, R.; Zayats, M.; Willner, I., *Angew. Chem. Int. Ed.* **2008**, 47, 7602-7625.
- (66) Klem, E. J. D.; MacNeil, D. D.; Levina, L.; Sargent, E. H., *Adv. Mater.* **2008**, 20, 3433-3439.
- (67) Zhao, Y.; Burda, C., *ACS Appl. Mater. Interfaces* **2009**, 1, 1259-1263.
- (68) Mokari, T.; Zhang, M.; Yang, P., *J. Am. Chem. Soc.* **2007**, 129, 9864-9865.
- (69) Zyubina, T. S.; Neudachina, V. S.; Yashina, L. V.; Shtanov, V. I., *Surf. Sci.* **2005**, 574, 52-64.
- (70) Yashina, L. V.; Zyubina, T. S.; Püttner, R.; Zyubin, A. S.; Shtanov, V. I.; Tikhonov, E. V., *J. Phys. Chem. C* **2008**, 112, 19995-20006.

- (71) Fu, H.; Tsang, S.-W.; Zhang, Y.; Ouyang, J.; Lu, J.; Yu, K.; Tao, Y., *Chem. Mater.* **2011**, *23*, 1805-1810.
- (72) Zhang, H.; Hu, B.; Sun, L.; Hovden, R.; Wise, F. W.; Muller, D. A.; Robinson, R. D., *Nano Lett.* **2011**, *11*, 5356-5361.
- (73) Gyorffy, B. L., *Phys. Rev. B* **1972**, *5*, 2382-2384.
- (74) Soven, P., *Phys. Rev.* **1967**, *156*, 809-813.
- (75) Volykhov, A.; Yashina, L.; Shtanov, V., *Inorg. Mater.* **2006**, *42*, 596-604.
- (76) Seto, J. Y. W., *J. Appl. Phys.* **1975**, *46*, 5247-5254.
- (77) Johnsen, S.; He, J.; Androulakis, J.; Dravid, V. P.; Todorov, I.; Chung, D. Y.; Kanatzidis, M. G., *J. Am. Chem. Soc.* **2011**, *133*, 3460-3470.
- (78) Rupp, J.; Birringer, R., *Phys. Rev. B* **1987**, *36*, 7888-7890.
- (79) Biswas, K.; He, J.; Blum, I. D.; Wu, C.-I.; Hogan, T. P.; Seidman, D. N.; Dravid, V. P.; Kanatzidis, M. G., *Nature* **2012**, *489*, 414-418.
- (80) May, A. F.; Fleurial, J.-P.; Snyder, G. J., *Phys. Rev. B* **2008**, *78*, 125205.
- (81) Scanlon, W. W., *Phys. Rev.* **1953**, *92*, 1573-1575.

# Conclusions

This dissertation has focused on three main topics: i) synthesis of colloidal nanoparticles with controlled size, morphology, composition, and crystal phase; ii) production of bulk nanomaterials from the bottom-up assembly of colloidal nanoparticles; iii) Characterization of the thermoelectric performance of the nanomaterials produced.

The work developed has allowed determining the following conclusions:

1. The conditions to establish the focusing or defocusing regime with a diffusion-reaction model has been extended for nanorods. The model has been tested experimentally for  $\text{Bi}_2\text{S}_3$  nanorods.
2. The nanoparticles synthesis control has been extended to quaternary compositions in Copper-based chalcogenides. A large excess of  $\text{SeO}_2$  is required to obtain stable quaternary NP. Their composition control has been achieved by controlling the precursor concentration or the reaction temperature. The average nanoparticles size could be tuned by the concentration of the amine in solution or the nucleation temperature.
3. The synthesized nanoparticles were successfully used as building blocks for the production of bulk nanomaterials or nanocomposites. Highly homogeneous nanocomposites could be produced by the bottom-up assembly of nanoheterostructures.
4. Copper-based chalcogenides has been proven as promising candidates for thermoelectrics applications.
5. Nanocomposites produced by the bottom bottom-up assembly of nanoheterostructures have been proven as excellent candidates to boost the thermoelectric performance.





## Future work

The design and engineering of nanocomposites by the bottom-up assembly of colloidal building blocks is a very recent research field. A lot of effort is still needed to optimize and completely understand the performance and properties of the nanomaterials produced by this method.

The huge versatility of colloidal synthetic routes has the potential to create new complex materials at the nanoscale with completely unpredicted results that can boost the thermoelectric performance. The endless possibilities of materials combinations are waiting for fearless researchers to undertake them. While hitting upon the proper combination of materials can be an exasperating task, there are several more concrete and practical problems to defeat.

1- *Removal of organic ligands to improve electrical conductivity.* In the present work, the strategy to remove the organic ligands has been the thermal treatment. Despite its partial effectiveness, the carbon species present in the final nanomaterial could detriment their final performance. During the last years several alternative post-synthetic treatments has been developed to remove or replace the highly insulating organic molecules used during the NPs synthesis. However, the practical application of such methods is still far to be truly useful at large scale. Problems such oxidation of the NPs surface, toxicity or/and highly reactivity of the compounds involved in the removal/replacement of the long-chain organic ligands need to be completely avoided.

2- *Nanoparticles assembly and compaction to obtain high density pellets.* In the work presented, bulk nanomaterials were obtained by pressing the annealed nanoparticles at room temperature. Most sophisticated techniques such hot pressing and spark plasma sintering can be

used to produce high density pellets. However, special care must be taken to avoid a large increase of the crystal size or in the case of nanoheterostructures to produce undesired alloys. Additionally, the nature of the species present in the NPs surface can play a crucial role during their compaction.

3- *Doping of nanoparticle to obtain the optimum charge carrier concentration.* One of the main problems of colloidal synthesis is also one of their main advantages: self-purification. In bulk materials or thin films, tuning the carrier density can be easily achieved by introducing specific impurities. Although doping has been achieved for several kind of particles, there is not a straightforward and general strategy valid in all the synthesized NPs. The reduced size of the NPs strongly hinders to maintain impurities within their crystal structure. While not-very pure precursors can help to reduce production costs, the use of nanoparticles for electronics and optoelectronics devices requires a precise control of the charge carrier density.

# Curriculum Vitae

## PERSONAL DATA

---

Maria Ibáñez i Sabaté

**Birthday:** 14th October of 1983

**Nationality:** Spanish

**Adress:** C. Angel Guimera, 12, P2 porta 4, St. Adria del Besos 08930 (Spain)

**Phone number:** +34 685170911

**E-mail:** [mariasabate@gmail.com](mailto:mariasabate@gmail.com), mariaibanez@ub.edu



## ACADEMIC TRAINING

---

2003/2008	Degree in Physics	University of Barcelona, Barcelona, Spain.
09/2009	Master in Engineering Physics	University of Barcelona, Barcelona, Spain.
2009-present	PhD Program	University of Barcelona, Barcelona, Spain.

## FELLOWSHIPS

---

01/2002-01/2003	Degree fellowship	Spanish Government
01/2006 -01/2007	Degree fellowship	Spanish Government
09/2007- 07/2008	Mobility Grant. Uppsala Universitet (Sweden)	Catalan Government
08/2009- 07/2013	PhD Fellowship	Spanish Government

## PROFESSIONAL EXPERIENCE

---

Period	Position/University/Advisor	Research topic
10/2008-12/2008	Junior researcher. Electronics department, University of Barcelona, Spain. <i>Head of the group M2E – J.R. Morante</i> <i>Head of the group FN - Andreu Cabot</i>	<b>Synthesis of Au Nanoparticles with different shapes and sizes.</b>
01/2008-08/2009	Junior researcher. Electronics department, University of Barcelona, Spain. <i>Head of the group M2E – J.R. Morante</i> <i>Head of the group FN - Andreu Cabot</i>	<b>Synthesis of nanoparticles and investigation of their assembly by LB</b>
09/2009-12/2010	Visiting researcher. Institute for Nanoscience and Cryogenics (INAC), CEA, France. <i>Head of the group - Peter Reiss</i>	<b>Synthesis of quaternary nanoparticles and their surface modification.</b>
06/2010-10/2010	Visiting researcher. Department of Chemistry. University of Chicago, USA. <i>Head of the group - Dmitri Talapin</i>	<b>Synthesis of core-shell structures for Thermoelectric applications</b>
08/2011-10/2011	Visiting researcher. Thermoelectrics group at Caltech Materials Science, USA. <i>Head of the group - G. Jeffrey Snyder</i>	<b>Thermoelectric measurements on quaternary Selenides</b>
05/2012-7/2012	Visiting researcher <i>Head of the group - Richard Robinson</i>	<b>Synthesis of semiconductor core-shell structures by cation exchange</b>

## RESEARCH INTEREST

---

**Synthesis and self-assembly of semiconductor and metallic nanocrystals:** Solution phase synthesis, structural and spectroscopic characterization. Self-assembly of nanocrystals into long range ordered superlattices. General aspects of nucleation and growth of nanometer sized semiconductor and metal particles in a colloidal solution.

**Energy-related applications of nanomaterials:** Applications of semiconductor nanomaterials in light-emitting, photovoltaic and thermoelectric devices. Charge and heat transport in nanocrystal solids. Field-effect devices on semiconductor nanowires and nanocrystal arrays

## PUBLICATIONS

---

1. A. Cabot, **M. Ibáñez**, P. Guardia and A. P. Alivisatos "Reaction regimes on the Synthesis of Hollow Particles by the Kirkendall Effect" *J. Am. Chem. Soc.*, 2009, 131 (32), pp 11326–11328
2. **M. Ibáñez**, P. Guardia, A. Shavel, D. Cadavid, J. Arbiol, J.R. Morante, and A. Cabot; "Growth Kinetics of Asymmetric Bi<sub>2</sub>S<sub>3</sub> Nanocrystals: Size Distribution Focusing in Nanorods"; *J. Phys. Chem. C*, 2011, 115 (16), pp 7947–7955
3. **M. Ibáñez**, J. Fan, W. Li, D. Cadavid, R. Nafria, A. Carrete, and A. Cabot; "Means and limits of control of the shell parameters in hollow cadmium chalcogenides obtained by the Kirkendall effect"; *Chem. Mater.*, 2011, 23 (12), pp 3095–3104
4. W. Li, A. Shavel, R. Guzman, J. Fan, D. Cadavid, **M. Ibáñez**, J. Arbiol, and A. Cabot; "Morphology Evolution of Cu<sub>2-x</sub>S Nanoparticles: From Spheres to Dodecahedrons" *Chem. Commun.*, 2011, 47, pp 10332-10334
5. **M. Ibáñez**, D. Cadavid, R. Zamani, N. García-Castelló, V. Izquierdo-Roca†, W. Li, A. Fairbrother, J. D. Prades, A. Shavel, J. Arbiol, A. Pérez-Rodríguez, J. R. Morante, and A. Cabot; "Composition Control and Thermoelectric Properties of Quaternary Chalcogenide Nanocrystals: The Case of Stannite Cu<sub>2</sub>CdSnSe<sub>4</sub>" *Chem. Mater.*, 2012, 24 (3), pp 562–570

6. **M. Ibáñez**, R. Zamani, A. LaLonde, D. Cadavid, W. Li, A. Shavel, J. Arbiol, J. R. Morante, S. Gorsse, G. J. Snyder, and A. Cabot; "Cu<sub>2</sub>ZnGeSe<sub>4</sub> Nanocrystals: Synthesis and Thermoelectric Properties" *J. Am. Chem. Soc.*, 2012, 134 (9), pp 4060–4063
7. **M. Ibáñez**, R. Zamani, W. Li, A. Shavel, J. Arbiol, J. R. Morante, and A. Cabot; "Extending the Nanocrystal Synthesis Control to Quaternary Compositions" *Cryst. Growth Des.*, 12, 1085-1090 (2012)
8. A. Shavel, D. Cadavid, **M. Ibáñez**, A. Carrete, and A. Cabot; "Continuous production of Cu<sub>2</sub>ZnSnS<sub>4</sub> nanocrystals in a flow reactor" *J. Am. Chem. Soc.*, 2012, 134 (3), pp 1438-1441
9. J. Fan, R. Zamani, C. Fábrega, A. Shavel, C. Flox, **M. Ibáñez**, T. Andreu, A. M. López, J. Arbiol, J. R. Morante, and A. Cabot; Solution-growth and optoelectronic performance of ZnO: Cl/TiO<sub>2</sub> and ZnO: Cl/Zn<sub>x</sub>TiO<sub>y</sub>/TiO<sub>2</sub> core-shell nanowires with tunable shell thickness, *J. Phys. D: Appl. Phys.* 2012, 45, 415301
10. **M. Ibáñez**, D. Cadavid, U. Anselmi-Tamburini, R. Zamani, S. Gorsse, W. Li, A. Shavel, A. M. López, J. Arbiol, J. R. Morante, and A. Cabot; Crystallographic Control at the Nanoscale to Enhance Functionality: Polytypic Cu<sub>2</sub>GeSe<sub>3</sub> Nanoparticles as Thermoelectric Materials, *Chem. Mater.* 2012, 24 (23), pp 4615–4622
11. **M. Ibáñez**, D. Cadavid, U. Anselmi-Tamburini, R. Zamani, S. Gorsse, W. Li, A. Shavel, A. M. López, J. Arbiol, J. R. Morante, and A. Cabot; Colloidal Synthesis and Thermoelectric Properties of Cu<sub>2</sub>SnSe<sub>3</sub> Nanocrystals, *J. Materials Chemistry A*, 2013, 1 (4), 1421
12. D. Cadavid, **M. Ibáñez**, S. Gorsse, A. M. López, A. Cirera, J. R. Morante, and A. Cabot; Bottom-up processing of thermoelectric nanocomposites from colloidal nanocrystals building blocks: the case of Ag<sub>2</sub>Te-PbTe, *J. Nanopart. Res.*, November 2012, 14:1328
13. **M. Ibáñez**, S. Gorsse, R. Zamani, J. Arbiol, J. R. Morante, and A. Cabot; Core-shell nanoparticles as building blocks for the bottom-up production of functional nanocomposites: PbTe-PbS thermoelectric properties, just accepted *ACS Nano*

14. D. Cadavid, **M. Ibáñez**, A. Shavel, O. J. Dura, A. M. López and A. Cabot; Organic ligand displacement by metal salts to enhance nanoparticle functionality: Thermoelectric properties of Ag<sub>2</sub>Te; *J. Materials Chemistry A*, 2013, DOI: 10.1039/c3ta01455j
15. W. Li, R. Zamani, **M. Ibáñez**, D. Cadavid, A. Shavel, J. R. Morante, J. Arbiol, and A. Cabot; Metal ions to control the morphology of semiconductor nanoparticles: Copper Selenide Nanocubes, just accepted in *J. Am. Chem. Soc.*

## **PARTICIPATION IN CONFERENCES AND SEMINARS**

---

1. **M. Ibáñez**, P. Guardia, A. Shavel, D. Cadavid, J. Arbiol, J.R. Morante, and A. Cabot; "Growth Kinetics of Asymmetric Bi<sub>2</sub>S<sub>3</sub> Nanocrystals: Size Distribution Focusing in Nanorods"NaNaX<sub>4</sub> (Nanoscience with Nanocrystals) 2010; Poster presentation
2. D. Cadavid, **M. Ibáñez**, A. Shavel, J. R. Morante, and A. Cabot; Thermoelectric properties of solution-processed nanocomposites; *EMRS Fall meeting 2011*; Oral presentation.
3. D. Cadavid, **M. Ibáñez**, V. Fernández-Altale, and A. Cabot; Thermoelectric properties of solution-processed nanocomposites; *9th European Conference on Thermoelectrics (ECT2011)*; Oral Presentation
4. **M. Ibáñez**, D. Cadavid, R. Zamani, J. Arbiol, N. Garcia; D. Prades, J. R. Morante, and A. Cabot; Thermoelectric properties of nanostructured I<sub>2</sub> II IV VI<sub>4</sub> Adamantines; *9th European Conference on Thermoelectrics (ECT2011)*, Oral Presentation
5. R. Zamani, **M. Ibáñez**, D. Cadavid, J.R. Morante, A. Cabot, and J. Arbiol; Structural and morphological Changes in I<sub>2</sub>II IV VI<sub>4</sub> adamantines for thermoelectric application; *Microscopy at the Frontiers of Science 2011*, Oral Presentation
6. A. Cabot, **M. Ibáñez**, D. Cadavid, W. Li, A. Shavel, and J. R. Morante, Bottom-up processing of nanocomposites for thermoelectric applications, NaNaX<sub>5</sub> (Nanoscience with Nanocrystals) 2012; Poster Presentation



7. **M. Ibáñez**, D. Cadavid, R. Zamani, Jordi Arbiol, N. Garcia, J. Daniel Prades, J. R. Morante, and A. Cabot; *Copper-based diamond-like semiconductors as thermoelectric materials* EMRS-Spring meeting 2012; Oral Presentation
8. R. Zamani, **M. Ibáñez**, W. Li, D. Cadavid, J.R. Morante, A. Cabot and J. Arbiol; *Structural and morphological Changes in I2II IV VI4 adamantines for thermoelectric application*; *European Microscopy Congress 2012 (EMC2012)*, Poster Presentation

# **Annex**

---